Quantum coherent control with an optical frequency comb

Yin Cai

Thesis for Doctor Diploma of École Normale Supérieur in Physics

Quantum Coherent Control with an Optical Frequency Comb

by

CAI Yin
蔡寅

Defense the 21st, October, 2015

Members of Jury:

Prof. Christine Silberhorn	Referee, Univ. Paderborn, Germany
Prof. Jiangrui Gao	Referee, Shanxi Univ., China,
Prof. Mikhail Kolobov	Univ. Lille 1, France,
Prof. Michel Brune	College de France, France
Prof. Claude Fabre (invited)	Univ. Pierre et Marie Curie, France

Supervisors:

Prof. Nicolas Treps	Univ. Pierre et Marie Curie, France
Prof. Xinye Xu	East China Normal Univ., China

Quantum Coherent Control with an Optical Frequency Comb

Yin CAI,
Laboratoire Kastler Brossel, UPMC Univ. Paris 6, ENS, CNRS;
4 place Jussieu, 75252 Paris, France;
State Key Laboratory of Precision Spectroscopy, ECNU,
3663 North Zhongshan Road, 200241 Shanghai, China.
yin.cai@spectro.jussieu.fr

February 2, 2016

Abstract:

Multimode squeezing plays an essential role in quantum information processing and quantum metrology. Using optical frequency combs, we generate multi-temporal-mode state from a synchronously pumped optical parametric oscillator (SPOPO). An on-demand quantum network simulator is developed using the SPOPO and ultrafast pulse shaping; up-to-twelve-node cluster states and a six-partite quantum secret sharing protocol are experimentally emulated with this simulator. Furthermore, frequency resolved multipixel detectors are employed, and used to realize a line-shape-eight-node cluster state. We also developed a multimode quantum spectrometer, which is able to exceed the standard quantum limit for measuring manifold parameters of ultrafast pulses.

Key words: Quantum optics, Quantum information, Optical frequency comb, Multimode squeezed light, Quantum secret sharing, Cluster states.

Résumé:

Les états quantiques multimodes sont au cœur des protocoles de traitement quantique de l'information et de métrologie quantique. À partir d'un peigne de fréquence optique injectant un oscillateur paramétrique optique pompé en mode synchrone (SPOPO) nous avons généré des états multimodes en temps/fréquence. Un simulateur quantique est alors mis en place à partir de ce SPOPO et de mise en forme d'impulsion, et permet de mettre en évidence de états clusters pouvant compter jusque 12 nœuds et un protocole de partage de secret quantique à six partenaires. De plus, une détection multipixel résolue en fréquence est développée et utilisée pour réaliser un état cluster linéaire à 8 nœuds. Nous avons également utilisé cette source pour développer un spectromètre ayant une sensibilité allant au delà de celle imposée par les fluctuations du vide quantique.

Mots clés: Optique quantique, information quantique, peigne de fréquence optique, états quantiques multimodes, partage de secret quantique, états clusters.

Acknowledgement

The present thesis is accomplished within the cooperation program between l'École Normale Supérieure de Paris (ENS – Paris) in France and East China Normal University (ECNU) in China. I would like to give my sincere gratitude to those people on both sides who worked for this program and helped me to achieve this PhD thesis.

Firstly, I want to record my thesis supervisors Prof. Nicolas Treps (Laboratoire Kastler Brossel, UPMC, Paris France) and Prof. Xinye Xu (State Key Laboratory of Precision Spectroscopy, ECNU, Shanghai, China), for their great guidance and kind support during these years (2011-2015). And with the help and support of them, I could have an opportunity to conduct my physics research and accomplish my PhD thesis in two excellent groups where I can interact with many talent and nice people.

In 2008, I entered Prof. Xu's group as a master student in ECNU, Shanghai, who introduced me into the world of optics. During this master period, with the guidance of Prof. Xu, I gradually understood many important conceptions of lasers, atoms, etc, and learned how to manipulate optical experiments. Importantly, I had many interesting discussions and worked with my colleagues: Wenli Wang, Guohui Li, Qinghong Zhou, Jie Ye, Min Zhou, Zhihong Zhou, Ling Chen, Haiyao Tang. I also thank the people who are still working in this group, Xiaohang Zhang, Yiling Xu, Peng Xu, Qi Gao, and many other young colleagues.

Thanks to the cooperation program between l'École Normale Supérieure de Paris (ENS – Paris) in France and East China Normal University (ECNU) in China, in 2010 I met my French supervisor, Prof. Nicolas Treps, many French professors: Claude Fabre, Pierre-François Cohadon and Julien Laurat, who gave lectures about Quantum Optics and Quantum Physics. And theses lectures open a new world of quantum physics for me, and let me have the chance to implement my PhD in France.

From 2011 to 2015, I was lucky to have the chance to get in Nicolas' Group in LKB, Paris, and started my PhD thesis with the topic about ultrafast quantum optics. In Paris, it is full of wonderful memories in these years. I have to thank again my supervisor Nicolas, who gave me so many helps about science and the life in France. Nicolas always gave patient explanations in quantum optics, which let me have a very clear physics picture in my field. Also I appreciate Prof. Claude Fabre, who always inspired us in physics and gave so many kind suggestions and support. They both learned me many physics,

also helped me a lot in the life in Paris. And I must record my chinese supervisor Prof. Xu in ECNU, who always gave me support wherever I was in France or China, and this is quite important and helpful for my PhD.

I must also appreciate my research partners Doctor Renné Medeiros de Araújo, who helped me a lot in the beginning of my PhD and told me many details of the experiment in LKB, and our Post-doc Jonathan Roslund, with whom I worked together for three years. They both learned me a lot of details about the experiment in terms of theoretical and technical aspects. Especially, in these years, Jon improved me many experimental skills, and made me understand how to manipulate light.

Furthermore, I must say thanks to the other colleagues: Giulia Ferrini, who built the theoretical model of the multimode quantum information; Roman Schmeissner and Valérian Thiel, who worked in the other optical table next to mine in the same room, and we all knew how bad is the dark noise for our experiments; Clement Jacquard, who worked in the same optical table with me; and I have to extend my thanks to all the other colleagues in the group: Zhan Zheng, Francesco Arzani, Valentin Averchenko, Vanessa Chille, Pu Jian, Alexandre Brieussel, Valentina Parigi, Adrien Dufour, Luca La Volpe, and Young-Sik Ra. I appreciate very much all your help in the research and your accompany during my PhD period. With all of you, I could have a great PhD experience, full of interesting discussions and activities, thus I must say again thanks very much to my dear colleagues. And I owe many thanks to my other colleagues: O. Morin, K. Huang, J. Liu, H. Le Jeannic, Y.-C. Jeong. Thanks very much for you being in my PhD memories.

I am grateful to my French professors and colleagues in LKB: Pierre-François Cohadon, Director Heidmann Antoine, Élisabeth Giacobino, Alberto Bramati, François Néz, who were always patient to give helps and answer questions. I also owe my gratitude to the administrative staff in the lab who provided me a lot of convenience and patience particularly when I could not speak good French: Monique Granon, Laetitia Morel, Romain Rybka, Thierry Tardieu and Nora Aissous. And the administration in ECNU: Mme. Qian Yunhua, Liu Xiaoling. I also very appreciate the people working in the electronics shop and mechanics shop: Brigitte Delamour, Jean-Pierre Okpisz, and Jean-Michel Isac.

I would also like to acknowledge our collaborators: Stefan Gerke, Jan Sperling, Werne Vogel, Universität Rostock, Germany; and Jingliang Feng, Hailong Wang, Jietai Jing in ECNU, China.

I also record the financial supports of my PhD from China Scholarship Council.

I must thank all my thesis reviewers: Prof. Christine Silberhorn, Prof. Jiangrui Gao, Prof. Mikhail Kolobov, Prof. Michel Brune, for their carefully reading this manuscript and giving many helpful suggestions.

I want to appreciate my family members, especially my mother Zhang Huiling, for the support and encouragement, when I was 10 000 km away from you.

In the end, I think I still should thank much more people and say more acknowledgements than I have written above. I would remember all your help, support, and accompany. In the future I will continue passing this spirit to help and support other people in science and in the life.

CAI Yin

Contents

Introduction

Since the beginning of the 20th century, quantum mechanics [24] has revolutionized the theory of physics, and has succeeded in solving difficulties emerged in classical physics, such as Max Planck's solution of blackbody radiation, Albert Einstein's photoelectric effect, discrete spectra of atoms, etc. Based on quantum mechanics, the semi-classical models of matter-light interaction, where matter is treated as a quantum system while light is a classical field [37], can handle many physical processes. Many important applications came out from this theory. In particular, in optics, laser that emits light coherently was created on the basis of the stimulated emission theory.

In 1935, Albert Einstein and his colleagues Boris Podolsky and Nathan Rosen claimed the famous EPR paradox [26], which indicates that two quantum-entangled particles can have nonlocal correlation in position and momentum quantum observables. This property of entanglement initiated a series of new physics, such as quantum cryptography [27], quantum teleportation of quantum states [94] [6] [12], etc.

To perform such entanglement-principle operations with light, the semi-classical model is not sufficient. After 1970s, quantum optics theory [35], where quantized light is described by bosonnic annihilation and creation operators, was initiated and developed. This has formed the basis of many new domains based on quantum states of light, such as quantum information processing [59] [60] and quantum metrology [14] [34].

In quantum optics in the continuous variable regime, the light field is represented with continuous quadrature observables, which are associated to the amplitude and phase of light. Compared to the discrete regime, where single photons are measured, the non-classical properties in the continuous variable regime are demonstrated by the quantum fluctuations. This is the reason why we study the noise characteristics of light. The quantum fluctuations of a perfect coherent source, for instance an ideal laser, are at the standard quantum noise limit, or shot noise limit, which originates from

vacuum fluctuations. Quantum states whose quadratures' fluctuations are exactly at the standard quantum noise limit are coherent states [35].

A quantum light resource in this regime, squeezed light, was demonstrated in many nonlinear optical experiments [7], such as parametric down conversion and optical parametric oscillator (OPO) with $\chi^{(2)}$ nonlinear crystals [79] [97] [81] [45], $\chi^{(3)}$ four wave mixing with Rubidium atomic gas [49], etc. Importantly, the quantum fluctuations of squeezed light are beyond the standard quantum noise limit, which is different from all the classical and coherent light sources. Furthermore, in the case of a two-mode squeezing source, one can generate strong quantum correlation between the quadratures of the two modes. This type of quantum correlations refers to EPR entanglement in continuous variable regime. Recently, e.g., deterministic quantum teleportation was realized using the continuous variable EPR state generated by OPOs [88].

In quantum optics in the continuous variable regime, quantum correlations are generated via basis change from squeezed modes [10] [61]. The concept of modes, in both classical and quantum description of light, originates from the solutions of Maxwell's equations. It is well known that continuous laser has polarization modes, frequency modes (plane waves modes), spatial modes, etc.; while ultrafast pulses have temporally shaped modes in the time domain, and spectral modes in the frequency domain. When a state needs at least two non-vacuum modes to be described, whatever the basis, it is called a multimode state. In this thesis, we will study quantum multimode property of the quantum frequency comb, which is generated by a synchronuously pumped optical parametric oscillator (SPOPO) [64] .

Optical frequency combs, as a kind of intrinsic multimode resource, are an essential tool in many fields, such as frequency metrology and time measurement [8] [42], where optical frequency measurement, performed by beating the light field with a frequency comb, can reach an ultrahigh precision $\sim 10^{18}$ [18]. They have appealed more and more attentions since the Nobel Prize in Physics of 2005 was awarded to Roy J. Glauber, John L. Hall and Theodor W. Hänsch. Nowadays the applications of optical frequency combs are quite various, ranging from the field of frequency measurements and its applications to fundamental physics [15] [50], to domains such as biology, chemistry, telecommunication, distance measurement, broadband spectroscopy, etc.

Multimode quantum states are important in constructing complex quantum networks [44] which can be used for quantum information processing and quantum metrology [14] [100]. They have been experimentally generated with

many optical parametric oscillators, in the form of multi-spatial-mode state [90], multifrequency-mode state [57], multimode EPR steering [3], multimode cluster [87] [86]. More recently, a large-scale multi-timing-mode cluster state has been generated: it has $\sim$ 10 000 entangled modes in time domain [98].

Quantum networks play an essential role in recent developments of quantum information processing. In this work, we are interested in one-way quantum computing, in particular, one-way measurement based quantum computing (MBQC) in the continuous variable regime [54] [48]. Cluster states [85] [38], which are multimode correlated quantum states, are the quantum resources of MBQC, where quantum operations can be implemented via one-way measurement processes. Many experiments of cluster states generation and related gaussian quantum computation have been done with many OPOs and complex linear optical networks [93], which lack flexibility and scalability [2].

In this thesis, we introduce a quantum simulator to emulate on-demand clusters with the multimode quantum resource, the SPOPO: a single physical system which is intrinsically multimode. We employ a spatial light modulator (SLM) to arbitrarily shape the mode of the local oscillator in a homodyne detection apparatus [55]. This means that we are able to implement different protocols by simply adapting the measurement basis on the desired quantum operations rather than changing the optical architecture.

Plan of the thesis:

Using optical frequency combs, we generate multi-temporal-mode state from the SPOPO. We use optical frequency combs to pump a $\chi^{(2)}$ nonlinear crystal in a synchronized optical cavity, where complex parametric down conversion processes involving all the frequencies of the comb occur at the same time. From this nonlinear mechanism, a full multipartite entangled multimode state is generated and characterized [32] [70]. An on-demand quantum network simulator is developed using the SPOPO and ultrafast pulse shaping; up-to-twelve-node clusters and a six-partite secret sharing protocol are experimentally emulated with this simulator. Furthermore, to implement measurement based quantum computing and quantum frequency metrology, we need to simultaneously measure all the modes of the multimode quantum state. To that aim, frequency resolved multipixel detectors are employed [2], and used to realize a line-shape-eight-node cluster state. We also developed a multimode quantum spectrometer, which is able to exceed

the standard quantum limit for measuring manifold parameters of ultrafast pulses.

This thesis consists of three parts, in Part I (chapters 1-4), the theory and experiment of the SPOPO are demonstrated; in Part II, quantum-network simulator is introduced using the quantum resource, SPOPO; in Part III, clusters for measurement based quantum computing and a multimode quantum spectrometer are implemented by using the frequency resolved multipixel apparatus.

Part I: In Chapter 1, we introduce the optical frequency combs, and synchronized optical cavities, which can resonate with all the frequencies of the frequency comb. In Chapter 2, multimode quantum description of light in continuous variable regime is demonstrated. In the chapters 3 and 4, the synchronized pumped optical parametric oscillator (SPOPO) are presented theoretically and experimentally. We present the simulation of the SPOPO; and the multimode quantum state of the SPOPO is characterized via mode-dependent homodyne detection; the sixteen-mode covariance matrix is obtained.

Part II: In Chapter 5, we theoretically introduce cluster states, the resource of measurement based quantum computing, including the stabilizers, nullifiers, and unitary transforms. In Chapter 6, We developed a quantum-network simulator with ultrafast pulse shaping. By employing the multimode squeezing of the SPOPO, many up-to-twelve-node clusters and a six-partite secret sharing protocol are simulated, where we obtained all the quantum-fluctuation properties of the simulated quantum networks.

Part III: To realize quantum computing and quantum metrology with the SPOPO, a frequency resolved multipixel apparatus, which is able to measure all the modes of the SPOPO simultaneously, is used in our experiment. We present the method for implementing measurement based quantum computing via multipixel homodyne detection in Chapter 7. In Chapter 8, we directly present the article made in collabration with East China Normal University, Shanghai, which is a theoretical proposal to implement versatile clusters with cascading four wave mixing. In the end, Chapter 9, a multimode quantum spectrometer is demonstrated. We achieve the signal-to-noise ratio (SNR) of central frequency shift in an optical frequency comb beyond the standard quantum noise limit; furthermore, multiple parameters of the frequency comb, corresponding to different spectral modes, are measured simultaneously via post-processing, and the SNR of the measurements also exceeds the standard quantum limit.

Part I

Theory and Experiment of the SPOPO

Chapter 1

Optical frequency combs

Contents

In this thesis, we are interested in realizing quantum information processing via using and controlling optical frequency combs. In the first chapter of the thesis, we start introducing the basic notions of the optical frequency combs, which are usually generated by ultrafast mode-locked lasers [82]; then the spectral phase of the ultrafast lasers and dispersion in a linear medium are presented.

1.1 Classical electric fields

Firstly we introduce some notions of the classical light fields. Classically, light is composed of electromagnetic waves with optical frequencies, which obey Maxwell's Equations. Using the description of classical electromagnetic fields, we can describe many nonlinear phenomena of light interacting with nonlinear medium.

Let us consider a real classical electric field $E(\vec{r}, t)$, expressed with its

frequency components,

$$E(\vec{r},t) = \int_{-\infty}^{\infty} E(\vec{r},\omega)e^{-i\omega t}\frac{\mathrm{d}\omega}{\sqrt{2\pi}}, \tag{1.1}$$

where $E(\vec{r},\omega) = E^*(\vec{r},-\omega)$.

Then we introduce a complex field $E^{(+)}$ which is the integral of all the positive frequencies,

$$E^{(+)}(\vec{r},t) = \int_{0}^{\infty} E(\vec{r},\omega)e^{-i\omega t}\frac{\mathrm{d}\omega}{\sqrt{2\pi}}, \tag{1.2}$$

Thus we have,

$$E(\vec{r},t) = E^{(+)}(\vec{r},t) + E^{(-)}(\vec{r},t), \tag{1.3}$$

where $E^{(-)}(\vec{r},t) = \left[E^{(+)}(\vec{r},t)\right]^*$ giving the relation between positive and negative frequency components.

With a Fourier transform of the complex electric field in time domain, we have the corresponding description of the electric field in spectral domain,

$$\begin{aligned} E^{(+)}(\vec{r},\omega) &\equiv \int_{0}^{\infty} E(\vec{r},t)e^{i\omega t}\frac{\mathrm{d}\omega}{\sqrt{2\pi}} \\ E(\vec{r},\omega) &= E^{(+)}(\vec{r},\omega) + E^{(-)}(\vec{r},-\omega), \end{aligned} \tag{1.4}$$

where similarly $E^{(-)}(\vec{r},\omega) = \left[E^{(+)}(\vec{r},\omega)\right]^*$.

1.2 Optical frequency combs

An optical frequency comb is, in frequency or wavelength domain, an optical spectrum which consists of equidistant lines [21], as seen in Fig. 1.1, with about $10^5 \sim 10^6$ frequency modes, and in time domain, is a train of ultrafast pulses, as seen in Fig. 1.2, in our case with a duration of $\sim$ 100fs.

Optical frequency combs are often generated by a kerr-lens mode-locked Ti-sappire laser [43] [82]. With a ultrahigh stability, optical frequency combs have the best precision amongst all of measurements of physical parameters and metrology meters [8] [92]. Furthermore, optical frequency combs, with a lot of properties, such as ultrafast, high energy, intrinsic multimodes of frequency, stable, low noise, etc., are acting as an important tool and technology for both industry and scientific aims [92] [36].

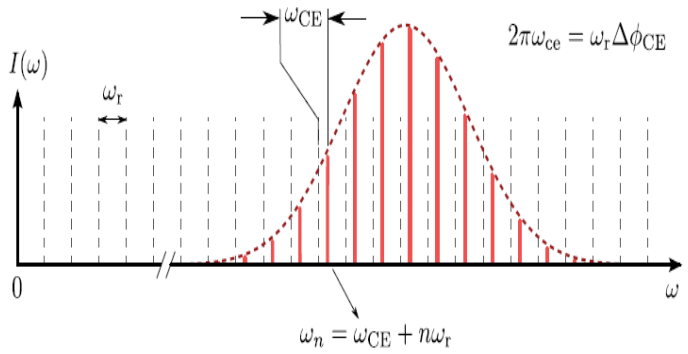

Figure 1.1: The spectrum of an optical frequency comb. Here the optical frequency comb is presented in the frequency domain, which consists of many equidistant frequencies (red lines). The distance between two neighboring frequencies correspond to the repetition rate of the comb. The dashed gaussian-shape profile is the envelop of the spectrum.

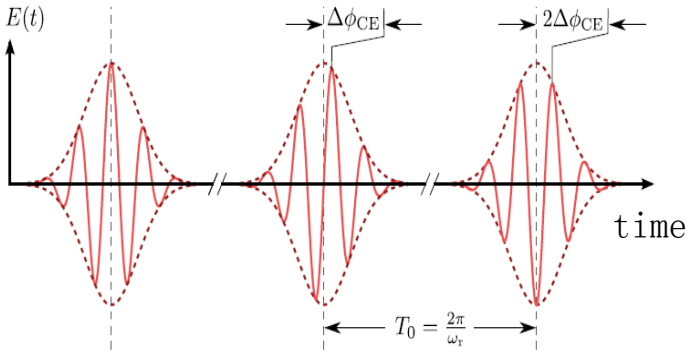

Figure 1.2: Temporal pulses of the optical frequency combs. In the time domain, frequency combs can be represented as a train of ultrafast pulses. The dashed gaussian-shape envelops are the corresponding temporal shapes of pulses, and the time distance between pulses is a round-trip time of light in the laser cavity.

1.2.1 Definitions of frequency combs and ultrafast pulses

In this part, basic conceptions of optical frequency combs will be presented. A standard way of generating a frequency comb is using mode-locked lasers [17]. As seen in Fig. 1.2, a train of ultrafast pulses with equidistance in time is generated by this kind of lasers, e.g. kerr-lens Ti-sappire lasers. Via Fourier transform, these pulses are equivalent, as seen in Fig. 1.1, as many frequency components in frequency domain. Therefore optical combs[1] can be equivalently represented in time or frequency domain. A typical duration of ultrafast pulses is in the femtosecond range.

The equidistance T_0 between pulses, in time domain seen in Fig. 1.2, is determined by a laser cavity length L_c, which is also called *Repetition Frequency (RF)* or *Free Spectral Range* $\omega_\mathrm{r} = 2\pi/T_0$ in frequency domain in Fig. 1.1.

Carrier-Envelope-Offset (CEO) is the frequency or phase offset between carrier waves and pulse envelopes, as seen Fig. 1.2, which is usually caused by the effect of intra-cavity dispersion and nonlinearities. It is expressed as $\Delta\phi_\mathrm{CE}$ and ω_CE respectively in time and frequency domain with a relationship as below,

$$\omega_\mathrm{CE} = \omega_\mathrm{r}\frac{\Delta\phi_\mathrm{CE}}{2\pi}. \tag{1.5}$$

Physically, the CEO itself is induced by the effect of intra-cavity dispersion. One round trip propagation in the cavity induces a phase shift as below,

$$\Delta\phi_\mathrm{CE} = \left(\frac{1}{v_\mathrm{g}} - \frac{1}{v_\phi}\right)\omega_0 L_0 \tag{1.6}$$

Where v_g and v_ϕ are the group velocity and phase velocity of light respectively, and ω_0 is the cavity resonant frequency, and L_0 is the cavity round trip optical path.

Carrier-Envelope-Phase (CEP) is difference of phases between carrier waves and pulse envelopes induced by CEO of light, as seen in Fig. 1.2, written as below,

$$\phi_\mathrm{CE} = m\Delta\phi_\mathrm{CE}. \tag{1.7}$$

Where m is the number of pulses counting from the reference pulse.

Therefore, as seen in Fig. 1.1, in frequency domain, the representation of a perfect frequency comb is a series of delta functions distributed as,

$$\omega_n = \omega_\mathrm{CE} + n\omega_\mathrm{r} \tag{1.8}$$

[1] In this thesis we think ultrafast pulses and optical frequency combs correspond to time domain and frequency domain respectively, which is equivalent via Fourier Transform. Sometimes optical frequency combs are, in particular, needed to lock the CEO.

Where ω_n is the n^{th} frequency of a comb, and ω_{CE} is Carrier-Envelop-Offset frequency, and ω_{r} is the repetition frequency of an optical cavity. We can see that the absolute frequency ω_n depends on both the repetition rate ω_{r} and the CEO frequency ω_{CE}. Therefore, when the cavity length and CEO are both locked perfectly the absolute frequency of the n_{th} tooth of frequency combs ω_{n} will be fixed; we can take the optical frequency comb as a frequency ruler for measuring unknown frequencies.

When CEO is zero, in time domain, $\Delta\phi_{\text{CE}} = 0$, a single pulse can be written in the function of pulse envelope $g(t)$,

$$E_{\text{pulse}}(t) = g(t)e^{-i\omega_0 t} \tag{1.9}$$

Then with the effect of CEO, the field of a train of pulses can be written as,

$$E_{\text{train}}(t) = \sum_n g(t - nT_0)\, e^{-i\omega_0(t-nT_0)} e^{-in\Delta\phi_{\text{CE}}} \tag{1.10}$$

Fourier transform of the light field is a frequency comb, as seen in Fig. 1.1, which can expressed as below,

$$E_{\text{train}}(\omega) = E_{\text{pulse}}(\omega) \sum_n \delta(\omega - \omega_{\text{n}}) \tag{1.11}$$

Where here $\omega_n = \omega_0 + n\omega_{\text{r}}$, and ω_0 is the central frequency of the comb.

Besides, as seen in Fig. 1.1, the bandwidth $\Delta\omega$ of the full comb is another important parameter, in gaussian case, it satisfies [58][2],

$$\Delta\omega \times \Delta t \geq 4\ln 2. \tag{1.12}$$

where Δt is the duration of a pulse.

Typically, when $\Delta\omega \ll \omega_0$, we have,

$$\Delta\lambda \simeq \frac{\lambda^2}{2\pi c}\Delta\omega. \tag{1.13}$$

Therefore, for example, the gaussian duration of pulses $\Delta t = 100$fs centered at 800nm corresponds to about $\Delta\omega = 10$THz bandwidth of the spectrum.

1.2.2 Frequency dependent phase

When the light pulses propagate in a disperse medium, the components with different colors will different phases. We call this *spectral phase* $\phi(\omega)$ of light, which is a function of frequency ω.

[2] Δt and $\Delta\omega$ are full width half maximum (FWHM).

To express the spectral phase of light, we consider a train of ultrafast pulses, whose central frequency is ω_0. We write the Taylor expansion of the spectral phase function,

$$\phi(\omega) = \phi(\omega_0) + \phi'(\omega_0)(\omega - \omega_0) + \frac{1}{2}\phi''(\omega_0)(\omega - \omega_0)^2 + ..., \tag{1.14}$$

where $\phi(\omega_0)$ is the carrier envelope phase (CEP), which corresponds to the phase between the envelope of the electric field and the carrier, as seen in Fig. 1.2; $\phi'(\omega_0)$ is simply a delay between the pulse and an arbitrary origin time. This leads to a constant *group delay* without changing the shape of the pulses; the quadratic phase $\phi''(\omega_0)$ is the most important term called *Group Delay Dispersion* (GDD), and we usually use fs^2 for the unit of GDD. In other words, each color component experience a delay that increase linearly versus the frequency, which is so called *chirp*. Therefore, the shape of the pulses is deformed because the GDD: with a Fourier-limited condition, the duration of the pulses always increases when there is a GDD.

1.3 Dispersion of linear media

If the pulses propagate in a linear, homogeneous and isotope material, the spectral phase is only dependent on the property of the material and the traversing thickness, keeping the relative phases between different colors, and is independent of the characters of the pulses, such as the duration of the pulses. In practice, all the optical components, including mirrors, glasses, etc., are possible to induce color dependent phases, also called *dispersion*.

The module $k(\omega)$ of the wave vector is the derivative of the spectral phase function versus the propagating direction z,

$$k(\omega) = \frac{\partial \phi}{\partial z}(\omega), \tag{1.15}$$

this gives,

$$k(\omega) = k(\omega_0) + k'(\omega_0)(\omega - \omega_0) + \frac{1}{2}k''(\omega_0)(\omega - \omega_0)^2 + \dots, \tag{1.16}$$

where the term $k'(\omega_0)$ is the *group velocity*, and the second term $k''(\omega_0)$ is the *group velocity dispersion* (GVD), which is just the GDD over the propagating distance z.

Importantly, the quadratic phase GDD broaden the duration of the pulses [58],

$$\Delta t_{\text{broaden}} = \Delta t \sqrt{1 + \left(\frac{4\ln 2 \phi''(\omega_0)}{\Delta t^2}\right)^2}, \tag{1.17}$$

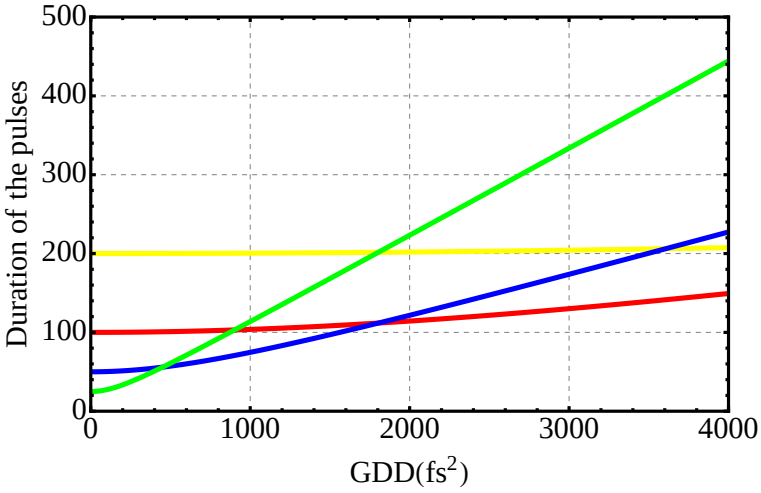

Figure 1.3: The durations of the pulses with different chirp (GDD). The green, blue, red, and yellow curves are the durations of the pulse with initial durations of $25fs^2, 50fs^2, 100fs^2, 200fs^2$, respectively.

where z is the propagating distance, and ϕ' is the GDD, and Δt is the initial duration without chirp. It is similar to the gaussian beam propagation,

$$\Delta w(z) = w_0\sqrt{1+\left(\frac{z\lambda/\pi}{w_0^2}\right)^2}, \tag{1.18}$$

where w and w_0 are the spatial waists of the beam.

According to the Equ. 1.17, we have the broadened pulse duration versus GDD, as seen in Fig. 1.3. We can see that when the initial duration is slower, the broadening effect of GDD is less. Therefore, for instance, the duration of $\sim 100fs$ pulses is not sensitive to the GDD effect, but the duration of $\sim 25fs$ pulses is much more sensitive compared to $\sim 100fs$ pulses.

1.4 Synchronized optical cavity

A synchronized optical cavity, differently usual monochromatic cavities, can resonate with a train of ultrafast pulses (or optical frequency combs); in other words, all the frequencies of the pulses are resonant in the synchronized cavity. Compared to monochromatic cavities, this type of cavities need to be resonant for the whole spectral components of frequency combs. Ideally, all the frequencies of light experience the same cavity properties. In practice, mirrors with a flat broadband reflectivity are used, usually called ultrafast or

femtosecond mirrors. Now, the optics companies, such as *Layertech. GmbH*, *CVI*, *Femto Lasers*, *Laser Components*, have good broadband ultrafast optics, with $\sim$ 100 nm wide reflectivity.

In this thesis, as we are interested with optical parametric oscillators (OPO) using optical frequency combs, we use a synchronized cavity to study the related nonlinear and quantum effect of the OPOs. Here we give some important notions for synchronized cavities.

Based on a linear Fabry-Perot interferometer, with two mirrors (r_1, r_2, t_1, t_2 are the corresponding coefficients of reflectivity and transmissivity, $r_i^2 + t_i^2 = 1$),

FSR, ω_{r}, called *free spectral range*, is the the spectral distance between two resonant peaks.

$$\omega_r = \frac{2\pi c}{L}, \tag{1.19}$$

where L is the cavity length.

And the repetition rate of pluses is defined similarly as above. All the frequencies $\{\omega_n\}$ of the pulses, such as the ω_n in Equ. 1.11, are resonant (synchronized) in the cavity when the length L satisfies the repetition rate of the pulses, $L = \frac{2\pi c}{\omega_r}$.

Finesse: is the ratio between the *FSR* and the FWHM of the resonant peaks $\Delta\omega_0$, $\omega_{\mathrm{r}}/\Delta\omega_0$.

$$\mathcal{F} = \frac{\pi}{2\mathrm{arcsin}\left(\frac{1-\sqrt{\rho}}{2\sqrt[4]{\rho}}\right)}, \tag{1.20}$$

where $\rho = (r_1 r_2)^2$, so $1-\rho$ is the loss of a round trip. For small loss $\leq 10\%$,

$$\mathcal{F} \simeq \frac{\pi}{1-\rho}. \tag{1.21}$$

Therefore the transmission of the cavity is,

$$T(\omega) = T_{\max}\frac{1}{1+\frac{\sin^2\left(\frac{\phi_{\mathrm{cavity}}(\omega)}{2}\right)}{\sin^2\left(\frac{\pi}{2\mathcal{F}}\right)}}, \tag{1.22}$$

where $T_{\max} = \left(\frac{t_1 t_2}{1-r_1 r_2}\right)^2$, and $\phi_{\mathrm{cavity}}(\omega)$ is the phase changed after a round trip.

For optical frequency combs, each frequency ω_n need be resonant in the cavity. To aims that, the phase $\phi_{\mathrm{cavity}}(\omega_n)$ need satisfy integral times of 2π for all frequencies $\{\omega_n\}$, $\phi_{\mathrm{cavity}}(\omega_n) = 0\,[2\pi]$.

To show how to synchronize the cavity to pulses, let us write the phase $\varphi(\omega)$ in details with the spectral phase $\phi(\omega)$ induced by the cavity media (air, glass, crystal) on pulses, after a round trip of a L long cavity, which is,

$$\phi_{\text{cavity}}(\omega) = \phi_{\text{Gouy}} + \frac{\omega L}{c} + \phi(\omega), \tag{1.23}$$

where ϕ_{Gouy} is called Gouy phase, which is associated to the property of cavity spatial modes, and the spectral phase $\phi(\omega)$ can be written in its Taylor expansion, as in Equ. 1.14,

$$\phi_{\text{cavity}}(\omega) = \phi_{\text{Gouy}} + \frac{\omega L}{c} + \phi(\omega_0) + \phi'(\omega_0)(\omega - \omega_0) + \frac{1}{2}\phi''(\omega_0)(\omega - \omega_0)^2 + ..., \tag{1.24}$$

By defining the constant part $\alpha = \phi_{\text{Gouy}} + \phi(\omega_0) - \omega_0\phi'(\omega_0)$, and $L_{\text{eff}} = L + c\phi'(\omega_0)$, we have,

$$\phi_{\text{cavity}}(\omega) = \alpha + \frac{\omega}{c}L_{\text{eff}} + \frac{1}{2}\phi''(\omega_0)(\omega - \omega_0)^2 + \dots. \tag{1.25}$$

From Equ. 1.8, for any frequency $\omega_n = \omega_{\text{CE}} + n\omega_{\text{rep}}$, when the dispersion part is all compensated ($\phi''(\omega_0) = 0$), we have,

$$\phi_{\text{cavity}}(\omega_n) = (\alpha + \frac{\omega_{\text{CE}}}{c}L_{\text{eff}}) + n\frac{\omega_{\text{rep}}}{c}L_{\text{eff}}, \tag{1.26}$$

where ω_{CE} is the CEO frequency of the pulses.

In the above equation, we make the two parts $(\alpha + \frac{\omega_{\text{CE}}}{c}L_{\text{eff}})$ and $n\frac{\omega_{\text{rep}}}{c}L_{\text{eff}}$ be both integral times of 2π. Strictly, to aim so, we can adjust the cavity length to make second part be integral times of 2π, then we can control the CEO of the pulse laser to make the first part satisfied.

When making $\alpha + \frac{\omega}{c}L_{\text{eft}}$ be 0, according to Equ. 1.22, the dispersion (the second order of the spectra phase ϕ'') effect is not very constrained for low finesse, e.g. in our case of OPO ($\mathcal{F} \simeq 20$), it need be less than ~ 700 fs^2; But for high finesse, e.g. $\mathcal{F} \geq 500$, the dispersion, such as the GDD of air and mirrors, has to be well controlled to be less than ~ 40 fs^2 [69].

In practice, when the duration of the pulse is not very big (our case, $\sim$100 fs) and the finesse is low, we can only adjust the cavity length to make the phase $\phi_{\text{cavity}}(\omega_0)$ for the central frequency $\omega_0 = \omega_{\text{CE}} + n_0\omega_{\text{rep}}$, in Equ. 1.26, be integral times of 2π. For the other frequencies $\omega_n = \Delta n\omega_{\text{rep}} + \omega_0$, as $\Delta n \propto \frac{\Delta\omega}{\omega_{\text{rep}}}$ and $\Delta\omega \ll \omega_0$, we have $\phi_{\text{cavity}}(\omega_n) \simeq \phi_{\text{cavity}}(\omega_0)$. Thus, in this case, the cavity can synchronize with all the frequencies of pulses only via adjusting the cavity length.

Chapter 2

Quantum optics in continuous variable regime

Contents

In this chapter, we will introduce multimode quantum optics in continuous variable regime and the related notions.

2.1 Quantization of free radiation

Semi-classical models of atom-radiation interaction can handle many physical processes, including absorption and stimulated emission in lasers, where matter is treated as quantum while light is a classical field [37]. However, some other phenomena can not be described in this semi-classical model. For instance, spontaneous emission can only be treated correctly using a fully quantum framework, where both the radiation and the matter are quantized [37]. Furthermore, it is found that *a free electromagnetic field*, far from sources, shows a series of new properties [35] such as *interference of photons* [39] [40] , *squeezed light* [97], quantum fluctuations of vacuum, etc., which can not be described by only the classical fields. This chapter will introduce the quantization of free electromagnetic fields and its associated quantum properties of light.

2.1.1 Annihilation and creation operators

It is well known how to quantize a system of material particles in quantum mechanics. The classical problem firstly is written in Hamilton's canonical form, which expresses the system energy as a function of the particle position $\vec{x}$ and the conjugate canonical momentum $\vec{p}$. Then the classical Hamiltonian $H(x_1, ..., x_i; p_1, ..., p_i)$ is replaced by the quantum operators as $\hat{H}(\hat{x}_1, ..., \hat{x}_i; \hat{p}_1, ..., \hat{p}_i)$, which obeys the canonical commutation relation [37]:

$$[\hat{x}_i, \hat{p}_j] = i\hbar\delta_{ij}, \tag{2.1}$$

where, $\delta_{ij} = 1$ if $i = j$, and $\delta_{ij} = 0$ if $i \neq j$. We can see that the operators of position $\hat{x}_i$ and momentum $\hat{p}_i$ commute with different labels of i, j, and don't commute with the same label $i = j$; the labels are associated to different particles. Importantly, being different from classical physics, the commutation relation introduces Heisenberg inequality in quantum mechanics.

To describe quantum properties of light we need introduce the quantization of light field, where the light field is expressed by quantum operators instead of classical electric field. Similarly, the procedures to quantize free radiation (the free electromagnetic field) are [37]:

I. Get the solutions of Maxwell's equation in the basis of plane waves, which are a set of electric fields with different frequencies and polarizations;

II. Write the solutions with the electric field *normal variables*, normalized to photon numbers;

III. Express the energy (Hamiltonian) in a form of harmonic models;

IV. Introduce the annihilation and creation operators of quantum harmonic oscillators and get quantized Hamiltonian of free radiation, so the

commutation relation is introduced in the conjugate canonical variables of radiation fields.

Using the solutions of Maxwell's equations, the analytic signal of electrical field, in a quantization volume with a size L, can be expressed of a sum of orthogonal plane waves with discrete frequencies[1],

$$E^{(+)}(\vec{r},t) = i\sum_l \mathcal{E}_l \alpha_l e^{i\left(\vec{k}_l\cdot\vec{r}-\omega_l t\right)}. \tag{2.2}$$

In the expression above, $\mathcal{E}_l = \sqrt{\hbar\omega_l/2\epsilon_0 L^3}$ is the normalization factor related to the energy of classical fields in the mode l; α_l is the complex normal variable of mode l associated to photon numbers.

The corresponding Hamiltonian with a set of modes of $\{l\}$ corresponding to the normal variables α_l is,

$$H_R = 2\epsilon_0 L^3 \sum_l [\mathcal{E}_l]^2 |\alpha_l|^2 = \sum_l \hbar\omega_l |\alpha_l|^2. \tag{2.3}$$

Thus, the radiation energy is given in a sum of the energies related to each normal mode l.

Let us introduce harmonic quantum operators of light also called annihilation and creation operators, which are associated to the normal variable α_l. The time-independent operators $\hat{a}_l$ satisfy the relation of commutation:

$$[\hat{a}_l, \hat{a}_{l'}^\dagger] = \delta_{l,l'} \quad \text{and} \quad [\hat{a}_l, \hat{a}_{l'}] = 0. \tag{2.4}$$

$\hat{a}_l, \hat{a}_l^\dagger$ are annihilation and creation operators of photons in the mode l, also called boson operators in quantum mechanics.

Replacing the amplitude α_l by the annihilation operator in Equ. 2.2, the quantization of the light field,

$$\hat{\mathbf{E}}^{(+)}\left(\vec{r},\vec{t}\right) = i\sum_l \vec{\epsilon}_l \mathcal{E}_l e^{i(\vec{k}_l\cdot\vec{r}-\omega_l t)}\hat{a}_l \tag{2.5}$$

Hence, the Hamiltonian of quantized filed can be written as below,

$$\hat{H}_0 = \sum_l \hbar\omega_l \left(\hat{N}_l + \frac{1}{2}\right), \tag{2.6}$$

where $\hat{N}_l = \hat{a}_l^\dagger \hat{a}_l$ is the photon number operator in mode l. And its eigenstates are called *Fock states* or *photon number states*, which form a basis of the radiation states in the Hilbert space,

$$\hat{N}_l|n_l\rangle = n_l|n_l\rangle, \quad \text{with} \quad n_l = 0, 1, 2, ... \tag{2.7}$$

[1]Here we assume there is only one polarization.

The eigenstates of the annihilation operators are *coherent states* or *quasi-classical states*, which in a mode l can be expressed as below [35],

$$\hat{a}_l|\alpha_l\rangle = \alpha_l|\alpha_l\rangle, \tag{2.8}$$

where, α_l is the eigenvalue, which is the complex amplitude of the field. Coherent states are the quantum states of classical light sources, for instance, the output of lasers. It is important to note that the annihilation operator $\hat{a}$ is non-Hermitian, and it is easy to prove that when time $t = 0$ any coherent state $|\alpha_l\rangle$ with a complex amplitude α_l is a superposition of Fock states,

$$|\alpha_l\rangle = e^{-|\alpha_l|^2/2} \sum_{n_l=0}^{\infty} \frac{\alpha_l^{n_l}}{\sqrt{n_l!}} |n_l\rangle. \tag{2.9}$$

Up to now we have quantized free radiation. Compared to classical fields, we introduced annihilation and creation quantum operators, and the corresponding commutation relations, which therefore can further describe quantum properties of non-classical states of light.

For the quantization of fields we have *narrow band approximation*. When $\omega - \omega_0 \ll \omega_0$, $\mathcal{E}_0 = \sqrt{\hbar\omega_0/2\epsilon_0 L^3}$ which is not photon frequency ω dependent. We can factorize $\mathcal{E}_0$ in the quantization of the field,

$$\hat{\mathbf{E}}^{(+)}(\vec{r}, t) = i\mathcal{E}_0 \sum_l e^{i(\vec{k}_l \cdot \vec{r} - \omega_l t)} \hat{a}_l. \tag{2.10}$$

In the above equation, the plane wave $e^{i(\vec{k}_l \cdot \vec{r} - \omega_l t)}$ is the classical mode, and $\hat{a}_l$ is the annihilation operator related to this mode.

2.1.2 The phasor representation and Heisenberg inequality

The annihilation and creation operators $\hat{a}$, $\hat{a}^\dagger$ are non-Hermitian, therefore non-observable. Thus in practical measurement, we define observable Hermitian operators using time-independent $\hat{a}$, $\hat{a}^\dagger$. The *quadrature operators* are formed as below,

$$\hat{x}_l = \hat{a}_l^\dagger + \hat{a}_l \quad \text{and} \quad \hat{p}_l = i\left(\hat{a}_l^\dagger - \hat{a}_l\right), \tag{2.11}$$

where $\hat{x}_l$ and $\hat{p}_l$ are called amplitude and phase quadrature operators respectively, which are either time-independent.[2] Classically, the quadrature

[2]The definition of quadrature operators sometimes has a $1/2$ coefficient, in consequence the shot noise is normalized differently. In our definition, shot noise is normalized to 1 in Equ. 2.15.

components correspond to real and imaginary parts of analytic signal in Equ. 2.2. A more general way, the quadrature operator can be defined with the angle θ as below,

$$\hat{x}_l^\theta = e^{i\theta}\hat{a}_l^\dagger + e^{-i\theta}\hat{a}_l. \tag{2.12}$$

A light field can be thus expressed in a quadrature representation with any θ.

As seen in Fig. 2.1, a complex light field, which corresponds to a coherent state, is represented with a vector arrow in *phasor representation*, where amplitude and phase quadrature components correspond to two axis of the coordinate[3]. The quadrature operators are Hermitian, and their eigenvalues indicate the classical quadratures of the fields. We can detect quadratures of a light field directly via *homodyne measurements*, which will be introduced in chapter 4.

According to the commutation relation between annihilation and creation operators, as in Equ. 2.4, we find the commutation relation between conjugate quadrature operators,

$$[\hat{x}_l, \hat{p}_{l'}] = 2i\delta_{l,l'} \quad \text{and} \quad [\hat{x}_l, \hat{x}_{l'}] = [\hat{p}_l, \hat{p}_{l'}] = 0. \tag{2.13}$$

Thus, we can get *Heisenbery inequality*,

$$\Delta x_l^2 \cdot \Delta p_l^2 \geq 1, \tag{2.14}$$

where $\Delta x^2 = \langle(\delta\hat{x})^2\rangle$ and $\delta\hat{x} = \hat{x} - \langle\hat{x}\rangle$ represent the fluctuations of the operator $\hat{x}$. The coherent states saturate the Heisenberg inequality in Equ. 2.14, and satisfy,

$$\Delta x_l^2 = \Delta p_l^2 = 1, \tag{2.15}$$

where the unit is an energy related term $[\mathcal{E}_l]^2$, defined in Equ. 2.2.

In intensity or phase measurements of light, the sensitivity always has a *standard quantum limit*, also called *shot noise* limit, which originates from the Heisenberg inequality of coherent states. Because the *coherent states*, and the *coherent vacuum* which has a zero mean field, have the same Heisenberg inequality 1, we call quantum fluctuation of coherent light *vacuum fluctuation*.

Here, for both amplitude and phase quadrature operators, the Heisenberg inequality is because of vacuum fluctuations of free radiation, which can not be described by a classical way. We can think the quantum description of free radiation corresponds to a classical field plus vacuum fluctuations, as seen in Fig. 2.1, where the red circle represent vacuum fluctuations.

[3]Sometimes it is also called phase representation

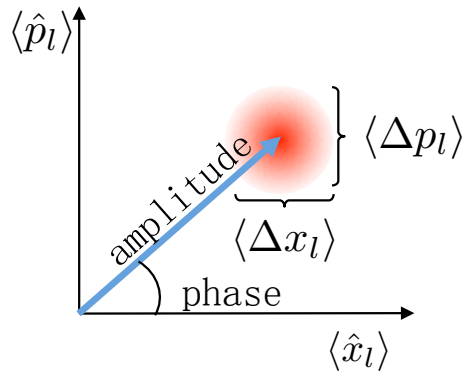

Figure 2.1: Phasor representation of a coherent state, where the vector arrow corresponds the field vector, and the red circle represents the quantum fluctuations, which obeys Heisenberg relation. Δx_l and Δp_l are standard deviations of amplitude quadrature and phase quadrature respectively.

Usually in lasers, the process of photon generation is random, and this random process gives rise to shot noise limit in intensity and phase measurements of laser light. For such coherent states, the photon number follows a Poisson distribution with a standard deviation of $\sqrt{N}$, which is a statistic property of classical radiation; sub-Poisson distribution corresponds to non-classical source, which is anti-bunch in the photon generation process.

2.1.3 Squeezed states

We have seen that the coherent states have the same vacuum fluctuations in both amplitude and phase quadratures, as seen in Equ. 2.15. The sensitivity of intensity and phase measurements with lasers will be limited by the shot noises, which origin from random generation processes of photons.

Here we will present a type of quantum resources, called squeezed light [37]. Interestingly, this type of light can exceed the standard quantum limit. As seen in Fig. 2.2, it is shown that the phase representation of squeezed states, where the fluctuation of one quadrature exceeds the quantum limit 1, and the fluctuation of the corresponding orthogonal quadrature is bigger than 1, conserving Heisenbery inequality. This means that potentially, we can increase measurement sensitivity by using squeezed light because of less quantum fluctuations [90].

The squeezing operator $\hat{A}_r$, where r is the real squeezing coefficient, is defined as below,

$$\hat{A}_r = \hat{a}\mathrm{cosh}r + \hat{a}^\dagger \mathrm{sinh}r, \quad \text{and,} \quad \left[\hat{A}_r, \hat{A}_r^\dagger\right] = 1. \tag{2.16}$$

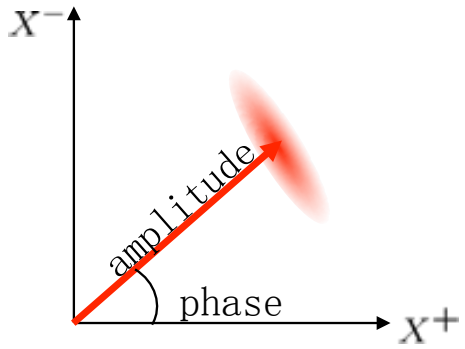

Figure 2.2: Phasor representation of a squeezed state. The vector arrow corresponds to the field vector, and the red circle represents the quantum fluctuations, which obeys Heisenberg relation. Different from coherent states in Fig. 2.1, the variance of the amplitude quadrature is less than 1; the phase part is bigger than 1.

In the corresponding quadrature representation, with a perfect squeezing operation K we have,

$$\begin{pmatrix} \hat{x}_r \\ \hat{p}_r \end{pmatrix} = K \begin{pmatrix} \hat{x} \\ \hat{p} \end{pmatrix} = \begin{pmatrix} e^{-r} & 0 \\ 0 & e^{r} \end{pmatrix} \begin{pmatrix} \hat{x} \\ \hat{p} \end{pmatrix}, . \tag{2.17}$$

where the squeezing operator $K = \begin{pmatrix} e^{-r} & 0 \\ 0 & e^{r} \end{pmatrix}$. Thus we have the variances $\delta x^2 = \langle x - \langle x \rangle \rangle^2$ for squeezed vacuum,

$$\begin{pmatrix} \delta x_r^2 \\ \delta p_r^2 \end{pmatrix} = \begin{pmatrix} e^{-2r} & 0 \\ 0 & e^{2r} \end{pmatrix} \begin{pmatrix} \delta x^2 \\ \delta p^2 \end{pmatrix}. \tag{2.18}$$

If $(\hat{x}, \hat{p})^T$ are quadratures of coherent states, with $\delta x^2 = \delta p^2 = 1$, we have,

$$\begin{pmatrix} \delta x_r^2 \\ \delta p_r^2 \end{pmatrix} = K^2 = \begin{pmatrix} e^{-2r} & 0 \\ 0 & e^{2r} \end{pmatrix}, \quad \text{and} \quad \Delta x_r \cdot \Delta p_r = 1. \tag{2.19}$$

From above equations, we see that with a squeezing operation K acting on coherent states, we can get a new state with squeezed variance e^{-2r} in a quadrature and anti-squeezed variance e^{2r} in the orthogonal quadrature.

Squeezed quadratures have less quantum fluctuations, so the sensitivity of measurements on the corresponding squeezed quadrature can be improved beyond shot noise limit. In metrology, the sensitivity of measurements can exceed the standard quantum limit via using squeezing on the corresponding quadrature [91] [100].

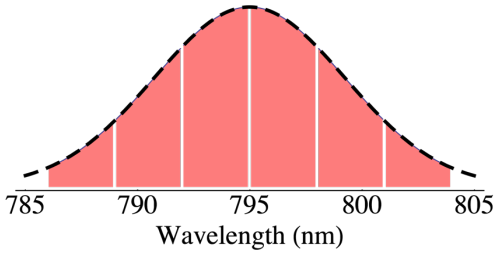

Figure 2.3: A spectral mode basis. The spectrum (envelope) of a frequency comb is divided into six bands, corresponding to a train $\sim$ 100 fs pulses centered at 795nm with a bandwidth of $\sim$ 10 nm in the time domain.

2.2 Modes of light fields

The quantization of free radiation in the previous chapter described electric field as a sum of harmonic oscillators, and the Hamiltonian is expressed as in Equ. 2.6. In this case, the harmonic oscillators correspond to the plane waves with the frequency $\omega_l = c \parallel \vec{k}_l \parallel$. These plane wave *modes* construct a basis carrying the energies and information, which are photon numbers in quantum description, and are the amplitude classically. The modes are classical conceptions originally from Maxwell's equations. However, in practice, many other kind of modes of light are also often used, such as Hermit-Gaussian spatial modes, temporal modes of ultrafast pulses, frequency modes, polarizations of light, and output modes of light resources[4]. In our work, we divide a $\sim$ 10 nm bandwidth spectrum of optical frequency combs into many frequency pixels (spectral bands), and these spectral bands construct a measurement basis, as seen in Fig. 2.3.

A set of orthogonal modes $\{u_i(\vec{r},t)\}$ of light, where z is the axis of propagation direction, $\vec{r} = (\vec{\rho}, z)$ and $\vec{\rho}$ is the transverse coordinate, constructs a mode basis, if it satisfies the condition as below,

$$\int_{t_0}^{t_0+T} \int_S u_i^*(\vec{r},t)\, u_j(\vec{r},t)\, \mathrm{d}\vec{r}\mathrm{d}t = \delta_{ij}, \tag{2.20}$$

where S is the surface of detection and T is the measurement time.

In this mode basis, the electric field operator can be expressed

$$\hat{E}^{(+)}(\vec{r},t) = \mathcal{A}\sum_j \hat{a}_i u_j(\vec{r},t)\,, \tag{2.21}$$

[4]For example, in the optical network, each of off-line OPOs has a output mode, and all the OPOs construct a basis.

where $\mathcal{A}$ is the normalization factor, which we will often omit in the rest of the manuscript. Here we express the field operator with sum of a set of orthogonal modes, which we will introduce in detail in next section.

2.2.1 Basis change

In Equ. 2.21, different modes can construct a different basis, and the same field can be expressed in different basis. Let us consider there is another basis consist of a set of modes $\{w_i(\vec{r},t)\}$, which equals a linear transform $\mathbf{U}$ acting on the basis $\vec{u}$,

$$U_{ij} = \int_{t_0}^{t_0+T} \int_S u_i^* (\vec{r},t)\, w_j (\vec{r},t)\, \mathrm{d}\vec{\rho}\mathrm{d}t, \tag{2.22}$$

where T and S are detecting time and aera. Thus,

$$w_j (\vec{r},t) = \sum_i U_{ij} u_i (\vec{r},t)\,. \tag{2.23}$$

Based on the Equ. 2.21, the modes $\{w_i(\vec{r},t)\}$ are associated to new annihilation and creation operators $\hat{a'}_i$ and $\hat{a'}_i^\dagger$, and the field can be written as,

$$\hat{E}^{(+)} (\vec{r},t) = \mathcal{A} \sum_j \hat{a'}_j w_j (\vec{r},t)\,. \tag{2.24}$$

We have the same filed operator expressed in different basis,

$$\sum_j \hat{a'}_j w_j (\vec{r},t) = \sum_{ij} \hat{a'}_j U_{ij} u_i (\vec{r},t) = \sum_i \hat{a}_i u_i (\vec{r},t) \tag{2.25}$$

The relation between operators is,

$$\hat{a}_i = \sum_j \mathcal{U}_{ij} \hat{a'}_j \tag{2.26}$$

Here $\mathcal{U}$ is unitary, with the properties, $\mathcal{U}^\dagger = \mathcal{U}^{-1}$, $\mathcal{U}^{-1}\mathcal{U} = \mathcal{U}\mathcal{U}^{-1} = \mathrm{I}$.

And similarly, as $\hat{E}^{(+)^\dagger} (\vec{r},t) = \mathcal{A}^* \sum_j \hat{a'}_j^\dagger w_j^* (\vec{r},t)$ and $\mathcal{U}_{ij} = \mathcal{U}_{ji}^*$, we have,

$$\hat{a}_i^\dagger = \sum_j \mathcal{U}_{ij}^* \hat{a'}_j^\dagger = \sum_j \mathcal{U}_{ji} \hat{a'}_j^\dagger \tag{2.27}$$

In general, with a basis change, a state of light can be represented in different basis; also a basis change can be any unitary transform, usually realized by linear optical networks [85]. In our experiment, S is big enough

compared to the beam transverse size, and the spatial mode is only TEM_{00}, so the integral of S can be neglected, and only frequency and temporal modes are considered.

Here U_{ij} is also a projection operation, where we project the modes $\{u_i\}$ onto another mode basis $\{w_j\}$. As the unitary transform corresponds to a square matrix, only when the two mode basis have the same number of dimensions, $\mathcal{U}$ is a unitary transform, or basis change; if not, it is only projection with the form of Equ. 2.22, but then it is not unitary.

The physical interpretation of a basis change is corresponding a unitary transform of the field, where the energy and commutation relations before and after transform are conserved. In practice, this can be implemented with linear optics without loss, such as optical beam splitter, phasors.

2.2.2 Monomode and multimode

In our work, the important property is that our quantum resource is multimode[65], not monomode, therefore we give the definition as following.

Definition: a pure state $|\psi\rangle$ is monomode if it exists a basis of modes $\{v_i\}$, in which we have,

$$|\psi\rangle = |\phi\rangle \otimes |0, ..., 0, ...\rangle, \tag{2.28}$$

where $|\phi\rangle$ which is not vacuum is the state in the first mode of the basis $\{v_i\}$, and the states of all the other modes are vacuum $|0\rangle$. A quantum state is multimode if it is not monomode.

Here we give an example of multimode squeezing, for example, it can be generated by 4 independent OPOs[99],

$$|\psi\rangle = |0_{sqz1}\rangle \otimes |0_{sqz2}\rangle \otimes |0_{sqz3}\rangle \otimes |0_{sqz4}\rangle \otimes |0, ..., 0, ...\rangle, \tag{2.29}$$

where the leading four modes are independently squeezed by four individual OPOs, and the other modes are vacuum, which can not be reduced into the form of Equ. 2.28.

Importantly, quantum correlation, for example, two-partite entanglement [61] can be generated via mixing monomode squeezing and vacuum by optical beam splitter as seen in Fig. 2.4, but this kind of entangled state can be reduced to the form of monomode as in Equ. 2.28. For instance, in the input basis, the state is expressed with only one squeezed mode and vacuum,

$$|\psi\rangle = |\text{squeezing}\rangle \otimes |0, ..., 0, ...\rangle, \tag{2.30}$$

thus it is still monomode.

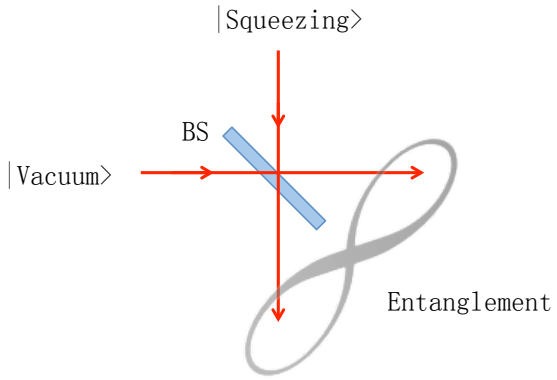

Figure 2.4: Entanglement generation with monomode. A squeezed state and vacuum are mixed with an optical beam splitter (BS), and the two transmitted beams are entangled. But the in the input basis, this entangled state has the form of monomode.

2.2.3 Basis change in the quadrature representation

More generally, we consider basis change in a multimode case, and we have $\vec{a} = (\hat{a}_1, \hat{a}_2, \hat{a}_3, \dots)^T$, $\vec{a'} = (\hat{a'}_1, \hat{a'}_2, \hat{a'}_3, \dots)^T$. According to Equ. 2.26, we define a basis change,

$$\vec{a'} = U\vec{a} \tag{2.31}$$

The corresponding unitary matrix of basis change can be written with real and imaginary parts,

$$U = X + iY \tag{2.32}$$

where X and Y are the real and imaginary part of the unitary transform, respectively. And it is easy to get $\vec{a'}^{\dagger} = U^*\vec{a}^{\dagger}$ from Equ. 2.27.

According to Equ. 2.11, we can write $\vec{a}$ and quadrature operators $(\vec{x}, \vec{p}) = ((\hat{x}_1, ..., \hat{x}_N), (\hat{p}_1, ..., \hat{p}_N))$. Thus Equ. 2.32 can be rewritten in the form,

$$\begin{aligned} \begin{pmatrix} \vec{x'} \\ \vec{p'} \end{pmatrix} &= \begin{pmatrix} X & -Y \\ Y & X \end{pmatrix} \begin{pmatrix} \vec{x} \\ \vec{p} \end{pmatrix} \\ &= S \cdot \begin{pmatrix} \vec{x} \\ \vec{p} \end{pmatrix}, \end{aligned} \tag{2.33}$$

where for a defined unitary transform $U = X + iY$, and S is,

$$S = \begin{pmatrix} X & -Y \\ Y & X \end{pmatrix}, \tag{2.34}$$

where S is the basis change in the quadrature representation, which is a type of sympletic transform which we will explain in details in the chapter of *Sympletic transform*.

2.3 Representation in the continuous variable regime

Previously, we defined quadrature operators in Equ. 2.11, which are continuous variables. In this chapter we will introduce how to represent a gaussian state in continuous variable regime. First we simply give the representation with density matrices, and also in continuous variable case with Wigner function. Then, in particular for gaussian case, the covariance matrix will be presented.

2.3.1 Density matrix and Wigner function

In quantum physics, usually a system can be described as a mixture of many pure states in *Hilbert space*, $|\psi_1\rangle$, $|\psi_2\rangle$, etc. This mixture of pure states is called *mixed* states. We can describe it with *density matrices*, defined by,

$$\hat{\rho} = \sum_i p_i |\psi\rangle\langle\psi|, \tag{2.35}$$

where the p_i represents the statistical weight of the different pure states in the mixed state, and we have $\sum_i p_i = 1$. The purity is defined,

$$P = \mathrm{Tr}\left[\rho^2\right]. \tag{2.36}$$

When $0 < P < 1$, it is a mixed state; when $P = 1$, it is a pure state. The density matrix is a general tool to describe a quantum state in quantum optics, but it is difficult to be applied in the continuous variable case, because it is hard to manipulate and contain an infinite number of elements in *Fock states* basis. Instead, the *Wigner* function is often used to represent quantum states in continuous variable regime. Here let us consider a N-mode quantum state with corresponding $2N$ quadrature variables $\{x_1, p_1, ..., x_N, p_N\}$. The *Wigner function* of the state is,

$$W\left(x_1, p_1, ..., x_N, p_N\right) = \frac{1}{(2\pi)^N} \int \mathrm{Tr}\left[\hat{\rho} e^{i\sum_i \left(x_i x_i' + p_i p_i'\right)}\right] e^{-i\sum_i \left(x_i x_i' + p_i p_i'\right)} \mathrm{d}x_1' \mathrm{d}p_1' ... \mathrm{d}x_N' \mathrm{d}x_N'. \tag{2.37}$$

The Wigner function is normalized to identity for the integral in all the quadratures $\{x_1, p_1, ..., x_N, p_N\}$. It is important that the integral of the Wigner function is the probability distribution of some specific quadrature, so we also call Wigner function *distribution of quasi-probability*. For instance, when we integrate the Wigner function over the quadrature $\hat{x}_\theta$, we obtain the probability distribution for the measurement of the orthogonal quadrature $\hat{x}_{\theta+\pi/2}$. In this thesis, we use *covariance matrix* to describe gaussian states, instead of using the Wigner function.

2.3.2 Gaussian states and covariance matrices

Quantum states are *gaussian states*, if their corresponding Wigner function has a gaussian shape, otherwise it is called *non-gaussian states*. In the gaussian case, the Wigner function is only determined by the first two moments of the quadratures. The first is the mean values of the quadratures in different corresponding modes; the second is the covariances of the quadratures in different modes, which originate from the fluctuations of the quadratures, such as $\langle(\delta\hat{x})^2\rangle$, $\langle(\delta\hat{p})^2\rangle$, $\langle\delta\hat{p}\delta\hat{x}\rangle$ and $\langle\delta\hat{x}\delta\hat{p}\rangle$. Hence, all the fluctuation property of gaussian states can be expressed with the *covariance matrix*. A quantum state, in the basis with N modes, can be written in a covariance matrix V, and the element of V is,

$$V_{ij} = \frac{\langle\delta\hat{q}_i\delta\hat{q}_j\rangle + \langle\delta\hat{q}_j\delta\hat{q}_i\rangle}{2}, \tag{2.38}$$

where $\hat{q}$ is a quadrature of the field (amplitude $\hat{x}$ or phase $\hat{p}$ quadrature), and $\delta\hat{q}_i = \hat{q}_i - \langle\hat{q}_i\rangle$.

When $i \neq j$, $\hat{q}_i$ and $\hat{q}_j$ commute, so

$$V_{ij} = \langle\delta\hat{q}_i\delta\hat{q}_j\rangle = \langle\delta\hat{q}_j\delta\hat{q}_i\rangle. \tag{2.39}$$

When $i = j$, for the $\langle\hat{x}\hat{p}\rangle$ correlation in off-diagonal blocks, we define,

$$\langle\delta\hat{x}_i\delta\hat{p}_i\rangle_{\mathrm{s}} = \langle\delta\hat{p}_i\delta\hat{x}_i\rangle_{\mathrm{s}} = \frac{\langle\delta\hat{x}_i\delta\hat{p}_i\rangle + \langle\delta\hat{p}_i\delta\hat{x}_i\rangle}{2} \tag{2.40}$$

Thus,

$$V = \begin{pmatrix} \langle(\delta\hat{x})_1^2\rangle & \langle\delta\hat{x}_1\delta\hat{x}_2\rangle & \dots & \langle\delta\hat{x}_1\delta\hat{p}_1\rangle_{\mathrm{s}} & \langle\delta\hat{x}_1\delta\hat{p}_2\rangle & \dots \\ \langle\delta\hat{x}_2\delta\hat{x}_1\rangle & \langle(\delta\hat{x})_2^2\rangle & \dots & \langle\delta\hat{x}_2\delta\hat{p}_1\rangle & \langle\delta\hat{x}_2\delta\hat{p}_2\rangle_{\mathrm{s}} & \dots \\ \vdots & \vdots & \ddots & \vdots & \vdots & \ddots \\ \langle\delta\hat{p}_1\delta\hat{x}_1\rangle_{\mathrm{s}} & \langle\delta\hat{p}_1\delta\hat{x}_2\rangle & \dots & \langle(\delta\hat{p})_1^2\rangle & \langle\delta\hat{x}_1\delta\hat{p}_2\rangle & \dots \\ \langle\delta\hat{p}_2\delta\hat{x}_1\rangle & \langle\delta\hat{p}_2\delta\hat{x}_2\rangle_{\mathrm{s}} & \dots & \langle\delta\hat{p}_2\delta\hat{p}_1\rangle & \langle(\delta\hat{p})_2^2\rangle & \dots \\ \vdots & \vdots & \ddots & \vdots & \vdots & \ddots \end{pmatrix} \tag{2.41}$$

According to the Heisenberg relation of quadratures, as in Equ. 2.14, the covariance matrices have a constrain [77] [96],

$$V + i\Omega \geq 0, \tag{2.42}$$

where[5]

$$\Omega = \begin{pmatrix} \mathbf{0} & \mathcal{I} \\ -\mathcal{I} & \mathbf{0} \end{pmatrix}, \tag{2.43}$$

where, $\mathcal{I}$ is a diagonal identity matrix. The above Equ. 2.42 indicates that all the eigenvalues of $V + i\Omega$ are non-negative, and this equation, in general, can be applied to all physical states. For all quantum states, including non-gaussian states, this above inequality is always satisfied. But covariance matrix is not enough to describe all the quantum properties of the non-gaussian states, then the Wigner function is employed [56].

The full covariance matrix is composed of four parts of correlations. The diagonal is amplitude quadrature correlation $\langle(\delta\hat{x})^2_{ij}\rangle$, and phase quadrature correlation $\langle(\delta\hat{p})^2_{ij}\rangle$; the off-diagonal is amplitude-phase correlation $\langle\delta\hat{x}_i\delta\hat{p}_j\rangle$, and phase-amplitude correlation $\langle\delta\hat{p}_i\delta\hat{x}_j\rangle$. Each of the four parts is a real and symmetry matrix, and most of quantum resources have only amplitude and phase quadrature parts, without off-diagonal parts, such as, SPOPO [70], cascading four wave mixing [13], ect. Therefore linear optical networks are applied to obtain amplitude-phase or phase-amplitude correlations, for instance, the implementation of controller-z gates with off-line OPOs [85] [99].

The covariance matrix is often measured via balanced homodyne detection, which will be presented later. Notice that, the covariance originates from both classical and quantum fluctuations [73], and when there is no classical noise (shot noise limited), the covariance matrix represents the quantum fluctuations and correlations.

In addition, the purity P of gaussian states [1] can be obtained for their corresponding covariance matrix as below,

$$P = \frac{1}{\sqrt{\det V}} \leq 1. \tag{2.44}$$

$P = 1$ means it is a pure state; $P < 1$ suggests mixed states.

Here we give two examples of gaussian states:

Coherent states: As we already mentioned, the coherent states are the eigenstates of the annulation operators. The variances of corresponding

[5]The form of Ω depends on the form of a covariance matrix. Here we give the form of covariances as in Equ. 2.41.

quadratures are both 1, and the quadratures of different modes are not correlated. Thus the covariance matrix of a pure coherent state is an identity matrix.

Squeezed states: As defined in Equ. 2.19, for a given mode l, the Heisenberg relation is $\Delta x_l^2 \cdot \Delta p_l^2 \geq 1$. If in the quadrature $\hat{x}_l$ we have $\Delta \hat{x}_l^2 < 1$ and the covariances are zero, we call the it is *squeezed* on this quadrature. Because of the Heisenberg relation, the other quadrature is *antisqueezed*. In particular, if the mean field is zero and it is also squeezed, we call it *squeezed vacuum*. Importantly, mean photon number of squeezed vacuum are not zero. For instance, the squeezing operator K in Equ. 2.17, acts on a coherent state, then the covariance matrix of the squeezed states has the form as below,

$$V_{\text{sqz}} = \begin{pmatrix} \Delta x^2 & 0 \\ 0 & \Delta p^2 \end{pmatrix} = K^2 = \begin{pmatrix} e^{-2r} & 0 \\ 0 & e^{2r} \end{pmatrix}. \tag{2.45}$$

2.3.3 Basis change of covariance matrix

In the provisos we introduced the basis change in the quadrature representation, defined in Equ. 2.33. Generally, from a covariance matrix V, we have a new covariance matrix V_S with a basis change S defined in Equ. 2.34,

$$V_S = SVS^T. \tag{2.46}$$

And the variance $\Delta^2(\vec{M})$ in a desired mode $\vec{M}$, which is in the quadrature representation, can be obtained via projecting the covariance matrix onto $\vec{M}$,

$$\Delta^2(\vec{M}) = \vec{M}V\vec{M}^T. \tag{2.47}$$

This equation above allows to study the noise property of a specific mode in a state.

As the covariance matrix is in the quadrature representation, the mode and the basis change should be also expressed in this representation. Generally, covariance matrix describe all the quantum property, quantum fluctuations, of gaussian states. And hence, we can study the quantum property of the state in some specific mode or basis via projecting the covariance matrix (the state) onto the desired mode or the corresponding basis change, respectively.

2.4 Symplectic transform

Quantum optics experiments, usually, are composed of a series of linear and non-linear optical elements after light resource, and a detection system. In

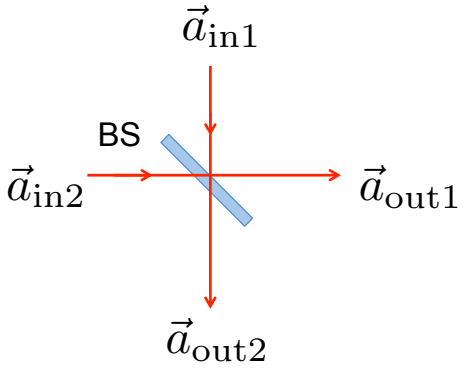

Figure 2.5: Two input beams $\hat{a}_{in1}$ and $\hat{a}_{in2}$ are mixed with an optical beam splitter, then two transmitted beams output $\hat{a}_{out1}$ and $\hat{a}_{out2}$ are synthesized.

this chapter we will talk about related *symplectic* transformation between input and output field. Here the field of light is expressed as in the Equ. 2.10,

$$\hat{E}^{(+)}_{\text{out}} = \sum_i \hat{E}^{(+)}_{\text{i,out}} = f\left(\{\hat{E}^{(+)}_{\text{i,in}}\}, \{\hat{E}^{(-)}_{\text{i,in}}\}\right), \tag{2.48}$$

where the output field $\hat{E}^{(+)}_{\text{i,out}}$ is output which is a function of input fields and their conjugates in corresponding modes, such as $\{\hat{E}^{(+)}_{\text{i,in}}\}$ and $\{\hat{E}^{(-)}_{\text{i,in}}\}$. This input-output relation can have many different forms according to experimental facts, but the output should be physical and obey the commutation relation.

Similarly, the same principle works on the annihilation and creation operators,

$$\hat{a}_{\text{out}} = \sum_i \hat{a}_{\text{i,out}} = f\left(\{\hat{a}_{\text{i,in}}\}, \{\hat{a}^{\dagger}_{\text{i,in}}\}\right). \tag{2.49}$$

In this chapter, we will present two examples of sympletic transform, which are beam splitter and the OPO squeezing operator.

Example 1: Optical beam splitter

Considering the optical beam splitter (BS), as seen in Fig. 2.5, mixes two input multimode beams $\vec{a}_{in1} = (\hat{a}^1_1, \hat{a}^2_1, ...\hat{a}^N_1)^{\text{T}}$ and $\vec{a}_{in2} = (\hat{a}^1_2, \hat{a}^2_2, ...\hat{a}^N_2)^{\text{T}}$, we can get transmitted beam $\vec{a}_{out1} = (\hat{a'}^1_1, \hat{a'}^2_1, ...\hat{a'}^N_1)^{\text{T}}$ and reflected beam $\vec{a}_{out2} = (\hat{a'}^1_2, \hat{a'}^2_2, ...\hat{a'}^N_2)^{\text{T}}$. Here we assume the two input beams are expressed in the same mode basis, so the ith mode of the two input fields interferes perfectly. When the BS has a reflectivity r and transmission t, where $r^2 + t^2 = 1$,

generally we have,

$$\begin{aligned} \vec{a}_{out1} &= t\vec{a}_{in1} + r\vec{a}_{in2} \\ \vec{a}_{out2} &= -r\vec{a}_{in1} + t\vec{a}_{in2}. \end{aligned} \tag{2.50}$$

In particular, for a semi-reflecting BS, where $r = t = 1/\sqrt{2}$ in the above equation, we have,

$$\begin{aligned} \vec{a}_{out1} &= \frac{1}{\sqrt{2}}(\vec{a}_{in1} + \vec{a}_{in2}) \\ \vec{a}_{out2} &= \frac{1}{\sqrt{2}}(-\vec{a}_{in1} + \vec{a}_{in2}). \end{aligned} \tag{2.51}$$

Hence we have the corresponding matrix form for the beam splitter,

$$\begin{pmatrix} \vec{a}_{\text{out1}} \\ \vec{a}_{\text{out2}} \\ \vec{a^\dagger}_{\text{out1}} \\ \vec{a^\dagger}_{\text{out2}} \end{pmatrix} = \begin{pmatrix} t & r & 0 & 0 \\ -r & t & 0 & 0 \\ 0 & 0 & t & r \\ 0 & 0 & -r & t \end{pmatrix} \begin{pmatrix} \vec{a}_{\text{in1}} \\ \vec{a}_{\text{in2}} \\ \vec{a^\dagger}_{\text{in1}} \\ \vec{a^\dagger}_{\text{in2}} \end{pmatrix}. \tag{2.52}$$

Example2: Squeezing operator

Beam splitter relation as in Equ. 2.50 is a linear unitary transform. Here we give another example of quadratic Hamiltonian, which is a $\chi^{(2)}$ non-linear parametric down conversion process,

$$\begin{aligned} \hat{a}_{\text{out1}} &= \hat{a}_1 \text{cosh}\gamma + \hat{a}_2^\dagger \text{sinh}\gamma \\ \hat{a}_{\text{out2}} &= \hat{a}_1^\dagger \text{sinh}\gamma + \hat{a}_2 \text{cosh}\gamma, \end{aligned} \tag{2.53}$$

where γ is a parameter proportional to $\chi^{(2)}$. Thus the corresponding matrix form is,

$$\begin{pmatrix} \vec{a}_{\text{out1}} \\ \vec{a}_{\text{out2}} \\ \vec{a^\dagger}_{\text{out1}} \\ \vec{a^\dagger}_{\text{out2}} \end{pmatrix} = \begin{pmatrix} \text{cosh}\gamma & 0 & 0 & \text{sinh}\gamma \\ 0 & \text{cosh}\gamma & \text{sinh}\gamma & 0 \\ 0 & \text{sinh}\gamma & \text{cosh}\gamma & 0 \\ \text{sinh}\gamma & 0 & 0 & \text{cosh}\gamma \end{pmatrix} \begin{pmatrix} \vec{a}_1 \\ \vec{a}_2 \\ \vec{a^\dagger}_1 \\ \vec{a^\dagger}_2 \end{pmatrix}. \tag{2.54}$$

Definition: Symplectic transform

The relations, as in Equ. 2.50 and Equ. 2.53, are the coupling between the annihilation and creation operators. They are both linear transformations also conserve commutations. All of these linear transforms are in the *group symplectic* [25], also called symplectic transforms in this thesis. Free propagation, linear optics, and quadratic Hamiltonian are symplectic transforms [74], and are linear processes in quantum mechanics.

Considering a multimode case, $\vec{a}_{in} = (\hat{a}^1, \hat{a}^2, ...\hat{a}^N)^{\mathrm{T}}$ and $\vec{a}_{out} = (\hat{a'}^1, \hat{a'}^2, ...\hat{a'}^N)^{\mathrm{T}}$. Here we can write input-output relation with a symplectic transform $\mathcal{R}$,

$$\begin{pmatrix} \vec{a}_{\mathrm{out}} \\ \vec{a}^{\dagger}_{\mathrm{out}} \end{pmatrix} = \mathcal{R} \begin{pmatrix} \vec{a}_{\mathrm{in}} \\ \vec{a}^{\dagger}_{\mathrm{in}} \end{pmatrix}, \quad \text{and,} \quad \mathcal{R} = \begin{pmatrix} \mathcal{C} & \mathcal{S} \\ \mathcal{S}^* & \mathcal{C}^* \end{pmatrix}, \tag{2.55}$$

where $\mathcal{C}$ and $\mathcal{S}$ are complex matrices. And,

$$\mathcal{R}^{-1} = \sigma \mathcal{R}^{\dagger} \sigma, \quad \text{and,} \quad \sigma = \begin{pmatrix} \mathbf{I} & 0 \\ 0 & -\mathbf{I} \end{pmatrix}, \tag{2.56}$$

where the $\mathbf{I}$ is a identity matrix with a $2N$ dimension. The symplectic transform $\mathcal{R}$ is the most general linear transform that preserves commutation relations, $\left[\hat{a'}^i, \hat{a'}^{i\dagger}\right] = \left[\hat{a}^i, \hat{a}^{i\dagger}\right] = 1$.

2.5 Williamson decomposition and Bloch Messiah reduction

In this section we will introduce *Williamson decomposition* [74] and *Bloch-Messiah Decomposition* [10] to provide a general description of multimode gaussian states. With this method, we can show that any gaussian states can be decomposed as a multimode squeezing operator acting onto a set of noisy modes with corresponding basis changes.

First let us recall the covariance matrix defined as Equ. 2.41, we give a simple form as below,

$$\vec{V} = \begin{pmatrix} V_{\text{Amplitude}} & V_{\text{Amp-Phase}} \\ V_{\text{Phase-Amp}} & V_{\text{Phase}} \end{pmatrix} = \begin{pmatrix} V_{XX} & V_{XP} \\ V_{PX} & V_{PP} \end{pmatrix}. \tag{2.57}$$

We assume this is the covariance matrix of a set of quadrature operators $(\hat{x}_1, \hat{x}_2, ..., \hat{x}_n, \hat{p}_1, \hat{p}_2, ..., \hat{p}_n)^T$. For example, the covariance matrix in this thesis, generated via SPOPO [20], has no off-diagonal part, with only amplitude and phase correlations, written as below,

$$V_{\text{SPOPO}} = \begin{pmatrix} V_{XX} & \mathbf{0} \\ \mathbf{0} & V_{PP} \end{pmatrix}. \tag{2.58}$$

Definition: *Williamson decomposition*, in general, for a covariance matrix $\vec{V}$, is the decomposition,

$$S^T \vec{V} S = D^2, \tag{2.59}$$

where S is a basis change in the quadrature representation, defined in Equ. 2.33, and D is a diagonal matrix with the form $diag(D1, D2, \dots, D1, D2, \dots)$, whose elements are real and bigger than 1.

And the symplectic matrix S satisfies:

$$S^{\mathrm{T}}\beta S = \beta, \quad \text{with} \quad \beta = \begin{pmatrix} 0 & \mathbf{I} \\ \mathbf{I} & 0 \end{pmatrix}, \tag{2.60}$$

where $\mathbf{I}$ is the identity matrix.

Definition: *Multimode squeezing*, we extend the squeezing operator K in the Equ. 2.17 to the multimode case. In the simplest case of a uniform squeezing distribution $K = \begin{pmatrix} e^{-r}\mathbf{I} & 0 \\ 0 & e^{r}\mathbf{I} \end{pmatrix}$ with a real and positive number r and the identity matrix $\mathbf{I}$.

Generally, we have K acting on a set of orthogonal modes, with quadrature operators $\left(\hat{x}_{(0)_1}, \hat{x}_{(0)_2}, \dots, \hat{p}_{(0)_1}, \hat{p}_{(0)_2}, \dots\right)^{\mathrm{T}}$, and the corresponding multimode squeezing is,

$$\left(\hat{x}_{r_1}, \hat{x}_{r_2}, \dots, \hat{p}_{r_1}, \hat{p}_{r_2}, \dots\right)^{\mathrm{T}} = K\left(\hat{x}_{(0)_1}, \hat{x}_{(0)_2}, \dots, \hat{p}_{(0)_1}, \hat{p}_{(0)_2}, \dots\right)^{\mathrm{T}}. \tag{2.61}$$

Each mode has the variance $\delta x^2_{r_i} = \langle (x_{r_i}) \rangle^2 - \langle x_{r_i} \rangle^2$, so we have,

$$\begin{pmatrix} \delta x^2_{r_1} \\ \delta x^2_{r_2} \\ \vdots \\ \delta p^2_{r_1} \\ \delta p^2_{r_2} \\ \vdots \end{pmatrix} = K^2 . \begin{pmatrix} \delta x^2_{(0)_1} \\ \delta x^2_{(0)_2} \\ \vdots \\ \delta p^2_{(0)_1} \\ \delta p^2_{(0)_2} \\ \vdots \end{pmatrix} = \begin{pmatrix} e^{-2r_1} & 0 & \dots & 0 & 0 & \dots \\ 0 & e^{-2r_2} & \dots & 0 & 0 & \dots \\ \vdots & \vdots & \ddots & \vdots & \vdots & \ddots \\ 0 & 0 & \dots & e^{2r_1} & 0 & \dots \\ 0 & 0 & \dots & 0 & e^{2r_2} & \dots \\ \vdots & \vdots & \ddots & \vdots & \vdots & \ddots \end{pmatrix} \begin{pmatrix} \delta x^2_{(0)_1} \\ \delta x^2_{(0)_2} \\ \vdots \\ \delta p^2_{(0)_1} \\ \delta p^2_{(0)_2} \\ \vdots \end{pmatrix}, \tag{2.62}$$

where $\left(\delta x^2_{(0)_1}, \delta x^2_{(0)_2}, \dots, \delta p^2_{(0)_1}, \delta p^2_{(0)_2}, \vdots\right)^{\mathrm{T}}$ is the variance of the amplitude and phase quadratures of coherent states.

For coherent states, as the normalized variance, $\delta x^2_{(0)_i} = \delta p^2_{(0)_i} = 1$, we simply have,

$$\begin{pmatrix} \delta x^2_{r_1} \\ \delta x^2_{r_2} \\ \vdots \\ \delta p^2_{r_1} \\ \delta p^2_{r_2} \\ \vdots \end{pmatrix} = \begin{pmatrix} e^{-2r_1} & 0 & \dots & 0 & 0 & \dots \\ 0 & e^{-2r_2} & \dots & 0 & 0 & \dots \\ \vdots & \vdots & \ddots & \vdots & \vdots & \ddots \\ 0 & 0 & \dots & e^{2r_1} & 0 & \dots \\ 0 & 0 & \dots & 0 & e^{2r_2} & \dots \\ \vdots & \vdots & \ddots & \vdots & \vdots & \ddots \end{pmatrix} = K^2. \tag{2.63}$$

Definition: *Bloch-Messiah Decomposition*, for any symplectic transformation, $\tilde{S}$, we can always decompose it into a multimode squeezer K and two basis changes, thus we have [10],

$$\tilde{S} = \mathcal{O}_1 K \mathcal{O}_2^T, \tag{2.64}$$

where $O_{1,2}$ are any two basis change defined in Equ. 2.33.

Any basis change of vacuum is always vacuum (coherent states). Therefore, if a quantum network is started from vacuum, we can cancel O_2,

$$\mathcal{O}_1 K \mathcal{O}_2^T |\mathbf{0}\rangle = \mathcal{O}_1 K |\mathbf{0}\rangle, \tag{2.65}$$

where $\mathbf{0}$ represent multimode vacuum.

Decomposition of covariance matrix

Above, we see that any gaussian state, covariance matrix, can be diagonalized via *Williamson decomposition* in Equ. 2.59. If we define $\tilde{S} = S^{-1^T}$ and apply *Bloch Messiah* decomposition, then the measured covariance matrix is expressed as,

$$\vec{V} = \mathcal{O}_1 K \mathcal{O}_2^T \left(D^2\right) \mathcal{O}_2 K \mathcal{O}_1^T \tag{2.66}$$

with the diagonal matrix K and the orthogonal transform $\mathcal{O}_{1,2}$. This allows to interpret (D^2) as the classical noisy input modes (noise modes) of the multimode squeezing.

Physically, $\mathcal{O}_1$ is the squeezing modes and $\mathcal{O}_2$ is noise modes, $\mathcal{O}_{1,2}$ are basis change in the quadrature representation; the diagonal K is the multimode squeezing operator.

2.5.1 Recipe of Williamson decomposition

In the Williamson decomposition of a given covariance matrix V, a $2n$-dimension and real symmetric matrix, there exits a real matrix $S \in Sp(2n, \mathcal{R})$ such that [76],

$$S^T V S = D^2 > 0, \tag{2.67}$$

with,

$$D^2 = \begin{pmatrix} \Omega^{-1} & 0 \\ 0 & \Omega^{-1} \end{pmatrix}, \tag{2.68}$$

where Ω^{-1} is a diagonal real matrix,

$$\Omega^{-1} = \begin{pmatrix} d1 & \cdots & 0 \\ \vdots & \ddots & \vdots \\ 0 & 0 & d_n \end{pmatrix}. \tag{2.69}$$

The above equation, associated to Heisenberg uncertainties as Equ. 2.42, physically means the classical modes have symmetric Heisenberg fluctuations in the $\hat{x}, \hat{p}$ quadratures [74].

We consider here the explicit recipe to derive the diagonal matrix D and the corresponding Williamson decomposition Equ. 2.67.

Consider the matrix $\mathcal{M} = V^{-1/2}\beta V^{-1/2}$. It is a real, nonsingular, antisymmetric matrix and hence its eigenvalues $\mathrm{i}\omega_i$ and eigenvectors $\vec{\eta}_i$ have the following properties:

$$\begin{aligned} -i\mathcal{M}\vec{\eta}_\alpha = \omega_\alpha \vec{\eta}_\alpha, \quad & \alpha = 1, ..., 2n, \\ \omega_k > 0, \quad k = 1, ..., n; \quad & \omega_{k+n} = -\omega_k, \\ & \vec{\eta}_{k+n} = \vec{\eta}_k^*. \end{aligned} \tag{2.70}$$

This already allows to find $\Omega = diag(\omega_1, \omega_2, ..., \omega_n)$ [6] and hence the decomposition of Equ. 2.67. Arrange the vectors $\vec{\eta}$ as the columns of a matrix U,

$$U = (\vec{\eta}_1, \vec{\eta}_2, \cdots, \vec{\eta}_{2n}) \,. \tag{2.71}$$

From Equ. 2.70 it follows that

$$U^\dagger \mathcal{M} U = \begin{pmatrix} i\Omega & 0 \\ 0 & i\Omega \end{pmatrix} \equiv \Lambda \tag{2.72}$$

This symplectic matrix realizing the Williamson decomposition Euq. 2.67 is determined as,

$$S = V^{-\frac{1}{2}} U \Delta D \quad \text{with} \quad \Delta = \frac{1}{\sqrt{2}} \begin{pmatrix} \mathcal{I} & -i\mathcal{I} \\ \mathcal{I} & i\mathcal{I} \end{pmatrix} \tag{2.73}$$

Using $S^T = S^\dagger$, the Williamson decomposition Equ. 2.67 can be obtained.

After getting the transform S from the Williamson decomposition, we can achieve the Bloch-Messiah decomposition matrix K and $\mathcal{O}_1$, via directly diagonalizing $\tilde{S}\tilde{S}^T$, and the corresponding eigenvalues and eigenvectors are referring to the diagonal elements of K and $\mathcal{O}_1$, respectively.

Above all, we presented a standard way of multimode analysis, the Williamson decomposition, which transforms a given covariance matrix to the uncorrelated squeezing basis via the transform S, including Bloch-Messiah decomposition. The squeezed modes form the Bloch-Messiah decomposition, and together with the noise modes construct the Williamson decomposition.

[6] $diag(\omega_1, \omega_2, ..., \omega_n)$ referers to a diagonal matrix with the diagonal elements $\omega_1, \omega_2, ..., \omega_n$.

When the noise modes have the noises close to the shot noise limit, thus without correlation [73], we can also directly diagonalize covariance matrix to get squeezing values and squeezed modes [65] which correspond to $\mathcal{O}_1$. As the purity, as defined in Equ. 2.36 is not 1, we get slightly different eigenmodes from the amplitude covariance matrix V_{XX} compared to the phase covariance matrix V_{PP} [13]. In a result, in the basis composed of the eigenmodes of the phase covariance matrix V_{PP}, a bit of correlation still exits in amplitude quadrature [70]. Also different from the Williamson decomposition, here the squeezing values are similar to the one that directly measured.

Up to now, we have two ways of multimode analysis: Williamson decomposition and directly diagonalizing covariance matrix, both of which give the squeezing values and squeezed modes. Next in the thesis, we will introduce a multimode quantum resource, *synchronously pumped optical parametric oscillator* (SPOPO), and analyze it using the methods.

Chapter 3

SPOPO model and simulation

Contents

In the previous chapter, we have presented the quantum description of light. We have seen that for coherent states of light [35], the quantum fluctuations are normalized to 1 in both amplitude and phase quadratures. We therefore have the shot noise limit in the intensity and phase measurements. However, with squeezed states of light, the quantum fluctuation can be less than 1 for one quadrature, beyond the shot noise. This is because, differently from a random process happening in a classical (coherent) source, during the generation of squeezed states, always even photons are generated via parametric down conversion processed [97], and consequently squeezing occurs.

Furthermore, EPR correlation [68] [22] in the continuous variable regime was generated based on this nonlinear optical process [61], and a deterministic quantum teleportation was described [12] and implemented [29] [88].

Nonlinear optics, such as parametric down conversion [7], four wave mixing [66], optical parametric oscillator [81] and etc., is an important tool in generating quantum resources of light.

We focus in using $\chi^{(2)}$ processes and ultrafast pulses to generate a broadband quantum resource [70] in this PhD project.

In this chapter, first, we will give the theoretical model of *synchronously pumped an optical parametric oscillator* (SPOPO) [63] [41]; then the simulation result, based on the model of SPOPO [20], will be presented.

3.1 Basic tools of nonlinear optics

3.1.1 Propagation equation of nonlinear optics

We define the electric field $E^{(+)}(\vec{r},\omega)$ as a function of the envelop $u(\vec{r},\omega)$,

$$E^{(+)}(\vec{r},\omega) = u(\vec{r},\omega)e^{i\vec{k}(\omega)\cdot\vec{r}}, \tag{3.1}$$

and assume the propagation direction is along z, we have

$$e^{i\vec{k}(\omega)\cdot\vec{r}} \rightarrow e^{ik(\omega)z}, \tag{3.2}$$

thus the propagation equation in a nonlinear medium is [69],

$$\frac{\partial u}{\partial z}(z,\omega) = \frac{i\omega}{2\epsilon_0 nc} P^{(+)}_{\mathrm{NL}}(z,\omega)e^{-ik(\omega)z}, \tag{3.3}$$

where the polarization is composed of linear and nonlinear parts,

$$P^{(+)}_{\mathrm{NL}}(z,\omega) = P^{(+)}(z,\omega) - P^{(+)}_{\mathrm{L}}(z,\omega). \tag{3.4}$$

For the linear part, we have[1],

$$\begin{aligned} P^{(+)}_{\mathrm{L}}(z,\omega) &= \epsilon_0 \sum_j \chi^{(1)}(\omega)E_j \\ k^2(\omega) &= n^2(\omega)\frac{\omega^2}{c^2} \\ n^2(\omega) &= 1+\chi^{(1)}(\omega) \end{aligned} \tag{3.5}$$

[1]Here we assume $\chi^{(1)}$ is symmetric and diagonalizable, so P_i depends on only E_i.

and with the term $E^{(+)}(z,\omega)$ we have the propagation equation,

$$\frac{\partial E^{(+)}}{\partial z}(z,\omega) = ik(\omega)E^{(+)}(z,\omega) + \frac{i\omega}{2\epsilon_0 nc}P^{(+)}_{\mathrm{NL}}(z,\omega). \tag{3.6}$$

Notice that, in the propagation equation, the first term and the second represent linear and nonlinear propagations, respectively.

We simply presented the nonlinear propagation equation, which will be used to describe nonlinear effects, such as, frequency doubling, parametric down conversion, etc. in the thesis. The propagation equation of free radiation with nonlinear properties depend on *the polarization* of the medium $P^{(+)}(z,\omega) = P^{(+)}_{\mathrm{L}}(z,\omega)+P^{(+)}_{\mathrm{NL}}(z,\omega)$, including the electric *susceptibility* $\left\{\chi^{(n)}\right\}$. In particular, with our interest, the $\chi^{(2)}$ effect originates from the corresponding polarization $P_i^{(+2)} = \epsilon_0 \sum_{jk} \chi^{(2)}_{ijk} E_j E_k$, so the efficiency of $\chi^{(2)}$ processes is proportional to nonlinear coefficient $\chi^{(2)}$ of the medium and the associated fields.

For ultrafast pulses with high peak intensities, it is, usually, a good candidate for nonlinear optics. And next we will present the interaction between ultrafast pulses and a $\chi^{(2)}$ nonlinear crystal to generate multimode quantum resources of light.

3.2 Nonlinear effect with ultrafast pulses

In the following, we will study the $\chi^{(2)}$ nonlinear processes with ultrafast pulses. The light is therefore non-monochromatic, and we will develop a method, adapting the broadband property of ultrafast pulses, to describe the second order nonlinear effects.

3.2.1 Second order polarization

Generally, the laser-induced second order polarization in a nonlinear medium is,

$$P_i^{(2)}(t) = \epsilon_0 \int \chi^{(2)}_{ijk}(\omega_1,\omega_2)\, E_j(\omega_1)\, E_k(\omega_2)\, e^{-i(\omega_1+\omega_2)t} \frac{\mathrm{d}\omega_1}{\sqrt{2\pi}} \frac{\mathrm{d}\omega_2}{\sqrt{2\pi}}, \tag{3.7}$$

where we assume j and k are the only two corresponding components of electric fields. On the frequency domain, we have,

$$\begin{aligned} P_i^{(2)}(\omega) &\equiv \epsilon_0 \int \chi^{(2)}_{ijk}(\omega_1,\omega_2)\, E_j(\omega_1)\, E_k(\omega_2)\, e^{-i(\omega_1+\omega_2-\omega)t} \frac{\mathrm{d}\omega_1}{\sqrt{2\pi}} \frac{\mathrm{d}\omega_2}{\sqrt{2\pi}} \mathrm{d}t \\ &= \epsilon_0 \int \chi^{(2)}_{ijk}(\omega_1,\omega_2)\, E_j(\omega_1)\, E_k(\omega_2)\, 2\pi\delta(\omega_1+\omega_2-\omega) \frac{\mathrm{d}\omega_1}{\sqrt{2\pi}} \frac{\mathrm{d}\omega_2}{\sqrt{2\pi}} \end{aligned} \tag{3.8}$$

Because the input fields are close to the transparent zone of the medium and the frequency bandwidth is not lagre, the frequency dependence of $\chi^{(2)}$ coefficient is negligible. We therefore have $\chi^{(2)}_{ijk}(\omega_1, \omega_2) \approx \chi^{(2)}$, and we can take the factor $\chi^{(2)}$ out of the integral in the equations 3.7 and 3.8.

We take a hypotheses, response of medium is instant. In consequence the polarization only depends on the analytic electric fields. With a given position in the time t, for $j = k$, we have,

$$P^{(2)}(t) = \epsilon_0 \chi^{(2)} E(t)^2 \tag{3.9}$$

To apply the propagation equation of Equ. 3.3, we write the polarization as

$$P_i^{(\pm,2)}(\omega) = 2\pi\epsilon_0\chi^{(2)} \int E_j^{(\pm)}(\omega_1)\, E_k^{(\pm)}(\omega_2)\, \delta(\pm\omega_1 \pm \omega_2 - \omega) \frac{\mathrm{d}\omega_1}{\sqrt{2\pi}} \frac{\mathrm{d}\omega_2}{\sqrt{2\pi}} \tag{3.10}$$

The choice of signs $\pm$ corresponds to the $\pm$ frequencies in the analytic fields, in practice, indicating different phenomena of nonlinear effects.

3.2.2 The wave number of ultrafast pulses

The wave number $k(\omega)$ is important in the propagation equation. Its frequency dependence in not negligible in the case of ultrafast pulses. Our source has a wide spectrum of $\simeq 10nm$.

Here to consider the dispersion property in the propagation, we write the wave number $k(\omega)$,

$$k(\omega) = k(\omega_0) + \frac{1}{v_\mathrm{g}(\omega_0)}(\omega - \omega_0) + \frac{1}{2}\mathrm{GVD}(\omega_0)(\omega - \omega_0)^2 + \ldots, \tag{3.11}$$

where,

$$v_\mathrm{g} = \left(\frac{\partial k(\omega)}{\partial \omega}\right)^{-1} = \frac{c}{n(\omega) + \omega \frac{\partial n(\omega)}{\partial \omega}} \tag{3.12}$$

$$\mathrm{GVD}(\omega) = \frac{\partial^2 k(\omega)}{\partial \omega^2} = \frac{\partial}{\partial \omega}\left(\frac{1}{v_\mathrm{g}}\right) \tag{3.13}$$

represent the *group velocity* and the *dispersion of group velocity*, respectively.

3.3 The SPOPO model

The interest of this thesis is to generate a multimode squeezing resource with a $\chi^{(2)}$ nonlinear effect. To aim that, we will synchronously pump an optical

parametric oscillator, SPOPO with an optical frequency combs. The $\chi^{(2)}$ processes, parametric down converting (PDC) a photon of the *pump* into two photons, occur in an optical cavity, and generate squeezed states. Yet, with optical frequency combs, the case is more complex, as all the frequencies of the frequency comb are possible to participate to the PDC process. Here we will give the theoretical description of the SPOPO.

Firstly we will present frequency doubling of ultrafast pulses with $\chi^{(2)}$ nonlinear crystals. A train of femtosecond pulses, centered at $\sim$ 800 nm, directly pass a $\chi^{(2)}$ crystal, and frequency doubled $\sim$ 400 nm pulses are generated, so call *pump* of the SPOPO. Then pumped with the 400 nm pulses, parametric down conversation occur in the SPOPO cavity, which generates a multimode quantum beam.

3.3.1 Preparation of *pump*, frequency doubling

In monochromatic case, the process of frequency doubling is that via passing a nonlinear medium, an input light wave, *signal*[2] , with a frequency ω_0 can be transformed into a output wave with a frequency doubled $2\omega_0$. However, when the monochromatic input is replaced by a frequency comb, as many frequencies exist in the input, therefore many individual sum frequency and frequency doubling processes happen in the same time, as seen in Fig. 3.1.

Let us consider an input of frequency combs, whose frequencies $\omega_n^{\mathrm{s}} = \omega_0 + n\omega_{\mathrm{r}}$, with $\omega_0 = \omega_{\mathrm{CE}} + N\omega_{\mathrm{r}}$. If similar to the monochromatic case, the frequency doubling will generate a frequency comb with a doubled repartition rate, $2\omega_n^{\mathrm{s}} = 2\omega_0 + n(2\omega_{\mathrm{r}})$. However, this is not true for frequency doubling with frequency combs.

In the case with optical frequency combs, the generated comb, *pump*, via frequency doubling, has the same repetition rate as the input one, *signal*. As in the process of frequency doubling with frequency combs, it contains all the possibilities of sum frequencies, with two same frequencies or two different frequencies in the *signal*, as seen in Fig. 3.1. After frequency doubling, we have the frequencies of the *pump*,

$$\omega_{m+n}^{\mathrm{p}} = \omega_m^{\mathrm{s}} + \omega_n^{\mathrm{s}} = 2\omega_0 + (m+n)\omega_r. \tag{3.14}$$

Therefore, the repetition rate of the *pump* is still ω_{r}.

Notice that, after the frequency doubling process with optical frequency combs, the central frequency of input comb has a doubled frequency, so we

[2]To be consistent with the SPOPO process, we call the pulses with the central frequency ω_0 *signal*, and *pump* refers to the $2\omega_0$ pulses.

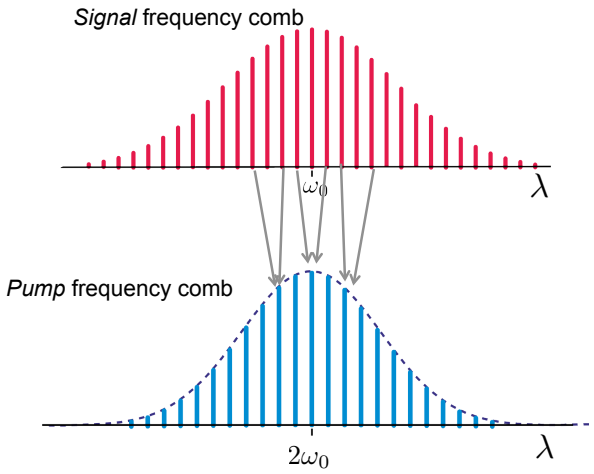

Figure 3.1: Multi-frequecy doubling with optical frequency combs. A new photon with a frequency $\omega^{\mathrm{p}}_{m+n}$ is generated by two photons with frequencies ω^{s}_{m} and ω^{s}_{n} in the input source. All the processes with energy conservation, $\omega^{\mathrm{p}}_{m+n} = \omega^{\mathrm{s}}_{m} + \omega^{\mathrm{s}}_{n}$ can happen in the same instant. After the frequency doubling with an optical frequency comb, a new frequency comb with a doubled center frequency is generated.

still call it *frequency doubling* in the case. Then, differently, the carrier-envelope-offset is doubled: $2\omega_0 = 2\omega_{\mathrm{CE}} + 2N\omega_{\mathrm{r}}$.

In the following we will present and solve the propagation equation for the frequency doubling. Based on the second order polarization expression of Equ. 3.10, we choose the positive signs and corresponding electric field E for the process of frequency doubling. Thus, we have,

$$P^{(+,2)}_{\mathrm{p}}(z,\omega) = \epsilon_0 \chi^{(2)} \int E^{(+)}_{\mathrm{s}}(z,\omega') E^{(+)}_{\mathrm{s}}(z,\omega-\omega') \frac{\mathrm{d}\omega'}{2\pi}, \tag{3.15}$$

where $E^{(+)}_{\mathrm{s}} = u_{\mathrm{s}}(z,\omega) e^{ik_{\mathrm{s}}(\omega)z}$.

The corresponding propagation equation, with the envelope u_{p} of the frequency comb, is

$$\frac{\partial u_{\mathrm{p}}}{\partial z}(z,\omega) = \frac{i\omega\chi^{(2)}}{2nc} \int u_{\mathrm{s}}(z,\omega') u_{\mathrm{s}}(z,\omega-\omega') e^{i\Delta k(\omega.\omega')z} \frac{\mathrm{d}\omega'}{2\pi}, \tag{3.16}$$

where $\Delta k(\omega,\omega') = k_{\mathrm{s}}(\omega') + k_{\mathrm{s}}(\omega-\omega') - k_{\mathrm{p}}(\omega)$, which is the *phase matching* of the frequency doubling. In the propagation equation Equ. 3.16, we can integrate over the length of the medium along the propagation direction z. For a $\chi^{(2)}$ crystal with a length l_c, we integrate from the beginning of crystal

$z_{\mathrm{A}} = -\frac{l_c}{2}$ to the end $z_{\mathrm{B}} = \frac{l_c}{2}$. Here we assume the efficiency of frequency doubling is small enough, so the intensity of input light has almost no change after traversing the medium, $u_{\mathrm{s}}(z,\omega) \simeq u_{\mathrm{s}}(\omega)$. We have the analytic solution of the Equ. 3.16,

$$u_{\mathrm{p}}(z_{\mathrm{B}},\omega) = \frac{i\omega\chi^{(2)}l_c}{2nc}\int u_{\mathrm{s}}(\omega')u_{\mathrm{s}}(\omega-\omega')\Phi(\omega,\omega')\frac{\mathrm{d}\omega'}{2\pi}, \tag{3.17}$$

where $\Phi(\omega,\omega')$ is a function associated with the phase matching defined by,

$$\Phi(\omega,\omega') = \mathrm{sinc}\left(\frac{\Delta k(\omega,\omega')l_c}{2}\right). \tag{3.18}$$

Because of the property of the *sinc* function, generally, for the phase matching, the function $\Phi(\omega,\omega')$ has a wider spectral response with a shorter nonlinear crystals. In our case with optical frequency combs, to get a wide bandwidth of spectral in the output of frequency doubling, therefore, we need choose short crystals.

In the ideal case of the phase matching, when the function $\Phi(\omega,\omega')$ equals 1, the envelope of the frequency doubled frequency comb u_{p} is the an auto-convolution of the input field envelopes.

An optical frequency comb with a central frequency ω_0 and a bandwidth $\Delta\omega$ can also generate a gaussian spectrum but centered at $2\omega_0$ and with a bandwidth $\sqrt{2}\Delta\omega$. Thus the generated pulses have a shorter duration by a factor of $\sqrt{2}$.

As to the corresponding spectra of the *pump* (frequency doubled) $\Delta\lambda_{\mathrm{p}}$ and the *signal* (input of frequency doubling) $\Delta\lambda_{\mathrm{s}}$, we have $\Delta\lambda_{\mathrm{p}} \simeq 0.3\Delta\lambda_{\mathrm{s}}$ when $\omega_0 >> \Delta\omega$ holds. Notice that, in the spectral domain, the *signal*, generally, has a wider spectrum compared to the *pump*.

In the real case, the phase matching is not always perfect while the function $\Phi(\omega,\omega')$ is close to a gaussian function, other than the constant 1. For the phase matching $\Delta k(\omega,\omega')$ of ultrafast nonlinear optics, we usually need consider the description effect induced by the propagation in the nonlinear medium.

To describe the phase matching $\Delta k(\omega,\omega')$, in Equ. 3.11, we need consider the dispersion property of medium (ω_0 for k_{s} and $2\omega_0$ for k_{p}),

$$\begin{aligned}\Delta k(\omega,\omega') &= k_{\mathrm{s}}(\omega') + k_{\mathrm{s}}(\omega-\omega') - k_{\mathrm{p}}(\omega)\\ &= \Delta k(2\omega_0,\omega_0) + \left(\frac{1}{v_{\mathrm{g,s}}} - \frac{1}{v_{\mathrm{g,p}}}\right)(\omega-2\omega_0) + \frac{1}{2}(\mathrm{GVD_s}-\mathrm{GVD_p})(\omega-2\omega_0)^2\\ &\quad -\mathrm{GVD_s}(\omega'-\omega_0)(\omega-\omega'-\omega_0),\end{aligned} \tag{3.19}$$

where the "s" and "p" correspond to the frequency combs with the central frequencies ω_0 and $2\omega_0$ respectively.

In the phase matching function $\Delta k(\omega, \omega')$, the term $\Delta k(2\omega_0, \omega_0)$ is constant 0 when the refractive index $n(\omega_0) = n(2\omega_0)$. This can give a perfect phase matching in the case monochromatic waves and satisfy the birefringence of medium. In practice of birefringence medium, we can realize $\Delta k(2\omega_0, \omega_0) = 0$ by choosing the cutting angle or controlling the temperature of nonlinear crystals.

When the case is large bandwidth spectra, the phase matching $\Delta k(\omega, \omega')$ will depend not only on the first term $\Delta k(2\omega_0, \omega_0)$ but also the group velocity and dispersion of the light, which are the other terms in the Equ. 3.19. Next we will consider the dispersive property of BiBO crystals.

Our source is an optical frequency comb centered at $\simeq 800nm$ with 76MHz repetition rate. The frequency doubling is the type I $e + e \to o$, where the polarization of signal E_s is aligned to the extraordinary axis and the frequency doubled pump E_p corresponds to the ordinary axis.

The dispersion effect in the frequency doubling with BiBO crystals [33]. Here we give the group velocity and dispersion values of BiBO crystals [62] [69], [3]

$$V_{\mathrm{g,s}}/c = 0.5319, \quad \mathrm{GVD_s} = 164\mathrm{fs}^2/\mathrm{mm} \tag{3.20}$$

$$V_{\mathrm{g,p}}/c = 0.5010, \quad \mathrm{GVD_p} = 472\mathrm{fs}^2/\mathrm{mm} \tag{3.21}$$

The calculation shows that the corresponding terms of Equ. 3.19 has $|\frac{1}{v_{\mathrm{g,s}}} - \frac{1}{v_{\mathrm{g,p}}}|\Delta\omega \geq |\mathrm{GVD_s} - \mathrm{GVD_p}|(\Delta\omega)^2$. Therefore, compared to the group velocity, the GVD contribute very little in the phase matching. With $\sim 10nm$ bandwidth spectra, the GVD contribution in the phase matching is negligible. Only when the spectrum is very large we need count the effect of GVD. Thus we have simply,

$$\Delta k(\omega, \omega') \simeq \Delta k(\omega) = \left(\frac{1}{v_{\mathrm{g,s}}} - \frac{1}{v_{\mathrm{g,p}}}\right)(\omega - 2\omega_0) \tag{3.22}$$

Then we can directly factorize $\Delta k(\omega, \omega')$ which is only a function of ω in this case, so we have an auto-convolution of signal envelope,

$$u_\mathrm{p} = \frac{i\omega\chi^{(2)}l_c}{2nc}\mathrm{sinc}\left(\frac{\Delta k(\omega)l_c}{2}\right)\int u_\mathrm{s}(\omega')u_\mathrm{s}(\omega - \omega')\frac{\mathrm{d}\omega'}{2\pi}, \tag{3.23}$$

and the corresponding intensity spectrum is,

$$I_\mathrm{p}(z_\mathrm{B}, \omega) \propto l_c^2\mathrm{sinc}^2\left(\frac{\Delta k(\omega)l_c}{2}\right)(u_\mathrm{s} \star u_\mathrm{s})^2(\omega). \tag{3.24}$$

[3] Usually we can use the free software SNLO to get nonlinear and dispersion parameters of many nonlinear crystals.

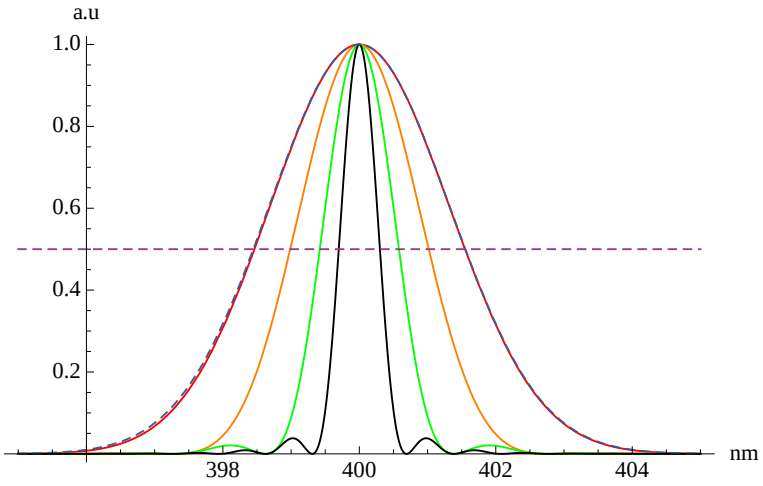

Figure 3.2: The spectral profiles of *pump* generated via frequency doubling. The red, orange, green, black lines correspond to 0.2 mm, 0.5 mm, 1 mm and 2 mm long crystals, respectively, and the dashed line is a gaussian fit of the profit on red color (0.2 mm BiBO crystal), whose bandwidth is $\sim 3.1nm$. The horizontal dashed purple line on the half hight of the profiles (FWHM).

We can see that, generally, we can get stronger frequency doubling with a longer crystal, but on the other hand, long crystals are not good for the phase matching of the wings of the spectrum. Also, in Equ. 3.23, if u_s is real, u_p is pure imaginary.

In the experiment, we use 0.2 mm long BiBO crystal for frequency doubling, which generates pulses centered at 400nm with $\sim$ 3.1nm bandwidth, which is used to pump the parametric down conversion process. As seen in Fig. 3.2, the red, orange, green, black lines correspond to 0.2 mm, 0.5 mm, 1 mm and 2 mm long crystals respectively, and the dashed is a gaussian fit of the red profile, whose bandwidth is $\sim$ 3.1 nm; the horizontal dashed purple line is on the half hight of the profiles.

Above all, we presented the theory and calculation of the frequency doubling with optical frequency combs. This process generates the *pump* for the SPOPO, which generates a multimode squeezing. We can see that, in Fig. 3.2, shorter crystals have wider spectral profiles.

Importantly, this model can predict the field of *pump* after the frequency doubling, and we can calculate the length of the BiBO crystal for a demand *pump*. We checked that the calculations match well with the experiments. To be more general, this model can be extended to other nonlinear crystals, such as KTP, PPKPT, etc., using the corresponding phase matching functions.

3.3.2 Parametric down conversion with optical frequency combs

The parametric down conversion (PDC), which is a $\chi^{(2)}$ nonlinear process, is usually used to generate entangled photons. In the process of PDC, a *pump* photon generates two new photons (*signal* and *idler*) simultaneously. When the two new photons have the same frequency, it is *degenerate* PDC in frequency. And when the two new photons are the same in spatial, frequency and polarization modes we call it *degenerate*.

In this chapter, we study the PDC process with optical frequency combs. As the frequency comb has many frequencies, a photon with a specific frequency of the pump generates a new pair of photons with any frequencies if satisfying phase matching and energy conservation conditions.

Thus, in the same time there are many possibilities of PDC for optical frequency combs, as seen in Fig. 3.3. Photons of each frequency in the pump can generate two photons with same or different frequencies. In a result, the complex case of PDC processes can generate a new frequency comb of *signal*. As we can the frequencies of the *signal*, here we call it *non-degenerate*. This is similar to an inverse process of frequency doubling with optical frequency combs, where many frequencies are associated.

Traditionally, in continuous variable regime, people generate squeezing using the PDC in an optical cavity, which is also called *optical parametric oscillator* (OPO) [81]. Here we also employ OPO to generate squeezing. Differently, instead of OPO with continuous laser, we use optical frequency combs.

As seen in Fig .3.3, we have complex PDC processes occurring in an optical cavity resonanting with all the frequencies of the *signal*. which is the interest of this thesis, and called *synchronously pumping an optical parametric oscillator, SPOPO*. Following the analysis of the PDC with optical frequency combs, the SPOPO is also a degenerate case of OPO.

Besides, similar to OPOs in the monochromatic case, according to the level of the *pump* power, we can distinguish the SPOPO with two regimes: *below threshold* and *beyond threshold*. We mainly perform the SPOPO below threshold to generate squeezing.

To describle the PDC process with optical frequency combs, we have he second order polarization,

$$P_{\mathrm{s}}^{(+2)}(z,\omega) = \epsilon\chi^{(2)} \int E_{\mathrm{p}}^{(+)}(z,\omega+\omega')E_{\mathrm{s}}^{(-)}(z,\omega')\frac{\mathrm{d}\omega'}{\sqrt{2\pi}}, \tag{3.25}$$

where $E_{\mathrm{p}}^{(+)}$ and $E_{\mathrm{s}}^{(-)}$ correspond to the analytic field of the *pump* and *signal*, respectively. In the PDC process, the generated *signal* has the frequency

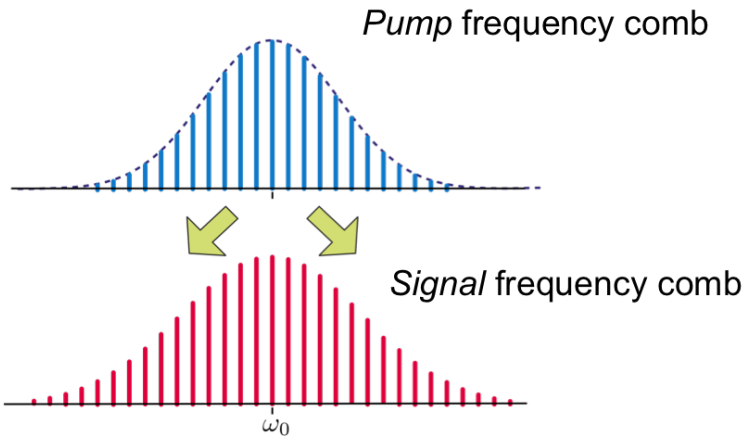

Figure 3.3: Parametric down conversion within an optical frequency comb. All the frequencies of the comb are involved in this process at the same time. A new frequency comb centered at ω_0 is generated, when the *pump* is centered at $2\omega_0$ in this process.

ω which is the difference between the frequency of *pump*, $\omega + \omega'$, and the frequency of *signal*, ω'.

From Equ. 3.3, we have the propagation equation of the PDC process,

$$\frac{\partial u_{\mathrm{s}}}{\partial z}(z,\omega) = \frac{i\omega\chi^{(2)}}{2nc}\int u_{\mathrm{p}}(z,\omega+\omega')u_{\mathrm{s}}^{*}(z,\omega')e^{i\Delta k(\omega,\omega')z}\frac{\mathrm{d}\omega'}{\sqrt{2\pi}} \tag{3.26}$$

with

$$\Delta k(\omega,\omega') = k_{\mathrm{p}}(\omega+\omega') - k_{\mathrm{s}}(\omega') - k_{\mathrm{s}}(\omega). \tag{3.27}$$

We can see that, compared to frequency doubling, the propagation equation of PDC contains the envelope of the signal itself. To solve the equation, here we assume that the envelope of signal is real, so we have $u^{*}(z,\omega) = u(z,\omega)$. Physically, this needs that the spectral phase of the envelope u_{s} is flat, 0 or π. This hypothesis make the case simpler in the calculation and more close to experimental conditions. More details in a general case are given in [41], which also considers the parameter the carrier envelope offset in optical frequency combs.

If the envelope of signal u_{s} is real, the propagation equation Equ. 3.26 can be written in the form as below,

$$\frac{\partial u_{\mathrm{s}}}{\partial z}(z,\omega) = \mathcal{K}(z)u_{\mathrm{s}}(z,\omega), \tag{3.28}$$

where $\mathcal{K}(z)$ is an integral form of the pump envelope propagating in the

nonlinear medium,

$$\mathcal{K}(z)u(z,\omega) = \int K(z,\omega,\omega')u(z,\omega')\frac{\mathrm{d}\omega'}{\sqrt{2\pi}} \tag{3.29}$$

and the core of the integral is,

$$K(z,\omega,\omega') = \frac{i\omega\chi^{(2)}}{2nc}u_{\mathrm{p}}(z,\omega+\omega')e^{i\Delta k(\omega,\omega')z}. \tag{3.30}$$

The solution of Equ. 3.28 is exactly,

$$u_{\mathrm{s}}(z_{\mathrm{B}},\omega) = e^{\mathcal{S}_0}u_{\mathrm{s}}(z_{\mathrm{A}},\omega), \tag{3.31}$$

where $z_{\mathrm{A}} = -l_{\mathrm{c}}/2$ and $z_{\mathrm{B}} = l_c/2$ are the two sides of the $\chi^{(2)}$ crystal and $\mathcal{S}_0$ is the integral [41],

$$\mathcal{S}_0 = \int_{z_{\mathrm{A}}}^{z_{\mathrm{B}}} \mathcal{K}(z)\mathrm{d}z. \tag{3.32}$$

Here we also assume the efficiency of the process is low enough so that the pump doesn't change during the propagation between z_{A} and z_{B} in the medium. We have the core $S_0(\omega,\omega')$,

$$S_0(\omega,\omega') = u_{\mathrm{p}}(\omega+\omega')\int_{z_{\mathrm{A}}}^{z_{\mathrm{B}}}\mathrm{d}z\int\frac{i\omega\chi^{(2)}}{2nc}e^{i\Delta k(\omega,\omega')z}\frac{\mathrm{d}\omega'}{\sqrt{2\pi}} \tag{3.33}$$

Thus we have $S_0(\omega,\omega')$ after the integral on z,

$$S_0(\omega,\omega') = \frac{i\omega\chi^{(2)}}{2nc}u_{\mathrm{p}}(\omega+\omega')\Phi(\omega,\omega'), \tag{3.34}$$

where phase matching associated function $\Phi(\omega,\omega')$ is the same defined in Equ. 3.18.

Here we define the *joint spectral distribution function*,

$$L(\omega,\omega') = u_{\mathrm{p}}(\omega+\omega')\Phi(\omega,\omega'). \tag{3.35}$$

Using the same *narrow bandwidth approximation*[4], $\omega/n \simeq \omega_0/n$, we have $S_0(\omega,\omega')$,

$$S_0(\omega,\omega') = \frac{i\omega_0\chi^{(2)}}{2nc}L(\omega,\omega'). \tag{3.36}$$

Above all, L is a pure imaginary square matrix, and S_0 is real, when u_{p} is imaginary. In frequency doubling, as seen in Equ. 3.23, if we use a real *signal*

[4]the bandwidth is far smaller than the central frequency $\Delta\omega << \omega_0$.

to generate the *pump*, which therefore is pure imaginary. Thus, the assumption $u^*(z,\omega) = u(z,\omega)$ is compatible with both the frequency doubling and the PDC process. This also indicates the absence of the $\langle \hat{x}\hat{p} \rangle$ correlation in the process, which is proved by the experiment [70].

According to Equ. 3.31, therefore, $S_0 = 0$ and $\pi/2$ corresponds to *amplification* and *deamplification* in an OPO [81], depending on the relative phase between the *signal* and the pump, which we can control during the experiment to get the *amplification* and *deamplification* for the SPOPO.

To calculate the solution of the propagation equation in the PDC process, we have the phase matching $\Delta k(\omega,\omega')$:

$$\begin{aligned}\Delta k(\omega,\omega') \quad &= \Delta k(\omega_0,\omega_0) + \left(\frac{1}{v_{\mathrm{g,p}}} - \frac{1}{v_{\mathrm{g,s}}}\right)(\omega+\omega'-2\omega_0) + \frac{1}{2}\mathrm{GVD_p}(\omega+\omega'-2\omega_0)^2 \\ &\quad -\frac{1}{2}\mathrm{GVD_s}\left[(\omega-\omega_0)^2 + (\omega'-\omega_0)^2\right], \end{aligned} \tag{3.37}$$

where the same as the case of frequency doubling, the term $k(\omega_0,\omega_0) = 0$. But different from frequency doubling, the second order of phase matching, also called dispersion, is not negligible in the PDC process[5].

3.3.3 Schmidt modes

Next we will calculate the joint spectral distribution function $L(\omega,\omega')$ with BiBO crystals, and analyze the eigenmodes of the function $L(\omega,\omega')$.

Using the solution S_0 of the propagate equation, we have the corresponding evolution in the envelope u, $u(z_\mathrm{B}) = e^{S_0}u(z_\mathrm{A})$. Because the $S_0(\omega,\omega')$ is proportional to the distribution function of joint spectra $L(\omega,\omega')$, we can get the eigenmodes via diagonalizing $L(\omega,\omega')$, which depends on the phase matching function $\Delta k(\omega,\omega')$ and the property of *pump* spectrum. In the PDC process, we can derive the spectra of signal envelope u_s in the corresponding eigenmodes, or called Schmidt modes, $v_\mathrm{s}^{(j)}$, of the the distribution function of joint spectra $L(\omega,\omega')$. In the decomposition of Schmidt modes,

$$L(\omega,\omega') = \sum_j \Lambda_j v_\mathrm{s}^{(j)}(\omega) v_\mathrm{s}^{(j)}(\omega'), \tag{3.38}$$

where the $\{\Lambda_j\}$ are the *Schmidt coefficients* and the $\{v_\mathrm{s}^{(j)}\}$ are the *Schmidt modes*, or called *Supermodes* [65].

[5] With larger spectra, the GVD need be considered in the phase matching function $\Delta k(\omega,\omega')$ for PDC.

If we consider the discrete frequencies ω_n of a frequency comb, the function $L(\omega, \omega')$ is a matrix of frequency elements,

$$L_{n,n'} = \sum_j \Lambda_j v_{s,n}^{(j)} v_{s.n'}^{(j)}, \tag{3.39}$$

with $L_{n,n'} = L(\omega_n, \omega_{n'})$ and $v_{s,n}^{(j)} = v_s^{(j)}(\omega_n)$. We have,

$$L = \sum_j \Lambda_j \vec{v}_{\mathrm{s}}^{(j)} \vec{v}_{\mathrm{s}}^{(j)\mathrm{T}}, \tag{3.40}$$

where we define the real modes[6], which is classical,

$$\vec{v}_{\mathrm{s}}^{(j)} = (\dots, v_{\mathrm{s,n\text{-}1}}^{(j)}, v_{\mathrm{s,n}}^{(j)}, v_{\mathrm{s,n+1}}^{(j)}, \dots)^{\mathrm{T}} \tag{3.41}$$

The *Schmidt modes* are the eigenmodes of L,

$$L\vec{v}_{\mathrm{s}}^{(j)} = \left(\sum_j \Lambda_j \vec{v}_{\mathrm{s}}^{(j)} \vec{v}_{\mathrm{s}}^{(j)\mathrm{T}} \right) \vec{v}_{\mathrm{s}}^{(j)} = \Lambda_j \vec{v}_{\mathrm{s}}^{(j)}. \tag{3.42}$$

We can diagonalize the matrice L to get the *Schmidt modes* of the PDC process. The real eigenmode $\vec{v}_{\mathrm{s}}^{(j)}$ gives the spectrum of the j^{th} eignemode and $\Lambda^{(j)}$ is the corresponding eigenvalue.

If the input envelope is proportional to an eigenmode, $u_s(z_A) \propto \vec{v}_{\mathrm{s}}^{(j)}$, after the beam propagating in the crystal from the initial position z_{A} to the end z_{B}, we have the input-output relation,

$$u_{\mathrm{s}}(z_B) = e^{igl_{\mathrm{c}}L} u_{\mathrm{s}}(z_A) = e^{igl_{\mathrm{c}}\Lambda_j} u_{\mathrm{s}}(z_A), \tag{3.43}$$

where $g = \omega_0 \chi^{(2)}/2n_0 c$. We can see that the signal is amplified (or deamplified) when the imaginary part of Λ_j is positive (or negative). The phase of Λ_j is determined by the phase of pump. Afterwards, we only consider the imaginary part of the eigenvalues.

Generally for $\chi^{(2)}$ crystals, if the *pump* and the phase matching function have gaussian profiles, the *Schmidt modes* of the PDC process are a set of *Hermite-Gauss* spectral modes, which are the eigenmodes of the matrix L, and the corresponding pure imaginary eigenvalues. These eigenmodes are often called *supermodes*, because they are the superposition of many monochromatic frequency modes of a frequency comb.

In the PDC process, we choose a train of ∼10 nm bandwidth pulses centered at ∼800 nm with the repetition rate 76 MHz as *signal*, and a train

[6] In our case, the envelope u_s is real.

of ∼3.1 nm bandwidth pulses centered at ∼400 nm with the same repetition rate as *pump*, thus we obtain the joint spectral distribution function as seen in Fig. 3.4.

In practice, because the reflectivity of mirrors has a range of bandwidth, which can not be infinite, we calculate with 50nm, 100nm, 400nm bandwidths of mirror reflectivity. In the figures. 3.5 and 3.6, we present the eigenvalues and the leading three eigenmodes with 50nm bandwidths of mirror reflectivity. We see that more than 20 *supermodes*[7] have a series of spectral shapes as Hermite-Gaussian functions. Besides odd orders ($j = 1, 3, 5, ...$) and even orders ($j = 2, 4, 6, ...$) of supermodes have positive and negative eigenvalues respectively, which are amplified and deamplified in the OPO respectively. Similarly, in the figures. 3.7 and 3.8, we also present the eigenvalues and the leading three eigenmodes with 100nm bandwidths of mirror reflectivity. In the figures. 3.7 and 3.8, we can see more *supermodes*, more than 40 modes, in the 100nm bandwidth case; but the leading eigenmodes has the same property as the 50nm case. In Fig. 3.9, the eigenvalues with the 400nm bandwidth of mirror reflectivity are presented, and we can see more than 100 *supermodes* in that case.

From the calculation, we can see that, the parametric down conversion with optical frequency combs is a good candidate generating multimode squeezing. With a lager bandwidth of mirror reflectivity, which is associated with a bigger matrix of the joint spectral distribution as seen in Fig.3.4, we can obtain more supermodes, and the leading supermodes have similar eigenvalues and eigenmodes. In the thesis, according to the real mirror reflectivity[8], we will use the simulation result with a 100nm bandwidth of mirror reflectivity. As seen in Fig.3.7, we have more than 40 supermodes, and the first supermode has a gaussian shape spectrum with a 7.5 nm bandwidth seen in Fig.3.8, correspondingly with a $7.5/\sqrt{2}$ nm intensity spectrum. To analyze the multimode property of the SPOPO resource we will simulate the squeezing and multimode entanglement based on OPO model and homodyne detection in the following section.

3.3.4 Squeezing of SPOPO

As seen in Fig.3.10, an optical frequency comb pumps a parametric down conversion in an optical cavity, which is called SPOPO (synchronously pumped

[7] We count the supermodes if the eigenvalues are significantly different from 0, in practice which are squeezed.

[8] In the experiment we use femtosecond optics, generally with a wide bandwidth of high reflectivity and zero GVD, from the companies such as Layertech GmbH, Femtolasers, Laser Components.

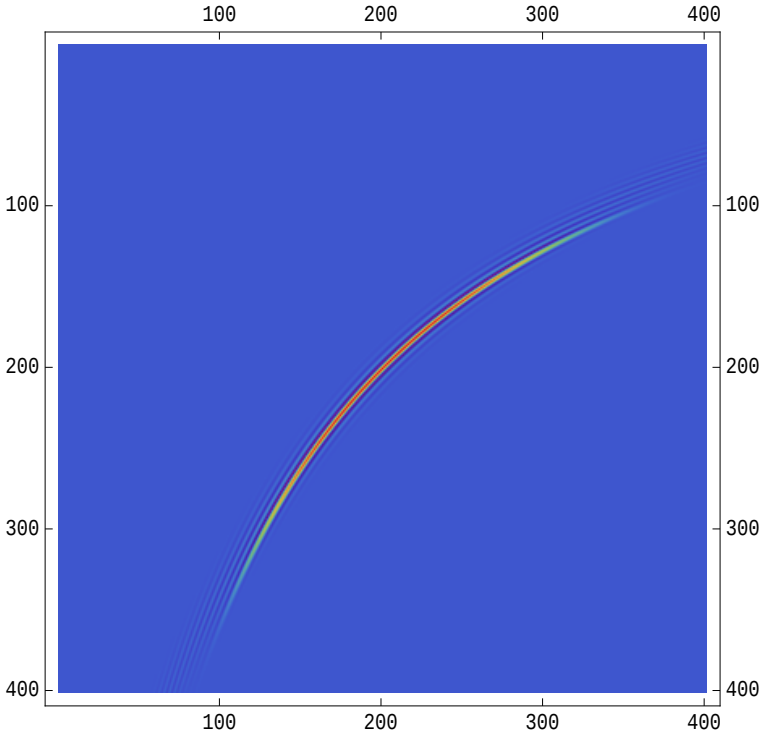

Figure 3.4: Joint spectral distribution function. A train of ∼10 nm bandwidth pulses centered at ∼800 nm with the repetition rate 76 MHz (*signal*), and a train of ∼3.1 nm bandwidth pulses centered at ∼400 nm with the same repetition rate (*pump*) are used in the calculation.

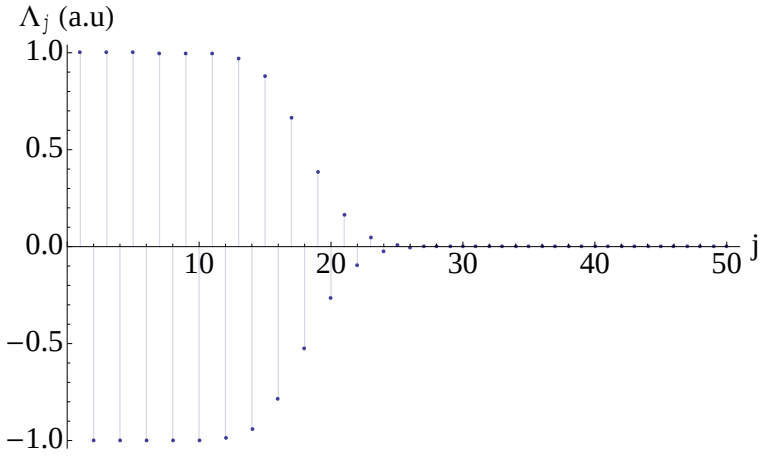

Figure 3.5: Eigenvalues of the joint spectral matrix with a 50nm bandwidth of mirror reflectivity .

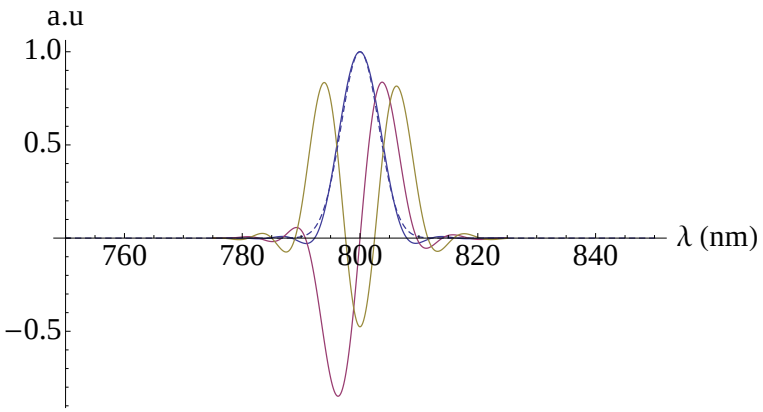

Figure 3.6: Eigenmodes of the joint spectral matrix with a 50nm bandwidth of mirror reflectivity. The dashed line is the gaussian fit of the first supermode with a 7.5nm bandwidth

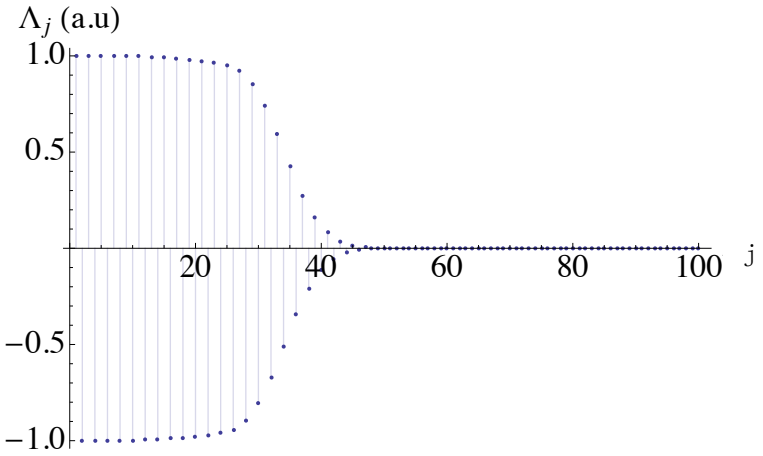

Figure 3.7: Eigenvalues of the joint spectral matrix with a 100nm bandwidth of mirrors' reflectivity.

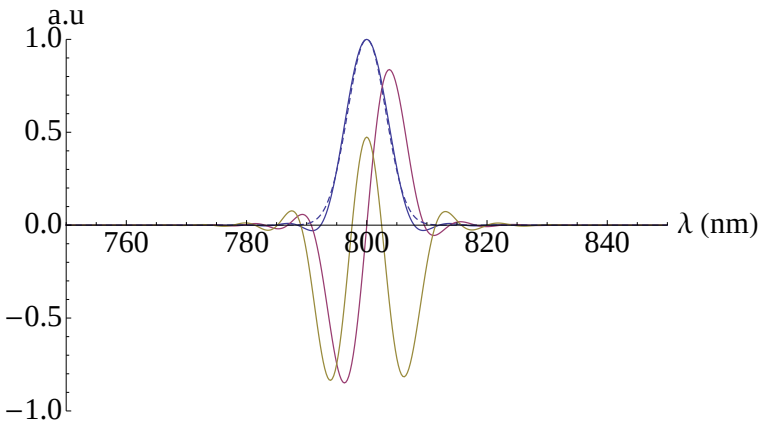

Figure 3.8: Eigenmodes of the joint spectral matrix with a 100nm bandwidth of mirror reflectivity. The dashed line is the gaussian fit of the first supermode with a 7.5nm bandwidth, which is same as in Fig.3.6.

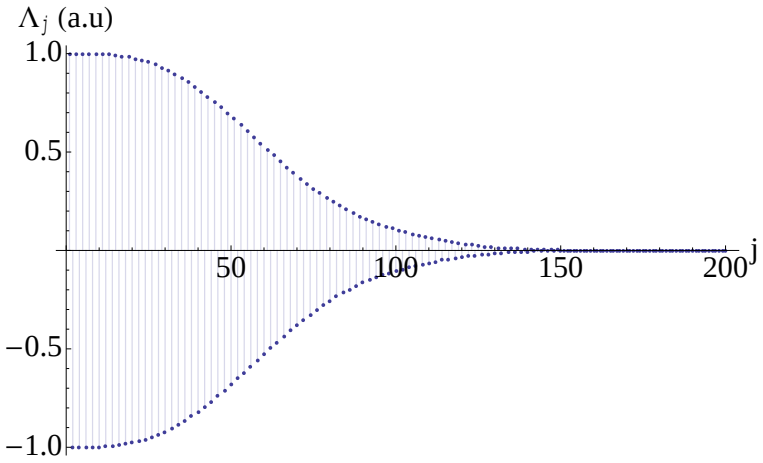

Figure 3.9: Eigenvalues of the joint spectral matrix with a 400nm bandwidth of mirror reflectivity .

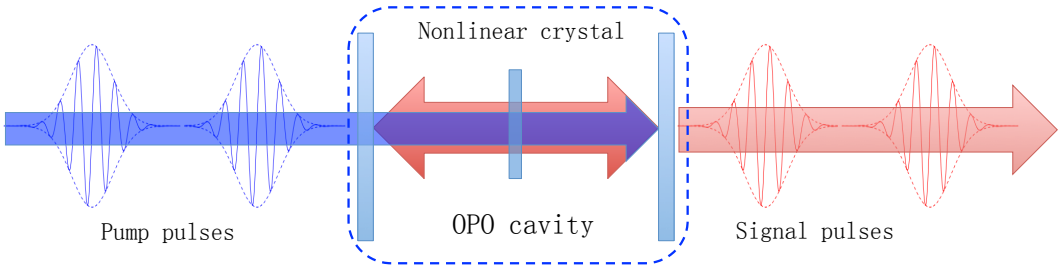

Figure 3.10: Configuration of the SPOPO. While a train of blue pulses pumps an nonlinear crystal in an OPO, the output is a new train of red pulses via the nonlinear process of parametric down conversion.

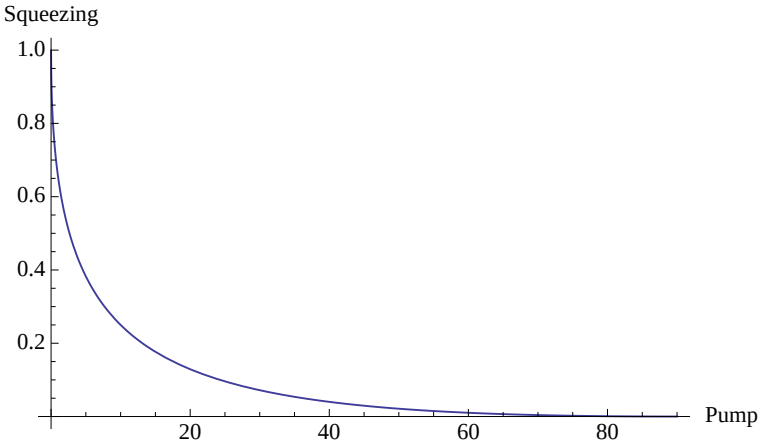

Figure 3.11: Squeezing V_{sqz} in the linear scale *vs* Pump power (mW).

optical parametric oscillator) [63]. As we discussed previously, parametric down conversion with optical frequency combs have huge possibilities to generate two photons satisfying the phase matching joint spectrum seen in Fig.3.4, and the cavity of the optical parametric oscillator select the corresponding modes. Therefore we obtain a comb via the SPOPO, whose frequencies are determined by the cavity modes. In practice, the cavity is the same as the source comb laser, so we obtain a comb with the exactly same frequency modes as the comb laser, however, in the generated comb all frequency modes are quantum correlated [70].

In the experiment, we use a train of pulses centered at 400nm with 3.1nm spectral bandwidth to pump a $\chi^{(2)}$ crystal in an optical cavity resonant with 800nm. The same as usual optical parametric oscilators, SPOPO can generate squeezing below threshold[81] [5]; also the PDC process with optical frequency combs has a multimode process as seen in the previous chapter[63].

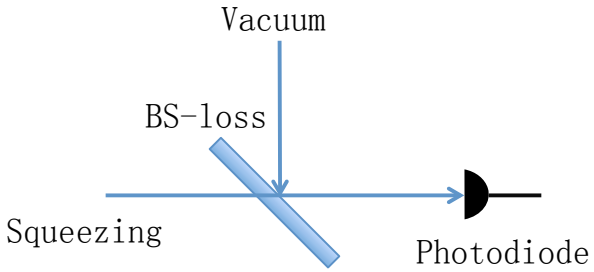

Figure 3.12: The model of squeezing with a loss T.

The squeezing V_{sqz} of an ideal OPO below threshold is [63],

$$V_{\text{sqz}} = \left(\frac{1 - \frac{P_{\text{exp}}}{P_{\text{thr}}}}{1 + \frac{P_{\text{exp}}}{P_{\text{thr}}}} \right)^2, \tag{3.44}$$

where P_{exp} and P_{thr} are experimental and threshold powers of pump respectively.

For the SPOPO, the threshold of the j^{th} order supermode is [63],

$$P_{\text{thr}}^{(j)} = \frac{\Lambda_0}{\Lambda_j} P_{\text{thr}}^{(0)}, \tag{3.45}$$

where $P_{\text{thr}}^{(0)}$ is the threshold of the first supermode.

Thus, for SPOPO, the squeezing of j^{th} order supermode is,

$$V_{\text{sqz}}^{(j)} = \left(\frac{1 - \frac{P_{\text{exp}}}{P_{\text{thr}}^{(j)}}}{1 + \frac{P_{\text{exp}}}{P_{\text{thr}}^{(j)}}} \right)^2. \tag{3.46}$$

In Fig.3.11, we give the squeezing of the first supermode versus the pump power of SPOPO baed on Fig. 3.46. We see that the squeezing, without loss, goes to infinity when the pump power is close to the threshold. Higher orders of supermodes have corresponding squeezing with a ratio factor $\frac{\Lambda_j}{\Lambda_0}$.

When the squeezing V_{Sqz} with a real loss T $(0 < T < 1)$, as seen in Fig. 3.12, the squeezing after loss V_{loss} [9], is,

$$V_{\text{loss}} = V_{\text{Sqz}}(1 - T) + T. \tag{3.47}$$

Based on the equations 3.46 and 3.47, and setting $T = 10\%$, $P_{\text{exp}} = 50\text{mW}$ and $P_{\text{thr}} = 150$ mW [9], we obtain the squeezing values of the supermodes via

[9]These settings are not exactly the same as the experimental ones, whose aim is to make the simulation have approximately the same squeezing for the first supermode as the experimental case.

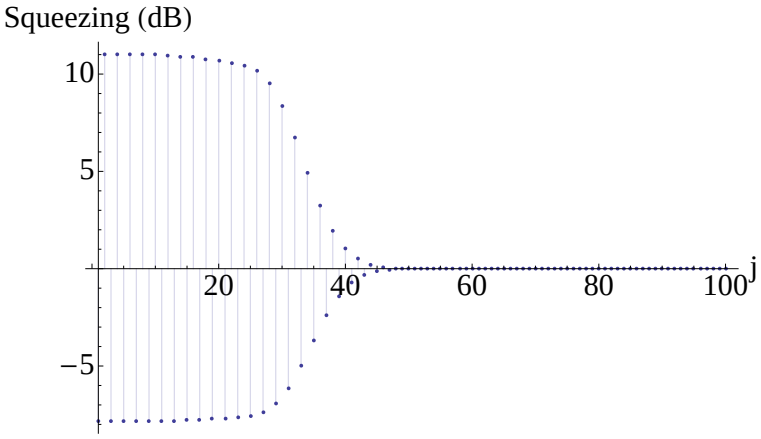

Figure 3.13: The variances of the supermodes in the amplitude quadrature expressed in dB scale, $V_{\mathrm{dB}} = 10 \log_{10} V_{\mathrm{sqz}}$. When it is negative (positive), the corresponding supermode is squeezed (anti-squeezed) in the amplitude quadrature.

a theoretical simulation as seen in Fig. 3.13, and the supermodes are similar as Hermite-Gaussian functions seen in Fig. 3.8. We can see more than 40 supermodes exist in the case, and the leading modes have close squeezing values.

Usually the loss is the biggest enemy in quantum information and quantum optics, whatever for photon in discrete regime, or here for squeezing in continuous variable regime. We see that loss reduces the squeezing level and the purity for the SPOPO.

In practice, to get better squeezing, all the possible loss after the generation should be mostly avoided, also in the OPO cavity, we should decrease all the loss except the output coupler and increase the transmission of the output coupler, which is also called *escape efficiency*. Besides, the classical noise of the *signal* also reduces squeezing and purity of the squeezed states, thus we often need a filtering cavity to filter the laser noise. In chapter 4, we will give the details about how to overcome practical loss in the SPOPO experiment.

Above all, we presented the model of the SPOPO with a practical loss considered. In this model, we obtain the joint spectral distribution function $L(\omega, \omega')$ of Equ. 3.35; then we get the Schemitz modes and the eigenvalues from the matrix L; using the quantum OPO model, we get the squeezing values of all the supermodes with a loss correction. Next we will analyze the property of the multimode correlation in a basis composed of frequency bands.

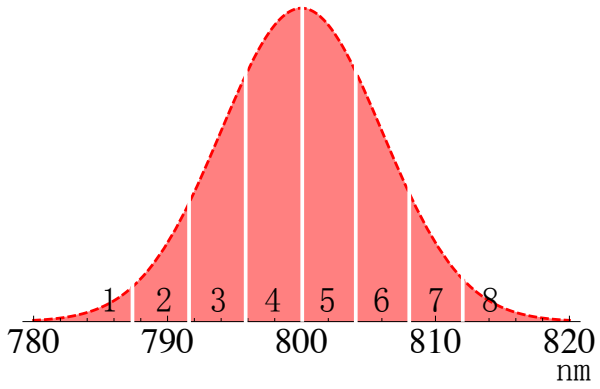

Figure 3.14: The spectrum is divided into 8 spectral bands, which construct a basis for characterizing multimode squeezing of the supermodes from the SPOPO.

3.4 Simulating multimode correlation of the SPOPO

3.4.1 Simulating covariance matrix

As we cannot access into individual frequencies of the output of the SPOPO, in order to study multimode correlation, we divide the reference spectrum into 8 spectral bands to construct a basis, as seen in Fig. 3.14. We will introduce a mode-dependent projective measurement in chapter 4, called *balance homodyne detection*, where the reference corresponds to the local oscillator.

As seen in Equ. 2.41, in order to construct the covariance matrix, we need get all the covariance terms $(\langle\delta\hat{q}_i\delta\hat{q}_j\rangle + \langle\delta\hat{q}_j\delta\hat{q}_i\rangle)/2$. For the SPOPO, as the joint spectral distribution function is pure imaginary, the cross correlation of $\langle\hat{x}_i\hat{p}_j\rangle$ is absent, thus the covariance matrix is cast with only diagonal blocks, and this is confirmed with our experiment [70].

In the 8-band basis, as seen in Fig. 3.14, we define that $S_i(\omega)$, $i = 1, 2, ...$ is the corresponding spectum of the frequency band i, and $\vec{w}_i$, $i = 1, 2, ...$ is the normalized mode of the frequency band i. In the simulation, we have,

$$P_i = \int |S_i|^2 \mathrm{d}\omega \quad \text{and} \quad |\vec{w}_i \cdot \vec{w}_j| = \delta_{ij}, \tag{3.48}$$

where $\delta_{ij} = 1$ if $i = j$, $\delta_{ij} = 0$ if $i \neq j$. We calculate the covariance matrix using the the squeezing of supermodes in SPOPO as seen in Fig. 3.13.

To construct the covariance matrix experimentally, we first get the quantum noises with the shot noise normalized to 1 for each individual band

and combinations of two bands. To aim so, in theory, we have normalized the squeezing for all the supermodes already; in practice, it is the measured squeezing variance divided by the corresponding shot noise, which is the noise of the coherent source, e.g. the laser. In the following we simulate the covariance with the eight-spectral-band basis in Fig. 3.14, and give the way how to normalize the combined-spectral-band modes and correlation elements using corresponding optical powers.

Projecting the supermodes of the SPOPO onto the frequency band basis, $\{\vec{w}_i\}$, as all the modes we consider here for the SPOPO are real, we obtain the projection quadrature,

$$\hat{x}_i = \sum_j \vec{w}_i^{\mathrm{T}} \cdot \vec{v}_{\mathrm{s}}^{(j)} \hat{x}_{\mathrm{s}}^{(j)} \tag{3.49}$$

and also because the supermodes are not correlated, the corresponding variance is,

$$\langle \hat{x}_i^2 \rangle = \sum_j |\vec{w}_i^{\mathrm{T}} \cdot \vec{v}_{\mathrm{s}}^{(j)}|^2 \Delta^2 \hat{x}_{\mathrm{s}}^{(j)} \tag{3.50}$$

We write $\langle \hat{x}_i^2 \rangle$ and $\langle (\hat{x}_i + \hat{x}_j)^2 \rangle$ for the quantum noises (variances) [10]of the modes $\vec{w}_i$ of individual bands S_i, and the modes $\vec{w}_{i+j}$ of combinations of two spectral bands S_{i+j}, respectively. Considering the relation between two individual modes and a combination mode, we have,

$$\vec{w}_{i+j} = \frac{\sqrt{P_i}\vec{w}_i + \sqrt{P_j}\vec{w}_j}{\sqrt{P_i + P_j}} \tag{3.51}$$

Thus, the relation between the corresponding quadratures is,

$$\hat{x}_{i+j} = \frac{\hat{x}_i\sqrt{P_i} + \hat{x}_j\sqrt{P_j}}{\sqrt{P_i + P_j}}, \tag{3.52}$$

Individual covariance elements are then constructed according to the following relation:

$$\langle \hat{x}_i \hat{x}_j \rangle = \left[\langle (\hat{x}_{i+j})^2 \rangle - \frac{P_i}{P_i + P_j} \langle \hat{x}_i^2 \rangle - \frac{P_j}{P_i + P_j} \langle \hat{x}_j^2 \rangle \right] \times \frac{P_i + P_j}{2\sqrt{P_i P_j}}, \tag{3.53}$$

where x is the amplitude quadrature, with a similar definition for the phase quadrature p; P_i and P_j are the optical powers of frequency bands i and j in the experiment, respectively, which are measured with the homodyne photodiodes.

[10]Both of $\langle \hat{x}_i^2 \rangle$, and $\delta\hat{x}^2$ in Equ. 2.41 equivalently represent variances in the thesis.

Sometimes, instead of the covariance matrix, we draw the noise correlation matrix, which is defined as

$$C_{ij} = \langle \hat{x}_i \hat{x}_j \rangle / \sqrt{\langle \hat{x}_i \rangle \langle \hat{x}_j \rangle} - \delta_{ij} \langle \hat{x}^2_{\text{vacuum}} \rangle / \langle \hat{x}_i^2 \rangle, \tag{3.54}$$

and the p quadrature has a similar definition for the correlation matrix.

3.4.2 The eigenmodes

Wo obtain the simulated correlation matrix of the SPOPO for the 8-band basis, including amplitude and phase quadratures. Here we directly diagonalizing the covariance matrix to get the corresponding eigenmodes $\{\vec{v}_i\}$, similar to the supermodes, and eigenvalues (squeezing) as seen in the figures. 3.15 and 3.16, which show similar properties as Hermite-Gaussian functions. Thus, all the individual eigenmodes are independently squeezed, and co-propagate in the single beam of the SPOPO output. But notice that the eigenmodes are slightly different for amplitude and phase quadratures, which depends on the purity of the covariance matrix. And ideally, in the eigenmode basis, there should be no quantum correlations, $\langle \hat{x}\hat{p} \rangle = 0$ and $\langle \hat{p}\hat{x} \rangle = 0$ in the covariance matrix.

Furthermore, we present the eight spectra $\{A_i\}$ corresponding to the eigenmodes of the amplitude quadrature as in Fig. 3.17, which are defined by,

$$A_i = \left(\frac{S_1}{\sqrt{P_1}}, \frac{S_2}{\sqrt{P_2}}, \ldots, \frac{S_8}{\sqrt{P_8}}\right) \cdot \vec{v}_i^{\mathrm{T}}. \tag{3.55}$$

We can also think the corresponding spectral shapes, or pulse shapes in time domain, are squeezed independently. Hence, the eigenmodes of the SPOPO are equivalent to a set of spectral modes in the spectral domain, whose the spectral profiles are seen in Fig. 3.17.

Above all, we did multimode analysis for the simulated covariance matrix of the SPOPO. From that, we obtained eight independently squeezed eigenmodes. Importantly, as the multimode resource, SPOPO has more 40 squeezed supermodes, the number of retrieved squeezed eigenmodes increases when the number of bands in the basis increases.

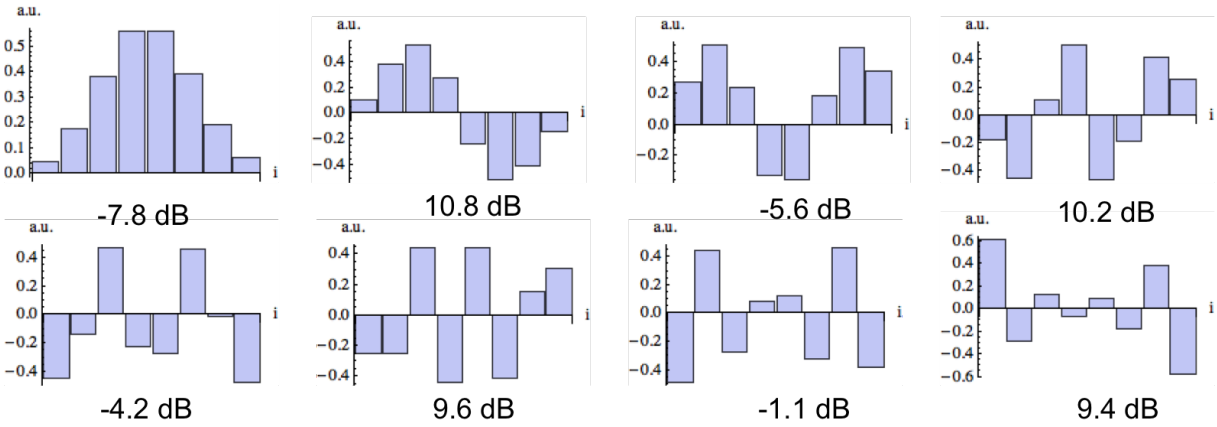

Figure 3.15: The eight eigenmodes and eigenvalues derived from the covariance matrix of the amplitude quadrature.

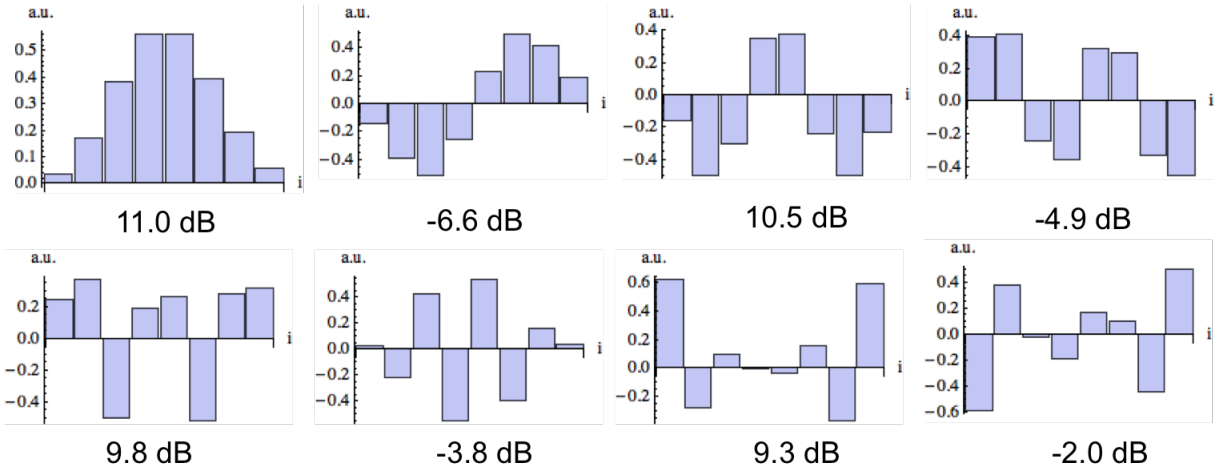

Figure 3.16: The eight eigenmodes and eigenvalues derived from the covariance matrix of the phase quadrature.

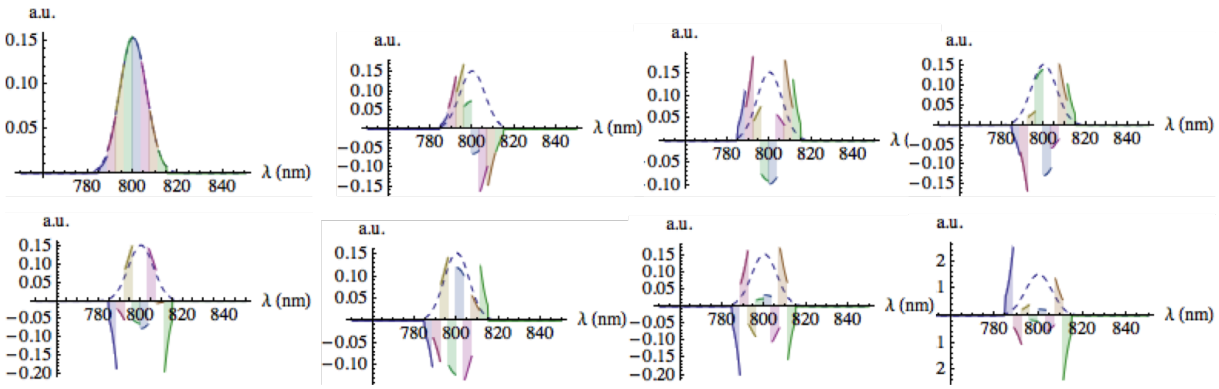

Figure 3.17: The eight spectra corresponding to the eigenmodes in the amplitude quadrature. The different color bands refer to the frequency bands in the basis of Fig. 3.14, and the dashed profile is the spectral shape of the first supermode.

Chapter 4

Principle of the SPOPO experiment and preparation of light source

Contents

Highly multimode squeezing plays an essential role to generate complex quantum networks for quantum information and quantum metrology. However, traditionally, in order to generate the multimode squeezing, the method, generating many single OPOs, lacks of flexibility and scalability [85] . In this thesis, instead of doing many OPOs, we present a *single-step* and scalable way of generating a multimode quantum resource via the SPOPO process [65]. Then based on the homodyne measurements, the multimode property are measured and characterized with arbitrary pulse shaping in the local oscillator [70].

In the previous chapter, with the SPOPO model, we theoretically obtained the covariance matrix, of which the eigenmodes (*supermodes*) are independently squeezed. Therefore, similar to many OPOs, we have many squeezers co-propagating in the output of the SPOPO.

Here we will present the experimental details of generating and characterizing multimode squeezing. Firstly we will give the principle and the general idea of the SPOPO experiment. The experimental objective and the procedure diagram are presented. Secondly the experimental procedures and related optics are explained in details.

4.1 Principle of the experiment

4.1.1 The objective

The objective of the SPOPO experiment is: (1) generating a multimode quantum frequency comb [65]; (2) realizing quantum controls, especially,

quantum networks, with the multimode quantum resource .

The multimode squeezing is generated in a *single-step* fashion in the SPOPO experiment. As all the longitudinal frequency modes of the frequency comb participate to the parametric down conversion processes, satisfying the phase matching condition of Equ. 3.35, the quantum state of the SPOPO is intrinsically multimode. In addition, ultrafast pulses[1] have a high peak intensity, which results in a high efficiency for nonlinear processes, such as frequency doubling, PDC, etc.

In practice, we use an optical comb to pump an OPO below threshold as seen in Fig. 3.10. With the OPO cavity, the transverse spatial mode is chosen, which is the TEM_{00} mode. The case is different from usual OPOs for the longitudinal modes. As the optical comb has many the frequency modes, all the modes with the resonant frequencies of the cavity ($\sim 10^5$ modes) are selected and involved in the PDC processes. Consequently, complex PDC processes occur in the SPOPO process. However, the complexity supplies a rich source of multimode quantum correlations, which is quintessential for quantum optics and quantum information. Here, also because of the complexity of the generation process, instead of considering all the frequency pairs in each possible PDC process, we use the supermodes, each of which consists of hundred thousands of longitudinal frequency modes, to describe the SPOPO picture. Equivalently, the supermodes are also a series of temporal pulse shapes in time domain. In practice, for generating the quantum resource, without input signal we obtain a squeezed vacuum (vacuum signal[2]), and with input signal we get bright squeezing.

From the theoretical analysis we have presented in the previous chapter, the main quantum property is that, in the output beam of the SPOPO, co-propagating supermodes are the eigenmodes of the joint spectra matrix, as seen in Fig. 3.4, whose spectral shapes depend on the phase matching and the *pump* property. Importantly, these independently squeezed supermodes, behaves as the outputs of many single OPOs, which co-propagate in the single laser beam with fixed relative phases, 0 or $\frac{\pi}{2}$. The squeezing levels of each supermode are associated to the total squeezing of the SPOPO and the corresponding eigenvalues.

In order to measure and characterize the multimode squeezing, projective measurement, *balanced homodye detection*, is employed. To that aim, a pulse shaping is built in the local oscillator of the homodyne detection. The state of the SPOPO can be projected onto a desired mode of local oscillator. Therefore, we can access any quantum correlation or squeezing via shaping

[1]Here ultrafast pulses are equivalent to an optical frequency comb in time domain.
[2]The squeezed vacuum is a squeezed state with zero mean value of amplitude.

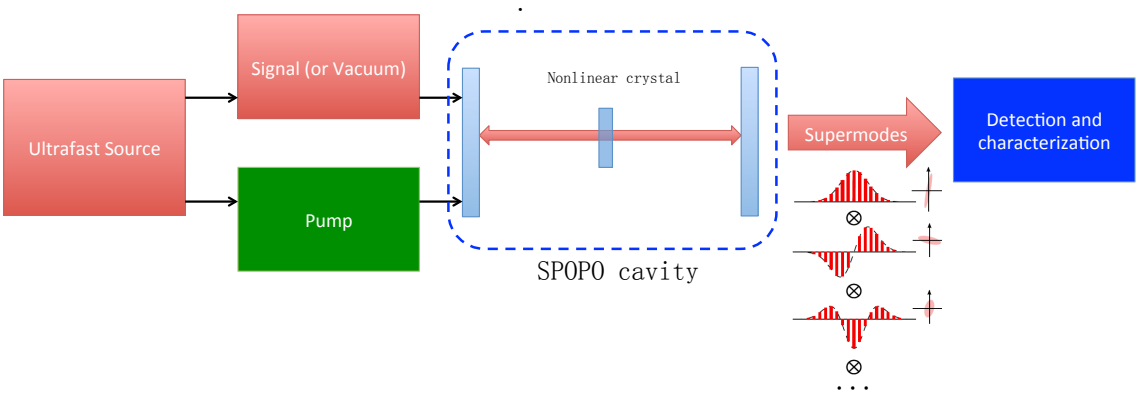

Figure 4.1: The scheme of the SPOPO experiment.

the local oscillator onto a specific mode.

4.1.2 Experimental configuration

The experimental scheme of the SPOPO is presented in the form of block diagram as seen in Fig. 4.1. The ultrafast laser source, the Mira laser, generates a train of femtosecond pulses. One part of the laser is used as *pump*, which is generated via frequency doubling, and then with the *signal* together participates to the parametric down conversion process in the SPOPO cavity. The output of the SPOPO cavity is the multi-supermode squeezing. Via shaping the local oscillator in the homodyne measurement, the multimode squeezing and quantum correlation is measured and characterized .

We will present in details the SPOPO experiment as following: (1) the laser source; (2) preparing the *signal* and the *pump*; (3)the SPOPO cavity (in practice, it is a ring cavity); (4) the homodyne detection with pulse shaping. The detailed experimental configuration is depicted as seen in Fig. 4.2.

It is important to note that we don't change the quantum resource of the SPOPO after generation, and quantum operations, e.g. to access different quantum correlations, are achieved via measurement processes.

4.2 Laser Source

In the experiment, we have two lasers on the optical table. The first is a continuous laser with the wavelength of 532 nm; the second is a Mira femtosecond laser pumped by the 532 nm continuous laser, which emits femtosecond pulses in the near-infrared.

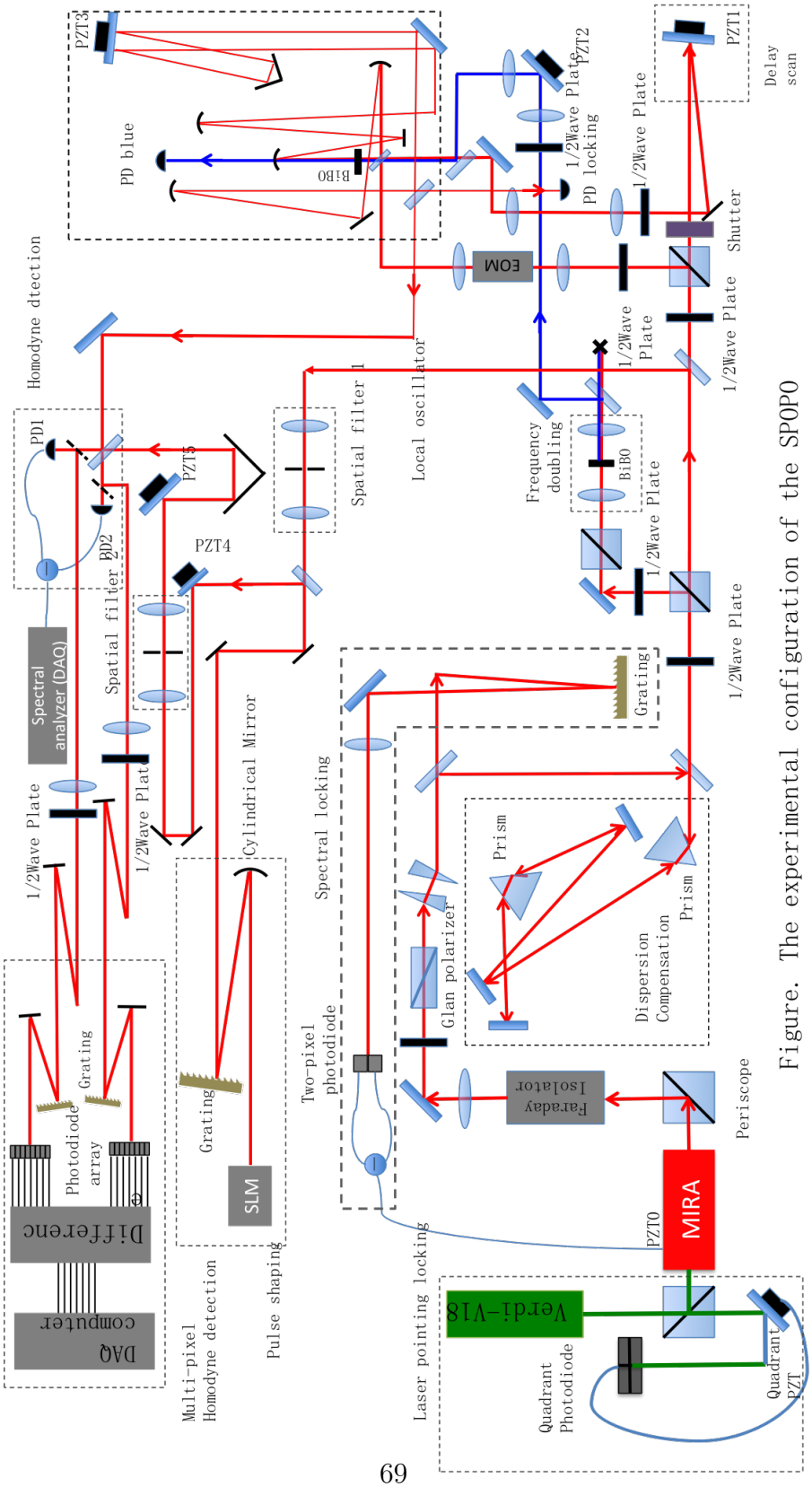

Figure. The experimental configuration of the SPOPO

Figure 4.2: The Experimental configuration

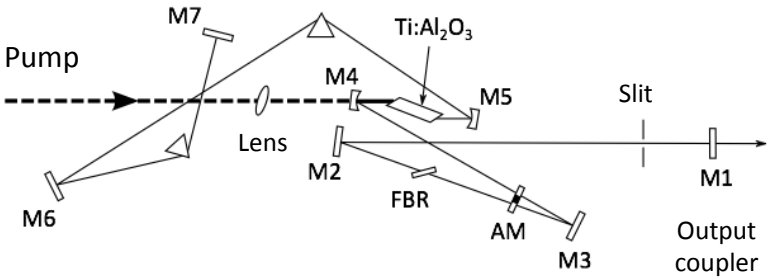

Figure 4.3: The configuration of the femtosecond laser cavity [17].

4.2.1 Pump laser

We use the model VERDI V-18 from the company Coherent as the pump of the femtosecond laser [16], which emits, optimally, up to 18 W of green monochromatic at 532nm. The output spatial profile is a TEM_{00} mode, and the waist ω_0 of the laser beam is $\sim$ millimeter. We operate the laser power at 13 W to pump the femtosecond laser.

This laser is driven with a current supply between 40-50 A for the pumping diodes inside, and a circulation of water cools down the plate on the laser head used for dissipating the heat, with a cost of electricity power about 60-80 W). The laser model, produced on 2005, consumes totally around 1, 300 W of the electric power.

The laser was broken on 2014 because the diodes inside were over the service life (almost 10 years). We have the laser repaired by changing the two diodes inside and the laser head.

4.2.2 Femtosecond laser

In the experiment, the femtosecond laser source is a Ti-sapphire mode-locked oscillator (The Coherent Mira Model 900-B Laser) delivering Δt =$\sim$100 fs pulses ($\Delta\omega$ =$\sim$10 nm FWHM) centered at 795 nm (D_1 transition of Rubidium atoms) with a repetition rate of 76.6 MHz (the cavity length is $\sim$3.92m) [17]. The temporal-frequency relation of the pulses is gaussian Fourier-limited satisfying $\Delta t \times \Delta\omega = 0.441$. In the normal condition, pumped by 13 W of 532 nm continuous green laser from the Verdi V-18, the femtosecond laser emits around 1.8$\sim$2.0 W power in the mode-locked femtosecond regime, and $\sim$2.5 W in the continuous regime.

The cavity configuration of the femtosecond laser, as seen in Fig. 4.3, is a linear cavity with a crystal of Ti-sapphire, which has a phase match-

ing for a large spectrum. The adjustable birefringent filter in the cavity is used to select the central wavelength of the laser spectrum between about 710 nm and 910 nm. A pair of prisms for the dispersion compensation is necessary for large spectra. The laser is able to achieve up to a 10 nm wide spectrum (FWHM), which is $\sim$ 80 fs centered at 795 nm. We can make the laser work in the femtosecond regime and slightly change the central wavelength of the output via adjusting the slit next to the output coupler, and control the bandwidth and central wavelength of the Mira via adjusting the corresponding buttons on the laser.

The stability of mode locking depends on the position of M5, and the efficiency (output power) depends on the focus in the crystal. The prism right after M5 can be moved to make the laser work in the continuous regime, which we need when aligning the laser cavity. However, these operations are not necessary to be often performed, and we only do when the laser power is very low or doesn't work at all. We only align the input mirrors every day to align the pump laser matching the Mira laser cavity.

In practice, we need to monitor the quality of the mode locking. In the MIRA laser, a fast photodiode is disposed to detect a small fraction of the laser output. We divide the signal detected by the intra fast photodiode in two parts. One part is sent to an oscilloscope to observe the temporal profile of the signal as seen Fig 4.4, which is taken from *R. M. de Arajo*'s PhD thesis[3], and the other part is sent to a spectrum analyzer to see the noise spectrum of the signal, whose repetition rate can be observed as seen in Fig. 4.5.

When the Mira laser works in the femtosecond regime we can see the pulse train by the oscilloscope, and when in the continuous regime, we only see a flat line of signal. With the spectrum analyzer, we possibly see a forest of radio frequencies centered at the repetition rate of the laser or only the repetition rate frequency and its harmonics. As seen in Fig 4.5 (a), we can see the 76MHz peak when the laser is working in the femtosecond regime; when the slit in the Fig. 4.3 is closed too much, we can see the forest of the peaks as seen in the Fig 4.5 (b), which indicate the Q-switched mode-locking regime. In the experiment, the quality of the femtosecond laser is very associated with the mode-locked laser power. When the laser power decreases, the laser is usually more noisy and has bad spatial and temporal characters, and we can improve by realigning the laser system.

[3] As this thesis is extended from the experiment of *R. M. de Arajo*'s PhD, in this chapter we take some figures from the PhD thesis [69] for the the similar experimental setups or phenomena, such as the figures 4.4, 4.5, 4.8, 4.9, 4.11 4.14, and 4.16.

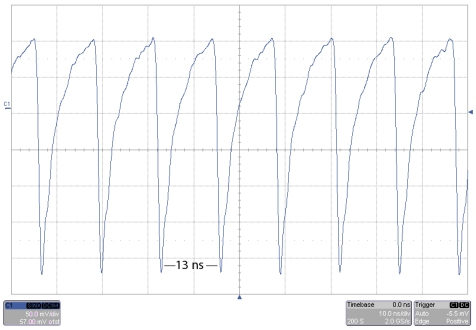

.

Figure 4.4: Signal of the pulses measured by a fast diode.

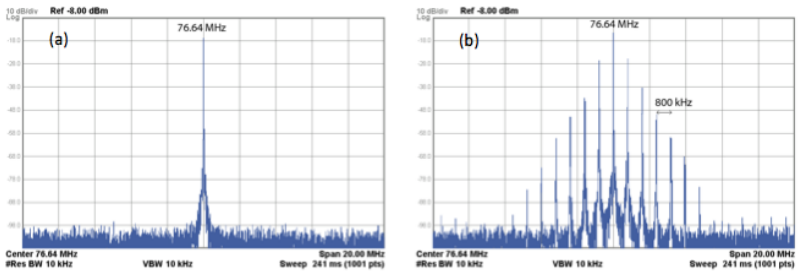

.

Figure 4.5: Signal of the pulses measured by a fast diode.

4.2.3 Pump pointing locking

In the experiment, in order to improve the laser system stability, we employ a commercial laser pointing locking on the pump laser (Thorlabs T-Cube Position Sensing Detector (PSD) Controller).

As seen in Fig. 4.2, the residual of the green laser, from the Verdi, shines on the *Quadrant Position Detector*, and the amplified signal controls the PZT before the Mira with a feedback loop. The locking is usually very robust during the experiment, yet an obvious shift of the pointing center can be found by the software when tuning off the locking after 2 to 3 hours. We checked that this deviation of pump alignment can make the Mira output lower by about 0.05 W. As we mentioned, the quality of the femtosecond laser is very linked with output power performance, and importantly, is sensitive for the squeezing generation. Therefore the pointing locking is important for the long-term stability of the Mira laser, which influences the squeezing indirectly.

4.2.4 Spectral locking

Generally, four parameters are enough to define an optical frequency comb with a gaussian profile spectrum: bandwidth of the spectrum, central wavelength, repetition rate, and frequency offset (CEO). The details about how to stabilize these four parameters are presented in the PhD thesis [72].

In our case, we shape the spectrum in many spectral bands to characterize the quantum correlation of the SPOPO [70]. Here the stability of the spectrum is quite important.

We lock the spectrum with a grating and a two-pixel photodiode, as seen in Fig. 4.2. The femtosecond pulses centered at 795 nm are dispersed spatially with the grating (D=1200 /mm). The dispersed spectrum is then focused (f=30 cm) and mapped on the two-pixel photodiode (model PDP90A, Thorlabs). The error signal for the locking is the power difference (DC) between the left and the right parts of the spectrum. As seen in Fig. 4.6, when the spectrum is in the center of the two-pixel photodiode, the difference signal $I_{\text{difference}}$ is zero, and we have,

$$I_{\text{difference}} \propto \Delta\lambda, \tag{4.1}$$

where $\Delta\lambda$ is the deviation of the spectrum.

The amplified $I_{\text{difference}}$ is used to control an actuator piezoelectric (PZT) installed on the back mirror M7, seen in Fig .4.3, which is in the end of the prism line. We designed a metal mount, which can slightly rotate the mirror M7 when applying a tension on the PZT. This kind of rotation is ignored for

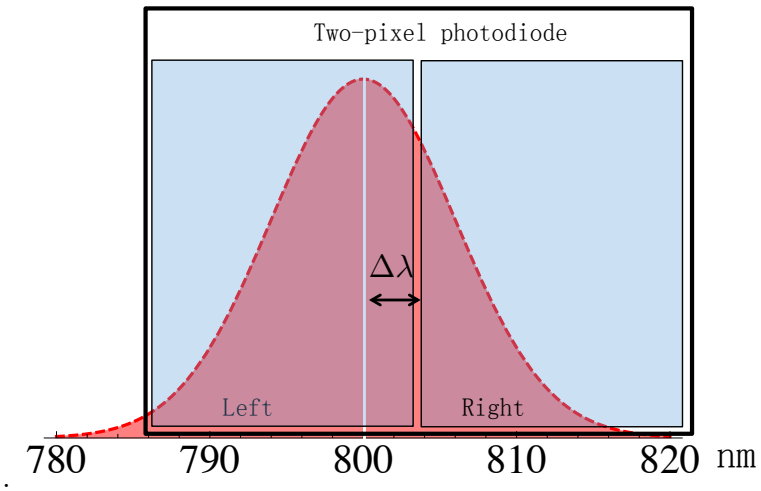

Figure 4.6: The error signal is the power difference between the left and the right parts of the spectrum, measured by a two-pixel photodiode.

the alignment of the laser cavity, but the spectral shift caused by this rotation is sensitive with the birefringent filter for selecting the spectral wavelength.

In practice, this locking servo system is very robust, and can last typically for several hours until the PZT reach the end of the controllable range. Importantly, the spectral locking contributes a lot for the long-term (several hours) quality of the experiment, such as the stability of the transmission peaks of the SPOPO cavity, the long-term squeezing level of the SPOPO, and the spectrum of the laser after pulse shaping.

4.3 Preparation of laser

4.3.1 Correction of the astigmatism

The output from the Ti-sapphire mode-locked femtosecond laser is very astigmatic spatially. The spatial profile is an ellipse, not a TEM_{00} mode. The horizontal axis is twice as big as the vertical one at the output coupler of the laser (M1, Fig. 4.3). In the experiment, after the periscope (the first element after the laser), for the astigmatism, the horizontal axis is then shorter than the vertical axis.

To correct the astigmatism, first we collimate the laser beam by a lens, then we use a pair of compact anamorphoses prisms (Thorlabs). Because the factor between the vertical and the horizontal axis is very close to 2, we directly use the prime pair with a fixed factor 2, which is easier to align

and avoiding inducing unexpected dispersion. After the correction of the astigmatism, we have a good TEM_{00} mode.

4.3.2 Dispersion compensation

Dispersion (Chirp) is an important factor for ultrafast pulses. As seen in Fig. 1.3, we see that the dispersion (GDD) broaden the duration of ultrafast pulses. The laser accumulates chirp when propagating through the optics and the air. In a result of dispersion, the peak intensity of the pulse field decreases, which degrades the nonlinear effect as demonstrated in Equ. 3.10. In principle, we need compensate the dispersion when the pulse arrives in the center the nonlinear crystal in the SPOPO cavity. In practice, rather than compensate directly for the SPOPO, we compensate the dispersion path from the output of the Mira laser and the frequency doubling crystal.

The reasons of doing so are: (1) the beam quality of the pump light is quite sensitive to the SPOPO, in particular in the case of generating vacuum squeezing (without signal) (2) there is very little dispersive components in between the two positions where the frequency doubling and the SPOPO occur.

Disperse elements

According to Equ. 1.17, the GDD ϕ'' broadening a factor $\sqrt{2}$ of the initial duration Δt,

$$\phi''(\omega_0) = \frac{\Delta t^2}{4\ln 2} \simeq 0.4\Delta t^2. \tag{4.2}$$

For instance, in the case of the initial duration which is 120∼130 fs, the total corresponding GDD is about 6000 fs^2.

In the experiment, the most disperse optical component is the optical isolator (model IO-5-795 HP, from OFR, Thorlabs). We measure the duration of the pulses after the isolator with a commercial auto-correlator, which gives about 2700 fs^2 chirp. Then the thick glass components induce a big amount of chirp[4]. The polarization cubes (PBS), made of BK7 (51 fs^2 /mm at 795 nm) and silicon (36 fs^2 at 795 nm), have two types of size: 1/4 inch and 1/2 inch. Each PBS introduces $\sim$ 230 and $\sim$ 650 fs^2 by the 1/4 inch and 1/2 inch ones respectively. The beam splitters of 45 degree, made of BK7 with 1/4 inch thickness, induce 460 fs^2 chirp. The lenses, with 2-4 mm thickness of silicon glassed, have the GDD approximately 150 fs^2. Besides, the air contributes the GDD about 20 fs^2/m.

Dispersion compensation prims

[4]In the experiment, all the mirrors are specially coated with zero GDD.

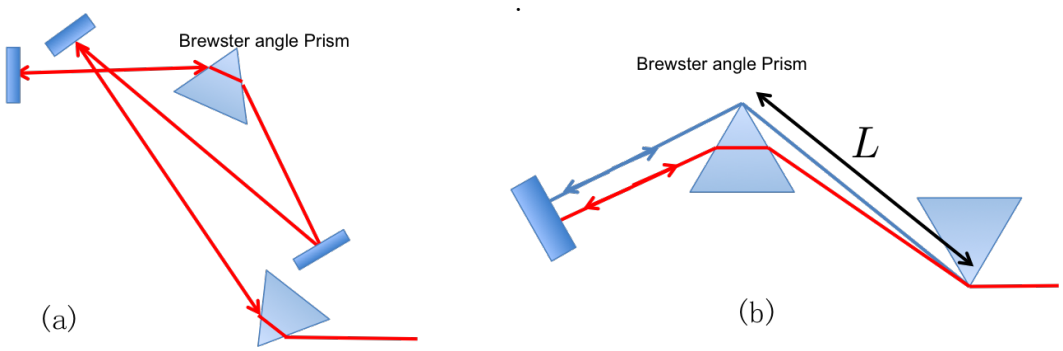

Figure 4.7: Dispersion compensation setup. (a) The experimental design. (b) The principle of dispersion compensation. The negative dispersion is proportional to L.

In the experiment, for compensating the dispersion of the dispersive optical components, we constructed a negative dispersion compensation setup using a pair of Brewster angle prisms made of SF10 [28], and the design is as seen in Fig. 4.7 (a).

As we see in Fig. 4.7 (b), in the optical path, higher frequencies have longer optical paths than the lower frequencies, which correspond a effect of a negative dispersion of GDD proportional to the length L. And the pair of prisms is designed in the Brewster angle $\theta_B = 59.7°$, with a corresponding summit angle $\alpha = 60.6°$.

Here we give, for the pair of prisms cut with Brewster angle, the linear relation between the GDD and the length L (the distance between the summits of the two prisms) [28],

$$\phi''_{\text{dispersion}} \simeq -\frac{2L\lambda_0^3}{\pi c^2}\left(\frac{\partial n}{\partial \lambda}|_{\lambda_0}\right)^2, \tag{4.3}$$

where λ_0 is the central wavelength of the pulses, and n is the refractive index of the material. The amount of negative dispersion can compensate positive dispersion induced by the disperse optical components. After the dispersion compensation we can obtain the Fourier-limited duration of the pulses in the position of the frequency doubling.

As nonlinear optical processes are sensitive to the spectral phase of the involved pulses, it is not important where to perform the dispersion compensation before the frequency doubling and the SPOPO. In the experiment we put the dispersion compensation setup after the correction of astigmatism, as seen in Fig. 4.2.

One tip for aligning the pair of prisms, we have to make the light beam

pass the summit of the prisms as much as possible, which induces a smallest amount of dispersion from the prism material.

Besides the duration of the *pump* pulses, the quality of the temporal and spatial mode is also essential for the SPOPO. Therefore we need carefully align the two lenses in the telescope setup, as seen in Fig. 4.8.

4.3.3 Frequency doubling

In the experiment, as seen in Fig. 4.2, after the dispersion compensation, the laser beam is divided into two parts with a half-wave plate and a polarizing beam splitter (PBS) cube. The laser is frequency doubled via passing directly a BiBO (BiB_3O_6) crystal, which is already introduced in the chapter 3. BiBO is a kind of biaxis crystals with similar disperse properties as uniaxial BBO crystals (β-BaB_2O_4). The advantages of the BiBO are with a higher $\chi^{(2)}$ nonlinear coefficient, a better resistance of the mechanical constraint, and less sensitive with the humidity.

Our BiBO crystals are ordered from the chinese company Fujian Castech Crystals. The cutting angles are: $\theta = 152°$ and $\phi = 90°$, which correspond to a nonlinearity of 3.72 pm/V, for the type I interaction of two fields (e+$e \rightarrow o$). The crystals are treated with anti-reflection coating on the two sides for the wavelengths of 397 nm and 795 nm. The dimension of the crystal for the frequency doubling is 3 x 3 x 0.2 mm (the thickness is 0.2 mm). The frequency doubling can generate enough power of pump with a 0.2 mm thick crystal. In the experiment the efficiency is about 25% ($\sim$ 400 mW), which is enough to pump the SPOPO above threshold.

As seen in Fig. 4.8, we focus the laser in the center of the crystal by the first lens, and collimate the generated blue, after the frequency doubling crystal, with the second lens. In practice, we found that if the beam quality of the blue is not good enough, we need to use more power of the blue to pump the SPOPO. Thus more laser noise will be injected into the squeezing generated via the SPOPO. Therefore, in order to have the mode matching of the pump as good as possible, we need carefully align the two lenses to avoid unexpected spatial astigmatism or chirp.

4.3.4 Mode matching and relative delay

After frequency doubling, for the SPOPO experiment, we have both 397 nm and three parts of 795 nm pulses as the pump, the locking beam, the signal and the local oscillator of homodyne respectively.

Right before injecting the laser beams into the cavity of the SPOPO, we need prepare the spatial mode matching and relative delay control between

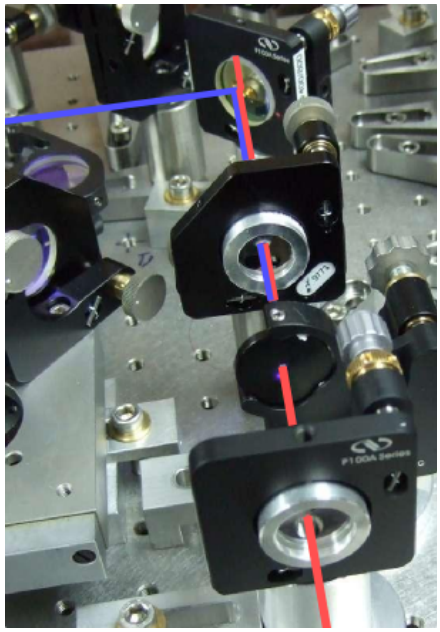

Figure 4.8: The single-pass frequency doubling in the experiment.

the signal and the pump. For the spatial mode matching, we have the SPOPO cavity as the reference, thus we match the signal and locking beam to the cavity; then we match the pump to signal mode. After the spatial mode matching, we control the relative delay between the pump and the signal to obtain a temporal overlap.

Compared to continuous lasers, ultrafast light is more difficult to have the same good modes matching. In the experiment, we use the XYZ adjustable lens mounts to perform precise alignments for the modes matching.

4.4 SPOPO cavity

In this chapter, we introduce the SPOPO cavity, which is a 4 m long ring cavity synchronized to the femtosecond pulses. The cavity is the third generation of the SPOPO cavity. The first generation is a linear cavity [64], and the second generation has the same design as now, with a ring cavity [70]. The cavity now we changed all the optics and the breadboard. For the optics, such as mirrors and curved mirrors, we choose specially femtosecond mirrors with a broad bandwidth of reflectivity instead of the old TLM1 mirrors (Company, CVI), which is associated with higher order supermodes as we discussed previously in chapter 3.

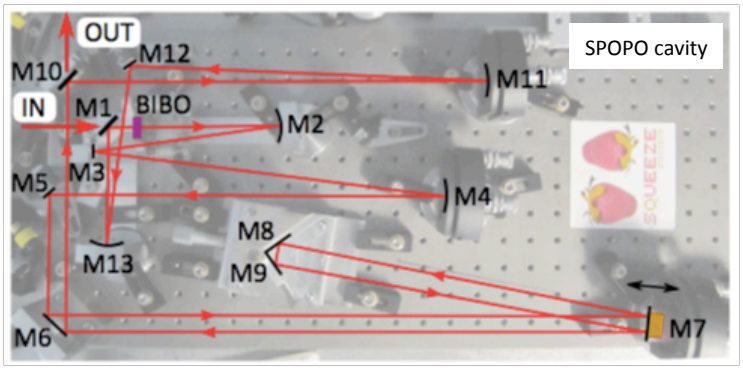

Figure 4.9: The configuration of the SPOPO cavity. In the new version of the cavity, we changed all the optics and the breadboard. The cavity design is the same as before.

4.4.1 Cavity configuration

Compared to the linear cavity, the ring cavity can have two independent laser beams circulating with two different directions in the same time. Using the property, we have one laser beam to lock the cavity, and the other for the signal of the SPOPO. Therefore, we can always have the SPOPO cavity locked even when the signal is vacuum; also we don't need a fraction of signal to lock the cavity compared to the linear cavity, which will introduce a loss in the squeezing generated by the SPOPO.

Besides benefiting the ring cavity, we can also change the power of the signal without influencing the lock of the SPOPO cavity. Similarly, we can optimize the locking beam independently without influencing the signal; further the dispersion in the locking beam induced from the EOM won't affect the signal for the SPOPO.

In the SPOPO cavity, as seen in Fig. 4.9, in practice, the ring cavity has totally 13 mirrors including 4 curved ones, which is multi-folded to be compact. The crystal is in the position of the waist $\omega_0 = 39\ \mu m$. The cavity configuration, as seen in Fig. 4.9, has 15 reflections in a round trip, with two mirrors double reflected. In the cavity, among the 13 mirrors, only five are in the adjustable mounts and the others are in fixed metal mounts[5]. Therefore, it is more robust with a good stability for the cavity.

The cavity is resonant for the signal $\lambda_{\text{signal}} = 795$ nm but not resonant for the pump $\lambda_{\text{pump}} = 397$ nm. The reflectivity of the input coupler M1 is: $R = 99.7\%$ at 795 nm; for the output coupler M10, the reflectivity $R = 70\%$ at 795 nm. All the other mirrors are high reflective (HR) at 795 nm. The

[5]In practice, they have very small adjustable space via controlling the screws on them.

mirrors M2 and M13 are with a curvature $R_c = 25$ cm. M4 and M11 are also curved with $R'_c = 6$ m. The cavity finesse is about 15, and the corresponding bandwidth is about 2-3 MHz.

In the low finesse case, as demonstrated in chapter 1, the dispersion induced by the air can be ignored. But in the case of large finesse, for ultrafast pulses, vacuum or dispersion compensation mirror are needed to compensate the dispersion. Besides, considering the effect of *escape efficiency* in OPO experiments, we make the transmission of the output coupler far bigger than all the loss in the cavity. In the experiment, we use a high reflection inout coupler (R=99.7%) and a high transmission output coupler (T=30%). Yet for this aim, as the threshold gets higher when the finesse is low, we need more pump power to get squeezing,

4.4.2 Alignment of the cavity

Because many mirrors are fixed in the cavity, it is slightly difficult to align the cavity in practice. We scan the length of the cavity via scanning the piezo (PZT) installed on the back of the mirror M7. If the cavity is aligned well, we can see good transmission peaks while scanning the PZT on M7.

Yet in practice, in the begging we align the cavity without the nonlinear crystal or scanning . Firstly we fix the input signal as the reference for the cavity, which passes the centers of the M1 and M2. Then we adjust M1 to make the beam go the center of M3. And we do mirror by mirror to make the beam pass until M10. In the end we use M11 and M12 to manage a round trip. Up to now, one can see the transmission power changing while blocking the beam between M10 and M11. This indicates the beam has round trips. Then we can scan the cavity, and optimize with the transmission peaks. After optimizing with M11 and M12 in the cavity, we continue with the two mirror right before the input coupler.

In addition, M4 and M7 can be used for alignning of the the double reflection to make the beam spots on the middle of the M6 and M7. Here although many mirrors are in the fixed mounts, they can still be modified a bit via change the pressure of the screws. After obtaining the transmission peaks, we can align the locking beam to the signal beam.

When having good transmission peaks, we stop aligning in the cavity. We then take the cavity as the reference without changing, and improve the mode matching of the signal and locking beam by the optics outside the cavity.

Then we can put the BiBO crystal in the cavity, but we need compensate the optical length using the stage where the M8 and M9 are, and get back most of the alinement with only M4. In the end we optimize the transmission

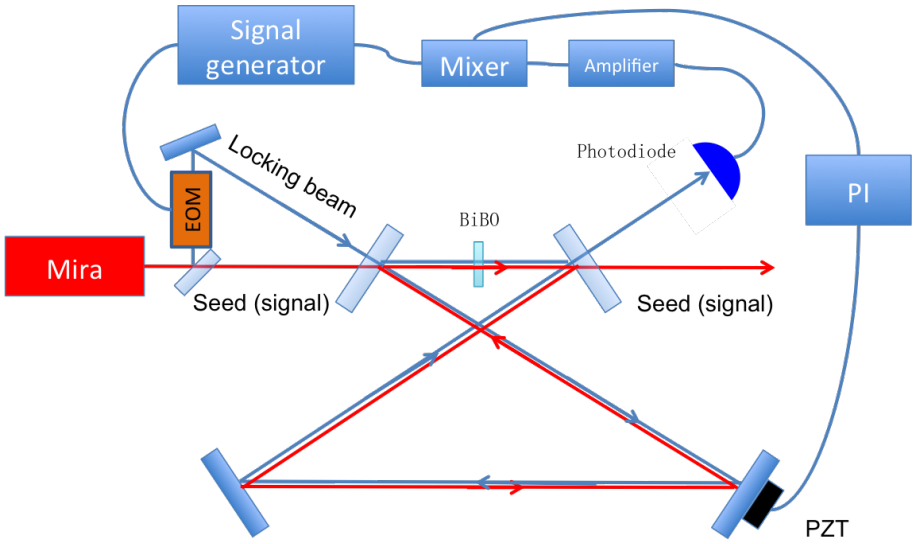

Figure 4.10: The PDH locking scheme of the SPOPO cavity.

peaks by the mirrors out of the SPOPO cavity.

In the alignment, importantly, we always set a reference and optimize the alignment one parameter once. If several parameters, such as modes matching, polarizations and components inside cavity, are adjusted together, it will be very difficult to get good transmission peaks.

4.4.3 PDH locking

Based on a standard approach of the Pound-Drever-Hall (PDH), the SPOPO cavity is locked with the locking beam propagating the opposite direction of the signal. We also call the signal *seed* beam in our degenerate case of SPOPO. In the locking regime, as seen in Fig. 4.10, the locking beam is phase modulated by ~ 1.4 MHz by a EOM, and the locking beam is measured by a photodiode. The measured transmission signal is amplified, and then mixed with the modulation signal of the same frequency, ~ 1.4 MHz. The demodulated signal (error signal) is sent to the servo controller PI, and the output controls the PZT installed on the back of cavity mirror to lock the cavity via modifying the cavity length, which is kept to be resonant with the pulses. Thus, as the signal beam is the same as the locking beam, which propagates in an opposite direction in the cavity, therefore, all the frequencies of the pulses can resonate in the cavity.

As the finesse of the cavity is low, the cavity locking is quite robust, and can last for several hours. Importantly, benefitting from the ring cav-

ity, the cavity locking is independent from the signal beam, which is not involved to the SPOPO process. This allows that we can control the signal beam independently from the cavity locking, such as for the amplification and deamplification locking, homodyne detection, and data collection, which is very helpful for the SPOPO experiment. However, as some unexpected weak reflection of the locking beam from mirrors or the nonlinear crystal can happen, this is still not perfect for photon detection, e.g., single photon extraction experiments [56].

4.4.4 Alignment of the nonlinear crystal and the pump

The principle here is to put the crystal exactly in the waist of the cavity between M1 and M2, and to optimize the temporal and spatial overlap between the signal and the pump. This alignment is very important to get good squeezing.

In practice, we have three steps:

I. When the SPOPO is aligned and locked, firstly we put the crystal in the cavity and get back the transmission peaks by decreasing the length of the cavity, because the refractive index of the crystal is bigger than in the air.

II. We roughly align the pump and the nonlinear crystal angle to get interference patterns from the pump and the frequency doubling of the signal beam (the signal is frequency doubled in the SPOPO crystal). We observe the interference after M2 in Fig. 4.9.

III. In the end, we do fine adjustment to optimize the contrast of deamplification and amplification, as seen in Fig. 4.11.

4.4.5 Amplification and deamplification

When we finish aligning the pump and crystal, scanning the relative phase between the pump and the signal (scan PZT 1 in Fig. 4.2), we can observe the amplification and deamplificaition oscillations of the SPOPO, as seen in Fig. 4.11. Then we need optimize the gain or the contrast of the amplification and deamplification oscillations via adjusting the mode matching of the pump.

As it is difficult to align, and in practice, it is hard to know whether this is optimized. We use the strategy: fixing the powers of the signal and the pump, and then we optimize once and note the contrast. For everyday preparation, we can check the contrast with the same power setting, thus, when we can know alignment is good enough when the contrast is close to the optimized one.

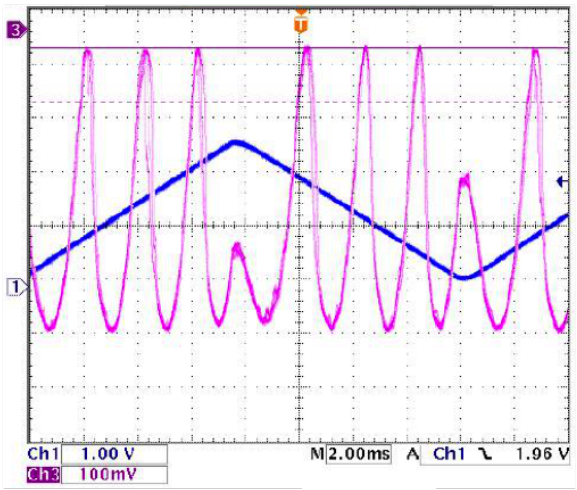

Figure 4.11: The oscillations of the amplification and deamplification observed by the oscilloscope. In the experiment now, we still optimize pump alignment with this oscillation curve of deamplification and amplification, but as this is very sensitive and hard to know if it is optimized or not, we fix the power setting and calculate the contrast in real time with a labview code, then we know it is optimized when the contrast is the same as last time. And in practice, usually when get the good contrast, the threshold and the squeezing from the SPOPO are both good.

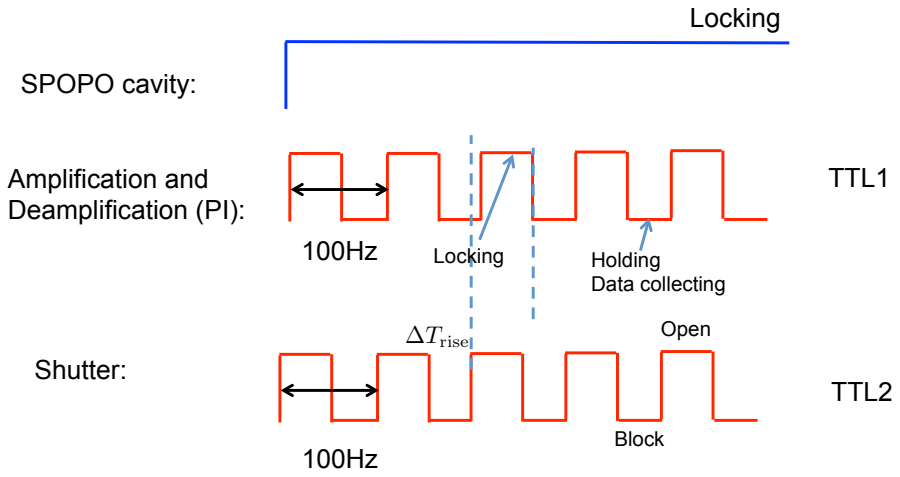

Figure 4.12: The time sequences in the locking of amplification and deamplification. The SPOPO cavity is always locked. Shutter and the PI are trigged by the 100 Hz TTL signals with a delay ΔT_{rise}, which is the rising time of the shutter mechanics. For the PI, the high voltage trigs the function of locking, when the low one refers holding the locking signal. For the shutter, the high voltage makes the shutter open, and during the low voltage the seed light is blocked.

In the experiment, the contrast of the amplification and deamplificaiton is very sensitive to the mode matching of the pump, including spatial and temporal modes matching. Therefore as we mentioned, in order to generate the pump with a proper TEM_{00} mode and without chirp, the alignment of the frequency doubling is important.

4.4.6 The threshold of the SPOPO

After optimizing the contrast of the amplification and deamplificaiton, we can obtain the threshold via increasing the pump power. Typically, in the experiment, when the input coupler has the reflectivity $R_{in} > 99\%$, we have the threshold $P_{\text{threshold}}$:

$$\begin{aligned} P_{\text{threshold}} &\simeq 90mW, \quad \text{with} \quad R_{out} = 90\%, \\ &\simeq 120mW, \quad \text{with} \quad R_{out} = 80\%, \\ &\simeq 160mW, \quad \text{with} \quad R_{out} = 70\%, \end{aligned} \tag{4.4}$$

where R_{out} is the reflectivity of the output coupler.

Importantly, the level of the threshold is a good indication for the quality of the experimental performance. Normally, we can measure ~ 4 dB squeez-

ing directly with a spectrum analyzer, when the threshold reached the values listed above[6]. We will discuss the measurement process in next chapter.

4.4.7 Relative phase locking between signal and pump

In the experiment, sometimes we need to lock on the amplification or deamplificaition, which is equivalent to lock the relative phase between the pump and signal. In the deamplification, the amplitude quadrature of the signal is squeezed and the phase quadrature is anti-squeezed; in the position of the amplification, the amplitude quadrature of the signal is anti-squeezed and the phase quadrature is squeezed. In this section, we will introduce the relative phase locking between signal and pump with seed (signal) and without seed (use a light shutter).

As seen in the experimental configuration in Fig. 4.2, in order to lock the deamplification (or amplification), when the cavity keeps locked, the pump beam is given a phase modulation ($\sim$ 1.7 MHz) performed with PZT 2 , and the error signal of the locking is obtained from demodulating the signal measured with the PD blue[7], and further controls PZT 1 to realize the locking.

Here, differently from the cavity locking, as the phase modulation is given by PZT (not EOM), we can only choose a resonant frequency of the PZT, which is not continuous and different for different PZTs. In practice, to find the resonant frequencies, we give a phase modulation on the PZT and scan the modulation frequency slowly; we mix the laser beam reflected by the mirror attaching the PZT and a reference beam; we can observe the resonant frequency peaks by spectrum analyzer. The way of phase modulating on the laser beam does not introduce dispersion compared to using a EOM, which is very useful for ultrafast pulses. For instance, if the pump has a chirp, the efficiency of the SPOPO will get reduced. But the modulation frequencies are not continuous or too high, a few MHZ, thus we have to choose carefully to avoid the frequency itself and its harmonics overlapped with the frequency where we observe squeezing.

To lock the relative phase between signal and pump, usually, we need always seed the cavity, as it is impossible to directly lock the pump to vacuum. Yet, sometimes, we prefer vacuum squeezing, which has less laser noise, and is easier to get higher squeezing.

To realize locking squeezed vacuum, we build a locking system with a mechanical shutter (Stanford SR574). In Fig. 4.12, here we present the time

[6]The detector has a 95% quantum efficiency and the shot noise is $\sim$ 10 dB higher than the electric dark noise

[7]It is named so in Fig. 4.2.

sequence control of the relative phase locking for a vacuum squeezing, where for each cycle there are two procedures: in the first half of the period, it is a normal process of deamplification (amplification) locking when the shutter is open (signal passes); during the second half of the cycle, the shutter blocks the signal, the voltage level on the PZT 1 is hold by the servo controller PI in Fig. 4.2.

In the experiment, the shutter and the PI are synchronously controlled by two channel TTL signals generated by a delay generator, as seen in Fig, 4.12. The frequency of the TTL signals is 100 Hz, which is limited by the rising time of the shutter mechanics, and the corresponding holding time is 5 ms. Because the holding period is very short, the phase change very little during the holding time in the laboratory environment.

4.4.8 The SPOPO above threshold

Above the threshold, the SPOPO, similar to usual OPOs, can emit the infrared laser without injecting the signal. In that case, the output is the first supermode when the SPOPO cavity is locked, which has the largest gain. We can measure the spectrum of the first supermode when the SPOPO is above the threshold.

For instance, as seen in Fig. 4.13 [69], when the spectral bandwidth of the *seed* is 6 nm, measured by the spectrometer (Ocean Optics), the spectral bandwidths of the SPOPO above threshold are 11 nm and 7.5 nm corresponding to the 0.5 mm and 2 mm long BiBO crystal respectively. With the 10 nm wide spectrum of the *seed*, we also measured the spectrum of the first supermode, which matched quite well with the theoretical results of Fig. 3.8. This indicates the SPOPO theoretical model can give quite a good prediction and guide for the experiment.

4.5 Homodyne detection with pulse shaping

4.5.1 Homodyne detection

In the laboratory, we usually use *homodyne detection* [37] to detect squeezing, which is quite a useful tool in quantum optics. As seen in Fig. 4.14, the two light fields, the signal and local oscillator, are mixed with the balanced optical beam splitter, then the difference signal between two intensity measurements $\hat{I}_1$ and $\hat{I}_2$ of outputs can directly give the quadrature measurement of the signal.

And importantly, when the the power of the local oscillator is much bigger

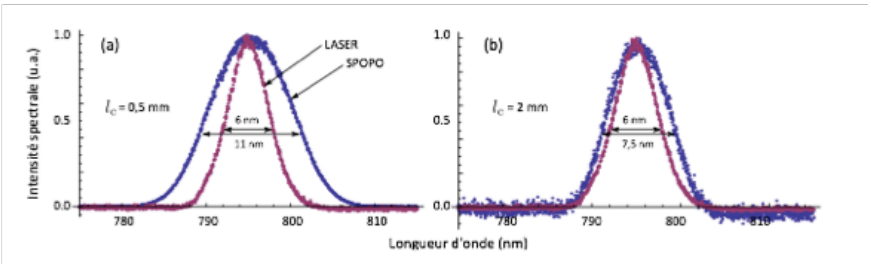

.

Figure 4.13: The spectra of the seed and the SPOPO above the threshold []. The blue curves are the spectra of the SPOPO above threshold, and the red curves are the spectra of the seed. (a) and (b) corresponds to he 0.5 mm and 2 mm long BiBO crystal respectively.

than the signal beam, $P_{\mathrm{LO}} \gg P_{\mathrm{signal}}$, homodyne detection is mode-dependent measurement, where the signal field, $\hat{E}_{\mathrm{s}} = \sum_j \hat{a}_{\mathrm{s}}^j u_{\mathrm{s}}^j$, with the modes $\{u_{\mathrm{s}}^j\}$, is projected onto the mode of local oscillator u_{LO} [37].

Here, when $P_{\mathrm{LO}} \gg P_{\mathrm{signal}}$, so $\langle \hat{a}_{\mathrm{LO}} \rangle \simeq \sqrt{P_{\mathrm{LO}}} e^{i\theta}$ we have,

$$\hat{I}_- = \hat{I}_1 - \hat{I}_2 \simeq \hat{a'}^\dagger \langle \hat{a}_{\mathrm{LO}} \rangle + \hat{a'} \langle \hat{a}_{\mathrm{LO}}^\dagger \rangle = \sqrt{P_{\mathrm{LO}}} \hat{x'}_\theta = \sqrt{P_{\mathrm{LO}}} \sum_j | \int u_{\mathrm{LO}}^* u_{\mathrm{s}}^j \mathrm{d}\Omega | \hat{x}_{\theta_j}^j, \tag{4.5}$$

where $\hat{a'} = \sum_j \int u_{\mathrm{LO}}^* u_{\mathrm{s}}^j \mathrm{d}\Omega \hat{a}^j$ is the quasi basis change (projection) and the quadratures are $\hat{x}_{\theta_j}^j = e^{-i\theta_j} \hat{a}_{\mathrm{s}}^j + e^{i\theta_j} (\hat{a}_{\mathrm{s}}^j)^\dagger$, $\hat{x'}_\theta = e^{-i\theta} \hat{a'}^\dagger + e^{i\theta} \hat{a'}$; θ is the global relative phase between $\hat{a'}$ and the local oscillator (LO) in the homodyne detection, θ_j is the relative phase between the mode $\hat{a}^j$ and the LO.

And the variance of the measurements, ΔI_-^2, gives the property of quantum fluctuation Δx_θ^2, e.g. squeezing of the signal, and when the input signal modes are not correlated, we have,

$$\Delta I_-^2 = P_{\mathrm{LO}} \sum_j | \int u_{\mathrm{LO}}^* u_{\mathrm{s}}^j \mathrm{d}\Omega |^2 \Delta x_{\theta_j}^{j2}. \tag{4.6}$$

For the SPOPO, the signal, which is a set of supermodes, which co-propagate in one single beam, and the local oscillator from the Mira laser both have flat spectral phases when the dispersion is properly compensated. As demonstrated in chapter 3, the odd order supermodes have the same phase 0, and the odd order supermodes have the same phase $\pi/2$, so we have,

$$\theta = \theta_{j_{odd}} = \theta_{j_{even}} + \frac{\pi}{2}. \tag{4.7}$$

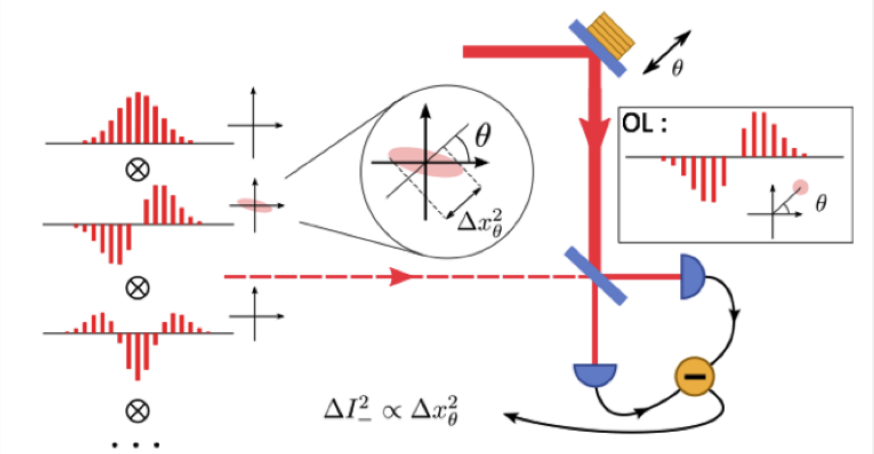

Figure 4.14: Homodyne detection configuration. The signal is projected onto the specific mode of the local oscillator. The squeezing of the signal in some specific mode can be measured by homodyne detection, where the squeezing ellipse angle θ is associated to the relative phase between the signal beam and the local oscillator.

Thus, as seen in Fig. 4.14, many supermodes co-propagate in the signal beam, which is projected onto the mode of the local oscillator; and we can access the corresponding squeezing with a relative phase θ via the measurement of $\hat{I}_-$. Therefore, we can access into any modes via shaping the local oscillator correspondingly.

Previously in chapert 3, we already theoretically studied the multimode property of the SPOPO in a 8-band band basis, and we sa that many supermodes co-propagate in the output of the SPOPO, which are a series of spectral modes in spectral domain or pulse shapes in time domain, as seen in Fig. 3.17 . Thus, in orde to explore multimode correlation, we project the output of the SPOPO onto some specific spectral modes of the local oscillator in the homodyne detection [65]. In practice we realize shaping specific modes in local oscillator via a SLM (spatial light modulator) [70] [55].

For data collection, from homodyne measurements, we can obtain quandature values using oscilloscopes, and noises (variance) of quadratures using spectrum analyzer.

In the experiment, we developped the homodyne measurement system, including commercial silicon photodiodes (Hamamastu, quantum efficiency 95%∼99%), and homemade electronics. For the electronics, the signal of individual detectors is firstly amplified and then a difference of high frequency

signals from two detectors is made to get the homodyne signal[8].

The measured squeezing is defined as the ratio, $\frac{V_{\mathrm{Msqz}}}{V_{\mathrm{Mshot}}}$, with $V_{\mathrm{Msqz}} = V_{\mathrm{sqz}} + V_{\mathrm{dark}}$ and $V_{\mathrm{Mshot}} = V_{\mathrm{shot}} + V_{\mathrm{dark}}$, where V_{Msqz}, V_{Mshot}, V_{dakr} are directly obtained from the measurement data, which are, in linear scale, variances of squeezing, vacuum noise (shot noise), and electric dark noise (without light signal), respectively. V_{sqz}, V_{shot} are the actual squeezing variance and shot noise, respectively. The difference of the measured squeezing and the actual squeezing is,

$$\frac{V_{\mathrm{Msqz}}}{V_{\mathrm{Mshot}}} - \frac{V_{\mathrm{sqz}}}{V_{\mathrm{shot}}} = \frac{V_{\mathrm{shot}} - V_{\mathrm{sqz}}}{(\frac{V_{\mathrm{shot}}}{V_{\mathrm{dark}}} + 1)V_{\mathrm{shot}}}. \tag{4.8}$$

When the dark noise V_{dark} is bigger, we lose more squeezing in the measurement. Thus this clearance $\frac{V_{\mathrm{shot}}}{V_{\mathrm{dark}}}$ is essential for homodyne detection, otherwise the dark electronic noise will reduce the squeezing. In our case, $10 \sim 15$ dB[9] clearance from the electric dark noise is obtained, which is good to observe squeezing.

4.5.2 Pulse shaping in the local oscillator

In the homodyne measurement, in order to access the noise property of specific modes, we shape the local oscillator via a spatial light modulator (SLM). With a 4-f configuration [55], the SLM can be employed to access arbitrary pulses shapes.

As seen in Fig. 4.15, the 4-f configuration is composed of two diffraction gratings and two lenses arranged in a 4-f set-up, where the SLM is put on the Fourier plane. All the spectral components of the input pulses are dispersed by the first grating horizontally, and after the first lens, the beam is focused to a small spot in the Fourier plane. Thus, in this Fourier plane, all the spectral components are spatially separated and focused. Then, the SLM can implement phase modulations on all the individual colors of light with the pixels of the SLM sensor. After that, the symmetry set-up recombines all the frequencies into a single beam, which has a new pulse shape associated with the phase modulation given on the SLM.

As seen in Fig. 4.16, it is the experimental configuration of the 4-f configuration. The SLM is composed of a reflective 2-D sensor with 512 x 512 pixels (XY Series of Boulder Nonlinear Systems). With ultrashort pulses, the lenses are replaced by cylindrical mirrors to avoid unwanted dispersion

[8] Another way, amplifying the difference, can get better clearance, usually. Here our configuration of electronics is easier for the alignment and enough to see squeezing.

[9] 15 dB=$10\mathrm{Log}_{10}\frac{V_{\mathrm{shot}}}{V_{\mathrm{dark}}}$.

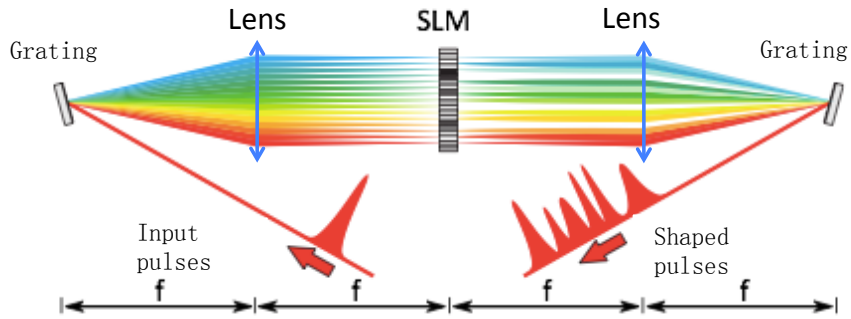

Figure 4.15: 4-f configuration of SLM. All the spectral components of the input pulses are dispersed by the first grating horizontally, and after the first lens, the beam is focused to a small spot in the Fourier plane. Then after shaping, the shaped pulses are recombined.

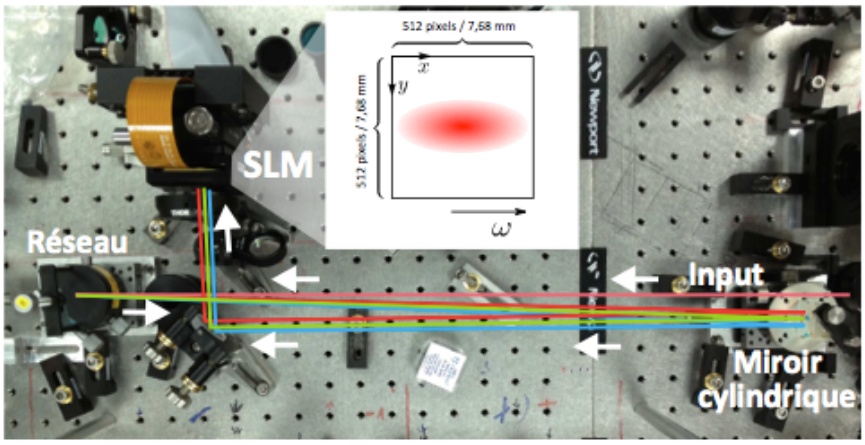

Figure 4.16: Experimental configuration of the pulse shaping. In practice, we use a reflective SLM, a grating and a cylindrical mirror to build the shaping setup. In the new version, we changed the cylindrical mirror and the grating to optimize the frequency resolution of the 4-f configuration.

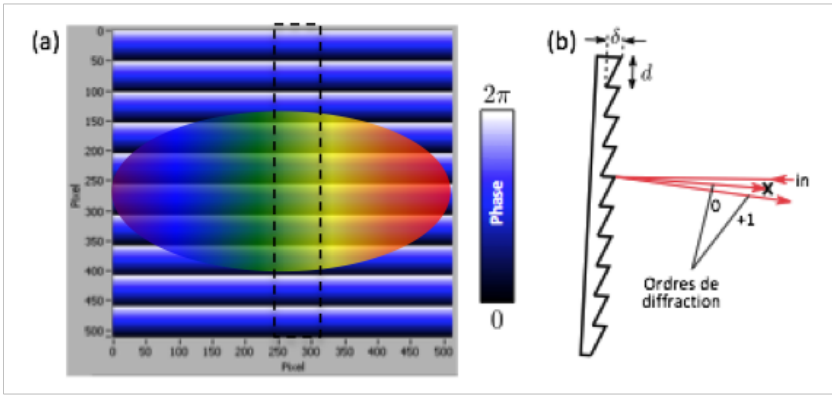

Figure 4.17: The "grating" on the phase mask of the SLM. (a) The light is dispersed and mapping on the phase mask (sensor) horizontally. The SLM has a "grating" like phase. (b) The "grating" shaped by the SLM directs the injected beam.

and chromatic aberrations, and the SLM is a reflective type. We can modify the phase of the light reflected from the SLM via controlling the electric tension of each pixel [78]. In the experiment, the beam is dispersed firstly by the grating (1800 /mm) and is focused horizontally by the cylindrical mirror (f=50 cm). Then the light is reflected from the SLM, and the reflection repass the cylindrical mirror and the grating with the same path to recombine in a single beam. This beam with shaped pulses behaves as the local oscillator for the homodyne detection.

With the 2-D SLM, we can do arbitrary amplitude and phase modulation on each frequency. In the 4-f configuration, each color of light is mapped on the SLM horizontally, as seen in Fig. 4.17. Thus to do the phase control on some color, we directly give a phase modulation with the vertical slice of pixels where the corresponding color is mapped, for instance, the dashed block part of the SLM refers to the color of "yellow-green" mapped on it, seen in Fig. 4.17.

Then as to the amplitude control, we apply a grating-like phase on the mask. As seen in Fig. 4.17, we write the phase to have a form of the horizontal grating, and the amplitude of the first (+1) order of diffraction can be controlled via changing the property of the "grating". The depth δ of the "grating" is 0 to 1 corresponding to the phase 2π to 0. Thus, when $\delta = 0$ (or 1), the the first (+1) order diffraction is 0 (or 1). The

amplitude of the first (+1) order diffraction is the function of δ, which we can control with the phase on the corresponding pixels. But the relation between the amplitude of the first (+1) order of diffraction and the δthis is slightly nonlinear. In practice, we don't need calibrate phase modulation; we need calibrate the amplitude modulation by measuring the relation curve of the diffracted amplitude vs the depth of the grating;

In a summary of pulse shaping in our experiment, for phase, we write the demand phase directly on the region of the dashed block; for amplitude, we apply the periodic "grating" phase with the corresponding depth δ. In a result, we implement a demand phase and amplitude modulation on the selected color.

The direction of the first order diffraction is determined by the d parameter of the "grating". In the experiment, d=10, and we use a pinhole (50 μm) to choose the diffracted beam in a configuration of spatial filter (as seen the spatial filter 2 in Fig. 4.2).

Above all, with the pulse shaping setup, an arbitrary pulse shape can be implemented , only limited by the resolution of the sensor of the SLM. However, in the experiment, we face the first limit which is not the resolution of the SLM at all, but the power of the laser, for instance, when we shape the local oscillator into $\sim$ 20 frequency bands, the power of each band is already very small for the homodyne measurement.

4.5.3 Measurements and data collecting

In the experiment, in order to interrogate the quantum correlations, we keep the output of the SPOPO and project it to the desired mode, as seen in Fig. 4.18 (a). Then as seen in Fig. 4.18 (b) and (c), we have two ways of collecting data: (1) we can observe the noise property of the SPOPO in specific modes by a spectrum analyzer; (2) we collect the quadrature with a data acquisition card (DAQ NI PCIe-6361 connected to a BNC connector block BNC-2110). The first way is easier and direct to see the noise, for example, the squeezing. The second way is much faster than with the spectrum analyzer, so this way is better when collecting many data, for instance, collecting data to build a covariance matrix. For the second method, the difference signal from the homodyne measurements are amplified (Amplifier), then are demodulate at 1 MHz by a Mixer (Mini Circuits), as seen in Fig. 4.18 (c).

With both methods, we obtained the vacuum squeezing of the SPOPO (The seed is vacuum). As seen in Fig. 4.19, when the local oscillator is a gaussian spectrum centered at 795 nm with 10 nm bandwidth (the output of the Mira laser), we got $\sim$ 5.5 dB squeezing without any correction when scanning the phase of local oscillator (PZT 5 in Fig. 4.2).

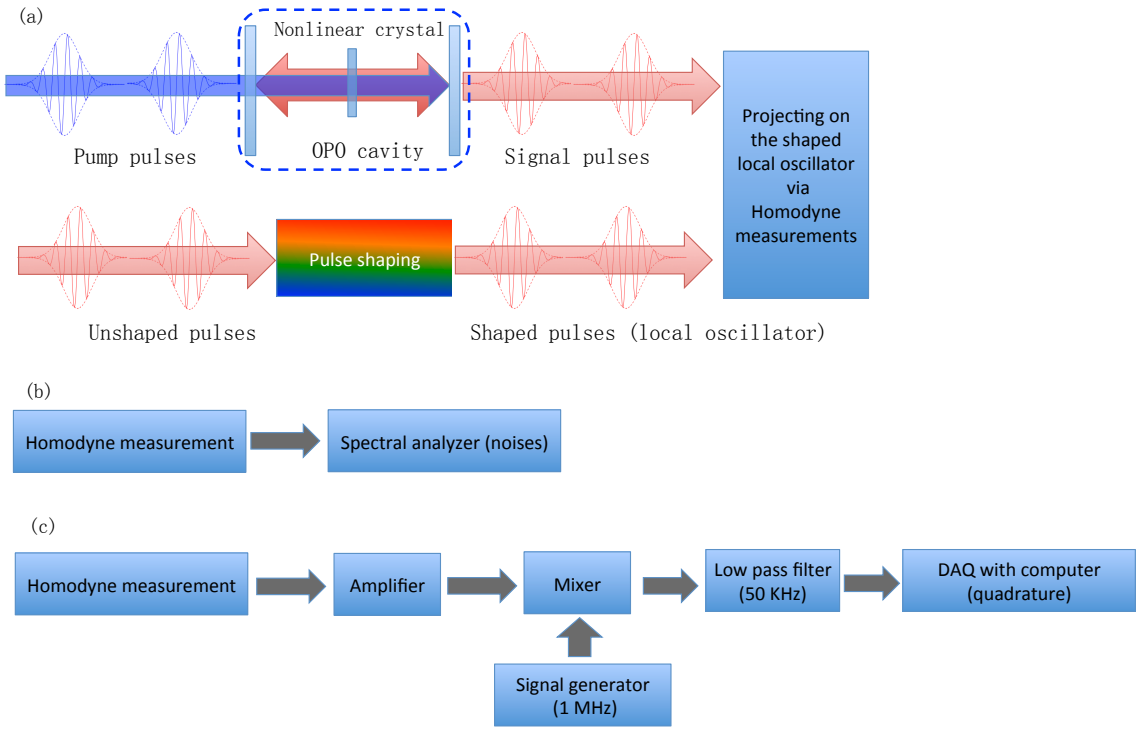

Figure 4.18: Projective measurements and data collection. (a) The state of the SPOPO is projected onto the specific mode of the local oscillator via the homodyne measurement. Two methods of data collecting: (b) Directly observing the quantum noises by a spectrum analyzer; (c) Collecting the quadrature values with the DAQ card.

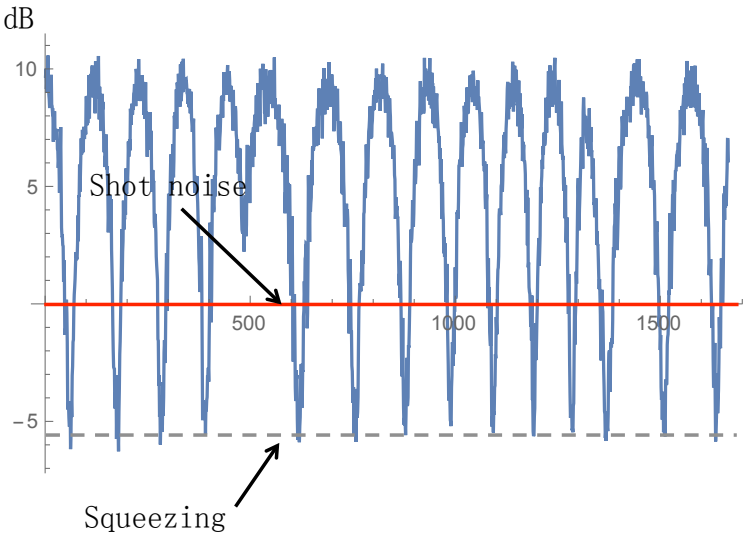

Figure 4.19: The vacuum squeezing of the SPOPO directly measured ($\sim$ 5.5 dB). The horizontal axis is the phase of the local oscillator.

In the squeezing measurement, the visibility of the homodyne contrast is about 94%, and the quantum efficiency of the silicon photodiode is $\sim$ 99% (Hamamatsu Photonics) [10]. We approximately have about 15% loss after the SPOPO cavity; the electric dark noise is $\sim$ 10 dB lower than the signal. According to Equ. 3.47, the squeezing, corrected by the dark noise and the measurement loss, is $\sim$ 8 dB.

Although vacuum has no regular phase, here we just make the scan phase of the local oscillator much faster than the random phase fluctuation of the vacuum. And the valley and peak correspond to the squeezing in different phase of quadratures, amplitude and phase, respectively.

4.6 State reconstruction with 16-pixel covariance matrix

4.6.1 Measuring multimode quantum noises of SPOPO and covariance matrix

In order to characterize the intra-comb entanglement across the entire spectrum, the LO is divided into 16 frequency bands of equal energy by the pulse

[10]This photodiode is specially selected with high quantum efficiency. Using usually photodiodes with more than 90% quantum efficiency, more than 4.5 dB is still available.

shaping, as seen in Fig. 4.21, and the amplitude and phase quadrature noises for each spectral region and all possible pairs of regions are determined. The spectrum of the local oscillator has a bandwidth of $\sim$ 10 nm (FWHM), and each band is $\sim$ 1.3 nm wide. The central gap in the spectrum is given on purpose to avoid saturating the detector for central bands. We can't go to more bands limited by the energy of the single frequency bands on the wings, which is so low that the signal-to-noise ratio is bad for the homodyne measurements. Up to now, each frequency band has an optical power of $\sim$ 70 mW, which is just close to saturate the homodyne detectors.

With the method as seen in Fig. 4.18 (c), the 136 requisite homodyne measurements are acquired in a period of approximately 5 minutes, and allow assembly of the states full covariance matrix [70]. To get all the elements of the covariance matrix, we collected 136 noise curves, such as seen in Fig. 4.20. The fit for the peak (anti-squeezing) and the valley (squeezing) gives the variance of individual bands $\langle \hat{x}_i^2 \rangle$ and the combinations $\langle (\hat{x}_i + \hat{x}_j)^2 \rangle$, respectively. According to the Equ. 3.53, the elements of the covariance matrix are normalized with corresponding optical powers of each band.

We have observed that cross-correlations of the form $\langle \hat{x}\hat{p} \rangle$ are absent, which permits the covariance matrix to be cast in a block diagonal form. Fluctuations and correlations departing from the vacuum level are shown in Fig. 4.22 for the amplitude and phase quadrature. And here we only corrected dark noise for the covariance matrix.

4.6.2 Multimode analysis

With the covariance matrix, shown in Fig. 4.22, as we discussed in chapter 2 we have two methods to do the multimode analysis: (1) we directly diagonalize it to get the eigenmodes and eigenvalues; (2) we can also do the Williamson decomposition. We directly diagonalize the covariance matrix to get the eigenmodes (squeezed modes) and eigenvalues (squeezing). As we mentioned, because of the purity issue, we can't get the same eigenmodes for the amplitude and phase quadrature covariance matrix. Thus, from Williamson decomposition, we also can get a set of eigemmodes, and the corresponding squeezing which is pure and corrected from the classical noise.

The main difference of the two methods is, the squeezing values from the first method, in principle, should be close to the detected measured squeezing if we shape the local oscillator onto the corresponding eigenmodes, yet the squeezing from the Williamson decomposition is pure and corrected, which is similar as the squeezing obtained from the first method with a loss correction. In the following, we present the results based on the first method.

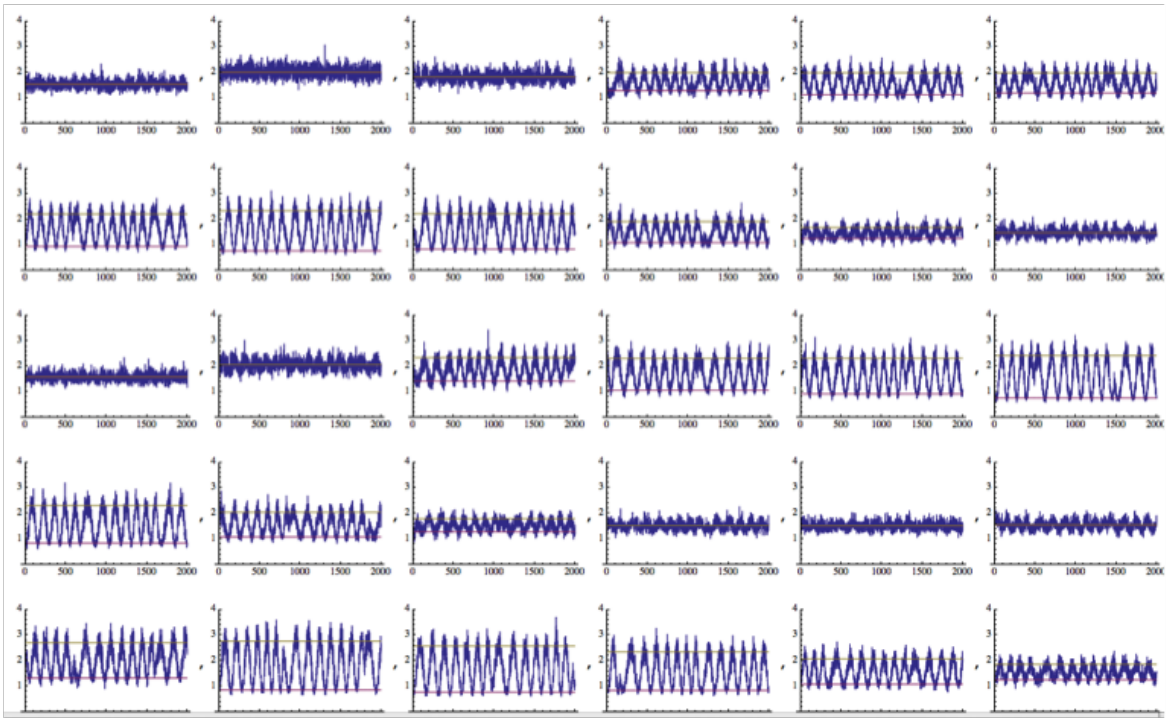

Figure 4.20: Examples of measurements data. We get the the amplitude and phase quadrature fluctuation from the valley and peak of the curves, respectively.

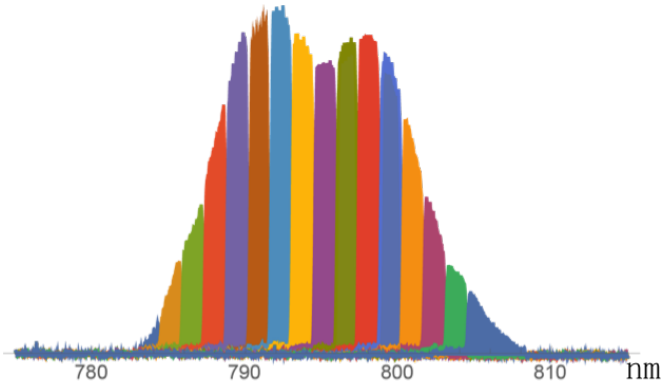

Figure 4.21: The spectrum of the local oscillator is divided into 16 frequency bands as the measurement basis. The middle hollow envelope in the spectrum is made by pulse shaping to avoid saturating the homodyne detectors.

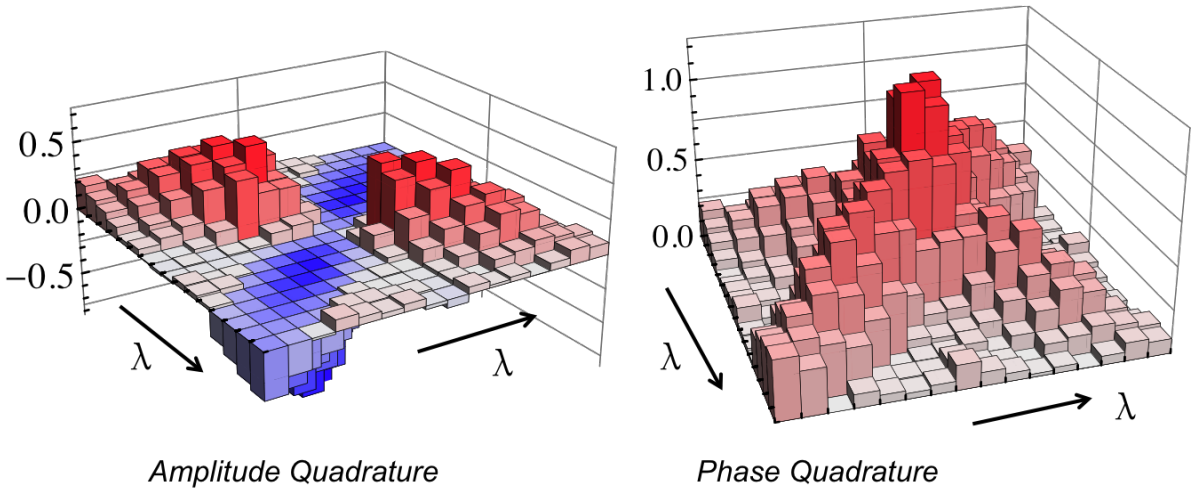

Figure 4.22: 16-partite covariance matrix in frequency-band basis. Off-diagonal shot noises are normalized to 1 and diagonal ones are normalized to 0 . In the correlation measurement, the spectrum of resource, which is a train of 150 fs pulses centered at 795nm with 10nm bandwidth, is divided into 16 equal frequency bands. All the correlations of the resource in the amplitude quadrature (left) and phase quadrature (right) are contained in the matrix.

After diagonalizing the covariance matrix from both amplitude and phase quadrature, we get the eigenvalues (squeezing) and eigenmodes. In Fig. 4.23, form the phase quadrature covariance matrix, we present the leading nine eigenmodes and the eigenvalues, and the squeezing of the ending seven eigenmodes are -0.95, -0.60, -0.57, -0.50, -0.30, 0.12, 0.15 dB. As the measurements, for the side frequency bands, have quite low signal-to-noise ratio, and this causes the covariance matrix to be slightly unphysical. Especially for the squeezing of the leading modes, e.g., the -10 dB squeezing of the first eigenmode.

Also because the purity of covariance matrix is low, $\sim$ 35%, the eigenmodes of Fig. 4.23 are different from the ones of the amplitude quadrature matrix. We also did Williamson decomposition on the measured covariance matrix following the recipe of the chapter 2.5. We verify the Williamson eigenmodes are similar to the ones of Fig. 4.23, and the shape of the eigenmodes are consistent during a long-term experiment. Thus, importantly, from the covariance matrix the shape of the eigenmodes we reconstruct is reliable. And such eigenmodes are not quantum correlated, and co-propagate in the single beam from the quantum source, SPOPO.

Furthermore, according to the eigenmodes we obtained, we then directly

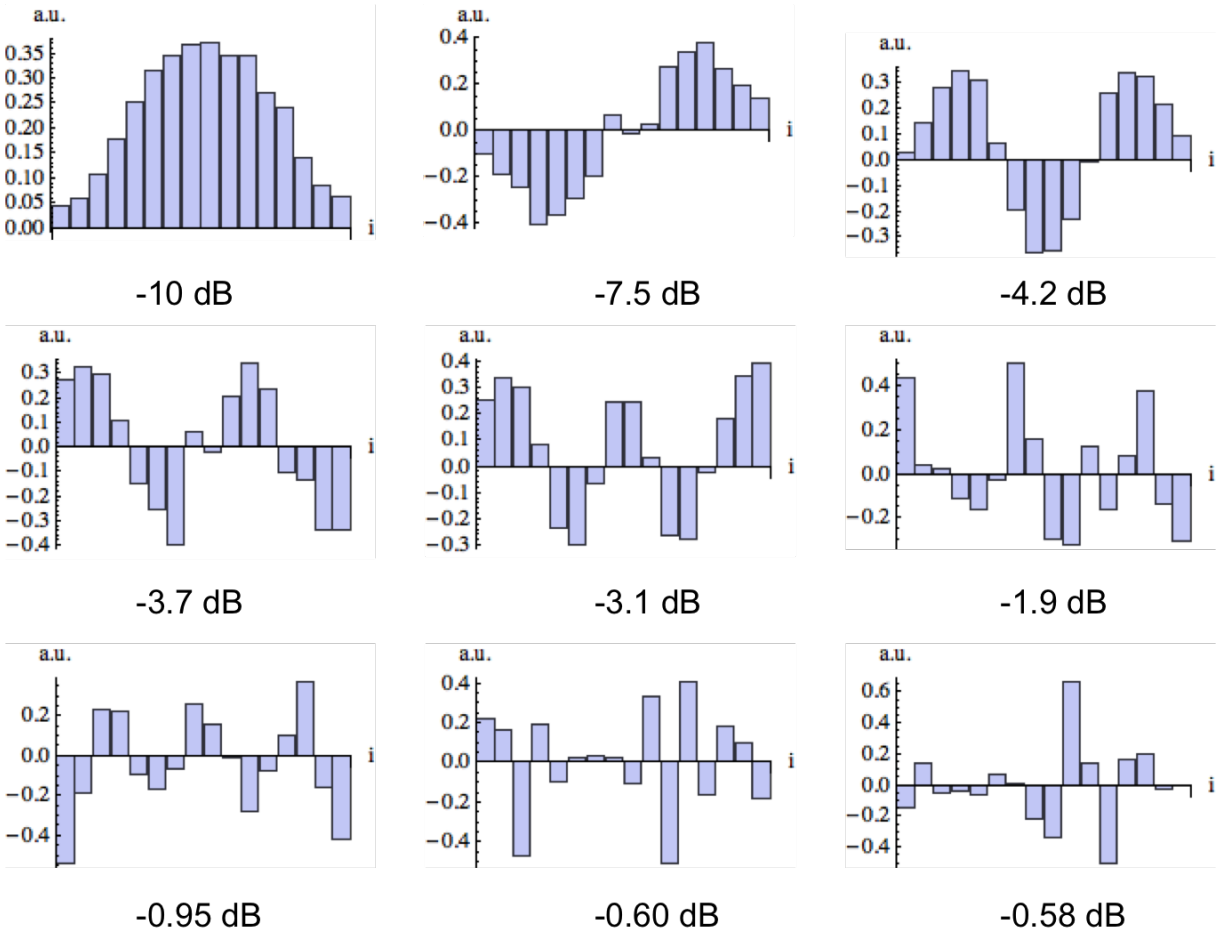

Figure 4.23: The leading nine of the sixteen eigenmodes and corresponding squeezing values from directly diagonalizing the measured covariance matrix with loss correction of 15%. The squeezing of the ending seven eigenmodes are -0.95, -0.60, -0.57, -0.50, -0.30, 0.12, 0.15 dB.

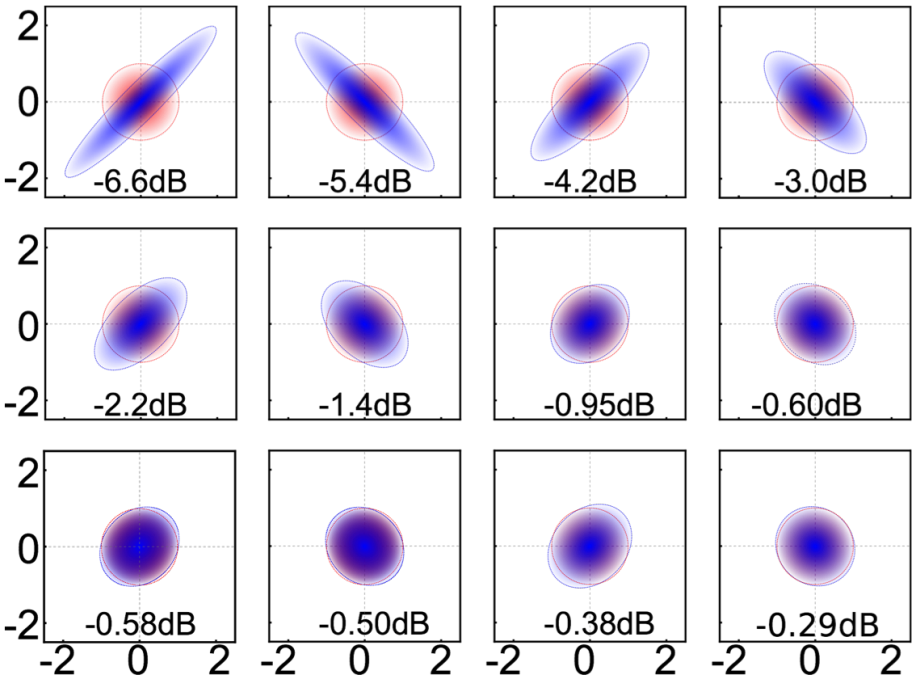

Figure 4.24: 12 squeezing ellipses(blue) are given in the boxes, which corresponds the leading 12 eigenmodes of the covariance matrix, and the circles(red) represent vacuum. The leading six squeezing values are directly measured via shaping the local oscillator onto the eigenmodes. All the 12 modes are squeezed and the squeezing values below ellipses are corrected by dark noise and 15% measurement total loss.

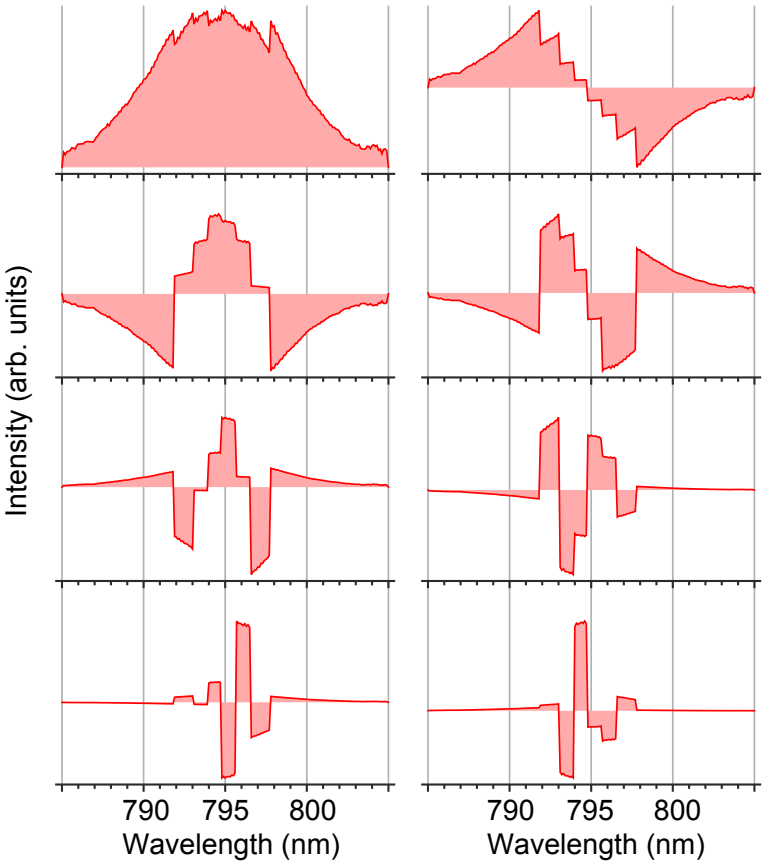

Figure 4.25: The measured spectra of the eignmodes [20].

measure the squeezing of the leading six modes via shaping the local oscillator onto these eigenmodes. In Fig. 4.24, 12 squeezing ellipses (blue) are given, which corresponds to the leading 12 eigenmodes of the covariance matrix, and the circles (red) represent vacuum. Yet the squeezing of the leading six modes are obtained directly from homodyne measurements with pulse shaping, and the others are from the diagonalization of the covariance matrix. We can see that all the 12 modes are squeezed and the squeezing values below ellipses are corrected by dark noise and 15% measurement total loss. The ellipse direction refers to the phase of the squeezed eigenmodes, which are 0 and $\pi/2$ alternately amongst the eigenmodes, referred to Equ. 4.7.

Each eigenmode refers to a specific spectrum of the field, which can be formed via pulse shaping. According to Equ. 3.55, the spectra of the leading eight eigenmodes are presented in Fig. 4.25 [20]. In particular, for the leading modes, the experimental results of the eigenmodes coincide well with the simulated ones as in Fig. 3.15. And in Fig. 4.26 [20], the squeezing curves of the first four eigenmodes via shaping the local oscillator exactly with the shape of the eigenmodes are presented, which are all squeezed.

Above all, we did multimode characterization of the measured covariance matrix. We experimentally show that the output of the SPOPO is multimode squeezing, and the shape of the squeezed modes and corresponding squeezing. And it is important to note that the number of the squeezed eigenmodes is associated with the number of modes in the measurement basis [20]. In next chapter, appealed to quantum information, in particular, cluster states for measurement based quantum computing, we will present how to do from multimode squeezing to a quantum network.

4.6.3 Full multipartite entanglement

Here, we want to evaluate multipartite entanglement within the gaussian state obtained from the SPOPO. This work has been done in collaboration with the group of W. Vogel in Rostock, and has been published in Physics review letter (114, 050501, 2015) [32].

In the multimode case, we obtained a 10-mode covariance matrix from the SPOPO. The 10 mode basis can be decomposed into many different partitions, each one distributing the 10 modes in K different and complementary partitions, with K being any integer between 1 and 10.

The multipartite entanglement of a quantum state $\hat{\rho}$ may be probed with the use of a general Hermitian operator $\hat{L}$ [84]. In particular, the state under question is entangled with respect to a given K partition if and only if it may be shown that

$$\mathrm{tr}(\hat{L}\hat{\rho}) < g^{\min}_{I1,\ldots,IK} \tag{4.9}$$

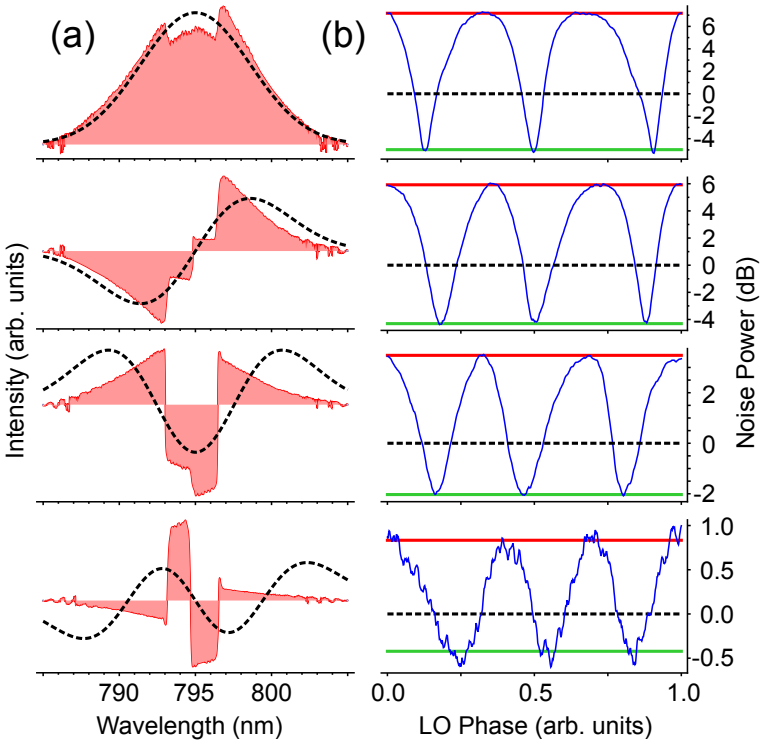

Figure 4.26: The squeezing of the leading four eigenmodes are directly measured via shaping the local oscillator exactly with the shape of the eigenmodes.

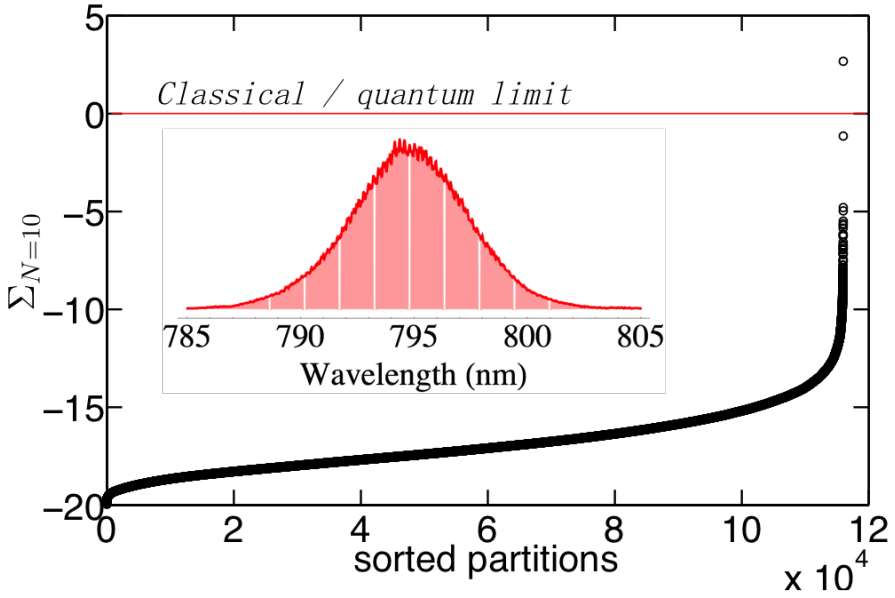

Figure 4.27: With a 10-mode basis, the verified entanglement for all 115 974 possible partitions is sorted by the significance Σ.

where $g^{\min}_{I1,\ldots,IK}$ is the minimum expectation value of $\hat{L}$ among all separable states of the K partition.

The partitions entanglement is characterized in terms of its statistical significance Σ, which compares the difference between the expectation value $\langle\hat{L}\rangle$ and its separable bound $g^{\min}_{I1,\ldots,IK}$ to the experimental standard deviation $\sigma(L)$ is:

$$\Sigma = \frac{\langle\hat{L}\rangle - g^{\min}_{I1,\ldots,IK}}{\sigma(L)}, \tag{4.10}$$

which is the considered entanglement metric. The experimental error $\sigma(L)$ is determined through error propagation of $\langle\hat{L}\rangle$, and we have,

$$\sigma(L) = \sqrt{\sum_{i,j=1}^{N} \left(\left[M^{ij}_{xx}\right]^2 \left[\sigma(C^{ji}_{xx}\right]^2 + \left[M^{ij}_{pp}\right]^2 \left[\sigma(C^{ji}_{pp}\right]^2\right)}, \tag{4.11}$$

where $\sigma(C^{ij}_{xx})$ and $\sigma(C^{ji}_{pp})$ are the experimental errors of the elements C^{ij}_{xx} and C^{ji}_{pp} in the corresponding covariance matrix; and the coefficient matrix M, associated to $\hat{L}$ in the gaussian case, is freely tuned to maximize the significance Σ in Equ. 4.10. The optimization is achieved with a genetic algorithm seen in the supplementary of [32].

We get $\sigma(C_{xx}^{ij})$ and $\sigma(C_{pp}^{ji})$ based on the Monte Carlo method. Firstly, we obtain the standard deviations from the experimental squeezing curves, as seen in Fig. 4.20. Then random numbers are generated corresponding to a gaussian distribution with the standard deviations. Using these random numbers, we get 1000 covariance matrix and finally get $\sigma(C_{xx}^{ij})$ and $\sigma(C_{pp}^{ji})$.

With the 10-mode covariance matrix of the SPOPO, the verified entanglement for all 115 974 possible partitions is sorted by the significance Σ [32], which is shown in Fig. 4.27. We can see, for all the partitions except one, which is no partition, all the 10 bands, the significance are all below the classical limit, and the distance is the defined by Equ. 4.10.

Consequently, the SPOPO exhibits full multipartite entanglement for all the partitions [32]. Importantly, the currently employed criterion was able to identify entanglement not recognizable with traditional separability metrics. The present approach allows for the identification of partially and fully entangled states for applications in quantum communication or cluster state computation.

Part II

Quantum Network

Chapter 5

Continuous-variable cluster states

Contents

Cluster states are the quantum resources for measurement based quantum computing [38], where quantum operations can be implemented via one-way measurement processes. Measurement based quantum computing, using clusters states and feed-forward strategy, has both continuous variable and discrete regimes implementations. In discrete regime, it is directly non-gaussian which can not be simulated by classical computers, however it is probabilistic and difficult to scale [6] [40] [95]; in continuous variable regime, it is deterministic to scale based on squeezed states and homodyne detection [29]. However, such as squeezer, controller-z gate, and homodyne are all gaussian operations on the coherent gaussian states, therefore to manipulate non-gaussian quantum computing, non-gaussian operations still need be developed to give non-trivial feed-forward in measurement processes [56] .

In this chapter, we will present the definition and generation of cluster states in continuous variable regime via using multimode squeezing.

5.1 Cluster states in CV

Conventionally, cluster states are expressed in the Schrödinger picture, evolving a set of infinitely squeezed states $|0\rangle_p^{\otimes N}$, where p indicates it is squeezed

on the phase quadrature. And in this section, we use $\hat{q}$ and $\hat{p}$ to represent the amplitude and phase quadrature operators, respectively.

Definition of a cluster state: any state that is obtained from a set of N infinitely squeezed states, applying C_z interactions, i.e. the two-mode controlled-Z gate $e^{\frac{i}{2}\hat{q}\times\hat{q}}$,

$$|\psi_{\mathrm{V}}\rangle = \hat{C}_{\mathrm{Z}}\left[V\right]|0\rangle_p^{\otimes N} = \prod_{j,k}^{N} e^{\frac{i}{2}V_{jk}\hat{q}_j\hat{q}_k}|0\rangle_p^{\otimes N} = e^{\frac{i}{2}\hat{q}^T V\hat{q}}|0\rangle_p^{\otimes N}, \tag{5.1}$$

where the $N \times N$ adjacency matrix V is real, and symmetric, in our case composed of 0 and 1. When the element V_{jk} is 1, the nodes j and k are correlated, corresponding to neighboring nodes in the graphic representation of the cluster states; when the element V_{jk} is 0, it refers to nodes which are not connected in the cluster. An example is shown in Fig. 5.1.

To describe *nullifiers* of cluster states, here we introduce an operator called a "stabilizer", which is defined: If an operator $\hat{K}$ satisfies for a state $|\phi\rangle$,

$$\hat{K}|\phi\rangle = |\phi\rangle, \tag{5.2}$$

we call it a *stabilizer* for a state $|\phi\rangle$.

The stabilizer of infinite squeezing is the displacement operator $\hat{X}(S)$,

$$\hat{X}(S)|0\rangle_p = e^{-is\hat{p}}|0\rangle_p = |0\rangle_p \ \forall_s. \tag{5.3}$$

And applying a C_z operation on the above equation, we obtain,

$$C_z\hat{X}(S)C_z^\dagger\left(C_z|0\rangle_p^{\otimes N}\right) = C_z|0\rangle_p^{\otimes N}, \tag{5.4}$$

thus we can obtain that the cluster state is stabilized by the set $\{K_i\}$,

$$\begin{aligned}
\hat{K}_i(s) &= \hat{C}_{\mathrm{Z}}\left[V\right]X_i(s)\hat{C}_{\mathrm{Z}}\left[V\right]^\dagger \\
&= e^{\frac{i}{2}\hat{q}^T V\hat{q}}X_i(s)e^{-\frac{i}{2}\hat{q}^T V\hat{q}} \\
&= \left(\prod_{j,k} e^{\frac{i}{2}V_{jk}\hat{q}_j\hat{q}_k}\right)e^{-is\hat{p}_i}\left(\prod_{l,m} e^{-\frac{i}{2}V_{l,m}\hat{q}_l\hat{q}_m}\right)
\end{aligned} \tag{5.5}$$

Using such as

$$e^{i\hat{q}_1\hat{q}_2}\hat{p}_1 e^{-i\hat{q}_1\hat{q}_2} = \hat{p}_1 - \hat{q}_2, \tag{5.6}$$

we calculate the stabilizer for a cluster state, and finally get,

$$\hat{K}_i(s) = e^{-is\hat{p}_i}\prod_{k\in\mathrm{neig(i)}} V_{i,k}e^{is\hat{q}_k} = X_i(s)\prod_{k\in\mathrm{neig(i)}} V_{i,k}Z_k(s), \tag{5.7}$$

where we simplify the calculation by using the symmetric property of the adjacency matrix, and k is related to the neighboring nodes of node i.

In the above equations, the set of stabilizers $\{\hat{K}_i\}$ is formally equivalent to its analog in the discrete case. One can demonstrate that $\{\hat{K}_i\}$ form a *Lie group*, whose generator $\hat{H}_i$ is defined by the derivative of stabilizers versus the parameter s. By the definition of the generator, we have $\hat{K}_i = e^{-is\hat{H}_i}$, and $\hat{H}_i = i\left(\frac{\mathrm{d}\hat{K}_i}{\mathrm{d}s}\right)_{s=0}$.

As when the parameter s is a small real displacement, we can express the stabilizer as the Taylor expansion only with the zero and first orders, $K_i(s) = \mathcal{I}_i + s\frac{\mathrm{d}K_i}{\mathrm{d}s}$, therefore, we have,

$$\left(\mathcal{I}_i + s\frac{\mathrm{d}\hat{K}_i}{\mathrm{d}s}\right)|\psi_V\rangle = |\psi_V\rangle + s\frac{\mathrm{d}\hat{K}_i}{\mathrm{d}s}|\psi_V\rangle \tag{5.8}$$

thus, according to the definition of the stabilizer, we have,

$$\frac{\mathrm{d}\hat{K}_i}{\mathrm{d}s}|\psi_V\rangle = 0 \tag{5.9}$$

and we obtain,

$$\hat{H}_i|\psi_V\rangle = 0 \ \forall_i. \tag{5.10}$$

Here $\hat{H}_i$ is called the **nullifiers** for the cluster state $|\psi_{\mathrm{V}}\rangle$,

$$\begin{aligned} H_i &= i\left(\frac{\mathrm{d}\hat{K}_i}{\mathrm{d}s}\right)_{(s=0)} = i\frac{\mathrm{d}}{\mathrm{d}s}\left[e^{-is\hat{p}_i}\prod_k V_{i,k}e^{is\hat{q}_k}\right]_{s=0} \\ &= i\left[-i\hat{p}_i e^{-is\hat{p}_i}\prod_k V_{i,k}e^{is\hat{q}_k} + e^{-is\hat{p}_i}\frac{\mathrm{d}}{\mathrm{d}s}\prod_k V_{i,k}e^{is\hat{q}_k}\right]_{s=0} \\ &= \hat{p}_i + i\left[e^{-is\hat{p}_i}\sum_k V_{i,k}i\hat{q}_k\prod_l e^{is\hat{q}_l}\right]_{s=0} \\ &= \hat{p}_i - \sum_k V_{i,k}\hat{q}_k. \end{aligned} \tag{5.11}$$

And this obeys,

$$\left(\hat{p}_i - \sum_k V_{i,k}\hat{q}_k\right)|\psi_V\rangle = 0. \tag{5.12}$$

Then it gives that the corresponding variances are zero directly,

$$\Delta^2\left(\hat{p}_i - \sum_k V_{i,k}\hat{q}_k\right) = \langle\psi_V|\left(\hat{p}_i - \sum_k V_{i,k}\hat{q}_k\right)^2|\psi_V\rangle = 0. \tag{5.13}$$

Here each nullifier is a linear combination of quadrature operators of the corresponding cluster nodes. In practice, the variance of nullifiers can be used as **the criteria of clusters states**: the corresponding state $|\psi_V\rangle$ is a cluster state, with a graph of adjacency matrix V, if all the nullifiers are squeezed, and when the squeezing used to construct the cluster state goes to infinite squeezing, the variances of nullifiers should be 0.

5.2 Cluster states with squeezed states and linear optics

We can construct a cluster state using a symplectic transform acting on a set of squeezed states. The symplectic matrix of the cluster sate with a adjacent matrix V, which is a transform from infinitely squeezing basis $\vec{a}_{\text{sqz}} = \left(\vec{a}_{\text{sqz}}, \vec{a}^{\dagger}_{\text{sqz}}\right)^{\text{T}} = \left(\hat{a}_{\text{sqz1}}, \hat{a}_{\text{sqz}}, ..., \hat{a}^{\dagger}_{\text{sqz1}}, \hat{a}^{\dagger}_{\text{sqz2}}, ...\right)^{\text{T}}$ to the target cluster state $\vec{a}_{\text{cluV}} = \left(\vec{a}_{\text{cluV}}, \vec{a}^{\dagger}_{\text{cluV}}\right)^{\text{T}} = \left(\hat{a}_{\text{cluV1}}, \hat{a}_{\text{cluV2}}, ..., \hat{a}^{\dagger}_{\text{cluV1}}, \hat{a}^{\dagger}_{\text{cluV2}}, ...\right)^{\text{T}}$, in Heisenberg picture, is given as below [53],

$$\vec{a}_{\text{cluV}} = S \cdot \vec{a}_{\text{sqz}} \quad \text{and,} \quad S = \begin{pmatrix} I & 0 \\ V & I \end{pmatrix}. \tag{5.14}$$

It is easy to see, from the above equation, that $\vec{a}_{\text{cluV}}$ satifies the nullifier criteria in Equ. 5.12. This associated transformations in the quadrature representation, including on-line non-linear operations, are not easy to be implemented experimentally.

Alternatively, according to Bloch Messiah reduction theorem [10], the same cluster state $\vec{a}_{\text{cluV}}$ can be generated, experimentally, by applying to infinite off-line squeezers the symplectic matrix composed of a unitary transform,

$$\vec{a}_{\text{cluV}} = S_U \cdot \vec{a}_{\text{sqz}} \quad \text{and,} \quad S_U = \begin{pmatrix} U & 0 \\ 0 & U^* \end{pmatrix}, \tag{5.15}$$

where U is the corresponding unitary transform acting on a set of squeezers squeezed in the phase quadrature $\hat{p}$, $\vec{a}^{\text{sqz}} = (\hat{a}^{\text{sqz1}}, \hat{a}^{\text{sqz2}}, ...)^{\text{T}}$, and we have,

$$\vec{a}^{\text{cluster}} = U\vec{a}^{\text{sqz}}, \tag{5.16}$$

With a given graph corresponding to an adjacency matrix V, the unitary matrix of a cluster state can be written,

$$U_{\text{cluster}} = U_V = X + iY \quad \text{and} \quad \vec{a}^{\text{cluster}} = U_{\text{cluster}}\vec{a}^{\text{sqz}}, \tag{5.17}$$

where X and Y are the real and imaginary part of the unitary transform, respectively. In the following, we will introduce the properties of U_V and the method we developed how to calculate from the adjacency matrix V.

According to Equ. 2.34, let us consider a set of orthogonal modes of coherent states, with quadrature operators $\vec{x}^{(0)} = \left(\hat{x}_1^{(0)}, ..., \hat{x}_N^{(0)}\right)$ and $\vec{p}^{(0)} = \left(\hat{p}_1^{(0)}, ..., \hat{p}_N^{(0)}\right)$, thus Equ. 5.17 can be rewritten in the symplectic matrices:

$$\begin{aligned}\begin{pmatrix} \vec{x'} \\ \vec{p'} \end{pmatrix} &= \begin{pmatrix} X_V & -Y_V \\ Y_V & X_V \end{pmatrix} \begin{pmatrix} K_\mathrm{x} & 0 \\ 0 & K_\mathrm{p} \end{pmatrix} \begin{pmatrix} \vec{x}^{(0)} \\ \vec{p}^{(0)} \end{pmatrix} \\ &= \begin{pmatrix} X_V K_\mathrm{x} \vec{x}^{(0)} - Y_V K_\mathrm{p} \vec{p}^{(0)} \\ Y_V K_\mathrm{x} \vec{x}^{(0)} + X_V K_\mathrm{p} \vec{p}^{(0)} \end{pmatrix}, \end{aligned} \tag{5.18}$$

where $\begin{pmatrix} \vec{x}^{squ} \\ \vec{p}^{squ} \end{pmatrix} = K = \begin{pmatrix} K_\mathrm{x} & 0 \\ 0 & K_\mathrm{p} \end{pmatrix} \begin{pmatrix} \vec{x}^{(0)} \\ \vec{p}^{(0)} \end{pmatrix}$, and K is the diagonal matrix representing the squeezing operation on each mode, defined in Equ. 2.62. It is important to note that here we assume all the modes are squeezed in the phase quadrature $\hat{p}$, so $K_\mathrm{p} \to 0$.

According to the definition of cluster states in Equ. 5.17 and the criteria of nullifiers in Equ. 5.13, we have:

$$\begin{aligned}\vec{p'} - V\vec{x'} = &\left(Y_V K_\mathrm{x} \vec{x}^{(0)} + X_V K_\mathrm{p} \vec{p}^{(0)}\right) \\ &-V\left(X_V K_\mathrm{x} \vec{x}^{(0)} - Y_V K_\mathrm{p} \vec{p}^{(0)}\right) \to 0, \end{aligned} \tag{5.19}$$

which leads,

$$\left(Y_V - V X_V\right) K_\mathrm{x} \to 0 \Rightarrow \left(Y_V - V X_V\right) = 0, \tag{5.20}$$

and

$$\left(Y_V + V X_V\right) K_\mathrm{p} \to 0. \tag{5.21}$$

Form above two relations, we see the physical interpretation of cluster unitary transform U_cluster, which satisfies Equ.5.20 and gives an *excess noise* because of finite squeezing. This excess noise is equal to the variances of corresponding nullifiers:

$$\Delta^2 \left(\hat{p}_i - \sum_k V_{i,k} \hat{q}_k\right) = \left[(X_V + V Y_V) K_\mathrm{p} (X_V + V Y_V)^T\right]_i. \tag{5.22}$$

Next, we seek an explicit and analytical expression for the unitary transform satisfying Equ. 5.20. The $\left(\vec{x}^\mathrm{C}, \vec{p}^\mathrm{C}\right)^T$ is a set of quadrature operators of corresponding cluster states,

$$\begin{pmatrix} \vec{x}^\mathrm{C} \\ \vec{p}^\mathrm{C} \end{pmatrix} = \begin{pmatrix} X_V & -Y_V \\ Y_V & X_V \end{pmatrix} \begin{pmatrix} \vec{x}^{squ} \\ \vec{p}^{squ} \end{pmatrix}. \tag{5.23}$$

As it is symplectic, it must satisfy,

$$XX^T + YY^T = \mathcal{I}, \tag{5.24}$$

$$XY^T = YX^T. \tag{5.25}$$

With the equations 5.20 and 5.24, we obtain,

$$XX^T = (V^2 + \mathcal{I}). \tag{5.26}$$

Thus, we can get the symmetric solution $X_s = X_s^T$,

$$X_s = (V^2 + \mathcal{I})^{-1/2}. \tag{5.27}$$

With Equ. 5.20 again, we get,

$$Y_s = V(V^2 + \mathcal{I})^{-1/2}. \tag{5.28}$$

Then we get the corresponding unitary transform from the above symmetric solutions $U_{Vs} = U_{Vs}^T$,

$$U_{Vs} = (\mathcal{I} + iV)(V^2 + \mathcal{I})^{-1/2}. \tag{5.29}$$

To be general, notice that if X_s and Y_s satisfy Equ. 5.20, with arbitrary real orthogonal matrix $\mathcal{O}$, $X = X_s\mathcal{O}$ and $Y = Y_s\mathcal{O}$ are also a solution of Equ. 5.20. Therefore, we give the general solution for the unitary matrix generating a cluster state with graph V (also called adjacent matrix), as below,

$$U_V(\vec{\theta}) = (\mathcal{I} + iV)(V^2 + \mathcal{I})^{-1/2}\mathcal{O}(\vec{\theta}), \tag{5.30}$$

where we use $\vec{\theta}$, which is the angle of orthogonal matrix $\mathcal{O}$, to replace the subscript "s". Importantly, the $N \times N$ matrix $\mathcal{O}$ is a linear operation of rotating basis, containing $N(N-1)/2$ degrees of freedom, and can be chosen, e.g., as Euler or Taint-Bryan angles.

From Equ. 5.30, as the orthogonal matrix $\mathcal{O}$ is not fixed, for a specific graph corresponding a adjacent matrix V, many solutions of unitary transforms exist. When the squeezers have identical squeezing, the nullifiers are not dependent on $\mathcal{O}$, but only upon the adjacent matrix V. However, when the squeezers have different squeezing, e.g. the supermodes of the SPOPO, there is an optimized orthogonal matrix $\mathcal{O}$ with a a adjacent matrix V. Thus it is possible to run a searching algorithm [71] to find an $\mathcal{O}$ matrix that, e.g., allows us to minimize the nullifiers [31].

Figure 5.1: The graph of the four-node-line-shape cluster. The circles represent the nodes of the cluster; the lines between two nodes correspond to the quantum correlations, and this is referred to $V_{ij} = 1$ in the adjacency matrix.

Here we give an example how to parametrize $\mathcal{O}$. For a line four mode cluster state, from Equ. 5.30, the symmetry solution is the product of six rotation transforms,

$$U_{4linS} = \begin{pmatrix} \frac{5}{6} & -\frac{1}{6} & \frac{i}{2} & -\frac{1}{6} \\ -\frac{1}{6} & \frac{5}{6} & \frac{i}{2} & -\frac{1}{6} \\ \frac{i}{2} & \frac{i}{2} & \frac{1}{2} & \frac{i}{2} \\ -\frac{1}{6} & -\frac{1}{6} & \frac{i}{2} & \frac{5}{6} \end{pmatrix} \quad \text{and,} \quad V_{4lin} = \begin{pmatrix} 0 & 1 & 0 & 0 \\ 1 & 0 & 1 & 0 \\ 0 & 1 & 0 & 1 \\ 0 & 0 & 1 & 0 \end{pmatrix}, \tag{5.31}$$

where the adjacency matrix V_{4lin} corresponds to the graph in Fig. 5.1.

Then, the 4-mode orthogonal matrix $\mathcal{O}_{4mode}(\theta_1, \theta_2, \theta_3, \theta_4, \theta_5, \theta_6)$ is,

$$\begin{pmatrix} \cos(\theta_1) & -\sin(\theta_1) & 0 & 0 \\ \sin(\theta_1) & \cos(\theta_1) & 0 & 0 \\ 0 & 0 & 1 & 0 \\ 0 & 0 & 0 & 1 \end{pmatrix} \cdot \begin{pmatrix} \cos(\theta_2) & 0 & -\sin(\theta_2) & 0 \\ 0 & 1 & 0 & 0 \\ \sin(\theta_2) & 0 & \cos(\theta_2) & 0 \\ 0 & 0 & 0 & 1 \end{pmatrix}$$
$$\cdot \begin{pmatrix} \cos(\theta_3) & 0 & 0 & -\sin(\theta_3) \\ 0 & 1 & 0 & 0 \\ 0 & 0 & 1 & 0 \\ \sin(\theta_3) & 0 & 0 & \cos(\theta_3) \end{pmatrix} \cdot \begin{pmatrix} 1 & 0 & 0 & 0 \\ 0 & \cos(\theta_4) & -\sin(\theta_4) & 0 \\ 0 & \sin(\theta_4) & \cos(\theta_4) & 0 \\ 0 & 0 & 0 & 1 \end{pmatrix}$$
$$\cdot \begin{pmatrix} 1 & 0 & 0 & 0 \\ 0 & \cos(\theta_5) & 0 & -\sin(\theta_5) \\ 0 & 0 & 1 & 0 \\ 0 & \sin(\theta_5) & 0 & \cos(\theta_5) \end{pmatrix} \cdot \begin{pmatrix} 1 & 0 & 0 & 0 \\ 0 & 1 & 0 & 0 \\ 0 & 0 & \cos(\theta_6) & -\sin(\theta_6) \\ 0 & 0 & \sin(\theta_6) & \cos(\theta_6) \end{pmatrix} \tag{5.32}$$

Thus, the general expression for a four mode line cluster state is $U_{4lin} = U_{4linS}.\mathcal{O}_{4mode}$, which is function with 6 variables, $\theta_1, \theta_2, \theta_3, \theta_4, \theta_5, \theta_6$.

Here we can extend to higher dimension of cluster states based the above example, which gives the avenue to do further optimization using a searching algorithm [31].

5.3 Generating cluster states with OPOs

Previously, we theoretically proved continuous-variable cluster networks can be generated using linear optics and many squeezers, which is also imple-

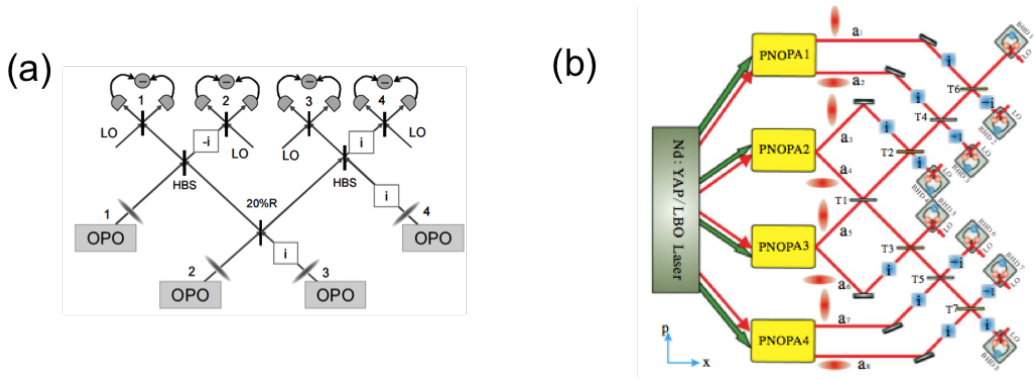

Figure 5.2: The generation of cluster states using linear optics and squeezers. (a) A four-mode line cluster states [99]; (b) A eight-mode line cluster state [86].

mented experimentally, [85], [99]. As seen in Fig. 5.2, a four-mode and a eight-mode cluster states generated.

In the generation of cluster states, in Fig. 5.2, in order the realizer the unitary transform U_V of Equ. 5.30, both employ linear optical network (unitary), composed of optical beam splitters and phasers, acting on the independent squeezers (OPOs).

Therefore, we conclude that any clusters state can generated via a specific unitary transform, a linear optical networks, and an array of squeezers. However, with this method, we have to build different optical architectures for different networks, which lacks scalability and flexibility.

In next chapter, we will present a scalable way of generating clusters, with multimode squeezing from the SPOPO.

Chapter 6

Simulating quantum networks via pulse shaping

Contents

Multimode squeezing is an important resource for the design and fabrication of quantum networks, which play a central role in quantum information processing and quantum metrology. For complex and practical tasks, however, multimode entanglement is required, where many quantum modes are entangled and form a so-called quantum network [44]. Modes are then called nodes, which are the fundamental information carriers, and these nodes are interconnected with a series of channels through which the information flows.

Traditionally, multimode entanglement is thought as a many-body properties, where each node is physically separated from the other and can be measured independently. However, now, many squeezed supermodes copropagate together, and the network is being constructed via the measurement process, in a spirit closely related to measurement based quantum computing (MBQC) [54].

In this chapter, we will present a scalable way of generating quantum networks via measurement processes, with a multimode resource, the SPOPO.

6.1 EPR network via pulse shaping

Before going to complex quantum networks, we show a new way, with the SPOPO, how to realize EPR correlation via pulse shaping. EPR state is a typical, and simplest quantum network, which usually contains two modes. Traditionally, in continuous variable regime, we can generate EPR network via the process, as seen in Fig. 6.1: two squeezers are mixed with a balanced beam splitter, and the two outputs are the sum and difference of the input squeezed modes [61].

Here, as seen in Fig. 6.1, we realize EPR entanglement via a different way, shaping the local oscillator in the homodyne detection, instead of using a beam splitter. To implement the function of the beam splitter, making a difference and sum of the input squeezed modes, we shape the pulse shapes of the local oscillator onto the difference and sum modes, and with a multimode resource, homodyne detection accesses the noises of corresponding EPR modes.

We shape the local oscillator using the SLM, and the principle is explained in Chapter 4. For instance, the shape in top left in Fig. 6.1, the blue and the red parts are refering to a amplitude modulation of 1 and a phase modulation of 0 and π, respectively, as seen in Fig. 4.17.

For the multimode quantum resource, the SPOPO, as seen in Fig. 6.1, the left two modes with the specific spectral shapes, similar to the first and the second supermodes, are independently squeezed; on the right side, the two modes with the blue and red shapes are the sum and difference modes, respectively.

Using the mode-dependent homodyne detection, in Equ. 4.5, therefore, in practice we checked the EPR witness by shaping the local oscillator onto the corresponding shapes. The quantum noises are, via homodyne detection, presented in Fig. 6.2, where the individual EPR modes have only the excess noises, and strong correlations (squeezing) are observed in the sum and difference shapes.

In addition, we checked the measurements with EPR-like criteria[22] [68],

$$\begin{aligned} \Delta^2 x_{\mathrm{R|B}} \cdot \Delta^2 p_{\mathrm{R|B}} &\simeq 0.59 < 1, \\ \langle (\hat{x}_{\mathrm{R+B}})^2 \rangle + \langle (\hat{p}_{\mathrm{R-B}})^2 \rangle &\simeq 0.48 < 1, \end{aligned} \tag{6.1}$$

where $\Delta^2 x_{\mathrm{R|B}}$ and $\Delta^2 p_{\mathrm{R|B}}$ are conditional variances. Thus the two modes of blue and red spectral bands are EPR entangled. More possibilities of EPR and Duan entanglement are included in the SPOPO [70].

Above, we presented a new method, with the SPOPO, how to generate EPR correlation network via ultrafast pulse shaping. Here, we can access

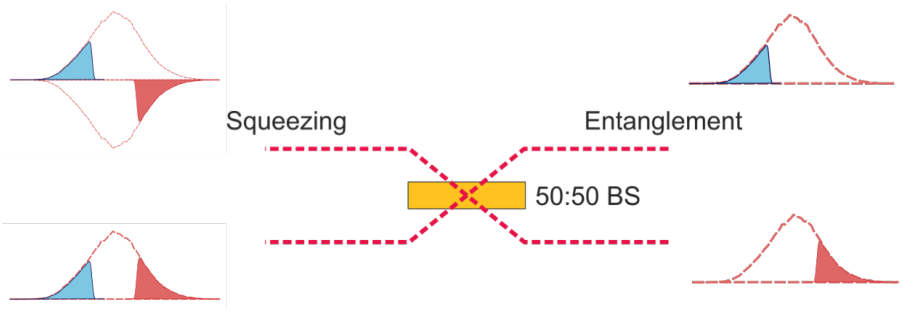

Figure 6.1: EPR generation via mixing squeezing with an optical beam splitter. Two squeezers are mixed with a half beam splitter, and the two outputs are the sum and difference of the input squeezed modes.

EPR entanglement without the beam splitter, as seen in Fig. 6.1, yet we realize the same physics, making difference and sum of the two squeezed modes. Both ways, the beam splitter and pulse shaping of the local oscillator, are equivalent to a basis change on the quantum resource, which we discussed in Chapter 2. Differently, the way of pulse shaping onto the local oscillator can not spatially separate the EPR modes with homodyne detection, however it supplies a new avenue to interrogate the noise property of multimode quantum resource in an arbitrarily shaped mode.

The advantage of the new way via pulse shaping, is that we can realize any basis change within the same photonics construction, but the conventional way to do so, using beam splitters and linear optics, as we mentioned in Chapter 5.3, has to change the optical networks for a different basis change, which lacks scalability.

Above all, we can access complex quantum networks, via projective measurements using multimode resource, and in next section, we will introduce, with multimode quantum resource, how to simulate arbitrary gaussian quantum networks via measurement processes.

6.2 Simulating quantum networks with SPOPO

Quantum network, conventionally, with multimode entanglement, may be fashioned by applying a unitary transformation U_{net} on many independent squeezers[85]. A quantum network can be described as below,

$$\vec{a}^{\,\text{net}} = U_{\text{net}} \cdot \vec{a}^{\,\text{psqz}} \tag{6.2}$$

where, $\vec{a}^{\,\text{psqz}}$ and $\vec{a}^{\,\text{net}}$ represent many squeezers and nodes of the quantum network, respectively. For instance, for cluster networks, U_{net} is the one of

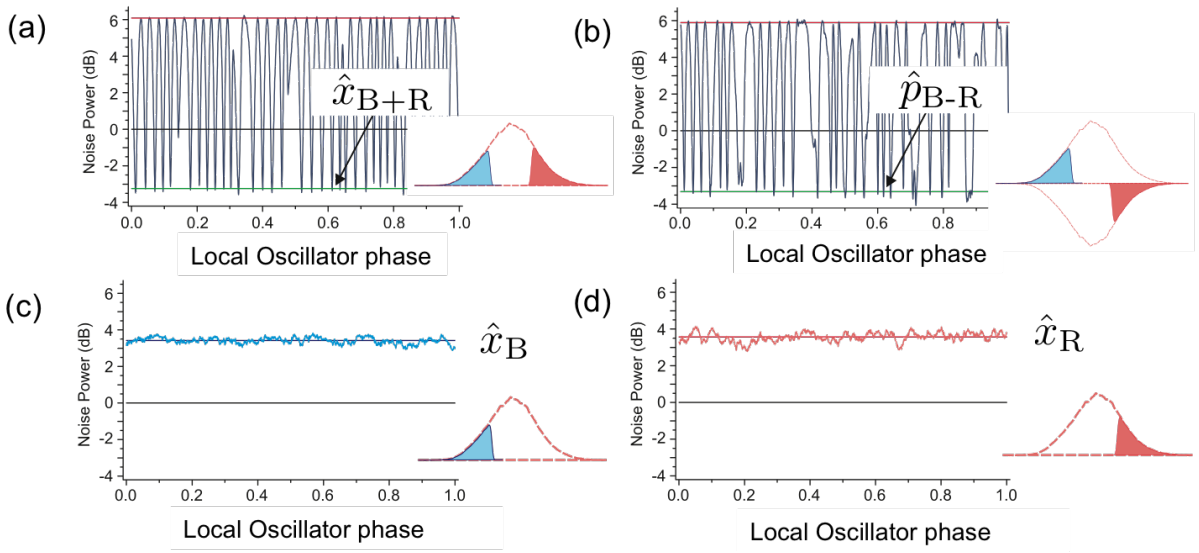

Figure 6.2: EPR witness via pulse shaping.

cluster unitary transform of Equ. 5.30.

In our case, let us call $\vec{a}^{\,\mathrm{sqz}} = (\hat{a}_1^{\mathrm{sqz}}, ..., \hat{a}_{16}^{\mathrm{sqz}})$ the annihilation operators associated to the eigenmodes of the light source. They can be constructed from the frequency band annihilation operators $\vec{a}^{\,\mathrm{pix}} = (\hat{a}_1^{\mathrm{pix}}, ..., \hat{a}_{16}^{\mathrm{pix}})$ through the matrix containing the covariance matrix eigenvectors U_{sqz}, such that $\vec{a}^{\,\mathrm{sqz}} = U_{\mathrm{sqz}}\, \vec{a}^{\,\mathrm{pix}}$, which is fully equivalent a basis change form frequency-band basis to squeezing basis. Among these 16 eigenmodes, the first 12 are the squeezed ones as represented in figure 4.23 , and are the ones we will consider to construct a quantum network. The squeezed quadratures of these modes alternate, from amplitude to phase. In order to simplify the description of the network we introduce the diagonal matrix $\Delta_{\mathrm{FT}} = \mathrm{diag}\{0, i, ..., 0, i\}$ so that $\vec{a}^{\,\mathrm{sqz}} = \Delta_{\mathrm{FT}}\, \vec{a}^{\,\mathrm{psqz}}$ where $\vec{a}^{\,\mathrm{psqz}}$ are the annihilation operators corresponding to the same modes but now phase shifted in order to all be squeezed on the p quadrature. Then the quantum network construction, starting from the frequency band basis, can be written as below,

$$\vec{a}^{\,\mathrm{net}} = U_{\mathrm{net}}\, \Delta_{\mathrm{FT}}\, U_{\mathrm{sqz}}\, \vec{a}^{\,\mathrm{pix}} \tag{6.3}$$

Where, the product of $U_{\mathrm{net}}\, \Delta_{\mathrm{FT}}\, U_{\mathrm{sqz}}$, experimentally, is the total unitary transform, which can be realized by ultrafast pulse shaping to generate on-demand quantum networks.

As seen in Fig. 6.3, a desired basis change on the multimode state $\hat{\rho}$ can be achieved by customizing the local oscillator (LO). The desired basis change is realized by measurement processes, where homodyne detection ac-

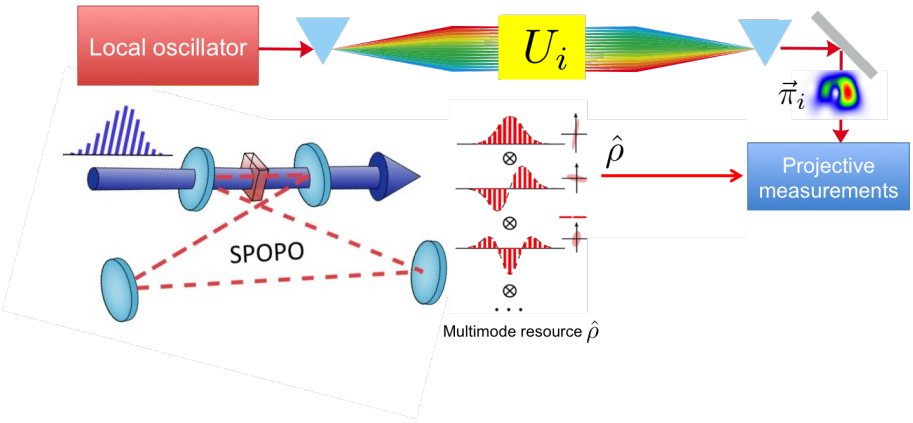

Figure 6.3: Actualizing quantum networks via measurement processes, where multimode state $\hat{\rho}$ of light is projected onto the desired mode $\vec{\pi}_i$. As the pules shape can be complex, which is represented with the corresponding *spectrogram*. The set of modes $\{\vec{\pi}_i\}$ is constructed with the total unitary transform, corresponding to U_{net} in Equ. 6.2.

tualizes the basis rotation by projecting the multimode state onto a LO that is adapted to be an arbitrary linear combination of the individual squeezed modes. Pulse shapes corresponding to such superpositions are readily generated with femtosecond pulse shaping methodologies, referring to Chapter 4. In this manner, the detection process emulates a linear optical network, and arbitrary Gaussian quantum networks may be synthesized simply be modifying the spectral detection basis.

Based on the principle in Equ. 6.3, we give an example of emulating a six mode cluster state, as seen in Fig. 6.4. Experimentally, in the basis of pixel modes $\vec{a}^{\text{pix}}$, we apply the product of corresponding unitary transforms $U_V\,\Delta_{\text{FT}}\,U_{\text{sqz}}$ on the SLM. Therefore, we can access the nodes of the cluster state via projecting the quantum resource onto the shaped local oscillator in homodyne detection, and the corresponding pulse shapes are represented in the form of spectrums, as seen in Fig. 6.4.

6.3 Witness of quantum networks

Appealed by measurement based quantum computing, here we simulate a series of different networks of cluster states defined in Equ. 5.17, and nullifiers of cluster states satisfy Equ. 5.13.

As each cluster node is represented as a superposition of the uncorrelated comb squeezers, it possesses a unique pulse shape. The cluster nullifiers,

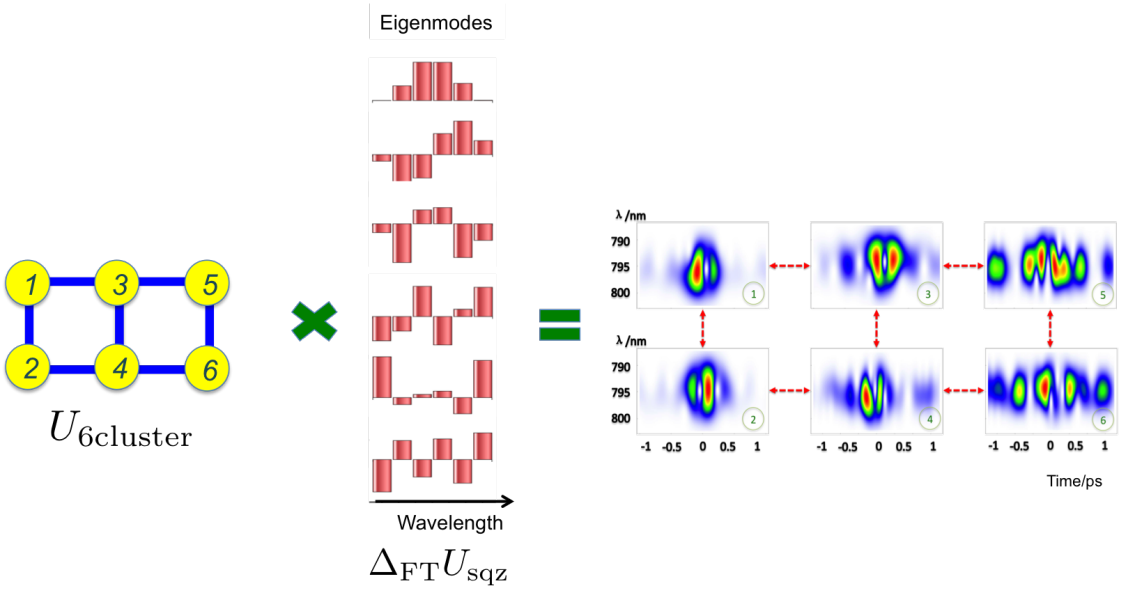

Figure 6.4: Generating a six mode cluster state via pulse shaping. The pulse shapes, for this six mode cluster state, are the product of the cluster transform $U_{6\text{cluster}}$, representing the cluster with the graph, and the p-squeezed eigenmodes $\Delta_{\text{FT}}U_{\text{sqz}}$. We represent the corresponding complex pulse shapes in the form of spectrograms. The shape of node i corresponds to U_{net_i}, the i^{th} colonum of U_{net}.

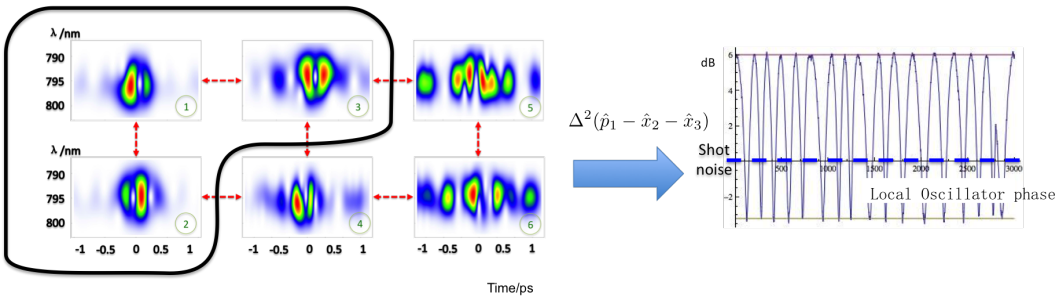

Figure 6.5: Witness of cluster states. For the simulated six mode cluster state, one of the nullifier modes is constructed by combining amplitude quadrature of node1 and phase quadrature of adjacent nodes 2 and 3. The noise of the nullifier mode is measured via homodyne detection. The noise of the nullifier is squeezed, which is below the shot noise limit (blue dashed line).

in Equ. 5.13, are superpositions of the individual cluster nodes, which also allow them to be directly constructed with the pulse shaper.

Thus, nullifiers can also be expressed into a series of modes, which can be shaped with the local oscillator. To characterize the clusters we simulate, from Equ. 6.3, we define nullifier modes in the quadrature representation,

$$\vec{\delta} = \begin{pmatrix} \vec{x}^{\text{nul}} \\ \vec{p}^{\text{nul}} \end{pmatrix} = (-V, \mathcal{I}) \begin{pmatrix} \vec{x}^{\text{net}} \\ \vec{p}^{\text{net}} \end{pmatrix} \tag{6.4}$$

where V is the adjacent matrix of the cluster state; $\vec{x}^{\text{net}} = \{\hat{x}_i^{\text{net}}\}$ and $\vec{p}^{\text{net}} = \{\hat{x}_i^{\text{net}}\}$ are the amplitude and phase quadrature operators of the cluster, $\vec{a}^{\text{net}} = \vec{x}^{\text{net}} + i\vec{p}^{\text{net}}$. In practice, we use the corresponding normalized nullifier modes $\{\hat{\delta}_i\}$ in the representation of the annihilation operators, then the nullifier mode related to the unitary transform can be obtained and applied to the SLM to shape the local oscillator.

For instance, in Fig. 6.5, for a six node cluster, the shape of node i corresponds to U_{net_i}, the i^{th} colonum of U_{net}. To measure the variance of the nullifier, we have the corresponding normalized nullifier mode 1, e.g. related to the combination $(U_{\text{net}_1} + iU_{\text{net}_2} + iU_{\text{net}_3})$, written on the shaper. Then via homodyne detection, the variances of the nullifiers are measured with the local oscillator shaped into specific pulse shapes.

According to Equ. 5.13, if all the nullifiers of the cluster state are squeezed,

$$\Delta^2(\hat{\delta}) \to 0, \tag{6.5}$$

it means we achieved simulating the corresponding cluster state. In practice, we did an optimization to get the unitary transform U_{net} which minimizes the variances of the nullifiers, which is presented in detail in Appendix 1. For the six-node cluster, we measured the variances of all the six nullifiers modes, which are all squeezed. Thus we can claim the cluster is achieved experimental. Each nullifier exhibits field fluctuations below the shot noise limit, which indicates that each node is entangled with its neighboring nodes.

Furthermore, a collection of other quantum networks from four up to twelve-node cluster states were also successfully fabricated utilizing this methodology. In Fig. 6.6 (a), versatile 4- and 6-node cluster networks are investigated, where the corresponding nullifier variances, which are constructed with suitable programming of the pulse shaper, are shown below each structure. Further the scalability is shown in the Fig. 6.6 (b), where from 4 to 12 node line and stair chain shape cluster states are exhibited. All of the nullifiers exhibit noise values below that of the 0 dB shot noise limit, which indicates successful creation of the various networks.

Interestingly, we found that, among different graphs of cluster states, the nullifier values are squeezing-source-dependent and cluster-dependent. Firstly as to the light source, the group of nullifiers for a given structure do not all possess the same variance, which is due to the non-uniform distribution of squeezing in the input qumodes, and the variances of nullifiers increases as the nodes number goes up because squeezing in high order of eigenmodes of the light source decreases, as seen in Fig. 6.6 (b). Secondly, the mean is approximately equal across the examine series, which indicates that the simulation of networks is decided by allocating the finite resources optimally. Besides and importantly, as to cluster graph property, when the same-number-of node graphs are with more neighboring connections, the nullifiers have lower mean variances. In Fig. 6.6 (a), the mean variance of nullifiers of the four-node square graph state is lower than line and T-shape graph, and also star graph six-node cluster state has lower variance than line-shape one, as well in Fig. 6.6 (b), all the stair-chain cluster states have bit lower variance than line shape ones.

It is important to note that the creation of these cluster structures does not necessitate any change of the optical architecture. Rather, the connectivity of the network structure is modified simply by varying the basis in which the state is detected. Given that an arbitrary, multimode Gaussian transformation of the squeezer set can be represented with a unitary matrix, a set of identifiable pulse shapes may be associated with the transformation output. In this manner, it is possible to directly probe any Gaussian entanglement criteria. The fact that each of these structures may be revealed by only modifying the measurement basis indicates that these networks are all implicitly embedded within the entanglement of the quantum comb.

6.4 Simulating a multipartite quantum secret sharing

Quantum secret sharing is a way sharing secret using a quantum correlation, which is secure and with better fidelity compared to classical method. Here we simulate a multipartite quantum secret sharing based on a six-mode linear optical network, which is the same as a unitary transform of the six-mode cluster, as seen the top right inset of Fig. 6.7. Node 1 to 5 are five receivers, at least three receivers together are able to recover the secret information encoded in the network, and the node 6 acts as a dealer, which need to be measured every time and send information to the three receivers who are sharing and reconstructing the secret [47] [52].

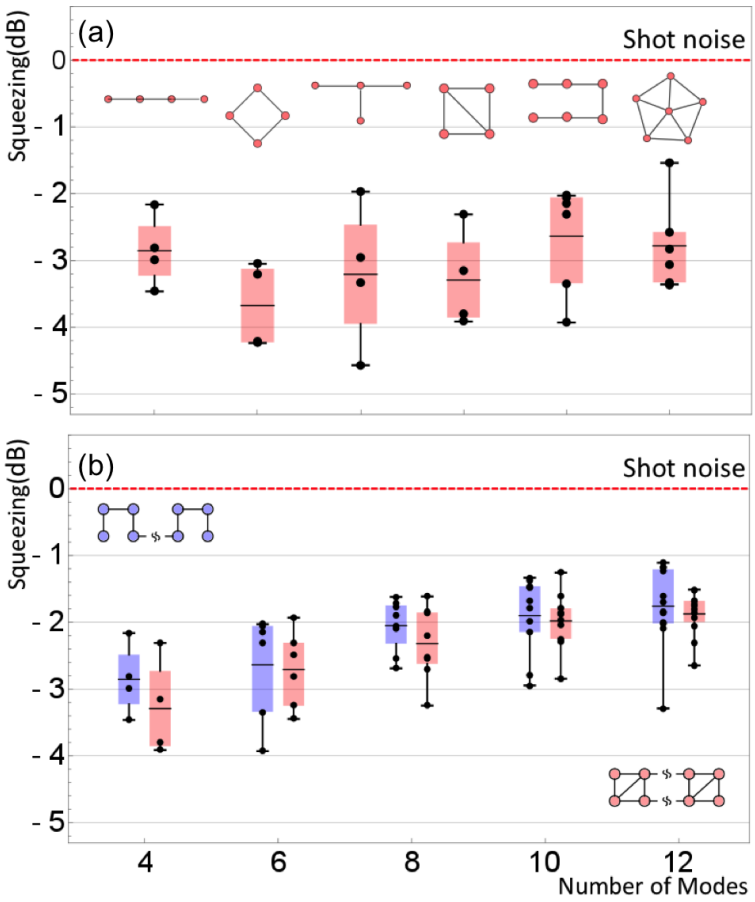

Figure 6.6: Witness of simulated clusters. The red lines represent the shot noise limit and the points in the boxwickers are mean squeezings of nullifiers. They are all below shot noise limit meaning achievements of all the simulated clusters states.

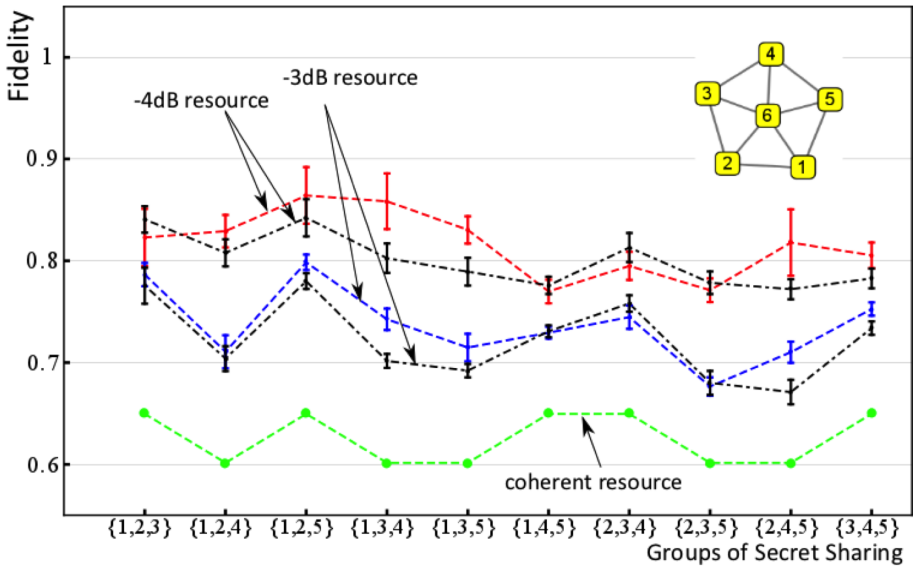

Figure 6.7: Fidelity of secret sharing. Up right inset is the graph of a simulated cluster state used for quantum secret sharing. Node 1 to 5 are receivers and node 6 is a dealer. The horizontal axis is consist of all 10 three-receiver sharing groups. Red and blue jointed points are respectively fidelities of reconstructed secret with a -4 dB and -3 dB squeezing resource respectively. The black curves are inferred from the individual squeezing of the eigenmodes. The green curve corresponds to fidelity using a coherent resource.

In our case, the states of the secret sharing network, $\vec{a}^{\text{secsh}}$, are constructed by the leading six eigenmodes of the SPOPO, $\vec{a}^{\text{secsh}} = U_{6\text{se}} \cdot \vec{a}_i^{\text{sqz}}$, as seen in Fig. 4.24, and the sixth eigenmode is used to carry classical secret information, $\hat{a}_6^{\text{sqz}} = \hat{a}_s$, thus, we have,

$$\begin{pmatrix} \hat{a}_1^{\text{cluster}} \\ \hat{a}_2^{\text{cluster}} \\ \hat{a}_3^{\text{cluster}} \\ \hat{a}_4^{\text{cluster}} \\ \hat{a}_5^{\text{cluster}} \\ \hat{a}_{6,\text{ dealer}}^{\text{cluster}} \end{pmatrix} = U_{6\text{se}} \cdot \begin{pmatrix} \hat{a}_1^{\text{sqz}} \\ \hat{a}_2^{\text{sqz}} \\ \hat{a}_3^{\text{sqz}} \\ \hat{a}_4^{\text{sqz}} \\ \hat{a}_5^{\text{sqz}} \\ \hat{a}_{\text{s}}^{\text{sqz}} \end{pmatrix}, \tag{6.6}$$

where the cluster matrix couples the five squeezers and the secret into a quantum network, and $U_{6\text{se}}$ is the same as the cluster unitary transform in Equ. 5.30. Differently from cluster states, the secret can be any gaussian state, and does not have to be squeezed. And this secret sharing network is constructed with same unitary transform as a six-node cluster, yet it doesn't have to be a cluster state. In particular, in the simulation of secret sharing, the secret is a squeezed vacuum.

As in practice the secret and the reconstructed secret are respectively two different modes, corresponding two different pulse shapes for our simulator, therefore, experimentally, we are able to tomography the gaussian sates of secret mode and reconstructed secret mode via homodyne detection with specific shaping local oscillator.

The relationship of reconstructed secret quadratures and secret quadratures are as below, which is an example of secret sharing revealed by the receivers 1, 2 and 3,

$$\hat{x}_{123} = \sum_{i=1}^{3} m_i \hat{x}^i + \sum_{j=1}^{3} n_i \hat{x}^j + \hat{p}^{\text{dealer}} = \hat{x}_s + \sum_{i=1}^{5} a_i \hat{p}_i^{\text{sqz}} \tag{6.7}$$

$$\hat{p}_{123} = \sum_{i=1}^{3} p_i \hat{x}^i + \sum_{j=1}^{3} q_i \hat{p}^j + \hat{P}^{\text{dealer}} = \hat{p}_s + \sum_{i=1}^{5} b_i \hat{p}_i^{\text{sqz}} \tag{6.8}$$

where $\hat{x}_{123}$ and $\hat{p}_{123}$ are the amplitude and phase quadratures of the reconstructed secret revealed via measuring the nodes 1, 2, and 3 of the corresponding cluster state, $\hat{a}_{123}^{\text{reS}} = \hat{x}_{123} + i\hat{p}_{123}$; $\hat{x}^i$, $\hat{p}^i$ and $\hat{p}^{dealer}$ are the amplitude and the phase quadratures of corresponding receiver nodes and phase quadrature of the dealer node respectively, $\hat{a}_i^{\text{secsh}} = \hat{x}^i + i\hat{p}^i$; $\{\hat{p}_i^{\text{sqz}}\}$ represent independently squeezed phase quadrature of eigenmodes which contribute excess noises, and $\hat{x}_s$, $\hat{p}_s$ are the secret amplitude and phase quadrature respectively. In the above equations 6.7 and 6.8, the reconstructed secret is

expressed in different basis, which are the basis of simulated cluster network and the squeezing basis of the quantum resource, the SPOPO. The detailed expressions for partitions of secret sharing are presented in Appendix 2.

In the simulation of secret sharing, we directly measure the reconstructed secret mode, which is referring to a pulse shape expressed in frequency-band basis, $\{\vec{a}^{\text{pix}}\}$ in Equ. 6.3, instead of measuring the nodes of cluster states individually [47]. Then we can obtain the state information of reconstructed secret and experimental fidelities. In the equations 6.7 and 6.8, it also suggests the quality of the secret reconstruction will depend on the level of the squeezing of the source, and will be perfectly rebuilt while increasing squeezing to infinite,

$$\hat{a}_{123}^{\text{reS}} \to \hat{a}_s, \quad \text{if} \quad \Delta^2(\hat{p}_i^{\text{sqz}}) \to 0. \tag{6.9}$$

Here, we give the fidelity [51] for two gaussian states,

$$\mathcal{F} = \frac{2}{\sqrt{A+B}-\sqrt{B}} \exp\left[-\alpha^T (V_1+V_2)^{-1}\alpha\right], \tag{6.10}$$

where V_1 and V_2 are the covariance matrix of two gaussain states. $A = det(V_1+V_2)$, $B = (detV_1 - 1)(detV_2 - 1)$, and α is the difference of the mean amplitudes of two gaussian states. When the secret is vacuum, $\alpha = 0$,

$$\mathcal{F} = \frac{2}{\sqrt{A+B}-\sqrt{B}}. \tag{6.11}$$

For secret sharing, the covariance matrix of the reconstructed secret and the secret are,

$$V_1 = V_{\text{reS}} = \begin{pmatrix} \Delta^2(\hat{x}_{\text{reS}}) & 0 \\ 0 & \Delta^2(\hat{p}_{\text{reS}}) \end{pmatrix} \quad \text{and,} \quad V_2 = V_s = \begin{pmatrix} \Delta^2(\hat{x}_s) & 0 \\ 0 & \Delta^2(\hat{p}_s) \end{pmatrix} \tag{6.12}$$

Experimentally, to calculate the fidelity, we measured the noises, in Equ. 6.12, via shaping the local oscillator onto the modes of reconstructed secret and the secret, which are expressed in the equations of 6.7 and 6.8. According to Equ. 6.11, we obtained the corresponding fidelities for all 10 partitions of secret sharing. In Fig. 6.7, the fidelities using the -4 dB (red curve), -3 dB (blue curve) quantum resource and coherent resource (green curve), are presented; for the quantum resource, according to the equations of 6.7 and 6.8, we also give the fidelities (black curves) inferred from the individual squeezing of the p-squeezed eigenmodes, $\hat{p}_i^{\text{sqz}}$. For a good simulator, the fidelities from the reconstructed secret mode should be similar to the inferred ones from the individual squeezing, which can be the reference to evaluate the simulator. As the eigenmodes are slightly different for phase

and amplitude quadratures, consequently, we have a deviation between the fidelity curves from directly reconstructed modes and individual squeezing of the eigenmodes (red and black, green and black). In principle, the deviation is from the purity of the multimode quantum state from the SPOPO, and we can improve it via reducing the loss in the generation and measurement process of the SPOPO.

In this quantum secret sharing simulation, it is shown both fidelities for measuring reconstructed secret modes and individual squeezings match well, which suggest the success of our quantum network simulating a quantum secret sharing process. Importantly, as the measurement mode of our simulator is on-demand, it gives a tremendous potential to simulate versatile MBQC protocols with the quantum network simulator.

6.5 Conclusion

In summary, versatility and scalability of an on-demand network simulation is presented, and also a multipartite quantum secret sharing in simulated based on a six-node cluster network. Instead of doing a lot of real optical network constructions, all of different simulated networks are achieved in the fixed setup, the simulator. Importantly, the simulation results can give a gaussian state information, such as nullifiers of cluster states, noise measurement of a gaussian state in an arbitrary pulse shape, experimental fidelity of a linear quantum gate and so on like what we did in this paper, exactly the same as measured in a real quantum network, but which is static.

All of simulations we did is because the discrete squeezers possess unique temporal or spectral mode patterns. This provides a unique opportunity for independently addressing them in a multimode beam. Then with spectral-selectivity in the detection process, which may be accomplished with pulse shaping, or more generally any variety of mode-dependent homodyne detection, allows the synthesis of any linear combination of the individual squeezed modes. In this manner, the detection process actualizes a basis change that emulates a linear optical network in a manner analogous to what has previously been implemented in the spatial domain [2]. Importantly, this does not necessitate a modification of the quantum resource, but only of the manner in which it is measured.

The limitation of this method is that all the quantum states co-propagate within the single beam. Yet for quantum computing, we need to control the nodes of quantum networks simultaneously, e.g. measurement-based quantum protocols [30]. To aim that, we will introduce multi-pixel homodyne detection to realize simultaneously detecting all the nodes of a network. In this

manner, any quantum control is implemented via measurement processes, and has no need to change the optical architecture. This fact suggests a tremendous flexibility when using femtosecond pulse trains as a basis for quantum networks.

6.6 Appendix 1: Optimization of cluster matrix

Based on Equ. 2.34, $S_{\rm net}$ is the sympletic form of the unitary matrix, $U_V\,\Delta_{\rm FT}\,U_{\rm sqz}$, in Equ. 6.2. For cluster states, the covariance matrix of the corresponding cluster state is,

$$V_{net} = S_{\rm net}^{\rm T} V_{\rm SPOPO} S_{\rm net}, \tag{6.13}$$

and from Equ. 2.34, the corresponding variances of the nullifiers are,

$$\Delta^2(\delta_i) = \vec{\delta_i}^{\rm T} V_{net} \vec{\delta_i}, \tag{6.14}$$

where $\vec{\delta_i}$ is the nullifier mode in Equ. 5.13.

Via parametrizing the $\mathcal{O}$ in U_V, we use a searching algorithm to optimize the sum of nullifier variances [31],

$$f(\theta_1, \theta_2, \dots,) = \sum_i \Delta^2(\delta_i). \tag{6.15}$$

With the solution of $\mathcal{O}(\theta_1, \theta_2, \dots,)$, we obtain the optimized unitary matrix U_V of cluster states.

6.7 Appendix 2: Reconstructed secret modes

For secret sharing, we present the six mode cluster matrix U_V in Euq.6.2, and the real part is,

$$\begin{pmatrix}
0.623367 & 0.00783019 & -0.137478 & -0.137478 & 0.00783019 & -0.0590805 \\
0.00783019 & 0.623367 & 0.00783019 & -0.137478 & -0.137478 & -0.0590805 \\
-0.137478 & 0.00783019 & 0.623367 & 0.00783019 & -0.137478 & -0.0590805 \\
-0.137478 & -0.137478 & 0.00783019 & 0.623367 & 0.00783019 & -0.0590805 \\
0.00783019 & -0.137478 & -0.137478 & 0.00783019 & 0.623367 & -0.0590805 \\
-0.0590805 & -0.0590805 & -0.0590805 & -0.0590805 & -0.0590805 & 0.482232
\end{pmatrix}, \tag{6.16}$$

and the corresponding imaginary part is,

$$\begin{pmatrix} -0.0434201 & 0.426808 & -0.188729 & -0.188729 & 0.426808 & 0.364071 \\ 0.426808 & -0.0434201 & 0.426808 & -0.188729 & -0.188729 & 0.364071 \\ -0.188729 & 0.426808 & -0.0434201 & 0.426808 & -0.188729 & 0.364071 \\ -0.188729 & -0.188729 & 0.426808 & -0.0434201 & 0.426808 & 0.364071 \\ 0.426808 & -0.188729 & -0.188729 & 0.426808 & -0.0434201 & 0.364071 \\ 0.364071 & 0.364071 & 0.364071 & 0.364071 & 0.364071 & -0.295403 \end{pmatrix}. \tag{6.17}$$

The reconstructed secret modes are,

$$\begin{aligned}
\hat{x}_{123} &= 0.696399\hat{p}_1 + 0.556742\hat{p}_2 + 0.696399\hat{p}_3 - 0.312492\hat{p}_4 - 0.312492\hat{p}_5 + \hat{x}_s \\
\hat{x}_{124} &= 1.56563\hat{p}_1 + 1.56563\hat{p}_2 - 0.312492\hat{p}_3 - 1.18173\hat{p}_4 - 0.312492\hat{p}_5 + \hat{x}_s \\
\hat{x}_{125} &= 0.556742\hat{p}_1 + 0.696399\hat{p}_2 - 0.312492\hat{p}_3 - 0.312492\hat{p}_4 + 0.696399\hat{p}_5 + \hat{x}_s \\
\hat{x}_{134} &= -1.18173\hat{p}_1 - 0.312492\hat{p}_2 + 1.56563\hat{p}_3 + 1.56563\hat{p}_4 - 0.312492\hat{p}_5 + \hat{x}_s \\
\hat{x}_{135} &= 1.56563\hat{p}_1 - 0.312492\hat{p}_2 - 1.18173\hat{p}_3 - 0.312492\hat{p}_4 + 1.56563\hat{p}_5 + \hat{x}_s \\
\hat{x}_{134} &= 0.696399\hat{p}_1 - 0.312492\hat{p}_2 - 0.312492\hat{p}_3 + 0.696399\hat{p}_4 + 0.556742\hat{p}_5 \ + \hat{x}_s \\
\hat{x}_{234} &= -0.312492\hat{p}_1 + 0.696399\hat{p}_2 + 0.556742\hat{p}_3 + 0.696399\hat{p}_4 - 0.312492\hat{p}_5 + \hat{x}_s \\
\hat{x}_{235} &= -0.312492\hat{p}_1 + 1.56563\hat{p}_2 + 1.56563\hat{p}_3 - 0.312492\hat{p}_4 - 1.18173\hat{p}_5 + \hat{x}_s \\
\hat{x}_{245} &= -0.312492\hat{p}_1 - 1.18173\hat{p}_2 - 0.312492\hat{p}_3 + 1.56563\hat{p}_4 + 1.56563\hat{p}_5 + \hat{x}_s \\
\hat{x}_{345} &= -0.312492\hat{p}_1 - 0.312492\hat{p}_2 + 0.696399\hat{p}_3 + 0.556742\hat{p}_4 + 0.696399\hat{p}_5 + \hat{x}_s \\
\hat{p}_{123} &= -0.717699\hat{p}_1 + 1.64001\hat{p}_2 - 0.717699\hat{p}_3 + 0.303388\hat{p}_4 + 0.303388\hat{p}_5 + \hat{p}_s \\
\hat{p}_{124} &= 0.618922\hat{p}_1 + 0.618922\hat{p}_2 + 0.303388\hat{p}_3 - 1.03323\hat{p}_4 + 0.303388\hat{p}_5 + \hat{p}_s \\
\hat{p}_{125} &= 1.64001\hat{p}_1 - 0.717699\hat{p}_2 + 0.303388\hat{p}_3 + 0.303388\hat{p}_4 - 0.717699\hat{p}_5 + \hat{p}_s \\
\hat{p}_{134} &= -1.03323\hat{p}_1 + 0.303388\hat{p}_2 + 0.618922\hat{p}_3 + 0.618922\hat{p}4 + 0.303388\hat{p}5 + \hat{p}_s \\
\hat{p}_{135} &= 0.618922\hat{p}_1 + 0.303388\hat{p}_2 - 1.03323\hat{p}_3 + 0.303388\hat{p}_4 + 0.618922\hat{p}_5 + \hat{p}_s \\
\hat{p}_{145} &= -0.717699\hat{p}_1 + 0.303388\hat{p}_2 + 0.303388\hat{p}_3 - 0.717699\hat{p}_4 + 1.64001\hat{p}_5 + \hat{p}_s \\
\hat{p}_{234} &= 0.303388\hat{p}_1 - 0.717699\hat{p}_2 + 1.64001\hat{p}_3 - 0.717699\hat{p}_4 + 0.303388\hat{p}_5 + \hat{p}_s \\
\hat{p}_{235} &= 0.303388\hat{p}_1 + 0.618922\hat{p}_2 + 0.618922\hat{p}_3 + 0.303388\hat{p}_4 - 1.03323\hat{p}_5 + \hat{p}_s \\
\hat{p}_{245} &= 0.303388\hat{p}_1 - 1.03323\hat{p}_2 + 0.303388\hat{p}_3 + 0.618922\hat{p}_4 + 0.618922\hat{p}_5 + \hat{p}_s \\
\hat{p}_{345} &= 0.303388\hat{p}_1 + 0.303388\hat{p}_2 - 0.717699\hat{p}_3 + 1.64001\hat{p}_4 - 0.717699\hat{p}_5 + \hat{p}_s
\end{aligned} \tag{6.18}$$

where $\hat{p}_i$ is the phase quadrature of node i in the secret sharing cluster, and $\hat{x}_s, \hat{p}_s$ are the amplitude and phase quadratures of the secret itself.

Part III

Multipixel-homodyne based Quantum Computing and Metrology

Chapter 7

Quantum computing with SPOPO

Contents

In previous chapters, we introduced an innovative method of realizing quantum networks, and it can simulate on-demand quantum networks via ultrafast pulse shaping. However, with the simulator, only one correlation with some specific mode can be accessed at one time. For quantum computing, such as measurement based quantum computing [67], it is required that entanglement of all the modes can be measured simultaneously, thus, all the correlations can be collected in real time among the measurement modes, which also can be controlled in real time to realize quantum computing. In this chapter we will introduce a new way of measuring multimode property of the quantum resource, *multi-pixel homodyne detection*, and its applications in quantum information processing and quantum metrology.

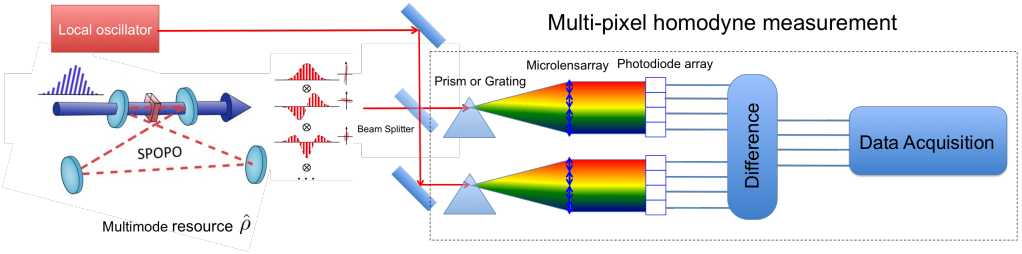

Figure 7.1: Multi-pixel homodyne detection. The signal and the local oscillator are mixed by a balance beam splitter; after the beam splitter, the two beams are dispersed by two prisms (or gratings) and focused on the Fourier plane, where two photodiode arrays are set to measure different colors of the beams, then we make differences between each color pairs; a multi-channel data acquisition system is employed. Besides, microlens arrays, in front of the photodiode arrays, are used to focus different spectral components in the corresponding pixel to avoid the loss induced by the gap between pixels on the photodiode arrays.

7.1 Multipixel homodyne detection

To realize the simultaneous detection of all the modes, *multi-pixel homodyne detection* is employed, whose scheme applied for the SPOPO is as seen in Fig. 7.1. Compared to the scheme of quantum network simulator in Fig. 6.3, we can see, here, in Fig. 7.1, the measurement part is replaced by the multi-pixel homodyne detection, while the quantum resource, the SPOPO, is still kept.

In the multi-pixel homodyne detection, as seen in Fig. 7.1, after the balance beam splitter, the two beams are dispersed by two prisms (or gratings) and focused on the Fourier plane, where two photodiode arrays are located to measure different color components of the beams, then we obtain the difference signals between each pixel pairs. Therefore, the multi-pixel homodyne detection is similar to many individual homodyne detections in the same time. The experimental set-up is as seen in Fig. 7.2. In practice, we used two gratings to disperse the input light horizontally, and the -1 order diffraction of the grating is focused by the microlens arrays and measured by the multipixel detector [1].

Here, in the multipixel homodyne detection, we assume the measurement basis is composed of the normalized pixel modes of the local oscillator $\{u_i\}$,

[1] As among the pixels of the photodiode array are gaps, which introduce a loss for measuring the light. The microlens array can focus each color component in the center of each pixel without loss because of the gaps in the photodiode array

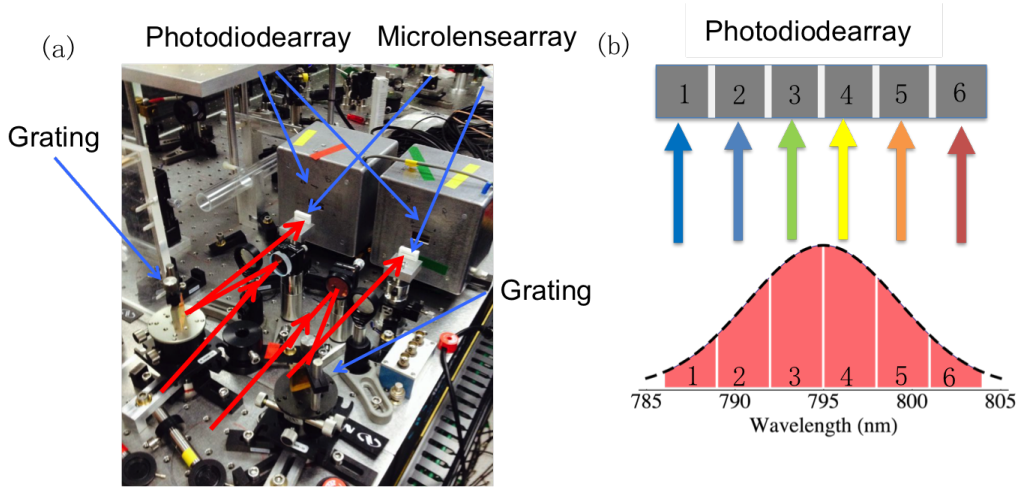

Figure 7.2: (a). The experimental setup of multi-pixel homodyne detection, where the red lines represent the laser beams, which are detected by a pair of home-made photodiode array detection system. (b) The detection process with a photodiode array, e.g. 6-pixel, where each spectral band is measured with a corresponding pixel of the photodiode array.

as seen in Fig.7.2 (b), which correspond to the spectral components mapped on each pixel of the photodiode array. Therefore, the difference of each individual pixel pairs is similar to a single homodyne detection associated to the pixel spectral bands, and gives the projection of the signal $\hat{E}_s = \sum_j \hat{a}_{\rm s}^{(j)} u_j^{\rm s}$ onto the corresponding pixels modes $\{u_i\}$ of the local oscillator [30]. When assuming the projection $\int u_i^* u_j^{\rm S} {\rm d}\Omega$ is real and the power of the local oscillator is much bigger than the signal one, $P_{\rm LO} \gg P_{\rm s}$, we have,

$$\hat{I}_i^- = \sqrt{2P_{\rm LO}^i} \sum_j \int u_i^* u_j^{\rm S} {\rm d}\Omega \hat{x}_\theta^{{\rm S}_j}, \tag{7.1}$$

where θ is the global relative phase between the local oscillator and the signal beams, the corresponding quadrature is $\hat{x}_\theta^{{\rm S}_j} = e^{-\theta}\hat{a}_{\rm s}^{(j)} + e^{\theta}(\hat{a}_{\rm s}^{(j)})^\dagger$ and $P_{\rm LO}^i$ is the optical power of the $i^{\rm th}$ pixel local oscillator. Similar as the single homodyne detection in Equ. 4.5, generally, we can adjust the phase of each signal mode $\hat{a}_{\rm s}^{(j)}$ to make the projection $\int u_i^* u_j^{\rm S} {\rm d}\Omega$ real, but here, to aim so for every pixel, we need additionally that the local oscillator has a flat phase for each pixel mode. As we discussed in Chapter 4 for single homodyne detection, in the SPOPO experiment, the signal, the supermodes, and the local oscillator from the Mira laser satisfy the conditions, and the projection for each pixel can be all real via adjusting the global phase of the signal consisting of many supermodes.

For the multi-pixel homodyne detection, we normalize the difference signals with the individual powers of the local oscillator (or corresponding shot noises)[2]. The normalized signals are defined as $\vec{S} = (\hat{S}_1, \hat{S}_2, \dots)^{\mathrm{T}} = (\hat{I}_1^- / \sqrt{2I_{\mathrm{LO}}^1}, \hat{I}_2^- / \sqrt{2I_{\mathrm{LO}}^2}, \dots)^{\mathrm{T}}$, thus, we can get,

$$\hat{S}_i = \sum_j \int u_i^* u_j^{\mathrm{S}} \mathrm{d}\Omega \hat{x}_\theta^{\mathrm{S}_j} = \sum_j U_{ij} \hat{x}_\theta^{\mathrm{S}_j}, \tag{7.2}$$

where U_{ij} is the projection, which is a quasi-basis change from the signal modes $\{u_j^{\mathrm{S}}\}$ to the pixel modes $\{u_i\}$.

Then we can obtain all the signals $\vec{S}$ simultaneously. As among the signal modes are no correlations, e.g. the supermodes of the SPOPO have no correlations, therefore, we can get the variances $\Delta^2(S_i)$ of all the individual pixels and correlations $\langle S_i S_k \rangle - \langle S_i \rangle \langle S_k \rangle$ between any two pixels in the same time, when it i

$$\Delta^2(S_i) = \sum_j (U_{ij})^2 \Delta^2 \hat{x}_\theta^{\mathrm{S}_j} \quad \text{and} \quad \langle S_i S_k \rangle - \langle S_i \rangle \langle S_k \rangle = \sum_j U_{ij} U_{kj} \Delta^2 \hat{x}_\theta^{\mathrm{S}_j}. \tag{7.3}$$

For the SPOPO, the signal modes are the supermodes as seen in Fig. 3.8m, which are projected onto each pixel modes $\{u_i\}$ simultaneously via multipixel homodyne detection. Here each pair of pixels is the same as a single homodyne detection with shaping the local oscillator onto a frequency band, however, as all the pixels process simultaneously, all the correlation information between different frequency bands is recorded. Hence this provides possibilities for one-way quantum computing [67], which need measure and destroy entanglement of all the modes in the same time. We will present how to measure all the correlations simultaneously and construct covariance matrix with the multi-pixel homodyne detection system in section 3 of the this chapter.

7.2 Setup and alignment

In practice, we develop a multi-pixel homodyne detection system, including commercial photodiode arrays, homomade electronics, and data acquisition system. The photodiode array is a 1-D silicon photodiode with 16 pixels(Hamamatsu, model S4111-16Q, $\sim 90\%$ quantum efficiency, sensor size one pixel 1.45×0.9mm). In the experiment, we use the central eight pixels

[2]The shot noises are proportional to the corresponding optical powers of the local oscillator in homodyne detection.

of the photodiode array for the multi-pixel homodyne detection. We design and fabricate the eight-channel amplifier in the electronics shop in the laboratory, as seen in Fig. 7.3 (a), whose electric circuit is in the appendix. The electronics for each pixel is the same as the single homodyne detection, where we amplify the signal from individual pixel sensors, and then make a difference of each pair.

And a multichannel data acquisition card (NI) is developed to collect the eight-channel data simultaneously from the eight difference signals of the multipixel homodyne measurement, as seen in Fig. 7.3 (b). To each channel we apply the configuration of Fig. 4.18 c, For the channels corresponding to the middle frequency bands, we achieve 7 dB clearance compared to electric dark noise. This is lower than single homodyne detection system (10 dB).

Besides, to overcome the gap between pixels in the photodiode arrays, we use microlens arrays (f=17mm) in front of the photodiode arrays to focus different spectral components in the corresponding pixel without loss, as seen in Fig. 7.1.

To align the photodiode arrays, first, we align horizontally the positions of the two photodiode arrays and the mircrolens to make the beam shine in the center of the photodiode arrays, according to the DC output; second, we give a fixed amplitude modulation (AOM) at 1.5 MHz, which is the same frequency we observer squeezing, on a single spectral band of the beam (by pulse shaping or an optical filter $\delta\lambda \simeq 1$ nm), and make each pixel of the two photodiode arrays have the same electric gain by adjusting a resistance in the electric circuit of the detectors.

In the experiment, the data acquisition system often has difficulties from the complexity of the setup, as seen in Fig. 7.3, such as leak radio noises[3] , saturations of the amplifiers, and grounding, etc. In the experiment, when we activate eight pixels of the photodiode array, firstly the multipixel homodyne detection generate sixteen photocurrents, which need many cables to connect with the electronics, such as amplifiers, mixers, data acquisition, etc.. Most of the problems originate from the connections, which induce radio noise leaked in the air. Therefore, as the system can extend to be more and more complex via just increasing the amount of the measurement pixels, we have to consider to develop a more compact, robust and high-efficiency detection system in future.

[3] As the electronics shielding is not good, the leak radio noises sometimes can be received by the detection system.

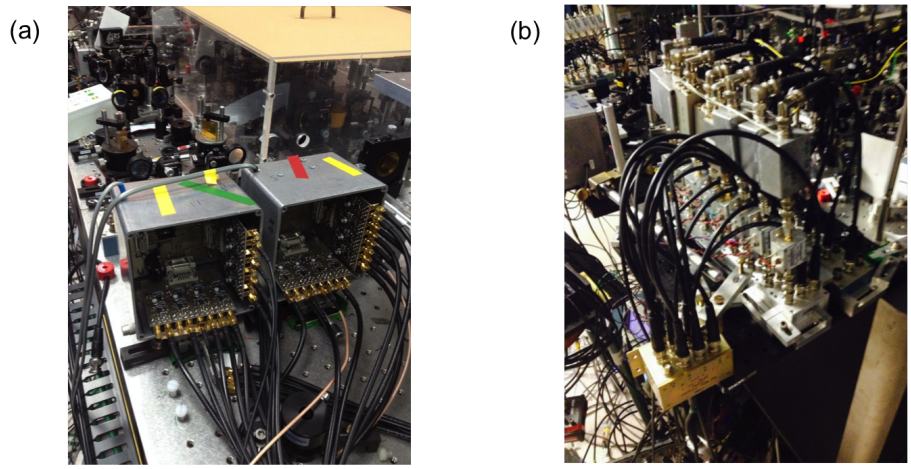

Figure 7.3: The experimental electronics. (a) The rear side the frequency-resolved detectors. (b) The data acquisition system.

7.3 Simultaneously measuring multimode covariance matrix

To construct the covariance matrix of the SPOPO with multi-pixel homodyne detection, when $\theta = 0$ and in the pixel basis $\{u_i\}$, the elements of amplitude quadrature are, assuming all the mean values are 0,

$$\Delta^2 \hat{x}_i = \Delta^2(S_i) \quad \text{and,} \quad \langle \hat{x}_i \hat{x}_k \rangle = \langle S_i S_k \rangle, \tag{7.4}$$

where $\Delta^2 \hat{x}_i$ and $\langle \hat{x}_i \hat{x}_j \rangle$ are the diagonal elements and off-diagonal elements of the amplitude quadrature covariance matrix, respectively, obtained by the corresponding variance $\Delta^2(S_i)$ and the mean of products $\langle S_j S_k \rangle$. It is similar for the phase quadrature, when $\theta = \pi/2$.

Here, as all the pixels of detection occur simultaneously, for the amplitude or phase quadrature, we don't need to measure many times or the combination modes of Equ. 3.52 compared to single homodyne detection. All the variances and correlations terms for constructing covariance matrix are obtained simultaneously, thus we can access the quantum correlation of all the modes in the same time, supplying the possibilities to do quantum computing.

Besides, for constructing the covariance matrix, we can also first construct the variance curves, as seen in Fig. 4.20, then obtain the elements of covariance matrix from Equ. 3.53. This way is useful when scanning the homodyne phase θ, which is not locked, and we can easily define the amplitude and phase quadratures with the peaks and valleys in the variance curves.

For a eight-pixel case, the covariance matrix, measured with eight-pixel homodyne detection, is presented in Fig. 7.4. For the SPOPO, the correalatios, $\langle \hat{x}_i \hat{p}_j \rangle$ and $\langle \hat{p}_i \hat{x}_j \rangle$ are absent. And the covariance matrix consists of the amplitude and phase quadratures, which is normalized by the shot noises.

Furthermore, via diagonalizing the covariance matrix, the eigemodes and corresponding squeezing are presented in Fig. 7.5. Importantly, the spectral shapes of the eigenmodes are similar to the ones obtained via the way of single homodyne detection and pulse shaping, as seen in Fig. 4.23, and all the eigemodes are squeezed, whose squeezing values are corrected with electric dark noise. The leading eigenmode is squeezed by -2.9 dB, and we see, for the similar mode, this is less squeezed compared to the squeezing when measured via single homodyne detection ($\sim$6 dB). The reason is that, in the squeezing measurement, we have more loss introduced by the quantum efficiency of the photodiode arrays and the gratings. But corrected by all the loss, $\sim$ 25%, we can get similar squeezing as in the single homodyne detection.

Above, we presented a eight-mode covariance matrix measured via multipixel homodyne detection, and similar multimode states, the eigenmodes and squeezing are obtained as via the single homodyne measurement with pulse shaping. After we access the multimode correlation simultaneously, we can post-process the data using a real digital gain by computer, which allows to implement a real unitary transform on the pixel modes.

However, arbitrary pulse shaping in the single homodyne detection can realize any unitary transform, and as only real transforms can be implemented in multi-pixel homodyne detection, and hence less operations can be implemented. Next we will give the criteria of feasible controls for quantum computing with multipixel homodyne detection.

7.4 Characterization of Feasible operations

Previously, we obtained a covariance matrix via simultaneously measuring the correlations of all the pixel modes, multi-pixel homodyne measurements. For measurement based quantum computing, we need access entanglement of all the entangled states at the same time. For instance, in the quantum computer composed of a cluster states, measuring on each node implement a specific computing program [67]. Here, we want to construct continuous-variable clusters [53] and quantum computing [93] with the multi-pixel homodyne detection. In the following we will characterize the experimental freedoms to implement quantum networks and quantum computing.

As seen in Fig. 7.6, the SPOPO experiment with multi-pixel homodyne detection is presented. Here, instead of shaping the local oscillator on any

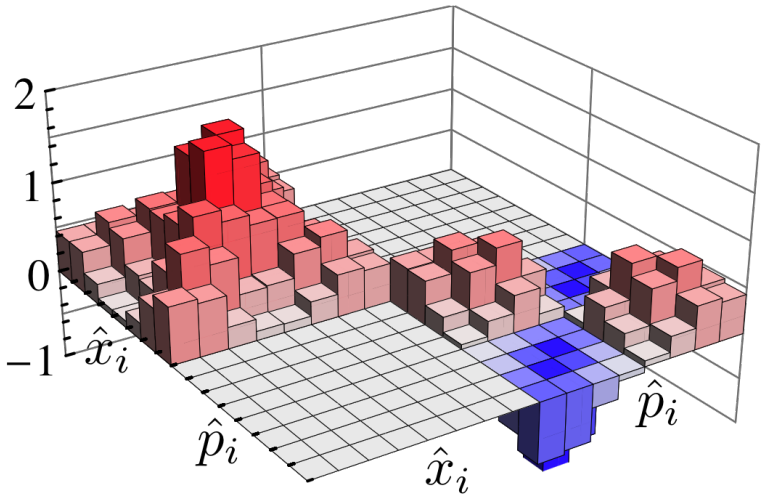

Figure 7.4: The covariance matrix from multipixel homodyne detection. For the SPOPO, the correalatios, $\langle \hat{x}_i \hat{p}_j \rangle$ and $\langle \hat{p}_i \hat{x}_j \rangle$ are absent. And the covariance matrix consists of the amplitude and phase quadratures, which are $\langle \hat{x}_i \hat{x}_j \rangle$ and $\langle \hat{p}_i \hat{p}_j \rangle$, respectively.

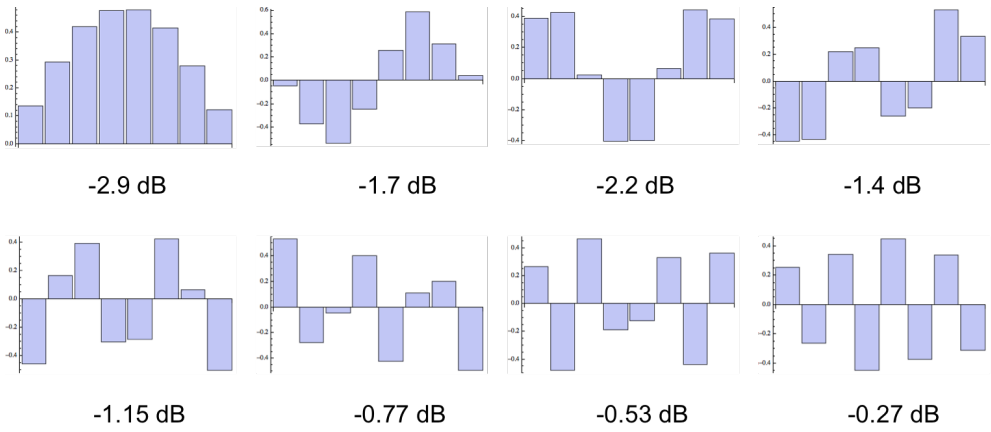

Figure 7.5: The eight eigenmods are obtained from the multi-pixel homodyne detection via diagonalizing the covariance matrix of the phase quadrature part. The squeezing values are corrected with electric dark noise.

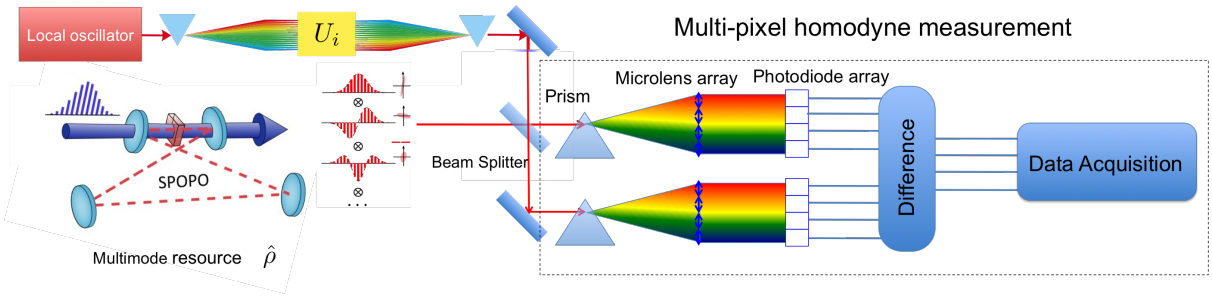

Figure 7.6: The experimental shemes of the SPOPO with multi-pixel homodyne detection.

mode via arbitrary pulse shaping, we do a simultaneous measurement with multi-pixel homodyne detection and post-processing to implement quantum computing.

Reacall the eigenmodes measured with multipixel homodyne dectection, in Fig. 7.5, $M = (m_{\text{eig1}}, m_{\text{eig2}}, \ldots, m_{\text{eign}})^{\text{T}}$. Les us consider corresponding annihilation operators of the p-squeezed modes, $\vec{a}_{\text{psqz}} = (\hat{a}_{\text{sqz1}}, \hat{a}_{\text{sqz2}}, \ldots, \hat{a}_{\text{sqzn}})^{\text{T}}$, then the pixel modes are,

$$\vec{a}_{\text{pix}} = M^{\text{T}} \Delta_{\text{OPO}} \vec{a}_{\text{psqz}}, \tag{7.5}$$

where the diagonal phase matrix $\Delta_{\text{OPO}} = diag(1, -i, 1, -i, ...)$, which is to rotate all the eigenmode to be p-squeezed.

In the scheme in Fig. 7.6, to implement quantum imformation processing, we can still use the shaper to control quadrature phases of the individual pixels, $\Delta_{\text{LO}} = diag(e^{i\phi_1}, e^{i\phi_2}, e^{i\phi_3}, \ldots)$, and perform a real unitary transform, O_{post}, in the data post-processing.

Thus, totally, the output modes $\vec{a}_{\text{out}}$ of the multipixel homodyne system are,

$$\vec{a}_{\text{out}} = O_{\text{post}} \Delta_{\text{LO}} \vec{a}_{\text{pix}} = O_{\text{post}} \Delta_{\text{LO}} M^{\text{T}} \Delta_{\text{OPO}} \vec{a}_{\text{psqz}}, \tag{7.6}$$

thus we have,

$$\vec{a}_{\text{out}} = U_{\text{MPHD}} \vec{a}_{\text{psqz}} \quad \text{and,} \quad U_{\text{MPHD}} = O_{\text{post}} \Delta_{\text{LO}} M^{\text{T}} \Delta_{\text{OPO}}. \tag{7.7}$$

For the experimental system, in Fig. 7.6, all of possible operations are included in the unitary transform U_{MPHD}.

Let us assume a target transform to be performed by the system, U_{target}, and it can be proved that a necessary and sufficient condition for finding feasible operations to achieve $U_{\text{MPHD}} = U_{\text{target}}$ is,

$$(U'_{\text{target}})^{\text{T}} U'_{\text{target}} = D, \tag{7.8}$$

where $U'_{\text{target}} = U_{\text{target}}G^{\dagger} = U_{\text{target}}(M^{\text{T}}\Delta_{\text{OPO}})^{\dagger}$, and D is a diagonal matrix with unit modulus complex elements.

For the *necessity*, we can get,

$$(U'_{\text{target}})^{\text{T}}U'_{\text{target}} = G^{*}G^{\text{T}}\Delta_{\text{LO}}^{\text{T}}O_{\text{post}}^{\text{T}}O_{\text{post}}\Delta_{\text{LO}}GG^{\dagger} = \Delta_{\text{LO}}^{2}. \tag{7.9}$$

As the matrix Δ_{LO} is diagonal phase matrix, Δ_{LO}^{2} is a diagonal matrix with unit modulus complex elements.

For the *sufficiency*, if Equ. 7.8 holds, we can always get,

$$\Delta_{\text{LO}} = D^{\frac{1}{2}} = \left[(U'_{\text{target}})^{\text{T}}U'_{\text{target}}\right]^{\frac{1}{2}}, \tag{7.10}$$

then,

$$O_{\text{post}} = U'_{\text{target}}\Delta_{\text{LO}}^{-1}, \tag{7.11}$$

where $O_{\text{post}}O_{\text{post}}^{\text{T}} = O_{\text{post}}^{\text{T}}O_{\text{post}} = U'_{\text{target}}\left[(U'_{\text{target}})^{\text{T}}U'_{\text{target}}\right]^{-1}(U'_{\text{target}})^{\text{T}} = \mathcal{I}$, so O_{post} is orthogonal.

Above we proved the necessary and sufficient condition for Equ. 7.8. If any transform satisfies the condition in Equ. 7.8, we can obtain the feasible experimental parameters in the post-processing matrix O_{post} and the relative phases of the local oscillator Δ_{LO}. These allows us to obtain the unitary transform U_{MPHD}, usually corresponding to a complex optical network, onto the input p-squeezed modes, and the same quadratures can be measured simultaneously.

Importantly, the change of the unitary transform U_{MPHD}, the quantum network, can be achieved via using different post-processing matrix O_{post} and the relative phases of the local oscillator Δ_{LO}. This way of doing quantum networks, using multi-pixel homodyne measurement, is then flexible and versatile.

7.5 Feasible quantum networks

Using the eigenmodes in Fig. 7.5, we implement two eight-mode line and cross cluster states, as seen in Fig. 7.7, satisfying the criteria of Equ. 7.8. For the cluster states,

$$U_{\text{MPHD}} = U_{\text{clusterS}}\mathcal{O}_{8mode}, \tag{7.12}$$

where U_{clusterS} is the symmetry solution of the cluster states corresponding to the graphs in Fig. 7.7, and the $\mathcal{O}_{8mode}$ is an orthogonal matrix, defined in Equ. 5.30.

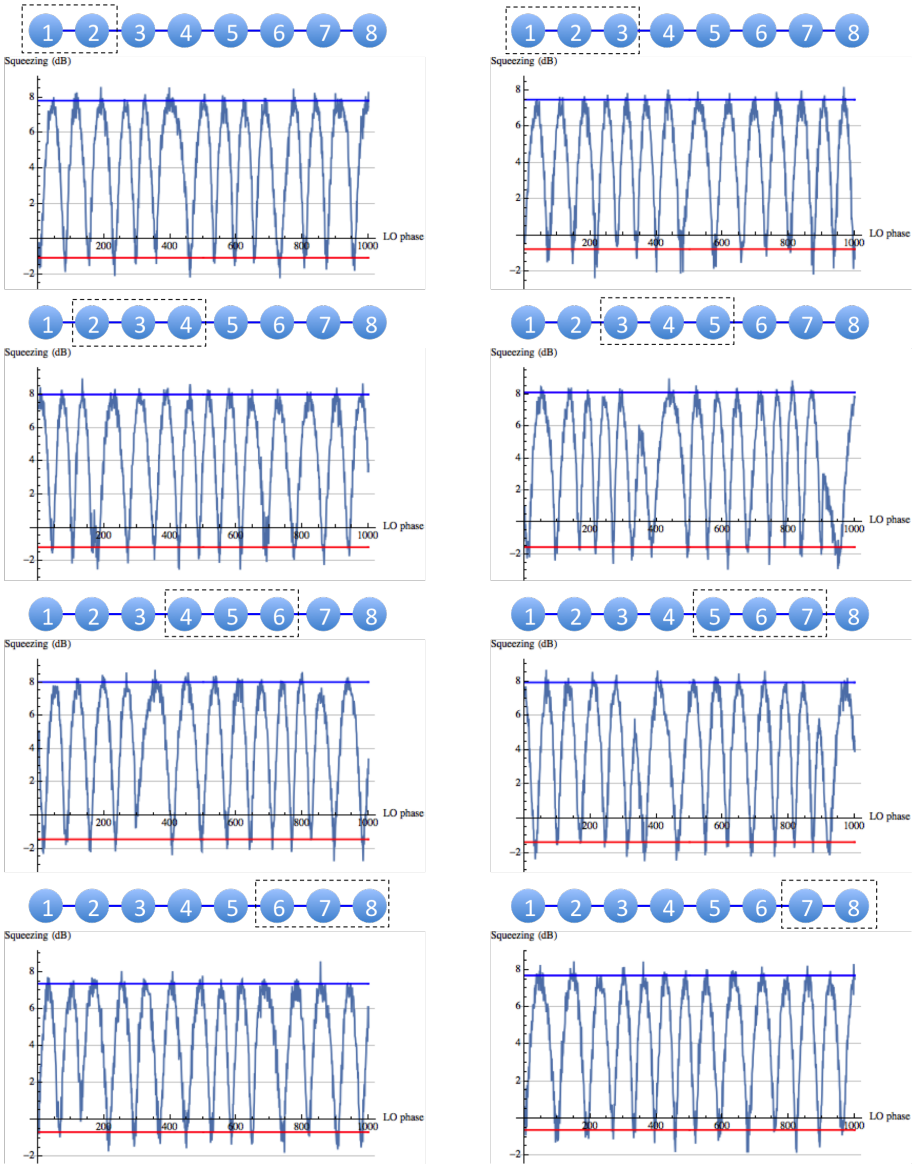

Figure 7.7: Squeezing curves of the eight-mode line cluster via multi-pixel homodyne measurements. The variances of the eight nullifiers are measured, and on top of each curve is the graph of the cluster states, where the corresponding nullifiers consist of the nodes in the dashed-line block. The red and the blue lines are the fit of the squeezing and antisqueezing, respectively.

We parametrize $\mathcal{O}_{8mode}(\theta_1, \theta_2, \ldots, \theta_{28})$ with 28 parameters, and use a searching algorithm to find a $\mathcal{O}_{8mode}$ to satisfy the criteria of Equ. 7.8 [31]. And with the multi-pixel homodyne measurement, we obtain the corresponding Δ_{LO} and O_{post} to realize the cluster states in Fig. 7.7, whose nullifiers are all squeezed experimentally, ~ 3 dB corrected with only dark noise.

The nullifiers in Fig. 7.7 are obtained via measuring further the corresponding nullifier modes M_{nul}, defined in Equ. 6.4. For instance, to measure the first nullifier in Fig. 7.7, we have,

$$U_{\mathrm{null}} = M_{\mathrm{null}} U_{\mathrm{MPHD}} = \frac{1}{\sqrt{2}}(1, i, 0, 0, 0, 0, 0, 0) O_{\mathrm{post}} \Delta_{\mathrm{LO}} = O'_{\mathrm{post}} \Delta'_{\mathrm{LO}} \quad (7.13)$$

where U_{null} is a complex vector corresponding the nullifier mode, including the new post-processing transform O'_{post}, and the new local phase Δ'_{LO} which is written onto the SLM.

Importantly, this system can realize different clusters without changing the optical architecture. We have found solutions for various clusters theoretically.

Fourier transform

Generally, in measurement based quantum computing, the procedures consist of two steps: building a cluster as the quantum computer, and measuring corresponding quadratures to implement computing program. Here, we did try a simple quantum computation, the Fourier transform of one gausssian state, where an input gaussian state $\rho(\hat{x}, \hat{p})$, after the quantum gate of Fourier transform, the output is $\rho(-\hat{p}, \hat{x})$.

To aim the Fourier transform of an eigenmode of the SPOPO, the target transform is [30],

$$U_{\mathrm{FT}} = D_{\mathrm{meas}} U_{\mathrm{BS}} U_{\mathrm{lin3}}, \quad (7.14)$$

where $D_{\mathrm{meas}} = diag(i, i, 1, 1)$ is the measurement phase of the network nodes, U_{BS} corresponds to a balanced beam splitter, and U_{lin3} is three-mode line cluster matrix.

However, for the Fourier transform U_{FT}, using real eigenmodes of the SPOPO, we didn't find good solutions to satisfy the criteria of Equ. 7.8.

Does this mean we can't implement Fourier transform U_{FT} in the system of the SPOPO?

To answer this question, we need to go back to the criteria of Equ. 7.8, where the eigenmodes M call for the same dimension as the target transform U_{MPHD} to satisfy $GG^{\dagger} = \mathcal{I}$. This means if we have a set of eight-pixel eigenmodes M, we can't use four of the eight squeezed eigenmodes to perform

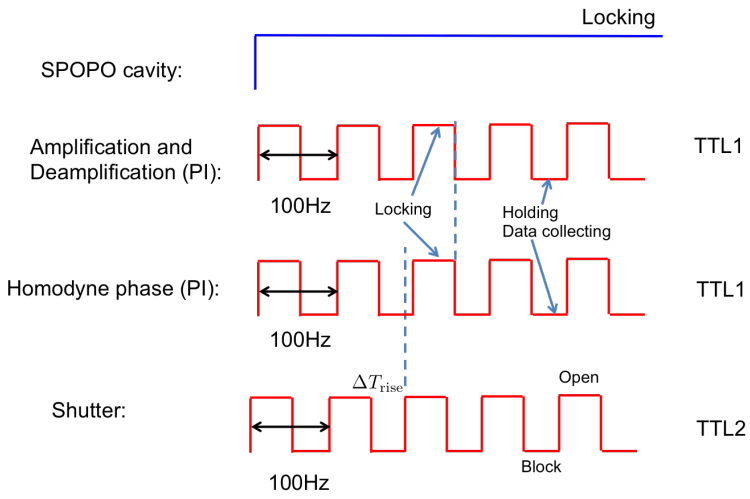

Figure 7.8: The time sequence of the vacuum squeezing locking. Two TTL signal sequences control the locking: TTL1 controls the same shutter as in the amplification and deamplification locking, TTL2 controls both PIs of amplification (deamplification) and homodyne measments locking. In each cycle, when the shutter is open, we can lock for both amplification and homodyne measurements; When the shutter blocks the signal, the two PIs hold the locking phase, and we collect the vacuum squeezing data.

a four-mode Fourier transform U_{FT}, as $GG^{\dagger}$ will never be a identity matrix $\mathcal{I}$. At some point, it is not physical that we can't improve the precision of a unitary transform when increasing the control freedoms of the system. For instance, here, it is impossible to use a eight-pixel system and eigenmodes to implememt a four-mode transform, e.g. the Fourier transform in Equ. 7.14. Thus this implies that the criteria of Equ. 7.8 only covers part of the freedoms in the system, and it might still be possible to implement the Fourier transform gate adapting the criteria to this situation.

7.6 Locking squeezed vacuum

To implement quantum computing, we need lock the phase of the quadratures Δ_{LO} in Equ. 7.6. In practice, we can lock the squeezing phase via locking the relative phase between the local oscillator and the signal in the homodyne detection, as seen in Fig. 4.14. When the SPOPO cavity and the deamplification are locked, we give a phase modulation, ∼600 KHz, on the local oscillator (PZT 4 in Fig. 4.2), and the error signal is obtained via demodulating the signal from one of the homodyne detectors, which is controls

Figure 7.9: Locked squeezing and scan squeezing measured by a spectrum analyzer. The blue oscillation is the squeezing curve when scaning the homo phase. The pink curve is the vacuum squeezing when the deamplicaiton and the amplitude quadrature are both locked with the shutter control. Similar for the green curve, when the amplication and the same homodyne quadrature phase are locked, we can see the locked anti-squezing of the squeezed vacuum.

the PZT 5 in Fig. 4.2.

Furthermore, similar to the principle of amplification (or deamplification) locking without signal, we employ the same shutter, used for deamplification locking, to realize the locking of squeezed vacuum. As seen in Fig. 7.9, the time sequences of the vacuum squeezing locking is presented. We use a delay generator to give two TTL signal sequences with a delay ΔT_{rise} to control the system: TTL1 controls the same shutter as in the amplification and deamplification locking; TTL2 controls both PIs of amplification (deamplification) and homodyne locking. In the first half of each cycle, the shutter is open, thus we can lock both deamplification and homodyne phase with signal normally; in the second half period, the shutter blocks the signal, the locking phase is hold via holding the voltage tension on PZT1 and PZT5 in Fig. 4.2. And the frequency of the two TTL sequences is 100 Hz.

The vacuum squeezing curves, measured by a spectrum analyzer, are presented in Fig. 7.9. The blue oscillation is the squeezing curve when scanning the relative phase between the local oscillator and the "signal" which is vacuum, which is similar to the squeezing curve in Fig. 4.18. And the valley and peak correspond to the squeezing in different phase of quadratures, amplitude and phase, respectively. The pink curve is the vacuum squeezing when the deamplificaiton and the amplitude quadrature in the homodyne detection are both locked with the shutter controlled with the TLL sequence. When the shutter is open, the deamplicaition and the homodyne phase are both locked, but the bright squeezing (with signal) saturates the detection system; then when shutter is closed, both lockings hold, thus we can see the locked vacuum squeezing. Similar for the green curve, when the deamplication and the phase quadrature in the homodyne detection are locked, we can see the locked anti-squeezing of the squeezed vacuum.

But here, compared to the squeezing when only scanning the phase of the local oscillator without phase modulation on the local oscillator, we lose $\sim$ 1dB squeezing. We verified the reason why lose squeezing is that the harmonics of phase modulation on the local oscillator introduce extra noise into the squeezing. Therefore, we move this phase modulation on the signal beam, which is presented in detail in Part III, thus when the signal is blocked by the shutter, the noise from the phase modulation can not affect the vacuum squeezing.

7.7 Conclusion

In this chapter we demonstrated the possibility of implementing quantum network in a versatile method. The method is based on the simultaneous

measurement of all the squeezed eigenmodes produced with SPOPO via multipixel homodyne detection, and uses the classical post-processing of the acquired signals, which are multiplied by computer. And we are able to lock the quadrature phase of the squeezing in the system, therefore, which is possible to implement continuous-variable measurement based quantum computing [53].

This procedure requires the determination of the suitable phase shape of the local oscillator to be employed in the multipixel homodyne detection, as well as the post-processing transform to apply to the traces recorded in each mode.

In particular, we find the solutions with a searching algorithm, satisfying the system criteria, to realize the eight-mode line and cross cluster states. But the attempt of Fourier transform is not achieved yet, as the criteria does not include all the possible operations in the system.

Thus, this system of multipixel homodyne detection with SPOPO is flexible and versatile way to do quantum computing, e.g. cluster states. However, because the criteria still doesn't cover all possibilities of feasible operations, we need explore the strategy how to fully use the multipixel homodyne detection both experimentally and theoretically. Besides, the criteria can be used for all the other multimode systems to do quantum computing [13]. In next chapter, we will present how to generate quantum networks based on cascading four wave mixing.

Chapter 8

Multimode entanglement with cascading FWM

We developed a theoretical proposal to implement versatile cluster states by cascading four wave mixing in rubidium atomic gas. We propose to use phase-controlled homodyne detection and post-processing. This work has been done in collaboration with the group of Prof. JING Jietai in the State Key Laboratory of Precision Spectroscopy, ECNU, Shanghai. And it has been published in Physics Review A 91, 013843 (2015). In this chapter, we present directly the article of this work.

Quantum-network generation based on four-wave mixing

Yin Cai,[1,2] Jingliang Feng,[2] Hailong Wang,[2] Giulia Ferrini,[1] Xinye Xu,[2] Jietai Jing,[2,*] and Nicolas Treps[1,†]
[1]*Laboratoire Kastler Brossel, Sorbonne Université, UPMC, ENS, Collège de France, CNRS, 4 place Jussieu, 75252 Paris, France*
[2]*State Key Laboratory of Precision Spectroscopy and Department of Physics, East China Normal University, Shanghai 200062, China*
(Received 8 October 2014; published 28 January 2015)

We present a scheme to realize versatile quantum networks by cascading several four-wave mixing (FWM) processes in warm rubidium vapors. FWM is an efficient $\chi^{(3)}$ nonlinear process, already used as a resource for multimode quantum state generation and which has been proved to be a promising candidate for applications to quantum information processing. We analyze theoretically the multimode output of cascaded FWM systems, derive its independent squeezed modes, and show how, with phase controlled homodyne detection and digital postprocessing, they can be turned into a versatile source of continuous variable cluster states.

DOI: 10.1103/PhysRevA.91.013843 PACS number(s): 42.65.Ky, 42.50.−p, 03.65.Ud, 03.67.−a

I. INTRODUCTION

Generation of versatile quantum networks is one of the key features towards efficient and scalable quantum information processing. Recently, their continuous variable implementation has raised a lot of interests [1], in particular in optics where practical preparation and measurement protocols do exist, both at the theoretical and experimental level. The most promising achievements have been demonstrated using independent squeezed resources and a linear optical network [2,3]. More recently, proposals have emerged where different degrees of freedom of a single beam are used as the nodes of the network, such as spatial modes [4,5], frequency modes [6,7], or even temporal modes [8]. In all these realizations, a given experimental setup corresponds to one quantum optical network. However, the specific structure of a quantum network depends on the mode basis on which it is interrogated; thus changing the detection system allows for on-demand network architecture. This has been applied in particular to ultrafast optics [9] where a pulse shaped homodyne detection is used to reveal any quantum network. In order to combine the flexibility of this mode dependent property with the simultaneous detection of all the modes, multipixel homodyne detection was introduced [4], and it was shown that combined with phase control and signal postprocessing it could be turned into a versatile source for quantum information processing [10].

Here we propose a scheme based on four-wave mixing (FWM) in warm rubidium vapors to generate efficiently flexible quantum networks. A single FWM process can generate strong intensity-correlated twin beams [11–13], which has been proved to be a promising candidate in quantum information processing and has many applications such as quantum entangled imaging [14], realization of stopped light [15], and high purity narrow-bandwidth single-photons generation [16]. Recently, it has been reported that by cascading two FWM processes, tunable delay of EPR entangled states [17], low-noise amplification of an entangled state [18], realization of phase sensitive nonlinear interferometer [19,20], quantum mutual information [21], and three quantum correlated beams with stronger quantum correlations [22] can be realized experimentally. Cascaded FWM presents several advantages toward standard multimode technics. Indeed, it is phase insensitive and single pass (i.e., no cavity); hence it does not require any locking either in an individual step, nor between successive steps, making it easily scalable. Inspired by these previous works we propose in the present work to cascade several FWM processes in which way we can turn this system into a controllable quantum network. We elaborate the theory of the optical quantum networks generated via cascading two and three FWM processes, calculating the covariance matrix and the eigenmodes of the processes from Bloch-Messiah decomposition [23]. We then study how cluster states can be measured using phase controlled homodyne detection and digital postprocessing.

II. SINGLE FWM PROCESS

A single FWM process in Rb vapor is shown in Fig. 1, where an intense pump beam and a much weaker signal beam are crossed in the center of the Rb vapor cell with a slight angle. During the process, the signal beam is amplified and a beam called idler beam is generated simultaneously. It propagates at the same pump-signal angle on the other side of the pump beam due to the phase-matching condition, having a frequency slightly shifted as compared to the signal beam. The input-output relation of the single FWM process is given by

$$\hat{a}_{s1} = G\hat{a}_{s0} + g\hat{a}_{v0}^{\dagger}, \quad \hat{a}_{i1} = g\hat{a}_{s0}^{\dagger} + G\hat{a}_{v0}, \tag{1}$$

where G is the amplitude gain in the FWM process and $G^2 - g^2 = 1$, $\hat{a}_{s0}$ is the coherent input, and $\hat{a}_{v0}$ is the vacuum input. $\hat{a}_{s1}$ is the generated signal beam and $\hat{a}_{i1}$ is the generated idler beam; see [24] for details. Defining the amplitude and phase quadrature operators $\hat{X} = \hat{a} + \hat{a}^{\dagger}$ and $\hat{P} = i(\hat{a}^{\dagger} - \hat{a})$, the input-output relation can be re-written as

$$\begin{pmatrix} \hat{X}_{s1} \\ \hat{X}_{i1} \end{pmatrix} = \begin{pmatrix} G & g \\ g & G \end{pmatrix} \begin{pmatrix} \hat{X}_{s0} \\ \hat{X}_{v0} \end{pmatrix}, \tag{2}$$

$$\begin{pmatrix} \hat{P}_{s1} \\ \hat{P}_{i1} \end{pmatrix} = \begin{pmatrix} G & -g \\ -g & G \end{pmatrix} \begin{pmatrix} \hat{P}_{s0} \\ \hat{P}_{v0} \end{pmatrix}. \tag{3}$$

We immediately see from this set of equations that the system does not couple X and P quadratures of the fields, which can thus be treated independently. Furthermore, input beams are

*jtjing@phy.ecnu.edu.cn
†nicolas.treps@upmc.fr

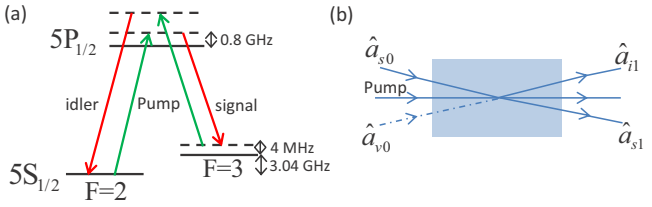

FIG. 1. (Color online) (a) Energy-level diagram for the FWM process. For experimental implementation the pump beam is tuned about 0.8 GHz to the blue of the D1 line of rubidium ($5S_{1/2}, F = 2 \rightarrow 5P_{1/2}$, 795 nm) and the signal beam is red tuned about 3 GHz to the pump beam. The two-photon detuning is about 4 MHz. (b) A single FWM process. $\hat{a}_{s0}$ is the coherent input and $\hat{a}_{v0}$ is the vacuum input. $\hat{a}_{s1}$ is the amplified signal beam and $\hat{a}_{i1}$ is the generated idler beam.

vacuum or coherent states, and as the global transformation is symplectic the system retains Gaussian statistic and can thus be fully characterized by its covariance matrix [1]. In our specific case, the covariance matrix is block diagonal:

$$C = \begin{pmatrix} C_{XX} & 0 \\ 0 & C_{PP} \end{pmatrix}, \tag{4}$$

where, by definition, $C_{XX} = \langle \binom{\hat{X}_{s1}}{\hat{X}_{i1}} \binom{\hat{X}_{s1}}{\hat{X}_{i1}}^T \rangle$, and the equivalent definition holds for C_{PP}. For coherent and vacuum input, the variances of input modes are normalized to one, and one obtains

$$C_{XX} = \begin{pmatrix} -1+2G^2 & 2Gg \\ 2Gg & -1+2G^2 \end{pmatrix} \tag{5}$$

and

$$C_{PP} = \begin{pmatrix} -1+2G^2 & -2Gg \\ -2Gg & -1+2G^2 \end{pmatrix}. \tag{6}$$

C_{XX} and C_{PP} are respectively the amplitude and phase quadrature parts of the covariance matrix of a single FWM process. The covariance matrix contains all the correlations between any two parties in the outputs. As the quantum state is pure, it is possible to diagonalize the covariance matrix to find the eigenmodes of the system, which are two uncorrelated squeezed modes, each one being a given linear combination of the output modes of the FWM process. In this pure case C_{PP} is simply the inverse of C_{XX}, so they share the same eigenmodes with inverse eigenvalues. We find that the eigenvalues of the C_{XX} matrix are $\eta_{a1} = (G-g)^2$, $\eta_{b1} = (G+g)^2$ and the corresponding eigenmodes are $\hat{X}_{a1} = \frac{1}{\sqrt{2}}(\hat{X}_{s1} - \hat{X}_{i1})$ and $\hat{X}_{b1} = \frac{1}{\sqrt{2}}(\hat{X}_{s1} + \hat{X}_{i1})$. The first eigenmode is amplitude squeezed, while the second one is phase squeezed, which is the well-known signature that, in a single stage FWM process, signal and idler beams are EPR correlated [17].

It is important to stress here that each eigenmode of the covariance matrix is squeezed independently and diagonalization of the covariance matrix corresponds to a basis change from the output basis of FWM to squeezing basis. Even if this basis change can be difficult to be implemented experimentally, as output beams have different optical frequencies, it nevertheless remains a linear operation that reveals the underlying structure of the output state of the FWM process.

III. CASCADED FWM PROCESSES

The above procedure can be readily applied to the more interesting multimode case, when one considers the multiple FWM processes, generating more than two output beams. We study here three-mode asymmetrical and four-mode symmetrical structures, whose input-output relation is derived by successively applying the matrix corresponding to the single FWM process of Eqs. (2) and (3).

A. Asymmetrical structure: Double FWM case

We first consider the case where two FWM processes are cascaded. Without loss of generality, we take the idler beam from the first FWM process as the seed for the second FWM process, as described in Fig. 2. The corresponding unitary transformation can be directly derived and written:

$$\begin{aligned} \begin{pmatrix} \hat{X}_{s1} \\ \hat{X}_{i2} \\ \hat{X}_{s2} \end{pmatrix} &= U_{X_{3\text{mode}}} \begin{pmatrix} \hat{X}_{s0} \\ \hat{X}_{v0} \\ \hat{X}_{v1} \end{pmatrix}, \\ \begin{pmatrix} \hat{P}_{s1} \\ \hat{P}_{i2} \\ \hat{P}_{s2} \end{pmatrix} &= U_{P_{3\text{mode}}} \begin{pmatrix} \hat{P}_{s0} \\ \hat{P}_{v0} \\ \hat{P}_{v1} \end{pmatrix}, \end{aligned} \tag{7}$$

where

$$\begin{aligned} U_{X_{3\text{mode}}} &= \begin{pmatrix} G_1 & g_1 & 0 \\ g_1 G_2 & G_1 G_2 & g_2 \\ g_1 g_2 & g_2 G_1 & G_2 \end{pmatrix}, \\ U_{P_{3\text{mode}}} &= \begin{pmatrix} G_1 & -g_1 & 0 \\ -g_1 G_2 & G_1 G_2 & -g_2 \\ g_1 g_2 & -g_2 G_1 & G_2 \end{pmatrix}. \end{aligned} \tag{8}$$

Using the same procedure as for Eqs. (5) and (6) we can get the covariance matrix of the double stage FWM. It is still block diagonal, and for coherent or vacuum input states each block is given by

$$C_{X_{3\text{mode}}} = U_{X_{3\text{mode}}} U_{X_{3\text{mode}}}^T, \tag{9}$$

$$C_{P_{3\text{mode}}} = U_{P_{3\text{mode}}} U_{P_{3\text{mode}}}^T. \tag{10}$$

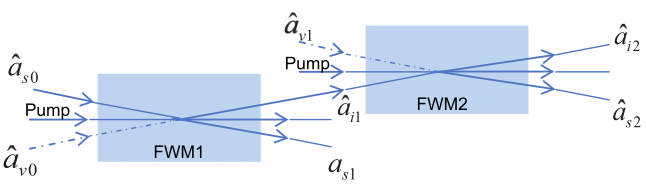

FIG. 2. (Color online) Double stage structure of FWM Rb system. $\hat{a}_{s0}$ is the coherent input and $\hat{a}_{v0}$ is the vacuum input for the first FWM process. $\hat{a}_{s1}$ is the amplified signal beam and $\hat{a}_{i1}$ is the generated idler beam from the first FWM process. $\hat{a}_{v1}$ is the vacuum input for the second FWM process. $\hat{a}_{s2}$ is the generated signal beam and $\hat{a}_{i2}$ is the amplified idler beam from the second FWM process.

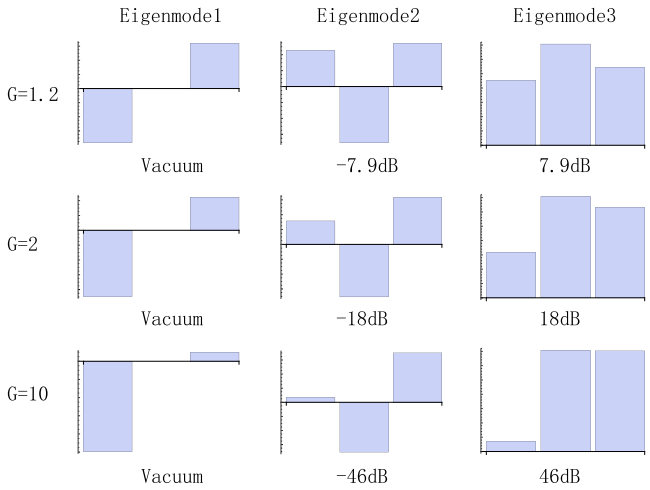

FIG. 3. (Color online) Eigenmodes of the asymmetrical FWM cascade, decomposed in the FWM output mode basis, for three different gain values. For each graph, the bars represent the relative weight of modes $\hat{a}_{s1}$, $\hat{a}_{i2}$, $\hat{a}_{s2}$, respectively. Below are given the noise variances η_{a3}, η_{b3}, and η_{c3} of the corresponding $\hat{X}$ quadrature. The state being pure, we see that eigenmode 3 shares the same squeezing as eigenmode 2 but on the phase quadrature.

We can now evaluate the eigenvalues and eigenmodes of these matrices. For the X quadrature, the eigenvalues of $U_{X_{3\text{mode}}}$ are

$$\begin{aligned}\eta_{a3} &= 1,\\ \eta_{b3} &= -1+2G_1^2G_2^2-2\sqrt{G_1^2G_2^2\left(-1+G_1^2G_2^2\right)},\\ \eta_{c3} &= -1+2G_1^2G_2^2+2\sqrt{G_1^2G_2^2\left(-1+G_1^2G_2^2\right)}.\end{aligned} \tag{11}$$

Remarkably, one sees that one of the eigenvalues is equal to one, meaning that the system is composed of only two squeezed modes and one vacuum mode. This property can be extended if one generalizes this system to the n-cell case in the similar asymmetrical way; there is always one vacuum mode. More expected, we also note that squeezing increases with gain, that eigenmode 2 and eigenmode 3 have the same squeezing but on different quadratures, and that both gains play an equivalent role and can be interchanged. The results for three different values of the gain, in the specific case where both processes share the same gain ($G_1 = G_2$) are shown in Fig. 3. We also show the shapes of the eigenmodes, i.e., their decomposition on the FWM output mode basis. The vacuum eigenmode appears to be composed only of modes 1 and 3 (i.e., $\hat{a}_{s1}$ and $\hat{a}_{s2}$), and tends to mode 1 when gain goes to infinity. This can be surprising, but it only reflects the fact that the noise of this mode becomes negligible compared to the two others when gain increases.

B. Symmetrical structure: Triple FWM case

We consider now the case of three cascaded FWM processes, where signal and idler of the first cell are used to seed each of the two other FWM processes, as shown in Fig. 4. For simplicity, we assume that all three FWM processes have the same gain value G. The evolution equations can be directly

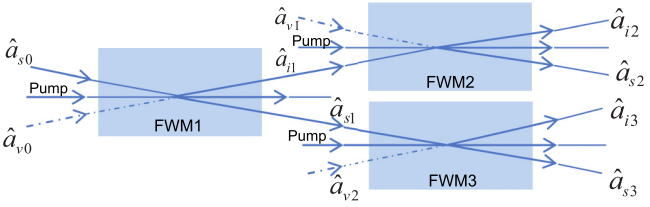

FIG. 4. (Color online) Symmetrical structure of FWM Rb system. $\hat{a}_{s0}$ is the coherent input and $\hat{a}_{v0}$ is the vacuum input for the first FWM process. $\hat{a}_{s1}$ is the amplified signal beam and $\hat{a}_{i1}$ is the generated idler beam from the first FWM process. $\hat{a}_{v1}$ and $\hat{a}_{v2}$ are the vacuum inputs for the second and third FWM processes. $\hat{a}_{s2}$ is the generated signal beam and $\hat{a}_{i2}$ is the amplified idler beam from the second FWM process. $\hat{a}_{s3}$ is the amplified signal beam and $\hat{a}_{i3}$ is the generated idler beam from the third FWM process.

derived and lead to

$$\begin{aligned}\begin{pmatrix}\hat{X}_{s3}\\ \hat{X}_{i2}\\ \hat{X}_{s2}\\ \hat{X}_{i3}\end{pmatrix} &= U_{X_{4\text{mode}}}\begin{pmatrix}\hat{X}_{s0}\\ \hat{X}_{v0}\\ \hat{X}_{v1}\\ \hat{X}_{v2}\end{pmatrix},\\ \begin{pmatrix}\hat{P}_{s3}\\ \hat{P}_{i2}\\ \hat{P}_{s2}\\ \hat{P}_{i3}\end{pmatrix} &= U_{P_{4\text{mode}}}\begin{pmatrix}\hat{P}_{s0}\\ \hat{P}_{v0}\\ \hat{P}_{v1}\\ \hat{P}_{v2}\end{pmatrix},\end{aligned} \tag{12}$$

where

$$\begin{aligned}U_{X_{4\text{mode}}} &= \begin{pmatrix}G^2 & gG & 0 & g\\ gG & G^2 & g & 0\\ g^2 & gG & G & 0\\ gG & g^2 & 0 & G\end{pmatrix},\\ U_{P_{4\text{mode}}} &= \begin{pmatrix}G^2 & -gG & 0 & -g\\ -gG & G^2 & -g & 0\\ g^2 & -gG & G & 0\\ -gG & g^2 & 0 & G\end{pmatrix}.\end{aligned} \tag{13}$$

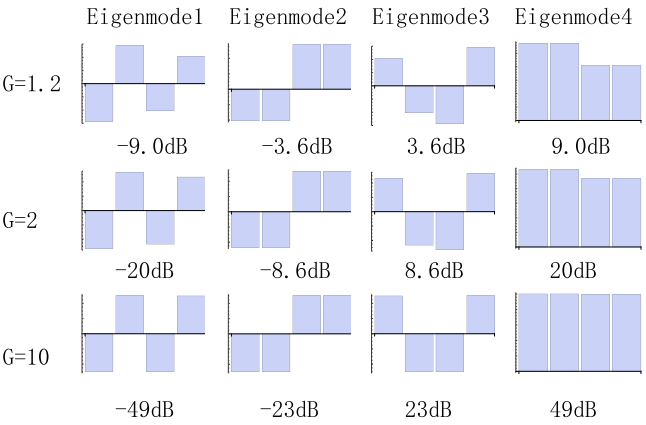

FIG. 5. (Color online) Eigenmodes of the symmetrical four-mode FWM cascade, decomposed in the FWM output modes basis, for three different gain values. For each graph, the bars represent the relative weight of modes $\hat{a}_{s3}$, $\hat{a}_{i2}$, $\hat{a}_{s2}$, $\hat{a}_{i3}$, respectively. Below are given the noise variances of the corresponding $\hat{X}$ quadrature.

No analytic expression of the eigenvalues can be simply given here, but for instance when $G = 1.2$, we find for the X quadrature the following levels of squeezing: $\{-9\,\text{dB}, -3.6\,\text{dB}, 3.6\,\text{dB}, 9\,\text{dB}\}$ (and opposite signs in the P quadrature). This system is indeed composed of four independent squeezed modes, with two different squeezing values. Figure 5 represents, similar as in the previous case, the mode shapes for three different values of the gain. As gain goes to infinity, we see that they tend to a perfectly symmetric decomposition, meaning that the output basis of FWM becomes mostly entangled then.

IV. CLUSTER STATES

We have shown in the previous section that the output states of different FWM processes were entangled states, whose underlying mode structure could be exactly calculated. We study here whether these outputs can be manipulated in order to generate cluster states, which are states of interest for quantum information processing.

A cluster state is a specific multimode entangled state, defined through an adjacency matrix V [25]. Let us call $\hat{X}_i^C$ and $\hat{P}_i^C$ the quadrature operators for the mode i of a given cluster state. The nullifier operators of the N-mode cluster states are defined by

$$\hat{\delta}_i = \left(\hat{P}_i^C - \sum_j V_{ij} \cdot \hat{X}_j^C \right). \tag{14}$$

Theoretically, a state is considered a cluster state of the adjacency matrix V if and only if the variance of each nullifier approaches zero as the squeezing of the input modes approaches infinity, assuming that the cluster is built from a set of independently squeezed modes. Experimentally, one compares the variance of each nullifier to the corresponding standard quantum limit.

It turns out that the output states of the FWM processes, as we have calculated in the previous sections, do not directly satisfy the cluster state criteria. However, it is still possible to derive cluster states when one can control the quadratures detected on each output mode (i.e., setting the phase of the homodyne detection local oscillator) and digitally postprocess the data, as explained in [10]. To apply this theory to the present case, we model the entangled states that one can produce with FWM, homodyne detection, and postprocessing, following the scheme of Fig. 6. We first introduce the annihilation operators $\hat{a}_i^{\text{sqz}}$ corresponding to the eigenmodes of the modeled FWM process (i.e., as displayed in Figs. 3 and 5, for instance). For consistency with the usual cluster states definition, we choose them to be squeezed on the P quadrature and thus introduce the diagonal matrix P_{sqz} to rotate the squeezing quadrature.

We now define the unitary matrix U_{FWM} so that $U_{\text{FWM}}\hat{\vec{a}}^{\text{sqz}}$ corresponds to the annihilation operators of the output modes, with the convention $\hat{\vec{a}}^{\text{sqz}} = (\hat{a}_1^{\text{sqz}}, \hat{a}_2^{\text{sqz}}, \ldots)^T$. For a given FWM process it can be written as

$$U_{\text{FWM}} = U_0 P_{\text{sqz}}, \tag{15}$$

where U_0 is the basis change matrix corresponding to the eigendecomposition performed in previous sections. Indeed, if for a given FWM process we call $D = \text{diag}(\eta_1, \eta_2, \ldots)$ the diagonal matrix composed of the eigenvalues of the unitary evolution, then by definition the covariance matrix can be decomposed as $C_{X n\text{modes}} = U_0 D U_0^T$. Finally, the total transformation can be written as

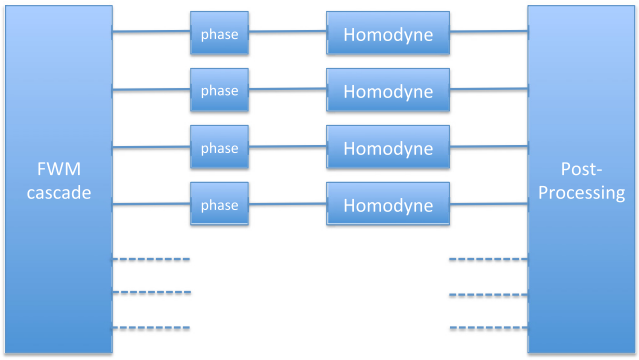

FIG. 6. (Color online) Quantum networks can be constructed by applying phase controlled homodyne detections and postprocessing the signals of the FWM outputs.

$$U_{\text{total}} = O_{\text{post}} P_{\text{homo}} U_{\text{FWM}}, \tag{16}$$

where P_{homo} is a diagonal matrix that sets the quadrature measured by each homodyne detection, and O_{post} is an orthogonal matrix describing postprocessing by computer on the photocurrents measured by the homodyne detections.

We now compare this transformation to a given cluster state matrix U_V. Traditionally, U_V is a matrix that moves from p squeezed modes to cluster state modes, with V the cluster adjacency matrix [26]. Thus the system is equivalent to a cluster state if one can find experimental parameters such that

$$U_V = O_{\text{post}} P_{\text{homo}} U_0 P_{\text{sqz}}. \tag{17}$$

In practice, it is possible to act on the gains of the different FWM processes, the local oscillators phases P_{homo}, and the postprocessing operations O_{post} to make the system achieve the transformation U_V of the clusters state. According to [10], defining $U_V' = U_V R^\dagger$ with $R = U_0 P_{\text{sqz}}$, this problem has a solution if and only if $U_V'^T U_V'$ is a diagonal matrix. Equivalently, if and only if one can write

$$P_{\text{homo}}^2 = U_V'^T U_V'. \tag{18}$$

In that case, one finds that O_{post} is given by

$$O_{\text{post}} = U_V' P_{\text{homo}}^{-1}. \tag{19}$$

Using this formalism, it is thus possible to exploit the entanglement naturally generated by the cascaded FWM processes in order to generate cluster states. We will see in the following how it is possible to optimize the different experimental parameters to achieve some specific clusters.

This concept of postprocessed states is relevant within the framework of measurement based quantum computing [27], where a quantum operation can be performed via the measurement of the nodes of a cluster state. Indeed, while in the current paper we only demonstrate cluster state generation to assess the flexibility of the source, it is possible to target a different

objective matrix U_V that also contains the measurement quadratures of a given quantum operation. More details can be found in [10] and [28]. In the following, we demonstrate how the quantum state generated via cascaded FWM can be easily reconfigured to target a given multimode entangled state U_V without any hardware change, via optimized postprocessing.

V. OPTIMIZATIONS AND SOLUTIONS

For a given cluster state specified by its adjacency matrix V, one can directly check whether using proper phases for homodyne detection (P_{homo}) and postprocessing with a computer (O_{post}) it is possible to realize the cluster state U_V. Furthermore, one can demonstrate that if U_V is a unitary matrix that leads to a cluster defined by V, then for any arbitrary orthogonal matrix O, $U_V O$ leads to the same cluster state [28]. Thus it is possible to run a searching algorithm to find an O matrix that allows us to satisfy our criteria of a on-demand cluster generation. In practice, and as this is numerical calculation, we never find the exact equality in Eq. (18); thus we run a searching algorithm [29] leading to the matrix which is the closest to a diagonal one, then keep only the diagonal terms (renormalized to one) to define the P_{homo} matrix, and finally calculate the values of the nullifiers. This is the optimization procedure which is applied to find the results below.

A. Three-mode cascaded FWM

We first start with the three-mode cascaded FWM process, which we have demonstrated is composed of only two squeezed modes and one vacuum mode. There are only two possible cluster graphs in that case, and as an example we study here only the possibility to generate a linear cluster state. The corresponding U_V matrix can be found in [3]. We choose gains values $G_1 = G_2 = 1.2$ as they give realistic experimental squeezing values. Performing the optimization with an evolutionary algorithm, we find solutions for the three-mode linear cluster state (matrix values given in the Appendix). The normalized nullifiers are {0.22,0.16,0.94}, all below the shot-noise limit, meaning that the three-mode linear cluster state can be generated by the structure of the FWM. But there is no feasible solution when $G_1 = G_2 = 2$, or for higher values of the gain. This can be surprising, but is directly linked to the mode structure at the output of the asymmetrical FWM, where one eigenmode is vacuum, and is getting closer to the first mode while gain increases, making it impossible to be transferred into a cluster state by postprocessing. The nullifier values are summarized in Table I.

TABLE I. (Color online) Normalized variances of the three-mode linear cluster state nullifiers, for different values of the gain.

FWM gain	Nullifier 1	Nullifier 2	Nullifier 3
$G = 1.2$	0.16	0.22	0.94
$G = 1.5$	0.06	0.11	0.93
$G = 2$	0.18	0.22	1.09

TABLE II. Normalized variances of the four-mode linear cluster state nullifiers, for different values of the gain.

FWM gain	Nullifier 1	Nullifier 2	Nullifier 3	Nullifier 4
$G = 1.2$	0.13	0.44	0.13	0.44
$G = 1.5$	0.04	0.25	0.04	0.25
$G = 2$	0.02	0.13	0.02	0.13

B. Four-mode cascaded FWM

In the case of four-mode symmetric cascaded FWM, there are several possible graphs of cluster states. We first focus here on the linear one, whose U_V matrix can also be found in [3]. Using our optimization strategy, we calculate the best possible nullifiers for different values of the gain, as shown in Table II. We see a completely different situation from the three-mode case. As the state impinging on the detectors is already an entangled state, it can be turned into a cluster state with phase controlled homodyne detection and postprocessing more efficiently. In particular, we see that the values of the nullifiers follow roughly those of the squeezing values.

The same procedure can be applied to other cluster shapes, for instance, we tested square and T shape clusters, which showed a very different behavior: in these cases, nullifier value evolution is not monotonous with G values, and there is an optimal gain for each shape. Other shapes could be tested, or other types of clusters such as weighted graph [30]. Hence this system is readily applicable for quantum information processing. One should stress, however, that in order to exhibit cluster statistics it is necessary to precisely control the phase of the local oscillator in each homodyne detection, which can be accomplished for instance with digital locking electronics. Otherwise, it is also possible to build in the optimization routine within a certain range of possible homodyne detection phase, and obtain solutions under these constraints.

VI. SUMMARY

In summary, we demonstrated that cascaded FWM is a scalable system for multimode state generation thanks in particular to its intrinsic phase insensitive character and high nonlinearity. As an example, we theoretically proposed to cascade two and three FWM processes to generate three-mode and four-mode cluster states, respectively, and demonstrated the versatility and reconfigurability. The three-mode cluster state generation is sensitive to the gain values of the FWM processes. We considered the specific situation where the two FWM processes share the same gain value and found that when the gain value is below a certain value, we can construct the three-mode cluster state, but the intrinsic two mode structure of the system prevents one from generating good clusters. Contrarily, in the four-mode case, we found that for a wide range of gain values when the three FWM processes share the same gain value, different graphs of four-mode cluster states can be constructed. Thus we expect that by cascading more FWM processes, multimode cluster states with different graphs can be constructed and this scheme for realizing versatile quantum networks promises potential applications in quantum information processing.

ACKNOWLEDGMENTS

This work is supported by the European Research Council starting grant Frecquam and the French National Research Agency project Comb. Y.C. recognizes the China Scholarship Council. J.J. acknowledge the support from NSFC (Grants No. 91436211, No. 11374104, and No. 10974057), the SRFDP (Grant No. 20130076110011), the Program for Eastern Scholar at Shanghai Institutions of Higher Learning, the Program for New Century Excellent Talents in University (No. NCET-10-0383), the Shu Guang project (No. 11SG26), and the Shanghai Pujiang Program (No. 09PJ1404400). X.X. thanks the National Natural Science Foundation of China (Grant No. 11134003) and Shanghai Excellent Academic Leaders Program of China (Grant No. 12XD1402400).

APPENDIX: CLUSTER MATRICES

Here is the solution for the three-mode linear cluster, with $G = 1.2$:

$$P_{\text{homo3-lin}} = \begin{pmatrix} 0.52 - 0.86i & 0 & 0 \\ 0 & 0.61 - 0.79i & 0 \\ 0 & 0 & 0.93 + 0.36i \end{pmatrix}, \tag{A1}$$

$$O_{\text{post3-lin}} = \begin{pmatrix} 0.97 & -0.12 & 0.23 \\ 0 & -0.88 & -0.48 \\ 0.26 & 0.46 & -0.85 \end{pmatrix}. \tag{A2}$$

The feasible cluster matrix is

$$\begin{pmatrix} 0.21 & 0.67 + 0.30i & 0.41 - 0.49i \\ -0.58i & 0.30 + 0.49i & -0.49 + 0.30i \\ -0.79 & -0.18 + 0.30i & -0.11 - 0.49i \end{pmatrix}. \tag{A3}$$

For the four-mode linear cluster, we find the line shape. The $P_{\text{homo4-lin}}$ is

$$\begin{pmatrix} 0.34 - 0.94i & 0 & 0 & 0 \\ 0 & 0.99 + 0.14i & 0 & 0 \\ 0 & 0 & 0.19 - 0.98i & 0 \\ 0 & 0 & 0 & 0.78 - 0.62i \end{pmatrix}. \tag{A4}$$

The $O_{\text{post4-lin}}$ is

$$\begin{pmatrix} 0.46 & 0.15 & -0.86 & 0.17 \\ 0.20 & -0.73 & 0.11 & 0.65 \\ 0.11 & -0.65 & -0.20 & -0.73 \\ 0.86 & 0.17 & 0.46 & -0.15 \end{pmatrix} \tag{A5}$$

and the cluster matrix is

$$\begin{pmatrix} -0.15 - 0.12i & -0.72 - 0.12i & -0.19 + 0.61i & -0.16 - 0.04i \\ -0.12 + 0.05i & -0.12 - 0.64i & 0.61 - 0.09i & -0.04 + 0.43i \\ 0.20 + 0.60i & 0.08 - 0.17i & 0.10 + 0.39i & 0.59 - 0.25i \\ 0.71 + 0.20i & -0.05 + 0.08i & -0.22 + 0.10i & -0.20 + 0.59i \end{pmatrix}. \tag{A6}$$

[1] S. L. Braunstein and P. van Loock, Rev. Mod. Phys. **77**, 513 (2005).

[2] X. Su, A. Tan, X. Jia, J. Zhang, C. Xie, and K. Peng, Phys. Rev. Lett. **98**, 070502 (2007).

[3] M. Yukawa, R. Ukai, P. van Loock, and A. Furusawa, Phys. Rev. A **78**, 012301 (2008).

[4] S. Armstrong, J.-F. Morizur, J. Janousek, B. Hage, N. Treps, P. K. Lam, and H.-A. Bachor, Nat. Commun. **3**, 1026 (2012).

[5] R. Pooser and J. Jing, Phys. Rev. A **90**, 043841 (2014).

[6] M. Pysher, Y. Miwa, R. Shahrokhshahi, R. Bloomer, and O. Pfister, Phys. Rev. Lett. **107**, 030505 (2011).

[7] M. Chen, N. C. Menicucci, and O. Pfister, Phys. Rev. Lett. **112**, 120505 (2014).

[8] S. Yokoyama, R. Ukai, S. C. Armstrong, C. Sornphiphatphong, T. Kaji, S. Suzuki, J.-i. Yoshikawa, H. Yonezawa, N. C. Menicucci, and A. Furusawa, Nature Photon. **7**, 982 (2009).

[9] J. Roslund, R. Medeiros de Araújo, S. Jiang, C. Fabre, and N. Treps, Nature Photon. **8**, 109 (2014).

[10] G. Ferrini, J. P. Gazeau, T. Coudreau, C. Fabre, and N. Treps, New J. Phys. **15**, 093015 (2013).

[11] C. F. McCormick, V. Boyer, E. Arimonda, and P. D. Lett, Opt. Lett. **32**, 178 (2007).

[12] C. Liu, J. Jing, Z. Zhou, R. C. Pooser, F. Hudelist, L. Zhou, and W. Zhang, Opt. Lett. **36**, 2979 (2011).
[13] Z. Qin, J. Jing, J. Zhou, C. Liu, R. C. Pooser, Z. Zhou, and W. Zhang, Opt. Lett. **37**, 3141 (2012).
[14] V. Boyer, A. M. Marino, P. C. Pooser, and P. D. Lett, Science **321**, 544 (2008).
[15] R. M. Camacho, P. K. Vudyasetu, and J. C. Howell, Nature Photon. **3**, 103 (2009).
[16] A. MacRae, T. Brannan, R. Achal, and A. I. Lvovsky, Phys. Rev. Lett. **109**, 033601 (2012).
[17] A. M. Marino, R. C. Pooser, V. Boyer, and P. D. Lett, Nature (London) **457**, 859 (2009).
[18] R. C. Pooser, A. M. Marino, V. Boyer, K. M. Jones, and P. D. Lett, Phys. Rev. Lett. **103**, 010501 (2009).
[19] J. Jing, C. Liu, Z. Zhou, Z. Y. Ou, and W. Zhang, Appl. Phys. Lett. **99**, 011110 (2011).
[20] J. Kong, J. Jing, H. Wang, F. Hudelist, C. Liu, and W. Zhang, Appl. Phys. Lett. **102**, 011130 (2013).
[21] J. B. Clark, R. T. Glasser, Q. Glorieux, U. Vogl, T. Li, K. M. Jones, and P. D. Lett, Nature Photon. **8**, 515 (2014).
[22] Z. Qin, L. Cao, H. Wang, A. M. Marino, W. Zhang, and J. Jing, Phys. Rev. Lett. **113**, 023602 (2014).
[23] S. L. Braunstein, Phys. Rev. A **71**, 055801 (2005).
[24] R. Boyd, *Nonlinear Optics* (Academic, New York, 1992).
[25] R. Ukai, J.-i. Yoshikawa, N. Iwata, P. Loock, and A. Furusawa, Phys. Rev. A **81**, 032315 (2010).
[26] P. van Loock, C. Weedbrook, and M. Gu, Phys. Rev. A **76**, 032321 (2007).
[27] R. Raussendorf and H. J. Briegel, Phys. Rev. Lett. **86**, 5188 (2001).
[28] G. Ferrini, J. Roslund, F. Arzani, Y. Cai, C. Fabre, and N. Treps, arXiv:1407.5318 (2014).
[29] J. Roslund, O. M. Shir, T. Bäck, and H. Rabitz, Phys. Rev. A **80**, 043415 (2009).
[30] N. C. Menicucci, S. T. Flammia, and P. van Loock, Phys. Rev. A **83**, 042335 (2011).

Chapter 9

Quantum frequency metrology

Contents

Optical frequency combs play a fundamental role in many types of precision measurements, including spectroscopy, absolute frequency determination, optical clocks, and time-distance synchronization. Measurement precision in these applications is generally limited by photon number fluctuations, which scale as $\sqrt{N}$. However, squeezed states of light may be utilized to achieve sensitivity beyond this standard shot-noise limit [14].

In this chapter, we will introduce quantum-enhanced multimode frequency metrology with the SPOPO. We demonstrate a shot-noise limited measurement of the central frequency of an optical pulse. This measurement employs a multi-pixel-spectrally-resolved detector. Furthermore, the signal-to-noise-ratio (SNR) of the central frequency measurement is enhanced by 20% with the appropriate use of an ultrafast squeezed light pulse. In the end, a multimode analysis is presented with the quantum spectrometer.

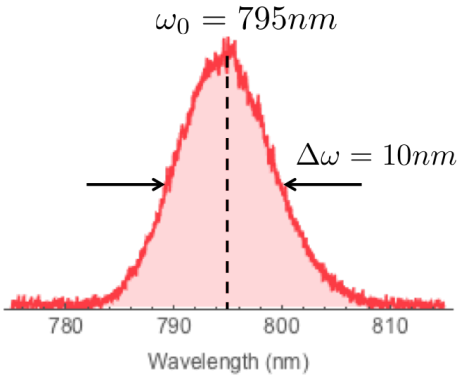

Figure 9.1: The spectrum of the ultrafast laser source. ω_0 and $\Delta\omega$ are the central frequency and the bandwidth of the spectrum, respectively.

9.1 Mode-dependent characters of ultrafast pulses

In chapter 1, ultrafast pulses (optical frequency combs), in frequency domain, are defined in Equ. 1.11. In practice, when we observe an optical frequency comb with a spectrometer, we can't see the individual frequencies, but only the gaussian envelope of Equ. 1.11, as seen in Fig. 9.1, where is presented the spectrum of our laser source, a train of pulses centered at 795 nm with a bandwidth of $\sim$ 10 nm.

In particular, we express the spectral envelop as a gaussian function of frequency ω,

$$\begin{aligned} E(\omega) &= E_0 u(\omega) \\ &\text{with} \quad E_0 \propto \sqrt{N}, \quad \text{and} \quad u(\omega) = \mathcal{A} e^{-\frac{(\omega-\omega_0)^2}{2(\Delta\omega)^2}} \end{aligned} \tag{9.1}$$

where E_0 is the amplitude of the field, and $u(\omega)$ is the mode corresponding a gaussian spectral envelope; N is the photon number within the pulses, ω_0 and $\Delta\omega$ are the central frequency and the bandwidth of the spectrum, respectively, as seen in Fig. 9.1; $\mathcal{A}$ is the normalization factors of the mode $u(\omega)$.

Thus, according to Equ. 9.1, in order to characterize the spectrum of gaussian ultrafast pulses, we need determine the three parameters of pulses: (1) energy (photon number), (2) central frequency (wavelength), (3) bandwidth.

As we did discuss in chapter 4, in practice we can directly adjust the Mira laser to define these three parameters of the spectrum envelope. In the

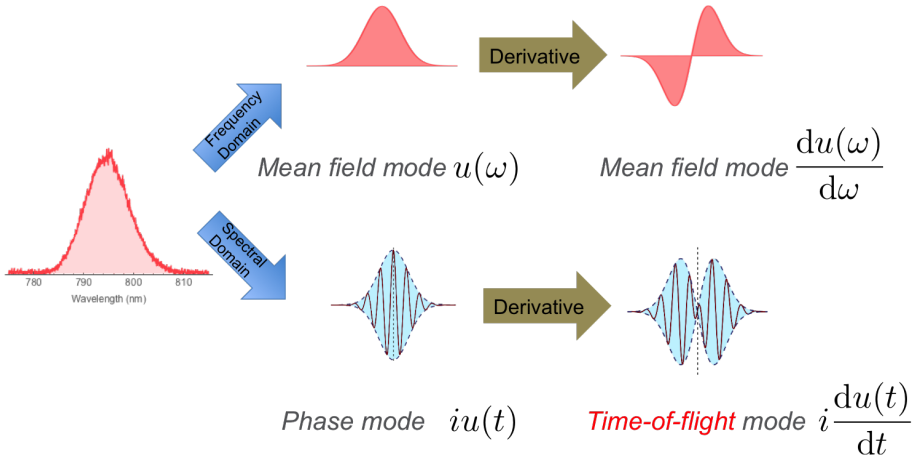

Figure 9.2: From the spectrum of the pulses, we can get the spectral modes and derivative modes in both spectral and time domain.

following, we describe the envelope when there is a small deviation of the these parameters [89].

In the spectral domain, for a small change of the energy δE_0, we have the envelope,

$$E_{\text{energy}}(\omega) \simeq E_0 u(\omega) + \delta E_0 u(\omega). \tag{9.2}$$

Therefore, the mean energy E_0 and the small change of the energy δE_0 are carried in the same mode $u(\omega)$, which is the spectral mode of the pulses, in Fig. 9.1.

For a small shift of the central frequency $\delta\omega$, we have the envelope,

$$\begin{aligned} E_{\text{cenfre}}(\omega) &\simeq E_0 u(\omega - \delta\omega) \\ &\simeq E_0(u(\omega) - \delta\omega \frac{du}{d\omega}), \end{aligned} \tag{9.3}$$

where we see the small shift of the central frequency $\delta\omega$ corresponds to the derivative mode $\frac{du}{d\omega}$ as seen in Fig.9.2, which is the derivative of the spectral mode $u(\omega)$ in Fig. 9.1.

In addition, we simply give a counterpart in time domain. For a small phase shift, $\omega_0 t_\phi$ in the carrier $e^{-i\omega_0 t}$, the electric field of pulses is,

$$\begin{aligned} E(t) &\simeq E_0 u(t) e^{-i\omega_0(t-t_\phi)} \\ &\simeq E_0(u(t) + i\omega_0 t_\phi u(t)) e^{-i\omega_0(t-t_\phi)} \end{aligned} \tag{9.4}$$

where i indicates a $\pi/2$ phase difference, the phase quadrature; t_ϕ is in the temporal mode $u(t)$, as seen in Fig. 9.2.

And for a small time delay t_g in the temporal envelope $u(t)$, the electric field of pulses is,

$$\begin{aligned} E(t) &\simeq E_0 u(t-t_g)e^{-i\omega_0 t} \\ &\simeq E_0(u(t)+t_g\frac{\mathrm{d}u(t)}{\mathrm{d}t})e^{-i\omega_0 t} \end{aligned} \tag{9.5}$$

where the displacement t_g is in the derivative mode $\frac{\mathrm{d}u(t)}{\mathrm{d}t}$, which has $\pi/2$ phase difference with the mode $u(t)$ in the gaussian case, as seen in Fig. 9.2.

9.2 Setup and frequency-resolved measurement

To implement a spectral-mode-dependent detection system, as seen in Fig. 9.3, we develop a frequency-resolved detector. In practice, we use one arm of the multipixel homodyne detection, which is one multipixel detector. As seen in Fig. 9.3 (a), the laser is diffracted with a prism or a grating, and is then focused on the Fourier plane, where we employ a photodiode array, and each pixel of the photodiodes is connected to an amplifier and a data acquisition channel. Therefore, frequency-resolved detection is able to be implemented, similar as the multi-pixel homodyne detection, in Fig. 7.2 (b), where each pixel of the photodiodes corresponds to a specific spectral band. After the data recording, different real gains can be applied to each spectral band. In a result, we can access different real spectral modes via the multipixel detector and the post-processing.

Compared to the multipixel homodyne detection, we can only measure the intensity of the input field via one multipixel detector, and we can always find a basis $\{v_j\}$, and then the electric field is,

$$\hat{E} = \sum_j \hat{b}_j v_j, \tag{9.6}$$

where $\langle \hat{b}_j \rangle \neq 0$, when $j = 1$, and $\langle \hat{b}_j \rangle = 0$, when $j \geq 1$. This is called *mean field basis*, where only the first mode has a mean field, then its shape correspond to the spectrum of pulses.

Hence, for the ith pixel, the pixel mode u_i is defined by the spectral component of the mode v_1, which has a mean field. We have,

$$\hat{I}_i = \hat{a}_i^\dagger \hat{a}_i = \sum_j \int u_i v_j^* \mathrm{d}\Omega \hat{b}_j^\dagger \sum_k \int u_i^* v_k \mathrm{d}\Omega \hat{b}_k, \tag{9.7}$$

where $\hat{a}_i = \sum_j \int u_i^* v_j \mathrm{d}\Omega \hat{b}_j$. The corresponding mean is,

$$\langle \hat{I}_i \rangle = \langle \hat{b}_1^\dagger \hat{b}_1 \rangle | \int u_i^* v_1 \mathrm{d}\Omega|^2. \tag{9.8}$$

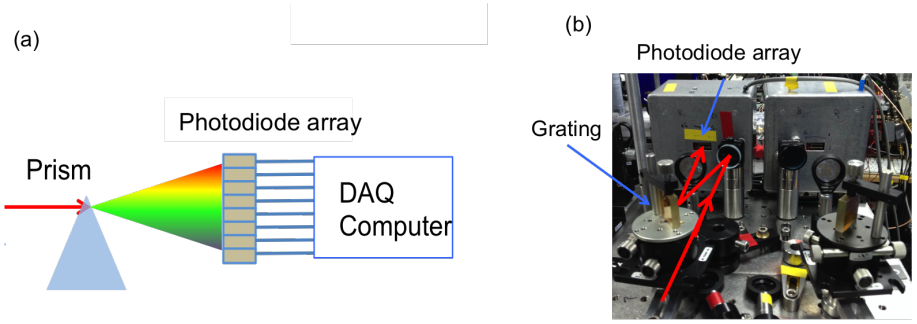

Figure 9.3: Multi-pixel-spectrally-resolved (MPSR) detector. (a) The laser is diffracted with a prism or a grating, and is the focused on the Fourier plane, where we employ a photodiode array, and each pixel of the photodiodes is connected to am amplifier and a data acquisition channel. (b) The experiment setup consists of the photodiode array and the dispersive optical component, the prism (grating).

And,

$$\delta\hat{I}_i \simeq \delta\hat{a}_i^\dagger\langle\hat{a}_\mathrm{i}\rangle + \langle\hat{a}_\mathrm{i}^\dagger\rangle\delta\hat{a}_i \tag{9.9}$$

where $\delta\hat{a}_i = \sum_j \int u_i^* v_j \mathrm{d}\Omega\delta\hat{b}_j$ and $\langle\hat{a}_\mathrm{i}\rangle = \int u_i^* v_1 \mathrm{d}\Omega\langle\hat{b}_1\rangle$.

The corresponding variance is,

$$\Delta^2 I_i = |\langle\hat{a}_\mathrm{i}\rangle|^2\Delta^2 x_i, \tag{9.10}$$

where $|\langle\hat{a}_\mathrm{i}\rangle|^2$ is the optical power on the pixel i, and the $\Delta^2 x_i$ is the variance of $\hat{a}_i$ in the amplitude quadrature.

Above, in the frequency-resolved detector, the pixel mode is defined by the corresponding pixel of the mean field mode, and the intensity of $\{\hat{a}_i\}$ in the pixel mode basis are detected simultaneously.

9.3 A quantum spectrometer

9.3.1 Principle

Here we present a quantum spectrometer with the frequency-resolved multi-pixel detector as seen in Fig. 9.4 [91]. A synthetic beam is created by mixing nonclassical vacuum state with the optical beam to be measured. The measurement is achieved with the frequency-resolved apparatus, which is able to select a desired mode by post-processing.

The vacuum squeezing from the SPOPO consists of a set of eigenmodes $\{u_j^\mathrm{s}\}$, as seen in Fig. 7.5, $\vec{a}^\mathrm{s} = (\hat{a}_1^\mathrm{s}, \hat{a}_2^\mathrm{s}, \dots)^\mathrm{T}$, and the intense beam is $\vec{a}^\mathrm{LO} =$

$(\hat{a}_1^{\mathrm{LO}}, \hat{a}_2^{\mathrm{LO}}, \dots)^{\mathrm{T}}$ with the modes $\{u_i^{\mathrm{LO}}\}$, which correspond to the spectral profile detected by the multipixel detector.

The squeezed vacuum and the intense beam are mixed by the beam splitter, as seen in Fig. 9.4. After the beam splitter, the mixed light field to be detected by the multipixel detector is,

$$\hat{a}_{\mathrm{BS}} = r\vec{a}^{\mathrm{LO}} + t\vec{a}^{\mathrm{s}}, \tag{9.11}$$

where real t, r are the transmitivity and reflectivity, respectively, $t^2 + r^2 = 1$.

As discussed in Equ. 9.7, the pixel modes are determined by the mean field modes of the intense beam, and hence, here the pixel modes are the $\{u_i^{\mathrm{LO}}\}$. And then for the pixel i of the photodiode array, the photocurrent is,

$$\hat{I}_i = \left(r(\hat{a}_i^{\mathrm{LO}})^\dagger + t(\hat{a}_i^{\mathrm{sprime}})^\dagger\right)\left(r\hat{a}_i^{\mathrm{LO}} + t\hat{a}_i^{\mathrm{sprime}}\right), \tag{9.12}$$

where $\hat{a}_i^{\mathrm{sprime}} = \sum_j \int (u_i^{\mathrm{LO}})^* u_j^{\mathrm{s}} \mathrm{d}\Omega \hat{a}_j^{\mathrm{s}}$.

Thus when $\hat{a}_i^{\mathrm{sprime}}$ is vacuum the corresponding mean is,

$$\langle \hat{I}_i \rangle = r^2 (\hat{a}_i^{\mathrm{LO}})^\dagger \hat{a}_i^{\mathrm{LO}} = r^2 P_{\mathrm{LO}}^i, \tag{9.13}$$

where P_{LO}^i is the intensity of $\hat{a}_i^{\mathrm{LO}}$.

When $t \gg r$, $\delta\hat{a}_i^{\mathrm{sprime}} = \hat{a}^{\mathrm{sprime}}$ (vacuum), and $\delta\hat{a}_i^{\mathrm{LO}} = \hat{a}_i^{\mathrm{LO}} - \langle \hat{a}_i^{\mathrm{LO}} \rangle$ (intense). And the corresponding fluctuation operator is,

$$\delta\hat{I}_i \simeq tr\left(\langle (\hat{a}_i^{\mathrm{LO}})^\dagger \rangle \delta\hat{a}_i^{\mathrm{sprime}} + (\delta\hat{a}_i^{\mathrm{sprime}})^\dagger \langle \hat{a}_i^{\mathrm{LO}} \rangle\right) = tr\sqrt{P_{\mathrm{LO}}^i}\hat{x}_i^{\mathrm{sprime}}, \tag{9.14}$$

where $\hat{x}_i^{\mathrm{sprime}}$ is the amplitude quadrature of $\hat{a}_i^{\mathrm{sprime}}$. And thus the variance of $\hat{I}_i$ is from the amplitude quadrature of $\hat{a}_{\mathrm{BS}}$,

$$\Delta^2\hat{I}_i = (\delta\hat{I}_i)^2 = t^2 r^2 P_{\mathrm{LO}}^i \Delta^2 \hat{x}_i^{\mathrm{sprime}} \tag{9.15}$$

where $r^2 P_{\mathrm{LO}}^i$ is the optical power detected on the pixel i.

When post-processing a real gain $\vec{g} = \mathcal{C}(m_1/\sqrt{P_{\mathrm{LO}}^1}, m_2/\sqrt{P_{\mathrm{LO}}^2}, \dots)^{\mathrm{T}}$ on each pixel $\delta\hat{I}_i$, which allows to access the mode $m = \{m_i u_i^{\mathrm{LO}}\}$, where $\sqrt{P_{\mathrm{LO}}^i}$ is the normalization factor and $\sum_i m_i^2 = 1$, the corresponding fluctuation operator is,

$$\delta\hat{I}_m = \mathcal{C}\sum_i \frac{m_i}{\sqrt{P_{\mathrm{LO}}^i}}\delta\hat{I}_i = \mathcal{C}tr\sum_i m_i \hat{x}_i^{\mathrm{sprime}} = \mathcal{C}tr\hat{x}_m^{\mathrm{Sprime}} \tag{9.16}$$

where $\hat{x}_m^{\mathrm{Sprime}} = \sum_i m_i \hat{x}_i^{\mathrm{sprime}}$, corresponding a new mode $u_m^{\mathrm{LO}} = (m_1 u_1^{\mathrm{LO}}, m_2 u_2^{\mathrm{LO}}, \dots)^{\mathrm{T}}$.

Therefore, the mean of $\hat{I}_m$ is proportional to the sum of the amplitude of the pixel mode $\hat{a}_m^{\mathrm{LO}}$,

$$\langle \hat{I}_m \rangle = \mathcal{C}\langle \sum_i \frac{m_i}{\sqrt{P_{\mathrm{LO}}^i}} \hat{I}_i \rangle = \mathcal{C} r^2 \sum_i m_i \sqrt{P_{\mathrm{LO}}^i} \tag{9.17}$$

And the variance is,

$$\Delta^2 \hat{I}_m = \mathcal{C}^2 t^2 r^2 \Delta^2 \hat{x}_m^{\mathrm{sprime}} \tag{9.18}$$

therefore the signal-to-noise ratio is,

$$\frac{\langle \hat{I}_m \rangle}{\sqrt{\Delta^2 \hat{I}_m}} = \frac{r \sum_i m_i \sqrt{P_{\mathrm{LO}}^i}}{t\sqrt{\Delta^2 \hat{x}_m^{\mathrm{sprime}}}} = \frac{r \sum_i m_i \sqrt{P_{\mathrm{LO}}^i}}{t \sum_j \int (u_m^{\mathrm{LO}})^* u_j^{\mathrm{s}} \sqrt{\Delta^2 \hat{x}_j^{\mathrm{s}}}}. \tag{9.19}$$

We see when the signal is fixed, the SNR is proportional to the inverse of the fluctuations, $\sum_j \int (u_m^{\mathrm{LO}})^* u_j^{\mathrm{s}} \sqrt{\Delta^2 \hat{x}_j^{\mathrm{s}}}$, which is from the fluctuations of the transmitted beam. Thus, the SNR can be enhanced via squeezing the corresponding mode of the transmitted vacuum.

In the SPOPO, the spectral mode and the derivative mode are similar to the first and the second eigenmodes as seen in Fig. 7.5, which are squeezed in the amplitude and phase quadrature, respectively. It is possible to use the SPOPO resource to enhance the measurement sensitivity of the parameters associated to the corresponding modes.

9.3.2 Experimental configuration

Based on the frequency-resolved multipixel detector, we measure a displacement of the central frequency $\delta\omega$, as seen in Fig. 9.4. First, a quantum limited measurement is implemented when the squeezing is blocked; second, we employ the vacuum squeezing of the SPOPO to do quantum-enhanced measurement.

The experimental configuration of the quantum spectrometer is presented in Fig. 9.5. The BS mixes the output of the SPOPO and the local oscillator, which are the squeezed vacuum and the laser output beam, respectively. In the experiment, to implement the quantum spectrometer, we locked the amplification and the relative phase between the local beam and the output of the SPOPO. We also use the shutter to control the locking system to achieve the locked vacuum squeezing.

In Fig. 9.5, SG 1 and SG 2 modulate the signal beam with 625 kHZ on PZT A , and the pump beam with 829.5 kHz on PZT B, respectively. The amplification and the relative phase between the local beam and the output

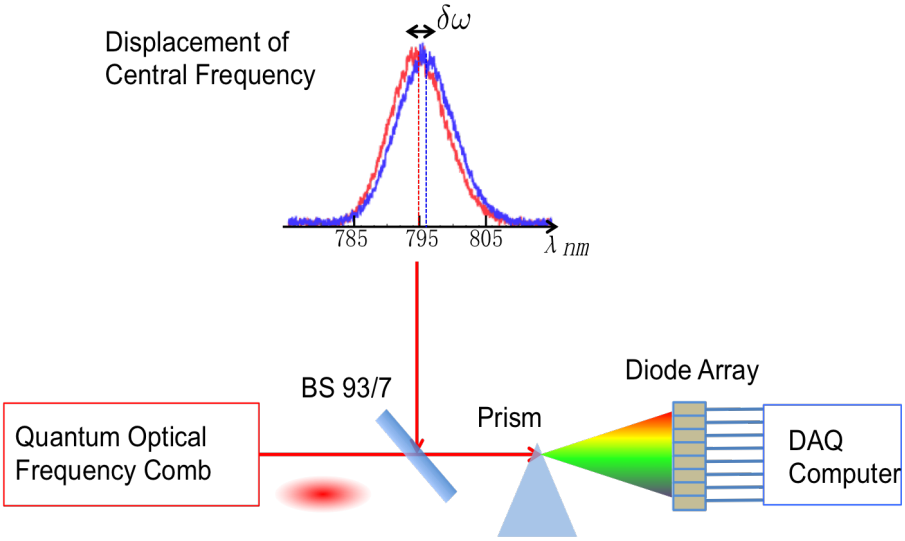

Figure 9.4: The scheme of the quantum spectrometer. The frequency displaced beam is detected by a frequency resolved multi-pixel apparatus after being mixed with pulses from a quantum frequency comb using a 93% transmission beam splitter (BS).

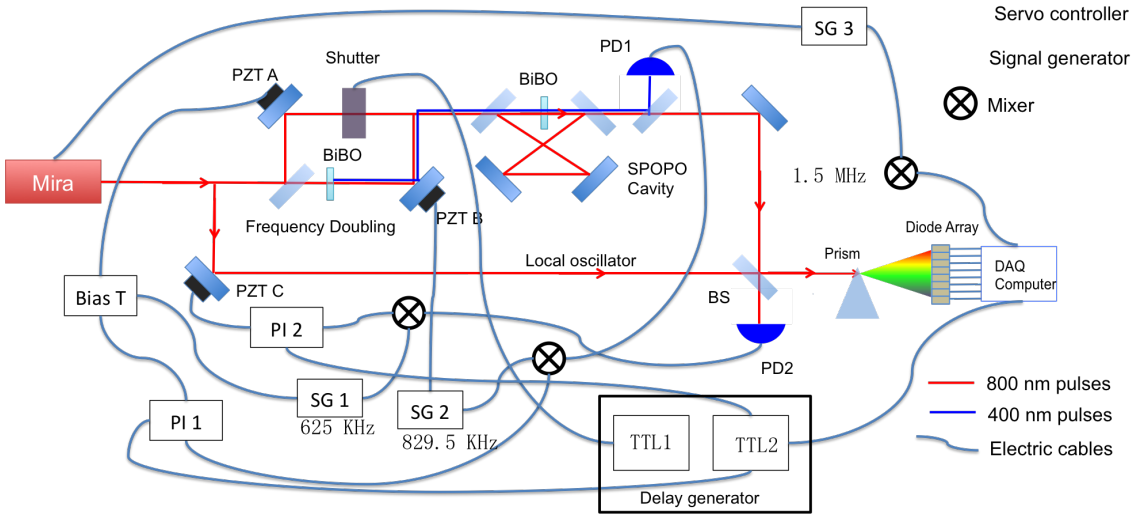

Figure 9.5: The scheme of the quantum spectrometer.

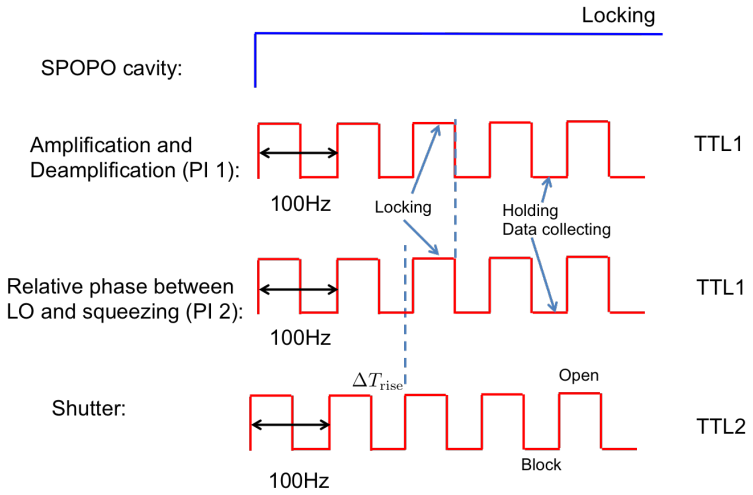

Figure 9.6: The time sequence of the vacuum squeezing locking. Two TTL signal sequences control the locking: TTL1 controls the same shutter as in the amplification and deamplification locking, TTL2 controls the both PIs of amplification (deamplification) and homodyne locking. In each cycle, when the shutter is open, we can lock both amplification and homodyne; When the shutter blocks the signal, the two PIs hold the locking phase, and we collect the vacuum squeezing data.

of the SPOPO are locked by the servo controllers PI1 and PI2, acting on PZT A and PZT C, respectively. PZT A , PTZ B and PZT C correspond to PZT 1, PZT2 and PZT 5 in Fig. 4.2. And a delay generator controls the locking system by two TTL sequences, as seen in Fig. 7.8. We collect 2000 points in each cycle, 5 ms for each pixel when locked.

As the quantum spectrometer, as seen in Fig. 9.4, can only measure the amplitude of the synthetic beam after the beam splitter, we make squeezing and anti squeezing via locking the SPOPO on deamplification and amplification, respectively.

Here we construct a covariance matrix directly from the measurements without normalizing to the corresponding shot noise, which is defined[1],

$$V_{ij} = \frac{1}{n}\sum_{k}^{n}(\vec{s}_i(k) - \mu_i)(\vec{s}_j(k) - \mu_j), \tag{9.20}$$

where $\vec{s}_i(k)$ is the kth data in the measurement data list of the pixel i, μ_i is the mean of $\vec{s}_i$. In the experiment, we obtained the vacuum covariance matrix with transmitted squeezing V_{sqz}, anti squeezing V_{asqz}, vacuum (the squeezing is blocked) V_{shot}, and without light (dark noise) V_{dark}, respectively, as seen in Fig. 9.7.

9.3.3 Central frequency measurement

Experimentaly, we modulate the Mira laser directly to give a displacement $\delta\omega$. We modulate on the same PZT used for the spectral locking inside the Mira laser.

The displacement of central frequency $\delta\omega$ corresponds to the derivative mode, as seen in Fig. 9.8. We obtain $\delta\omega$ by post-processing the data via projecting onto the corresponding derivative mode.

In practice, the normalized spectral modes is composed of the diagonal elements of the shot noise covariance matrix V_{shot}, which is quantum limited,

$$m_{\text{spec}} = diag(V_{\text{shot}}) \tag{9.21}$$

And the derivative mode m_{de} is the derivative of the gaussian function which is the fit of the m_{spec}, as seen in Fig. 9.8.

The spectral mode and the derivative mode are similar to the first and the second eigenmodes of the SPOPO, as seen in Fig. 7.5. The spectral mode is

[1]Here the covariance corresponds to what is directly measured, and it is convenient for data collection and analysis, which is different from the covariance matrix representing a gaussian state, introduced in Chapter 2.

squeezed when the deamplificiation is locked; the derivative mode is squeezed when the amplification is locked. According to the principle of the quantum spectrometer, to increase the SNR of the central frequency measurement, we can apply the corresponding derivative mode.

In practice, as in Equ. 9.16, we apply a gain $\vec{g}_{\mathrm{de}} = \{\frac{m^i_{\mathrm{de}}}{\sqrt{P^i_{\mathrm{LO}}}}\}$ on each pixel[2], where $\sqrt{P^i_{\mathrm{LO}}}$ is the normalization factor. Then the corresponding signal is

$$S_{\mathrm{spec}} = \sum_i \langle \vec{g}^i_{\mathrm{de}} \vec{I}_i \rangle. \tag{9.22}$$

As the derivative mode is squeezed when deamplificaition is locked, the corresponding variance is

$$\Delta^2 \hat{x}_{\mathrm{spec}} = \vec{g}^{\mathrm{T}}_{\mathrm{de}} V_{\mathrm{asqz}} \vec{g}_{\mathrm{de}}. \tag{9.23}$$

Thus the signal-to-noise ratio is $\frac{S_{\mathrm{spec}}}{\sqrt{\Delta^2 \hat{x}_{\mathrm{spec}}}}$. And we verify the noise doesn't depend on the shift of the center frequency we modulate, which is almost the same as the one when without modulation.

After applying a gain corresponding to the derivative of the optical spectral mode on the mean of each pixel and the covariance matrix shown in the previous section, a 15% quantum enhancement of the signal-to-noise ratio is observed as seen in Fig. 9.8, where the red and the blue curves correspond to the SNR with coherent vacuum (the squeezing is blocked) and squeezed vacuum, respectively.

The sensitive of the shot-noise limited measurement (quantum Cramer-Rao band) is defined as [89],

$$\delta\omega_{\mathrm{SQL}} = \frac{\Delta\omega}{\sqrt{N}} = \frac{\Delta\omega_{\mathrm{FWHM}}}{2\sqrt{2ln2} \cdot \sqrt{N}}, \tag{9.24}$$

where in the experiment, $\Delta\lambda \simeq$10 nm and $N \simeq 4 \times 10^{16}$ photons/second ($\sim$ 10 mW power). Therefore, the sensitive of shot noise limit is $\sim$ 60 kHz/$\sqrt{\mathrm{Hz}}$, which is much smaller the repartition rate of the pulses 76 MHz. The quantum spectrometer increases the signal-to-nosie ratio by $\sim$15%, thus the sensitivity is quantum-enhanced to $\sim$ 50 kHz/$\sqrt{\mathrm{Hz}}$.

9.3.4 Multimode analysis of frequent metrology

As in the quantum resource of the SPOPO many modes are squeezed, here we present a multimode analysis of the quantum spectrometer. Using the same

[2]Here we can replace P^i_{LO} by corresponding shot noise, which is to normalize the data for each pixel.

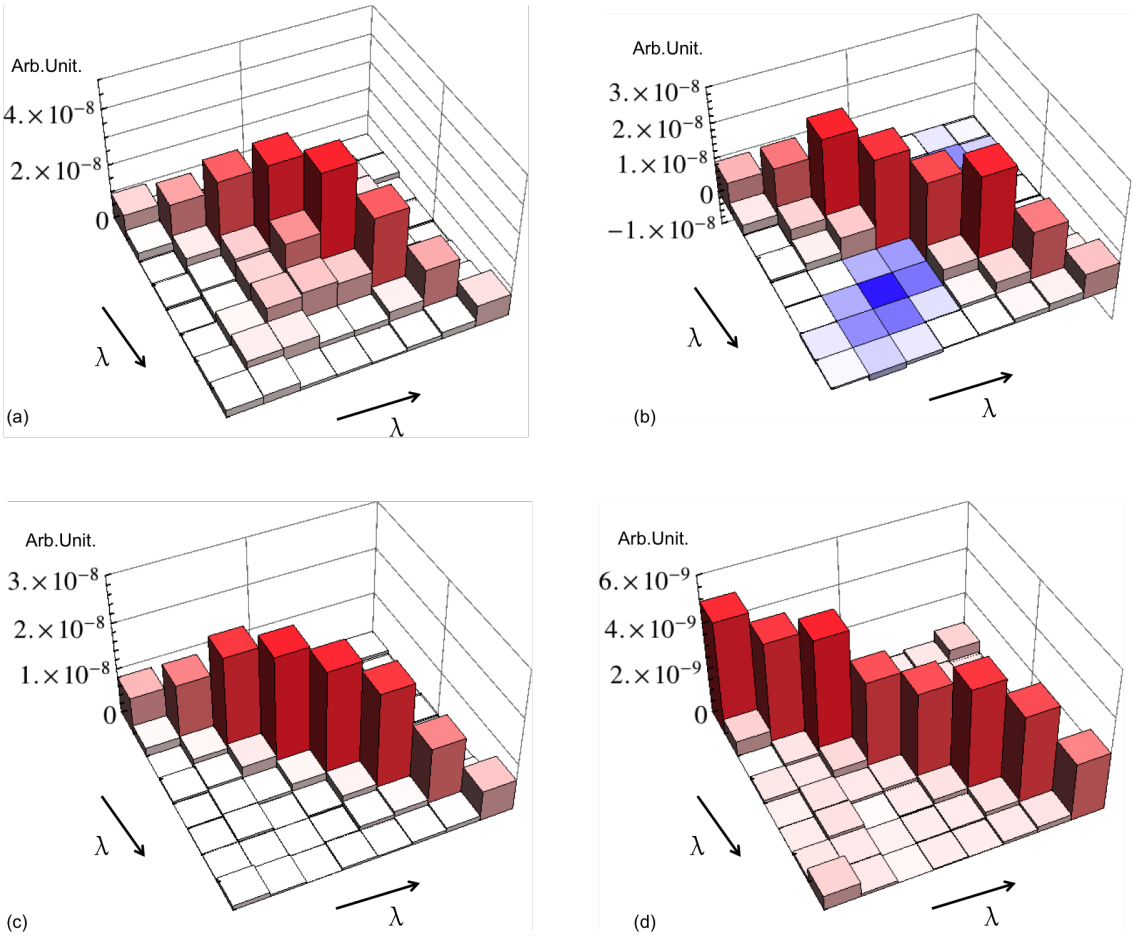

Figure 9.7: The covariance matrix measured via the multi-pixel detector. (a) (b) (c) (d) are the covariance matrix of squeezing $V_{\rm sqz}$, antisqueezing $V_{\rm asqz}$, shot noise $V_{\rm shot}$ and electric dark noise $V_{\rm dark}$, respectively.

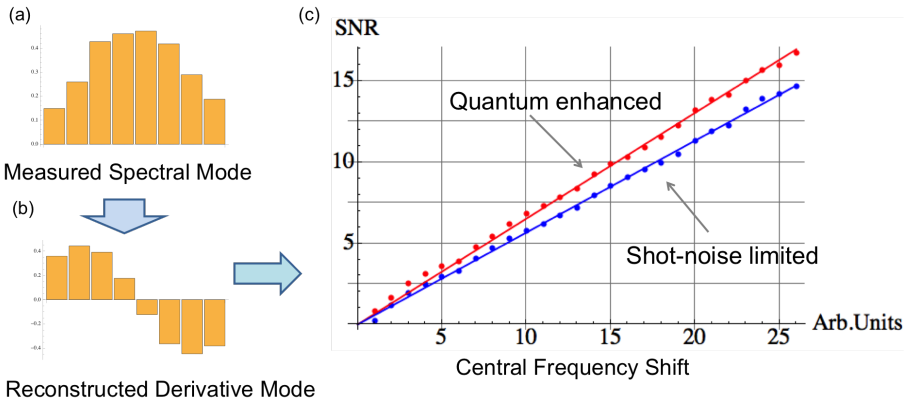

Figure 9.8: Quantum enhanced signal-to-noise ratio (SNR). (a) and (b) are the specral mode and the derivative mode, corresponding the displacement of the mean power and the central frequency, respectively. (c). The red and the blue curves correspond to the SNR with coherent vacuum (the squeezing is blocked) and squeezed vacuum, respectively.

experimental setup for measuring the central frequency shift, we apply the spectral mode and the derivative mode, corresponding to the mean energy shift and central frequency shift, respectively.

In the experiment, we modulate the Mira similarly as in the previous experiment, the transmitted beam is vacuum, the output of the SPOPO with amplification locking and deamplification locking. As seen in Fig. 9.9, the signal-to-noise ratio of the energy shift (blue curve) and the central frequency shift (red curve), corresponding to the spectral mode and the derivative mode, respectively, is presented. As the spectral mode is squeezed and the derivative mode is anti-squeezed, when the amplification of the SPOPO is locked, the SNR of the energy shift is best in Fig. 9.9 (d), and similarly, the SNR of the central frequency shift is best in Fig. 9.9 (c), the same as the in Fig. 9.8.

Benefitting from the multimode squeezing of the SPOPO, multimode quantum enhanced frequency metrology can be achieved. The quantum spectrometer can extend to measure more parameters of the electric field of pulses, such as the bandwidth $\Delta\Omega$, the group velocity, etc., via post-processing different modes. We can potentially improve the sensitivity of many parameters of ultrafast pulses beyond shot noise limit.

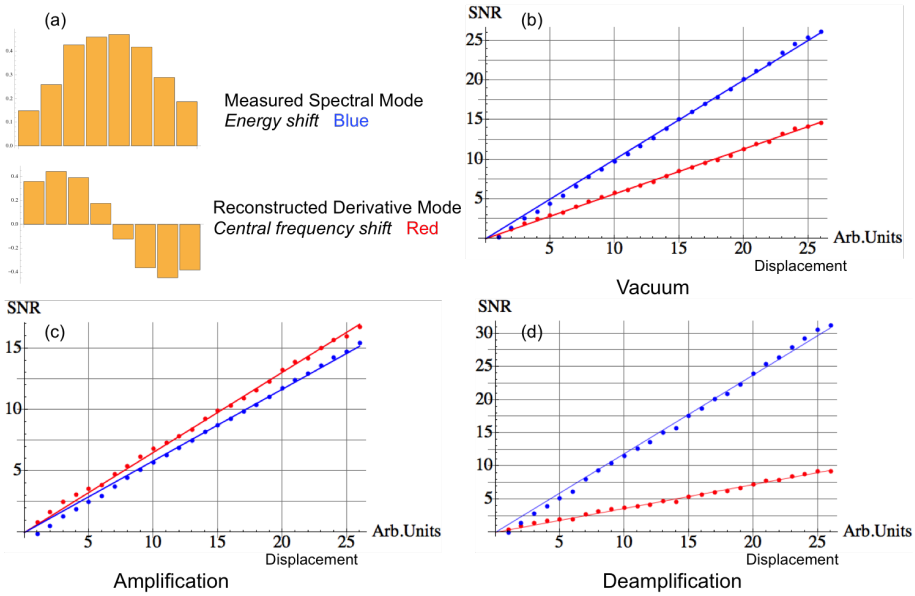

Figure 9.9: The signal-to-noise ration (SNR) of the energy shift and the central frequency shift. The SNR of the energy shift (blue curve) and the central frequency shift (red curve), corresponding to the spectral mode and the derivative mode, respectively, are measured with the quantum spectrometer. (a) The spectral mode (up) and the derivative mode (down); (b) corresponds to the SNR of shot noise limit, (c) and (d) are the SNR when the quantum comb is operated in amplification and deamplification, respectively.

Conclusion and Perspective

Conclusion

In this thesis, we have demonstrated a multimode quantum resource, synchronized pumped optical parametric oscillators (SPOPO), and its applications, such as constructing cluster states, quantum computing, and quantum frequency metrology.

From the SPOPO theory, we have built a model to simulate the quantum state of the SPOPO. Using this model, we simulated the processes of the SPOPO with experimental parameters, and calculated the corresponding supermodes and squeezing values; furthermore, we projected the supermodes onto a chosen spectral-band basis, similar as the homodyne measurements, and then obtained an eight-mode covariance matrix.

Experimentaly, we directly obtained ~ 5.5 dB squeezing for the SPOPO, which is ~ 8 dB with correction of the measurement loss and the electric dark noises. In order to characterize multimode property of the SPOPO, we constructed a sixteen-spectral-band basis with the ultrafast pulse shaping technique. The sixteen-mode covariance matrix, describing the state of the SPOPO, is obtained via homodyne measurements. More than 12 eigenmodes are significantly squeezed.

With the multimode resource, the SPOPO, we developed a quantum-network simulator via ultrafast pulse shaping. This simulator is able to access the quantum fluctuation of any specific mode via shaping the local oscillator in the homodyne detection. Hence, for the simulator, arbitrary gaussian quantum networks are achieved via measurement processes. We emulated many up-to-twelve-node clusters, and verified that all the nullifiers were squeezed experimentally. And we implemented a six-partite secret sharing protocol. The simulator gave the experimental fidelities of the secret sharing in all the ten partitions, which match well with the predictions.

To implement quantum computing and quantum metrology, we devel-

oped a frequency resolved multipixel apparatus, which is able to measure all the frequency-band modes simultaneously. We demonstrated the feasibility criteria of multipixel homodyne detection to realize measurement based quantum computing. Using the criteria, a line-shape-eight-node cluster is implemented by multipixel homodyne detection; more clusters are potentially to be realized with this flexible system.

With the frequency resolved multipixel apparatus, we developed a multimode quantum spectrometer. We obtained the signal-to-noise ratio (SNR) of the central frequency shift in optical pulses beyond the standard quantum noise limit. $\sim 15\%$ enhancement of sensitivity, compared to using a coherent resource, was obtained. Also we extended the quantum spectrometer to multimode via post-processing different modes. With the setup, the measurement of the mean energy shift also exhibited the SNR beyond the standard quantum noise limit.

In the collaboration with East China Normal University, Shanghai, based on the system, cascading four wave mixing of Rubidium atomic gas, we developed a proposal to implement versatile cluster states via phase-controlled homodyne measurements and post-processing.

Perspective

Scalability and coherence

Generally, for quantum computers, complex task demands large-scale and highly correlated quantum networks. Scalability and coherence are two big challenges for quantum resources, which are referring to highly multimode and highly squeezed in continuous variable regime. The SPOPO is an intrinsic multimode resource. We can access more modes and different correlations via measurement processes.

However in practice, we still have some unexpected losses in the generation and measurement processes, and as a result, we didn't get very good squeezing compared to the OPO using continuous lasers or as many supermodes as the SPOPO theory predicted, as seen in Fig .9.10 [20]. We see that, in Fig. 9.10, experimental squeezing values in 4-, 6-, 8-band cases and simulation results in 8-band case have the same trend, but in the simulation, high order eigenmodes are better than that from experiments.

In the generation, from the calculation in Chapter 3, we see that the number of supermodes depends on the bandwidth of corresponding reflectivity spectra. Thus the optics, especially in the SPOPO cavity, need have a wide

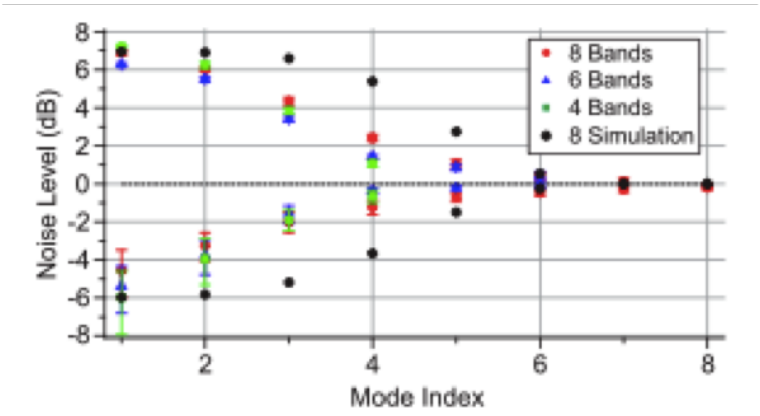

Figure 9.10: Squeezing of eigenmodes. Experimental squeezing values in 4-, 6-, 8-band cases and simulation results in 8-band case are presented.

flat reflectivity spectrum. In the work we were using the mirrors with ~ 100 nm wide reflectivity spectrum, which has the same high reflectivity in the range of 750-800 nm. But the crystal coating has narrower reflectivity spectrum, so improving the crystal coating is possible to get more supermodes. Besides, we didn't compensate the dispersion in the SPOPO cavity or lock the CEO of the source laser, which are both possible to introduce some loss in especially high order supermodes.

In the measurement, as the spectral bandwidth of Hermit-Gaussian-function-like supermodes are wider and wider in high orders, therefore, the local oscillator can not match with the high order supermodes. Furthermore, in the multipixel homodyne detection, we can only obtain less than 4 dB squeezing compared to 5 dB in the single homodyne detection. The is because, in the multipixel homodyne detection, we have extra loss from the grating, bad quantum efficiency and electric dark noise properties. Therefore, in the near future, we can improve the multipixel homodyne detection from these mentioned aspects.

Besides, the feasibility criteria we had for measurement based quantum computing doesn't fully use all the experimental degrees of freedoms, such as the pixels in the shaper or in the multipxiel homodyne detection. Although the multipxiel homodyne dectection and post-procesing can only do a sub-universal quantum operations, if fully use the experimental setup, it is still very promising to do quantum computing in a flexible fashion.

Going to non-gaussian

For measurement based quantum computing, the universal computation

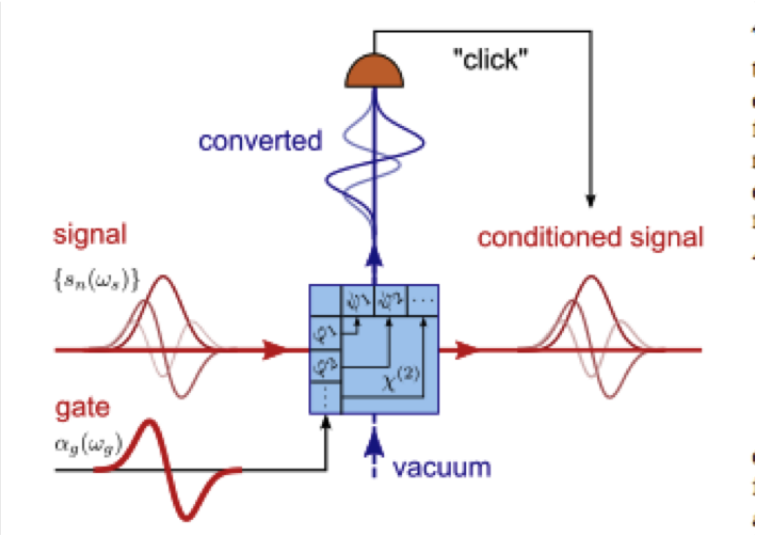

Figure 9.11: Nonlinear pulse gate.

set [54] in the continuous variable regime is $\{e^{is\hat{x}}, e^{is\hat{x}^2}, e^{i\hat{x}^3}, e^{is(\hat{x}^2+\hat{p}^2)}\}$, which are the phase gate, controlled-z C_z gate, cubic gate, Fourier transform, respectively. Except the non-gaussian cubic gate, the others are gaussian operations, which can be implemented with gaussian states (squeezing) and homodyne measurements.

Yet till now, we haven't found efficient experiments to implement the cubic gate in the continuous variable regime. Without non-gaussian operations we cannot fully use the advantage of quantum computing [11]. And the first step to do non-gaussian is single photon extraction from squeezed states [56].

In the multimode case of the SPOPO, our colleagues V.Averchenko et al developed a theory of nonlinear pulse gate, as seen in Fig. 9.11. Based on the principle of $\chi(2)$ sum frequency process, we can extract single photons in a specific mode (pulse shape).

Pump shaping

We already knew that the shape of supermode depends on the pume shape and the phase matching, demonstrated in Equ. 3.35 in Chapter 3. Thus if use different pump shapes, we can get a set of different supermodes. In practice, we can arbitrarily shape the pump with ultrafast pulse shaping. As seen in Fig. 9.12, for the SPOPO, we can control both the pump and the measurement process to get a desired quantum state. Furthermore, the computer can do a real-time feedback loop to automatically search a target quantum state based on the principle of the evolution algorithm.

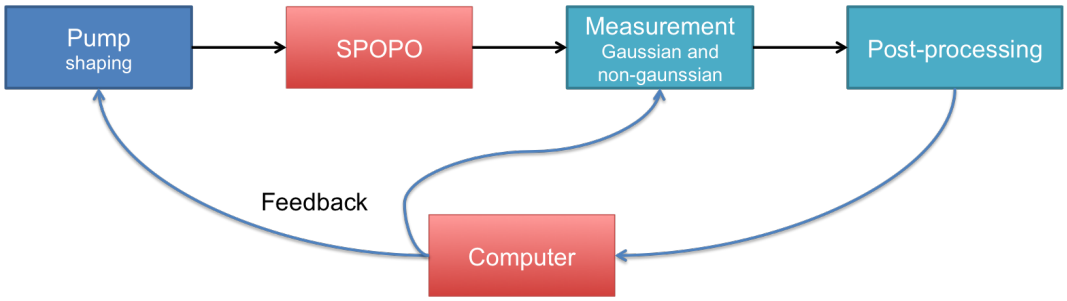

Figure 9.12: Squeezing of eigenmodes.

Implement new physics

As the SPOPO is intrinsically a multimode quantum resource, it is a good candidate to explore multimode quantum physics. For instance, topological entanglement entropy (TEE), a kind of highly multimode entanglement [19], which potentially has an advantage in quantum computing, demands less squeezing and has less errors. Therefore, we can implement TEE when we can access more modes in the SPOPO. Besides, many quantum protocols, such as boson sampling in the continuous variable regime [80] [23], and multimode EPR steering, etc. are possible to be implemented with the SPOPO.

Appendix

We present the design of the electric circuits for the multipixel detector, which is applied for a 1-D silicon photodiode array with 16 pixels(Hamamatsu, model S4111-16Q, $\sim 90\%$ quantum efficiency, sensor size one pixel 1.45×0.9mm).

15/02/2013

Schéma Ampli Photodiode

1/16 pour 16 voies.

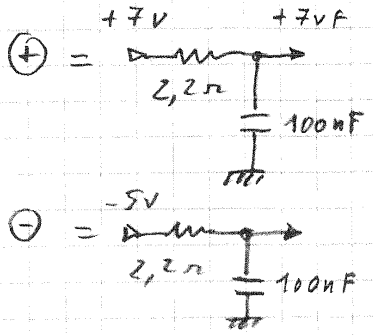

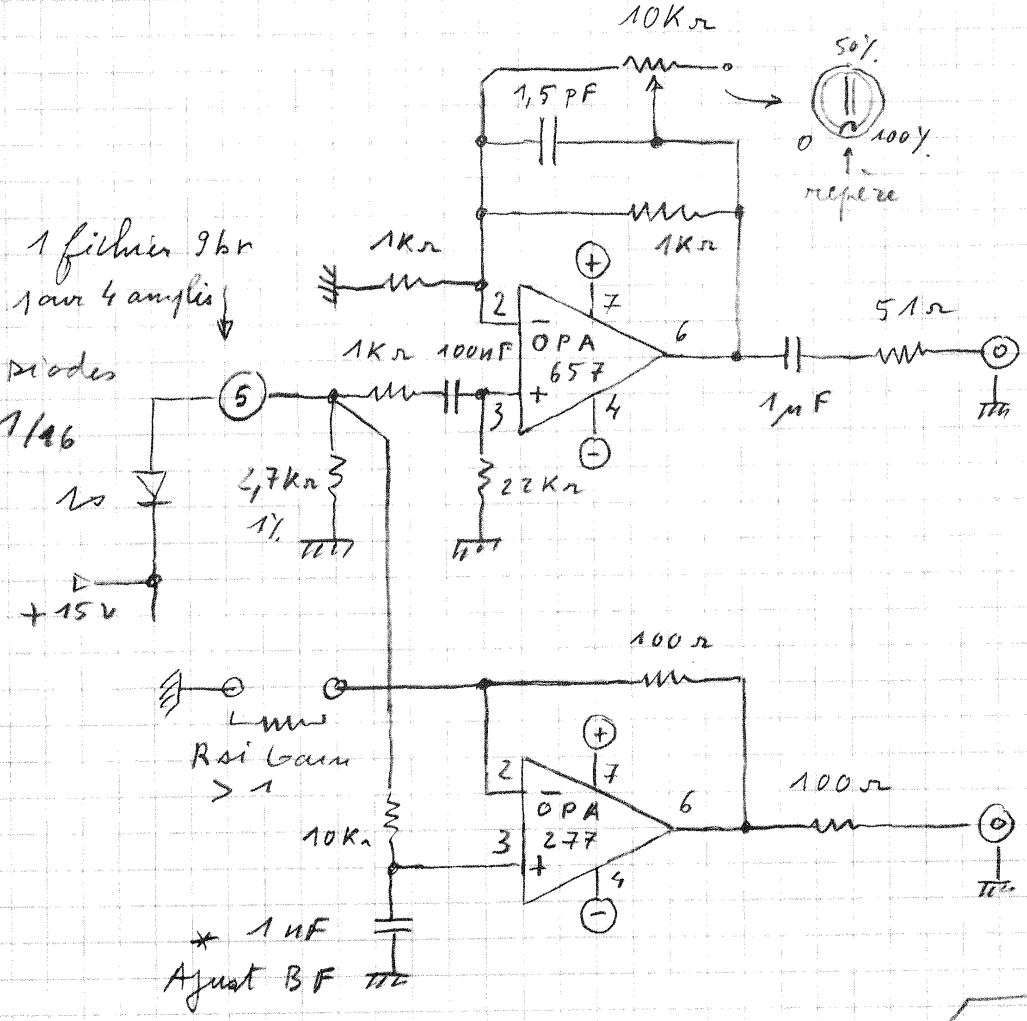

Schéma du Support.

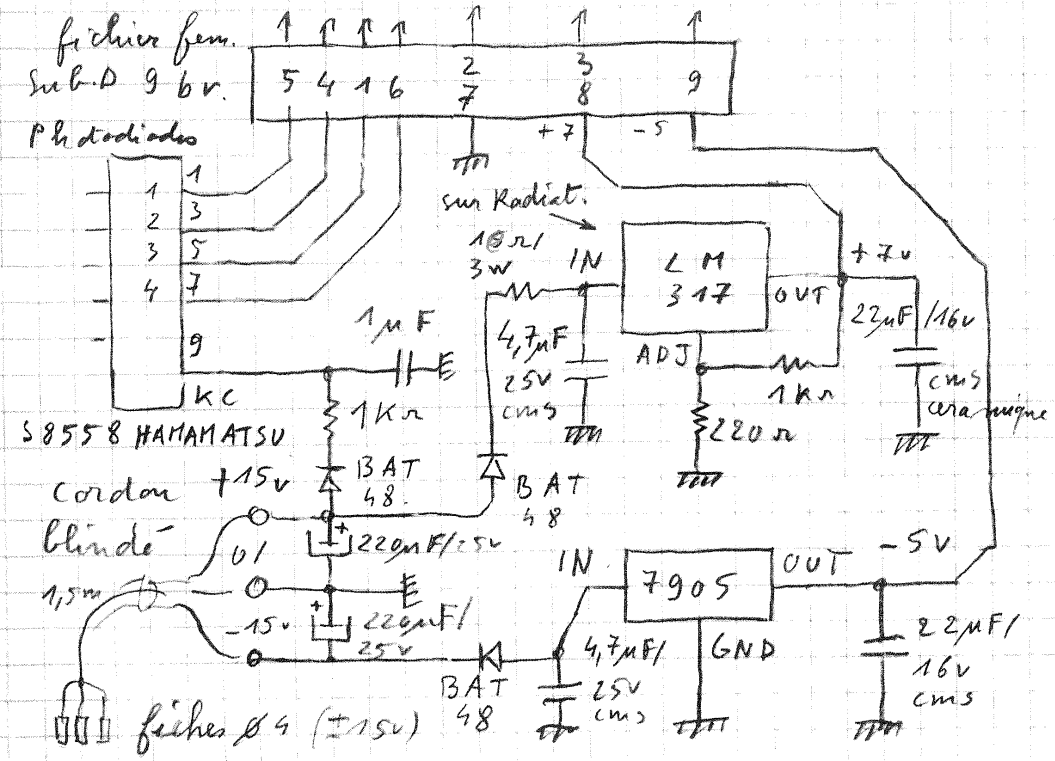

Ent.	N° b	Fichier
+7v	3, 8	1, 2, 3, 4
-5v	9	"
0/	2, 7	"
1 (1ht)	5	
2	4	1
3	1	
4	6	
5	5	
6	4	2
7	1	
8	6	
9	5	3
10	4	
11	1	
12	6	
13	5	4
14	4	
15	1	
16	6	

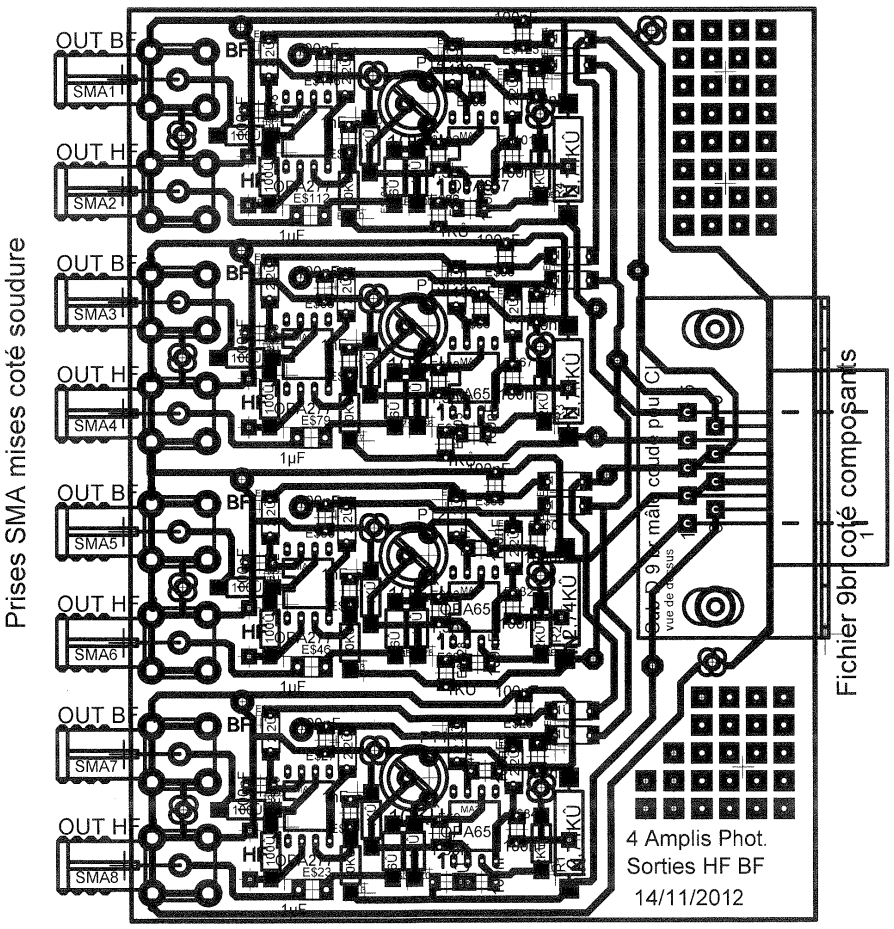

Pin	Fonction
1	Anode phot. 3
2	GND
3	+7V
4	Anode phot. 2
5	Anode phot. 1
6	Anode phot. 4
7	GND
8	+7V
9	-5V

Bibliography

[1] G. Adesso, A. Serafini F. Illuminati, Extremal entanglement and mixedness in continuous variable systems, Phys. Rev. A 70, 2, 022318 (2004).

[2] S. Armstrong, J.-F. Morizur, J. Janousek, B. Hage, N. Treps, P. K. Lam, and H.-A. Bachor, Nature Communications 3, 1026 (2012).

[3] S. Armstrong, M. Wang, R. Y. Teh, Q. Gong, Q. He, J. Janousek, H.-A. Bachor, M. D. Reid, and P. K. Lam, Nature Physics 11, 167 (2015).

[4] V. A. Averchenko, V. Thiel, and N. Treps, Phys. Rev. A 89, 063808 (2014).

[5] Hans. A. Bachor and Timothy C. Ralphy, A guide ot experiments in quantum optics, Book (2003).

[6] D. Bouwmeester, J.-W. Pan, K. Mattle, M. Eibl, H. Weinfurter, and A. Zeilinger, Nature 390, 575 (1997).

[7] Robert W. Boyd, Nonlinear optics, the third version, Book (2003).

[8] B. J. Bloom, T. L. Nicholson, J. R. Williams, S. L. Campbell, M. Bishof, X. Zhang, W. Zhang, S. L. Bromley, and J. Ye, Nature 506, 7175 (2014).

[9] W. P. Bowen, R. Schnabel, and P. K. Lam, Phys. Rev. Lett. 90, 043601 (2003).

[10] S. L. Braunstein, Phys. Rev. A 71, 055801 (2005).

[11] S. L. Braunstein and Peter van Loock. Rev. Mod. Phys. vol. 77. pages 513-517 (2005).

[12] S. L. Braunstein and H. J. Kimble, Phys. Rev. Lett. 80, 4 (1998).

[13] Y. Cai, J. Feng, H. Wang, G. Ferrini, X. Xu, J. Jing, and N. Treps, Phys. Rev. A 91, 013843 (2015).

[14] C. M. Caves, Phys. Rev. D. 23, 1693 (1981).

[15] C. W. Chou, D. B. Hume, T. Rosenband, D. J. Wineland. Science 329, 5999 (2010).

[16] Coherent. Operator's Manual. Verdi V-18 Diode-Pumped Laser, 2005.

[17] Coherent. Operator's Manual. The Coherent Mira Model 900-B Laser, 1993.

[18] S. T. Cundiff, J. Ye, and J. L. Hall, Rev. Sci. Instrum. 72, 3749 (2001).

[19] T. F. Demarie, T. Linjordet, N. C. Menicucci, and G. K. Brennen, New J. Phys. 16, 085011 (2014).

[20] R. M. de Arajo, J. Roslund, Y. Cai, G. Ferrini, C. Fabre, and N. Treps, Phys. Rev. A 89, 053828 (2014).

[21] S.A. Diddams, J.K. Ranka, A. Stentz, R.S. Windeler, J.L. Hall, Science 288 (5466), 635-639 (2000).

[22] L.M. Duan, G. Giedke, J.I. Cirac and P. Zoller. Inseparability criterion for continuous variable systems. Phys. Rev. Lett. 84, 12, 2722–2725 (2000).

[23] A. P. Lund, et al, Phys. Rev. Lett. 113, 100502 (2014).

[24] Paul Dirac, The principles of quantum mechaics, Book (1930).

[25] B. Dutta, N. Mukunda, R. Simon, The real symplectic groups in quantum mechanics and optics. Pramana, 45, 6, 471–497 (1995).

[26] A. Einstein, B. Podolsky, and N. Rosen, Can quantum-mechanical description of physical reality be considered complete? Phys. Rev. 47 777 (1935).

[27] A.K. Ekert. Phys. Rev. Lett. 67, 6, 661–663 (1991).

[28] R. L. Fork, O. E. Martinez, and J. P. Gordon, Negaitive dispertsion using prism paris, Opt. Lett. 9. 5 (1984).

[29] A. Furusawa, J. L. Srensen, S. L. Braunstein, C. A. Fuchs, H. J. Kimble, and E. S. Polzik, Science 282, 706 (1998).

[30] G. Ferrini, J.-P. Gazeau, T. Coudreau, C. Fabre, and N. Treps, New J. Phys. 15, 093015 (2013).

[31] G. Ferrini, J. Roslund, F. Arzani, Y. Cai, C. Fabre, and N. Treps, Phys. Rev. A 91, 032314 (2015).

[32] S. Gerke, J. Sperling, W. Vogel, Y. Cai, J. Roslund, N. Treps, and C. Fabre, Phys. Rev. Lett. 114, 050501 (2015).

[33] M. Ghotbi and M. Ebrahim-Zadeh. Optical second harmonic gene- ration properties of BiB3O6. Optics Express 12, 24, 6002–6019 (2004).

[34] V. Giovannetti, S. Lloyd, L. Maccone, Advances in quantum metrology. Nature Photonics 5, 4, 222–229 (2011).

[35] R. J. Glauber. The quantum theory of optical coherence. Phys. Rev. 131, 2766 (1963).

[36] C. Gohle, T. Udem, M. Herrmann, J. Rauschenberger, R. Holzwarth, H. A. Schuessler, F. Krausz, and T. W. Hnsch, Nature 436, 234 (2005).

[37] G. Grynberg, A. Aspect and C. Fabre. Introduction to quantum optics: from the semi-classical approach to quantized light. Cambridge Univ Pr (2010).

[38] M. Gu, C. Weedbrook, N. Menicucci, T. Ralph, and P. van Loock, Phys. Rev. A 79, 062318 (2009).

[39] C. K. Hong, Z. Y. Ou, and L. Mandel, Phys. Rev. Lett. 59, 2044 (1987).

[40] Y F Huang, et al. Nature Communication 2, 546 (2011)

[41] S. Jiang, N. Treps, and C. Fabre, New J. Phys. 14, 043006 (2012).

[42] H. Katori, Nature Photonics 1 (2011).

[43] U. Keller, Nature 424, 831-838 (2003).

[44] H. J. Kimble, Nature 453, 1023-1030 (2008).

[45] P. Kumar. Quantum frequncy conversion. Opt. Lett. 15. 24. 1476-1478 (1990)

[46] Mikhail I. Kolobov. The spatial behavior of nonclassical light. Rev. Mod. Phys. 71, 1539–1589 (1999).

[47] A. M. Lance, T. Symul, W. P. Bowen, B. C. Sanders, and P. K. Lam, Phys. Rev. Lett 92, 177903 (2004).

[48] P. van Loock, C. Weedbrook, and M. Gu, Phys. Rev. A 76, 032321 (2007).

[49] C. F. McCormick, V. Boyer, E. Arimonda, and P. D. Lett, Opt. Lett 32, 178 (2007).

[50] M. J. Martin, et al., Science, 341, 6146, 632-636 (2013).

[51] P. Marian and T. A. Marian, Phys. Rev. A 86, 022340 (2012).

[52] D. Markham and B. C. Sanders, Phys. Rev. A 78, 042309 (2011).

[53] N. C. Menicucci, S. T. Flammia, and P. van Loock, Phys. Rev. A 83, 042335 (2011).

[54] N. C. Menicucci et al., Phys. Rev. Lett. 97, 110501 (2006).

[55] A. Monmayrant, S. Weber, and B. Chatel, J. Phys. B: at. Mol. Opt. Phys. 43, 103001 (2010).

[56] O. Morin, K. Huang, J. Liu, H. Le Jeannic, C. Fabre, and J. Laurat, Nature Photonics 8, 570 (2014).

[57] M. Chen, N. C. Menicucci, and O. Pfister, Phys. Rev. Lett. 112, 120505 (2014).

[58] http://www.newport.com/The-Effect-of-Dispersion-on-Ultrashort-Pulses/602091/1033/content.aspx

[59] M.A. Nielsen and I.L. Chuang, book, Quantum computation and quantum information. Cambridge university press, 2010.

[60] J.L. OBrien, J.V. Akira Furusawa and J. Vuckovic, Photonic quantum technologies. Nature Photonics 3, 12, 687–695 (2009).

[61] Z. Y. Ou, S. F. PEREIRA, H. J. Kimble, and K. C. PENG, Phys. Rev. Lett. 68, 3663 (1992).

[62] G. Patera. Quantum properties of ultra-short pulses generated by SPOPOs : multi-mode squeezing and entanglement. PhD thesis, 2008.

[63] G. Patera, N. Treps, C. Fabre, and G. J. de Valcrcel, Eur. Phys. J. D 56, 123 (2009).

[64] O.Pinel, Optique quantique multimode avec des peignes de frequence. PhD thesis, 2010.

[65] O. Pinel, P. Jian, R. M. De Araujo, J. Feng, B. Chalopin, C. Fabre, and N. Treps, Phys. Rev. Lett. 108, 083601 (2012).

[66] Z. Qin, L. Cao, H. Wang, A. M. Marino, W. Zhang, and J. Jing, Phys. Rev. Lett 113, 023602 (2014).

[67] R. Raussendorf and H. J. Briegel, Phys. Rev. Lett. (2001).

[68] MD Reid and PD Drummond. Quantum correlations of phase in non-degenerate parametric oscillation. Physical review letters, 60, 26, 2731–2733, 1988.

[69] Renne Medeiros de Arujo, Generation et manipulation de peignes de frequency quantique multimodes, PhD thesis, 2012.

[70] J. Roslund, R. M. De Araujo, S. Jiang, C. Fabre, and Nicolas Treps, Nature Photonics 8, 109 (2013).

[71] J. Roslund, O. M. Shir, T. Ba ck, and H. Rabitz, Phys. Rev. A 80, 043415 (2009).

[72] R. Schmeissner, Frequency combs at the quantum limit, PhD thesis, 2014.

[73] R. Schmeissner, J. Roslund, C. Fabre, and N. Treps, Phys. Rev. Lett. 113, 263906 (2014).

[74] R. Simon, ECG Sudarshan and N. Mukunda. Gaussian pure states in quantum mechanics and the symplectic group. Physical Review A 37. 8. 3028–3038 (1988).

[75] R. Simon, N. Mukunda and Biswadeb Dutta, Phys. Rev. A 49, 1567–1583 (1994).

[76] R. Simon, S. Chaturvedi, and V. Srinivasan, Journal of Mathematical Physics 40, 3632 (1999).

[77] R. Simon. Peres-Horodecki Separability Criterion for Continuous Variable Systems. Phys. Rev. Lett. 84, 2726–2729 (2000).

[78] http:// www.bnonlinear.com/products/xyslm/XYSeriesDS0909.pdf

[79] R.E. Slusher, LW Hollberg, B. Yurke, JC Mertz and JF Valley. Observation of squeezed states generated by four-wave mixing in an optical cavity, Phys. Rev. Lett. 55, 22, 2409–2412 (1985).

[80] Justin. B Spring, et al. Science 339, 6121, 798-801 (2013).

[81] R.E. Slusher, P. Grangier, A. LaPorta, B. Yurke and MJ Potasek. Pulsed squeezed light. Phys. Rev. Lett. 59, 22, 2566– 2569 (1987).

[82] D. E. Spence, P. N. Kean, and W. Sibbett, Opt. Lett. 16, 42 (1991).

[83] X. Su, A. Tan, X. Jia, J. Zhang, C. Xie, and K. Peng, Phys. Rev. Lett. 98, 070502 (2007).

[84] J. Sperling and W. Vogel, Phys. Rev. Lett. 111, 110503 (2013).

[85] X. Su, A. Tan, X. Jia, J. Zhang, C. Xie, and K. Peng, Phys. Rev. Lett. 98, 070502 (2007).

[86] X. Su, S. Hao, X. Deng, L. Ma, M. Wang, and X. Jia, Nature Communication (2013).

[87] X. Su, Y. Zhao, S. Hao, X. Jia, C. Xie, and K. Peng, Opt. Lett. 37, 5178 (2012).

[88] S. Takeda, T. Mizuta, M. Fuwa, P. van Loock, and A. Furusawa, Nature 500, 315318 (2013).

[89] Valrien Thiel, Modal analysis of ultrafast frequency combs: from classical to quantum spectral correlations, PhD Thesis (2015).

[90] N. Treps, N. Grosse, W. P. Bowen, C. Fabre, H.-A. Bachor, and P. K. Lam, Science 301, 940 (2003).

[91] N. Treps, U. Andersen, B. Buchler, P. Lam, A. Matre, H. A. Bachor, and C. Fabre, Phys. Rev. Lett. 88, 203601 (2002).

[92] T. Udem et al., Optical frequency metrology, Nature 416, 233 (2002).

[93] R. Ukai, S. Yokoyama, J. Yoshikawa, and P. van Loock, Phys. Rev. Lett. 107, 250501 (2011).

[94] Lev Vaidman. Teleportation of quantum states. Phys. Rev. A, 49, 1473–1476 (1994).

[95] X.-L. Wang, X.-D. Cai, Z.-E. Su, M.-C. Chen, D. Wu, L. Li, N.-L. Liu, C.-Y. Lu, and J.-W. Pan, Nature 518, 516 (2016).

[96] AM Weiner, Femtosecond pulse shaping using spatial light modulators. Review of scientific instruments 71, 5, 1929–1960 (2000).

[97] L.-A. Wu, H. J. Kimble, J. L. Hall, and H. Wu, Phys. Rev. Lett. 57, 2520 (1986).

[98] S. Yokoyama, R. Ukai, S. C. Armstrong, C. Sornphiphatphong, T. Kaji, S. Suzuki, J.-I. Yoshikawa, H. Yonezawa, N. C. Menicucci, and A. Furusawa, Nature Photonics 7, 982-986 (2013).

[99] M. Yukawa, R. Ukai, P. van Loock, and A. Furusawa, Phys. Rev. A 78, 012301 (2008).

[100] The LIGO scientific collaboration, Nature Physics 7. 962 (2011).